

**ISOTOPIC AND GEOCHEMICAL STUDIES OF THE LADAKH
ACCRETIONARY PRISM, NORTH WEST HIMALAYA**

By

ADITYA KHARYA

WADIA INSTITUTE OF HIMALAYAN GEOLOGY

DEHRADUN

Submitted



**IN PARTIAL FULFILLMENT OF THE REQUIREMENT OF
THE DEGREE OF DOCTOR OF PHILOSOPHY**

TO

UNIVERSITY OF PETROLEUM AND ENERGY STUDIES

DEHRADUN

OCTOBER, 2014

**ISOTOPIC AND GEOCHEMICAL STUDIES OF THE LADAKH
ACCRETIONARY PRISM, NORTH WEST HIMALAYA**

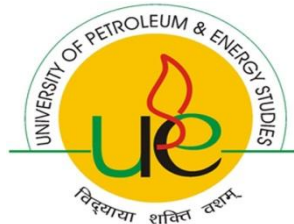
By

ADITYA KHARYA

WADIA INSTITUTE OF HIMALAYAN GEOLOGY

DEHRADUN

Submitted



**IN PARTIAL FULFILLMENT OF THE REQUIREMENT OF
THE DEGREE OF DOCTOR OF PHILOSOPHY**

TO

UNIVERSITY OF PETROLEUM AND ENERGY STUDIES

DEHRADUN

OCTOBER, 2014

Dedicated to my parents

DECLARATION

I hereby declare that this submission is my own work and that, to the best of my knowledge and belief, it contains no material previously published or written by another person nor material which has been accepted for the award of any other degree or diploma of the university or other institute of higher learning, except where due acknowledgment has been made in the text.



Aditya Kharya



वाडिया हिमालय भूविज्ञान संस्थान

(भारत सरकार के विज्ञान एवं प्रौद्योगिकी

विभाग का एक स्वायत्तशासी संस्थान)

33, जनरल महादेव सिंह मार्ग,

देहरादून - 248001 (उत्तराखण्ड)

WADIA INSTITUTE OF HIMALAYAN GEOLOGY

(An Autonomous Institution of

Deptt. of Science & Technology, Govt. of India)

33, General Mahadeo Singh Road,


DEHRA DUN - 248001 (UK)

THESIS COMPLETION CERTIFICATE

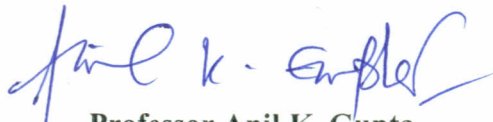
This is to certify that the thesis on **“ISOTOPIC AND GEOCHEMICAL STUDIES OF THE LADAKH ACCRETIONARY PRISM, NORTH WEST HIMALAYA”** by **ADITYA KHARYA** in Partial completion of the requirements for the award of the Degree of Doctor of Philosophy (Earth Sciences) is an original work carried out by him under our joint supervision and guidance.

It is certified that the work has not been submitted anywhere else for the award of any other diploma or degree of this or any other University.

Co Guide:


Dr. P. K. Mukherjee

Guide:


Professor Anil K. Gupta

ACKNOWLEDGEMENTS

My days at Wadia Institute have been the journey of learning towards acquainting concepts of Himalayan Orogeny which helped in pursuing my thesis. This has been possible with sincere guidance, help and wishes from many individuals.

I sincerely express my gratitude to **Prof. Anil K. Gupta (Director, WIHG)** and **Dr. P. K. Mukherjee** my guides, with whom I have the pleasure of working despite being a novice in this field. I learned the intricacies of the subjects through their meticulous ways of pursuing every aspect of science. Sincere guidance, involvement and concerns from Dr. H.K. Sachan and Dr. Santosh K. Rai are highly appreciable. Their scientific suggestions and support helped me in various laboratory and field activities. Though, there was ample freedom to pursue my own plans including field campaigns to the final data acquisitions but they always prevailed upon critically on the quality of the data. Their innovative suggestions on experimental protocols and discussions were very fruitful.

I express deep sense of gratitude to the Authorities of University of Petroleum and Energy Studies, Dehradun for their guidance and support.

I thank **Prof. Zachary Sharp (University of New Mexico, USA)** **Dr. Sunil K. Singh (PRL, Ahmedabad)**, **Dr. V. C. Thakur**, **Dr. S. K. Ghosh**, **Dr. R. Jayangondaperumal**, **Dr. Vikash** and **Mr. Satheesh Deekshith (Thermo Scientific, India)** for scientific discussion and encouragement during various sessions of interactions with them. Most of the results described in this thesis

would not have been obtained without a close collaboration with **Dr. Sunil K. Singh** of PRL Ahmedabad and **Dr. V. Balram** of NGRI, Haydarabad.

I would also like to thank the academic programme committee WIHG for suggestions in improving the thesis.

I take this opportunity to sincerely acknowledge the Department of Science and Technology (DST), Ministry of Science and Technology, Government of India, New Delhi, for providing financial assistance in the form of Fellowship which buttressed me to perform my work comfortably.

Life at Wadia Institute was really pleasant with the companies of **Shri Sameer Tiwari, Som Dutt, Anil Kumar, Tanuj Shukla, Ms. Manju Negi, Nikita G. Parmar, Rakhi Rawat, Suman Lata Rawat, Divya Thakur, Dr. Kavita Tripathi, Dr. Shivani Pandey** for their untried help during various measurements and compiling the Ph.D. thesis. I am also thankful to **Dr. P. P. Khanna, Dr. N. K. Saini, Dr. R. Islam, Dr. Rajesh Sharma, Dr. A.K. Singh, Dr. S. S. Thakur, Dr. V. Balram and Dr. M. Satynarayanan** for their constant support and encouragement during the experimentation.

I also acknowledge the support of library, thin section, documentation unit and stores and purchase section for help during my thesis.

Last but not the least, I owe this thesis to my parents and family members who always stood by me and provided strength in pursuing this work. Their sincere encouragement and inspiration throughout my research work has helped me to lift myself uphill this phase of life. Besides this, several people have knowingly and unknowingly helped me in the successful completion of this PhD dissertation are respectfully acknowledged.

Aditya Kharya

EXECUTIVE SUMMARY

The Ladakh Accretionary prism is well developed in the fore arc basin of the magmatic arcs of the Ladakh region along the Indus–Tsanspo Suture Zone (ITSZ). There are two accretionary wedges identified that are related to two different subduction events. The first one was developed at the forefront of Dras island arc some times during 120 to 100 Ma and is referred to as the Paleo Accretionary Prism (PAP). While, a second subduction ensued to the south following continued northward push of the Indian Plate giving rise to the Ladakh-Kohistan magmatic arc and the development of the second accretionary prism at the forearc basin called South Ladakh Accretionary Prism (SLAP) sometimes during 55 to 23 Ma, i.e. post India-Asia continental collision. In view of the paramount importance and crucial tectonic set-up in relation to the Himalayan orogeny, these accretionary prisms form the basis of this research. These two accretionary complexes, jointly referred to as the Ladakh Accretionary Prism (LAP), have been the point of attraction for previous workers and detailed study related to the structure, geochemistry, stratigraphy and sedimentological attributes have been carried out. However, copious quartz-calcite veining occurring within are ignored. Preliminary study on these veins revealed that these are no ordinary veins, but have some deep rooted connections and tectonic implications.

With this background, the present research topic was undertaken with the specific aim to extract the records of tectono-magmatic activity occurring at deep underneath the collision zone at the later stages of the Himalayan orogeny. The present work is to address these problems and explains the source of vein fluid and their entrapment process along with its tectonic implications. To accomplish this study, four transverse sections across the LAP were systematically sampled and studied using tools like, petrography, fluid inclusion studies, stable (C, O) isotopic and radiogenic isotopic studies ($^{87}\text{Sr}/^{86}\text{Sr}$, $^{206}\text{Pb}/^{204}\text{Pb}$, $^{207}\text{Pb}/^{204}\text{Pb}$, and $^{208}\text{Pb}/^{204}\text{Pb}$). Whereas Shergol and Zildat sections belong to PAP; the Nimu–Chilling (NC) and Lato–Miru–Upshi (LMU) sections are part of the SLAP.

The fluid inclusion study suggests that the vein forming fluid was highly saline in nature and tectonically induced. It also suggests that the veins were derived from the deeper part of the Earth's crust and rapidly exhumed at the surface. The presence of various re-equilibrated fluid inclusion textures in quartz-calcite veins indicate isothermal decompression, which signify the very fast rate of fluid flow due to high surge of tectonic activity. The REE pattern of quartz and calcite are shown nearly flat pattern alongwith or without Eu positive anomaly (or $\text{Eu}/\text{Eu}^* > 1$). Some calcite samples also show high REE contents upto >10 times chondrite levels, which may indicate strong reducing condition similar to mantle and magmatic systems. The REE concentration of calcite is >40 times higher (partition coefficient) than that of co-paired quartz. Partition coefficients are thus,

similar to the immiscible carbonate–silicate melts suggesting magmatic linkage to the fluid extraction.

The fluid source is also verified through isotopic systematics using stable (C and O) isotopes and radiogenic (Sr and Pb) isotopes of carbonate veins. The stable isotope systematics suggests the mantle, magmatic or ophiocarbonate affinity of the fluid source. Whereas, the radiogenic (Sr and Pb) isotopes are strongly suggest mantle derivation of fluid source. The $\delta^{18}\text{O}$ ratios of quartz minerals were analyzed, which also indicate its kinship to a magmatic origin.

The oxygen isotope thermometric estimates (in Co-existing Quartz and Calcite minerals pair) suggest the temperature of crystallization in the range of 120–470°C. The oxygen isotopic ratio of the same fluid calculated using the quartz-water and calcite-water fractionation equations derived by Shiro and Sakai (1972) and O’Neil et al. (1969), respectively. The calculated oxygen isotopic composition of the fluids varies in range from -3.5‰ to +8.6‰ (VSMOW) which are well within the range of fluids of mantle/ophiocarbonate.

The isotopic studies of veins in LAP collectively suggest that the fluid were derived through mantle activity beneath the collision zone during Miocene and emplaced within the LAP as quartz-calcite veins. We infer that there was a late phase of mantle magmatic activity which was otherwise not known earlier and these veins are the only manifestations of this activity. The magmatic activity also

reported from Ladakh-Kohistan magmatic arc during this period is, therefore, concomitant to this mantle fluid activity in LAP. Deep seated thrust (Indus thrust) and several local thrust were observed in the LAP lithounits into which these fluids emplaced, as surface expressions of the same event though the younger magmatism at Kohistan arc may be correlated to the coeval to this mantle activity. It is therefore worthwhile to mention that earlier tectonic model (e.g. Clift et al., 2000) envisaged locking up of the Indian plate beneath the Asian plate well before the early Miocene. However, recent geophysical imaging below the collision zone and other indirect evidences revealed presence of broken part of the Indian slab (Chemenda et al., 2000; Ji et al., 2009). If so, then it becomes important to know when was it happened and what are its manifestations. Results of the present study finds support to this phenomena as also proposed by Ji et al (2009) based on felsic magmatism in space and time in the back arc setup of Gangdesh. Taking clue from this, we propose a new modified model of late stage development in the collision zone that explains a plausible mechanism for derivation of fluid at deeper level into the mantle and its transportation to the surface and attendant interaction with the marine components of LAP. According to this model, following the breakoff of the down going Indian continental plate, mantle upwelling took place resulting in decompressional fluid release and melting. Whereas the younger Kohistan part of magmatic arc may be part of this magmatic activity, the extensive veining sweeping through the accretionary prism is caused by the fluid activity. However, the isotopic signatures of these fluids were modified through fractionation and interaction with the marine sediments

towards southern margin. The fluid involved in the formation of veins migrated in small pulses from the mantle simultaneously with the formation of Kohistan magmatic arc during the Miocene period. As against the general wisdom, that the Indian plate swept beneath the Asian plate and seized the subduction process during late Oligocene-early Miocene, the results of the present study imply reactivation of mantle magmatic activity at the collision zone during the Miocene epoch.

Table of Contents

Acknowledgements	iv
Executive Summary	vi
Table of Contents	xi
List of Figures	xiii
List of Tables	xx
Chapter 1: Introduction	1
1.1 Overview and Research Motivation	2
1.2 Literature Review and Background.....	10
1.3 Objectives	13
1.4 The Study Area.....	16
1.5 Contribution of Present Research.....	18
Chapter 2: Geological Setting	20
2.1 Evolution of The Himalaya	21
2.1.1 Geographical Divisions of The Himalaya	26
2.1.2 Litho– and Tectono– Stratigraphical Divisions of The Himalaya.....	29
2.2 Regional Geology of The Ladakh Himalaya.....	31
2.3 Geological Setting of The Ladakh Accretionary Prism (LAP)	37
2.3.1 Geology of Paleo Accretionary Prism (PAP).....	39
2.3.2 Geology of South Ladakh Accretionary Prism (SLAP)	42
2.3.2.1 Geology of Nimu–Chilling (NC) Section	44
2.3.2.2 Geology of Lato–Miru–Upshi (LMU) Section	50
2.3.3 Geology of Zildat Section	55
2.4 Sampling Strategy and Field Relation.....	59
Chapter 3: Petrography and Fluid Inclusion	66
3.1 Analytical Techniques	68
3.1.1 Petrography.....	68
3.1.2 Microthermometry.....	68
3.1.3 Micro–Raman Spectroscopy	69
3.2 Results	72
3.2.1 Mineral Petrography and Microstructures.....	72
3.2.2 Fluid Inclusion Petrography	79
3.2.3 Microthermometric Measurements	94
3.2.4 Micro–Raman Spectroscopy	104

3.2.5 P-T conditions for the formation of veins	106
Chapter 4: Isotopic and Trace Elemental Geochemistry	114
4.1 Analytical Techniques.....	117
4.1.1 Analytical Technique of Trace Elemental Geochemistry	119
4.1.2 Analytical Technique of Stable Isotope Geochemistry	125
4.1.2.1 Determination of $\delta^{13}\text{C}$ and $\delta^{18}\text{O}$ in carbonate phase.....	129
4.1.2.2 Determination of $\delta^{18}\text{O}$ in silicate phase	130
4.1.2.2.1 The Laser Fluorination Technique.....	132
4.1.3 Analytical Techniques for Measurement of Radiogenic Isotopic Composition	141
4.1.3.1 Strontium Isotopic Measurements	143
4.1.3.2 Lead Isotope Geochemistry	145
4.2 Results	147
4.2.1 Trace and REE Geochemistry of Quartz and Calcite.....	147
4.2.2 Isotope Geochemistry in Carbonate Phase	159
4.2.2.1 $\delta^{13}\text{C}$ and $\delta^{18}\text{O}$ of calcite	159
4.2.2.2 $^{87}\text{Sr}/^{86}\text{Sr}$ ratio of calcite	164
4.2.2.3 Lead Isotopic ratio of calcite	166
4.2.2.4 Isotopic correlations of calcite	169
4.2.3 Isotope Geochemistry in Silicate Phase.....	171
4.2.3.1 $\delta^{18}\text{O}$ of quartz	171
4.2.3.2 Oxygen Isotope Thermometry	173
4.2.4 $\delta^{18}\text{O}$ of Fluid Species.....	176
4.3 Discussion.....	178
Chapter 5: Proposed Evolutionary Model of The Ladakh Accretionary Prism	184
Chapter 6: Conclusions and Future Prospectives.....	200
6.1 Conclusions	201
6.2 Future Prospectives.....	206
Chapter 7: References	207
Appendixes.....	236
Appendix A: Sample Locations	237
Appendix B: Microthermometric Measurements.....	243
Appendix C: Isotopic Results.....	265

List of Figures

- Figure 1.1:** A generalized sketch of the plate tectonics model showing different tectonic set-ups. Plate boundary and their deformation process (adopted from http://en.wikipedia.org/wiki/Plate_tectonics)6
- Figure 1.2:** Regional Geological Map of the Study area (Ladakh Himalaya) modified after Thakur and Mishra (1984); Mahéo et al (2004, 2006). The rectangular box refers to the investigation sections of this study- [A] represent Shergol area (see Figure 2.4); [B] the Nimu–Chilling (NC) Section (see Figure 2.6 for detail); [C] Lato–Miru–Upshi (LMU) Section (see Figure 2.8 for detail) and [D] the Ziladt Section (see Figure 2.10 for detail).....17
- Figure 1.3:** Cross sectional view of the Ladakh Accretionary prism (LAP)18
- Figure 2.1:** Schematic diagram of the Himalayan orogeny and shaping of accretionary prisms, modified after Clift et al (2000); Mahéo et al (2006) and Meng et al (2012).....25
- Figure 2.2:** A generalized Litho-Tectonic Map of the Himalaya (modified from Searle et al., 2003 and Law et al., 2004).....28
- Figure 2.3:** Regional Geological Map of the Study area (Ladakh Himalaya) modified from Thakur and Mishra (1984); Mahéo et al (2004, 2006). The rectangular box refers to- [A] Shergol area (see Figure 2.4); [B] the Nimu–Chilling (NC) Section (see Figure 2.6 for detail); [C] Lato–Miru–Upshi (LMU) Section (see Figure 2.8 for detail) and [D] the Ziladt Section (see Figure 2.10 for detail)33
- Figure 2.4:** Geological Map of the Shergol ophiolitic mélangé (SOM) or western paleo accretionary prism (western PAP), modified from Honegger et al (1989) ..40
- Figure 2.5:** Photographs of Shergol Ophiolitic mélangé (or western PAP). (a) Panoramic view of western PAP, and (b) Contact metamorphism of serpentinite and rodingite.....41
- Figure 2.6:** Geological Map of the Nimu–Chilling Section modified from Searle et al (1990) and Henderson et al (2010b).....47

Figure 2.7: Panoramic view of Zanskar Gorge and Nimu–Chilling section. (a) confluence of Indus–Zanskar River; (b) Zanskar Gorge at Choksti bridge; (c) Deposition of Mud stone, Sand/Silt stone and the presence of veins	48
Figure 2.8: Geological Map of the Lato-Miru-Upshi (LMU) section, modified from Henderson et al (2011)	51
Figure 2.9: Panoramic view of LMU Section.....	52
Figure 2.10: Geological Map of the eastern paleo accretionary prism (eastern PAP), modified after De Sigoyer et al (2004).....	57
Figure 2.11: Panoramic view of eastern PAP along with the exotic blocks of limestone	58
Figure 2.12: Field photographs of various types of veins present in Shergol area. (a-d) Fault/Fracture Filling veins, and (e-f) Network type veins.....	62
Figure 2.13: Field photographs of veins from NC section. (a-d) Fault/Fracture Filling veins, (e-f) Network type veins, (g) Bounded Neck, and (h) Sigmoidal type veins	63
Figure 2.14: Field photographs of veins Intruded in the sediments of LMU section. (a-d) Fault/Fracture Filling veins, (e) Sigmoidal type veins, and (f) Network type veins	64
Figure 2.15: Field photographs of veins from Zildat section. (a-c) Fault/Fracture Filling veins, (d) Network type veins, and (e) Bounded Neck type veins	65
Figure 3.1: A schematic diagram of Raman principle and analytical technique ..	70
Figure 3.2: Micro photographs of mineralized veins showing various microstructures. a) very thin calcite twining pattern, b) slightly thick twining pattern of calcite, c) 3D view of calcite grain along with micro-fracture, d) thin to oval twining pattern of calcite along with micro fractures, e) thick fractured twining pattern of calcite, and f) 3D view of thick twining pattern of calcite. Where CC = Calcite and Qtz = Quartz	73
Figure 3.3: Micro photographs of mineralized veins, showing various microstructures. a) oval morphology of fractured calcite, b) thick to oval twining morphology of fractured calcite grain, c-d) oval shape morphology of calcite	

mineral, e) pillow like twining pattern of calcite, and f) highly fractured calcite grains showing thin to thick with oval morphology74

Figure 3.4: Micro photographs of mineralized veins, showing various microstructures. a) Mosaic of quartz grains with flow like calcite twining pattern, b) co-existing pair of quartz and calcite minerals, c) calcite mineral bracketed by the quartz grains, d-e) elongated quartz and calcite minerals in same manner, and f) Quartz inclusion within the calcite mineral grain. CC = Calcite and Qtz = Quartz.....75

Figure 3.5: Micro photographs of mineralized veins, showing various microstructures. a-b) Quartz inclusion within the calcite mineral grain, c) Mosaic of quartz grains, d) triple point junction and recrystallization of quartz grains, e) elongated quartz grains, and f) triple point junction along with bulging of quartz grain. CC = Calcite and Qtz = Quartz.....76

Figure 3.6: Microstructures and Deformation Temperature of veins adopted after Ferrill et al. (2004), Passchier and Trouw (2005), Stipp et al. (2002 and 2010) ...78

Figure 3.7: Primary mono phase, bi phase and three phase inclusions of PAP. Where V = Vapor, L = Liquid, S = Solid and G = Gas80

Figure 3.8: Various primary re-equilibration inclusions of PAP.....81

Figure 3.9: Trails of secondary inclusions of PAP82

Figure 3.10: Mono phase gas rich primary fluid inclusions of SLAP85

Figure 3.11: Bi phase primary and pseudosecondary fluid inclusions of SLAP ..86

Figure 3.12: Bi phase and Three phase primary inclusions of SLAP87

Figure 3.13: Bi phase negative crystal and stretched fluid inclusions of SLAP...88

Figure 3.14: Re-equilibration pattern of primary bi phase inclusions of SLAP ...89

Figure 3.15: Re-equilibration pattern from SLAP indicating the tectonic event..90

Figure 3.16: Re-equilibrated mono phase and ‘C’ shape inclusions of SLAP91

Figure 3.17: Implosion texture and trail of pseudosecondary inclusions of SLAP92

Figure 3.18: Trails of secondary inclusions from SLAP	93
Figure 3.19: Homogenization temperature (Th) of various types of fluid inclusions present in the Shergol area. (a) Th of Primary CH ₄ inclusions, (b) Th of Primary CO ₂ inclusions, (c) Th of Primary H ₂ O-NaCl inclusions, and (d) Th of Secondary H ₂ O-NaCl inclusions.....	98
Figure 3.20: Homogenization temperature (Th) of various types of fluid inclusions present in the Nimu–Chilling (NC) Section (Zanskar Gorge). (a) Th of Primary CH ₄ inclusions, (b) Th of Primary CO ₂ inclusions, (c) Th of Primary H ₂ O-NaCl inclusions, and (d) Th of Secondary H ₂ O-NaCl inclusions	100
Figure 3.21: Homogenization temperature (Th) of various types of fluid inclusions present in the Lato–Miru–Upshi (LMU) Section. (a) Th of Primary CH ₄ inclusions, (b) Th of Primary CO ₂ inclusions, (c) Th of Primary H ₂ O-NaCl inclusions, and (d) Th of Secondary H ₂ O-NaCl inclusions	102
Figure 3.22: Homogenization temperature (Th) of various types of fluid inclusions present in the Zildat section. (a) Th of Primary CH ₄ inclusions, (b) Th of Primary CO ₂ inclusions, (c) Th of Primary H ₂ O-NaCl inclusions, and (d) Th of Secondary H ₂ O-NaCl inclusions.....	103
Figure 3.23: Raman shift of fluid inclusions in both quartz and calcite mineral phase	105
Figure 3.24: Exhumation path with entrapment P-T condition of fluid for paleo accretionary prism (PAP).....	107
Figure 3.25: Bi variant plot of Th vs Tfm of primary and secondary fluid inclusions for paleo accretionary prism (PAP)	109
Figure 3.26: Exhumation path with entrapment P-T condition of fluid for South Ladakh Accretionary Prism (SLAP).....	111
Figure 3.27: Bi variant plot of Th vs Tfm of primary and secondary fluid inclusions for South Ladakh accretionary prism (SLAP).....	112
Figure 4.1: A schematic diagram showing the Mass Spectrometric measurement protocol	118
Figure 4.2: Schematic diagram of quadrupole type ICPMS illustrating the working principle of the technique	121

Figure 4.3: Author at work on ICPMS in Mass Spectrometer Lab at WIHG, for trace elemental analysis	122
Figure 4.4: A Schematic diagram of Inductively Coupled Plasma Mass Spectrometer (ICPMS).....	123
Figure 4.5: A Schematic diagram of isotope Ratio Mass Spectrometer (IRMS) illustrating the working principle and configuration of the instrument used in the study	127
Figure 4.6: Photograph of Stable isotope facility at WIHG	128
Figure 4.7: A Schematic diagram of stable isotopic analysis in carbonate phase	130
Figure 4.8: A Schematic flow sheet diagram of Laser fluorination system for oxygen isotope measurement in silicate phase	133
Figure 4.9: A Schematic diagram of sample chamber and Ni sample holder used in the laser fluorination system.....	136
Figure 4.10: Photograph of MC–ICPMS facility (Nu Plasma) used in this study for Pb isotope systematic at University of Cape Town, Cape Town, South Africa	145
Figure 4.11: Trace elemental plots of SLAP with Sr concentration. (A) Sr vs Th, (B) Sr vs Hf, and (C) Sr vs Sc.....	150
Figure 4.12: Trace elemental plots of SLAP with U concentration. (A) U vs Th, (B) U vs Hf, and (C) U vs Sc	151
Figure 4.13: Trace elemental plots of SLAP with Sc concentration. (A) Sc vs Th, (B) Sc vs Hf, and (C) Sc vs Y	152
Figure 4.14: Trace elemental plots of PAP with U concentration. (A) U vs Sr, and (B) U vs Rb	153
Figure 4.15: Co-paired Quartz and Calcite vein REE plots of PAP. (A) Represent the data set of Shergol area, (B) Shows the REE trend of Zildat section	155
Figure 4.16: Co-paired Quartz and Calcite vein REE plots of SLAP. (A) Represent the data set of NC section, (B) Shows the REE trend of LMU section	156

Figure 4.17: Bi-variant plot of La/Gd vs Eu/Eu*	158
Figure 4.18: Stable C and O isotopic distribution of vein calcite from Shergol section. (a) Systematic distribution of $\delta^{13}\text{C}$, and (b) Systematic distribution of $\delta^{18}\text{O}$	160
Figure 4.19: Stable C and O isotopic distribution of calcite veins between two (Indus and Zaskar) thrust in NC and LMU sections of South Ladakh accretionary prism (SLAP). (a) Systematic distribution of $\delta^{13}\text{C}$ in NC Section, (b) Systematic distribution of $\delta^{18}\text{O}$ in NC Section, (c) Systematic distribution of $\delta^{13}\text{C}$ in LMU Section, and b) Systematic distribution of $\delta^{18}\text{O}$ in LMU Section.....	161
Figure 4.20: Systematic Stable C and O isotopic distribution of calcite veins between Zildat Detachment Fault (ZDF) and Nidar Ophiolite Complex (NOC) in Zildat section of PAP	162
Figure 4.21: Two Isotope $\delta^{13}\text{C}$ and $\delta^{18}\text{O}$ plot of calcite veins from the Ladakh Accretionary Prism. Data Source for Mantle Carbonate Field (Taylor et al., 1967); Primary Carbonatite field (Ray and Ramesh, 2006); Ophicarbonates (Perkins et al., 2006); South American carbonatite (Bell and Simonetti, 2010).....	163
Figure 4.22: Distribution of $^{87}\text{Sr}/^{86}\text{Sr}$ ratio between two (Indus and Zaskar) thrust in NC and LMU sections of SLAP. (a) Systematic distribution of $^{87}\text{Sr}/^{86}\text{Sr}$ in NC Section, and (b) Systematic distribution of $^{87}\text{Sr}/^{86}\text{Sr}$ in LMU Section. Data source for Ladakh Magmatic arc is Honegger et al (1982); Weinberg and Dunlap (2000).....	165
Figure 4.23: Bi-variant plots of a) $^{206}\text{Pb}/^{204}\text{Pb}$ vs $^{87}\text{Sr}/^{86}\text{Sr}$, b) $^{206}\text{Pb}/^{204}\text{Pb}$ vs $^{208}\text{Pb}/^{204}\text{Pb}$, and c) $^{206}\text{Pb}/^{204}\text{Pb}$ vs $^{207}\text{Pb}/^{204}\text{Pb}$ of LAP (all four studied sections). Data source for OIBs: N-MORB, normal MORB; EM I, Enrich Mantle I; EM II, Enrich Mantle II; DMM, Depleted MORB Mantle and HIMU, high U/Pb Mantle are Hart et al (1986); Hart (1988); NHRL, Northern Hemisphere Reference Line (Hart, 1984). Data source for carbonatites and limestone: AmbaDogar Carbonatites (Simonetti et al., 1995); East African Carbonatites (Kalt et al., 1997); Tamil Nadu Carbonatites (Schleicher et al., 1998); Sung Vally Carbonatites (Veena et al., 1998); and Vindhyan Limestones (Ray et al., 2003)	168
Figure 4.24: Bi-variant plot of two isotopes in SLAP to trace the fluid source. (a) $^{87}\text{Sr}/^{86}\text{Sr}$ vs $\delta^{18}\text{O}$, and (b) $^{87}\text{Sr}/^{86}\text{Sr}$ vs $\delta^{13}\text{C}$. The Sr isotope value of Mantle/Magmatic field obtained from the Ladakh magmatic area.....	170

Figure 4.25: Systematic $\delta^{18}\text{O}$ distribution of quartz veins between two (Indus and Zaskar) thrust in NC and LMU sections of SLAP. (a) Systematic distribution of $\delta^{18}\text{O}$ in NC Section, and (b) Systematic distribution of $\delta^{18}\text{O}$ in LMU Section ...172

Figure 4.26: The crystallizing Temperature of veins from Indus to Zaskar thrust using oxygen isotope thermometry in NC and LMU sections of SLAP. (a) variation in crystallizing temperatures of veins between Indus and Zaskar thrust, (b) difference in $\delta^{18}\text{O}$ composition between two mineral (quartz and calcite) phase, and (c) Systematic distribution of $\delta^{18}\text{O}_{(\text{Qtz})}$ and $\delta^{18}\text{O}_{(\text{Calcite})}$ in NC and LMU Sections between Indus and Zaskar thrusts174

Figure 4.27: $\delta^{18}\text{O}$ of vein fluid from LAP. The mantle field has been plotted by using the $\delta^{18}\text{O}$ value from Mantle carbonate field (Taylor et al., 1967) and the $\delta^{18}\text{O}$ value of marine carbonate field were used from Sharp (2007). The homogenization temperatures were assumed 50, 100, 150, 200, 250, 300 and 350°C178

Figure 5.1: Generalized schematic sketch diagram showing stage wise progressive development of accretionary prism in Himalayan orogeny, modified after Mahéo et al (2006); Meng et al (2012). Where LMA referred to Ladakh Magmatic Arc; PAP for Paleo Accretionary Prism and SLAP for South Ladakh Accretionary Prism190

Figure 5.2: Deposition of sediments for shaping LAP and locking of Indian plate, modified after Clift et al (2000); Ji et al (2009); Henderson et al (2011).....191

Figure 5.3: Proposed evolutionary model of development of Ladakh Accretionary Prism (LAP) at penultimate stage of Himalayan orogeny. (a) Slab break off and opening path for intrusion of mantle fluid in LAP, (b) Systematic distribution of fluid along the thrust/fault plane and their isotopic variation with changing of litho units195

Figure 5.4: Inversion model obtained by inverting TM mode and magnetic field transfer functions (Arora et al., 2007). The location of Indian Moho obtained from Rai et al (2006). MHT, Main Himalayan Thrust; HHC, Higher Himalayan Crystalline; TMD, Tso Morari Dome; ITSZ, Indus Tsangpo Suture zone197

List of Tables

Table 2.1: Geographical, Stratigraphic and Structural divisions of the Himalaya	31
Table 2.2: Stratigraphical succession/ compression of NC and LMU section.....	54
Table 3.1: Fluid composition of the study area.....	95
Table 3.2: Summary of micro-thermometric measurements for Primary Inclusions	96
Table 3.3: Summary of micro-thermometric measurements for Secondary Inclusions	97
Table 3.4: Summary of P–T condition of the veins and exhumation depth of the study area at penultimate stage of evolution of the Himalaya	106
Table 4.1: Various analytical techniques used in this study	116
Table 4.2: Physical Parameters of ICPMS used in this study (After Khanna et al., 2009 and Mukherjee et al., 2014)	124
Type 4.3: Distribution coefficient (K_D CC/Qtz) of REEs between calcite and quartz.....	157
Table 4.4: Stable C and O isotopic distributions of calcite veins from LAP.....	160
Table 4.5: Distribution of $^{87}\text{Sr}/^{86}\text{Sr}$ ratio in calcite veins from NC and LMU sections of SLAP.....	166
Table 4.6: Stable C and O isotopic distribution of vein calcite from the Ladakh Accretionary Prism	167
Table 4.7: $\delta^{18}\text{O}$ Distribution of quartz veins from the South Ladakh Accretionary Prism	171
Table 4.8: Table 4.8: Crystalline Temperature of veins of NC and LMU sections using Oxygen Isotope Thermometry	175
Table 4.9: Oxygen Isotope values of Fluid from LAP.....	177
Table 5.1: Source of vein forming fluid(s)	187

CHAPTER 1:

INTRODUCTION

CHAPTER 1:

INTRODUCTION

1.1 OVERVIEW AND RESEARCH MOTIVATION

The Himalaya is the youngest mountain chain on the planet Earth having an arcuate shaped 2400 Km long mountain front and comprising of numerous highest peaks of the world, including the highest peak on the Earth, the Mount Everest (8,848 meter height). The average elevation of Himalayan mountain chain is about 4,500 meter (in Ladakh), which makes it a cold desert. The Himalaya has a great significance to the people of India which plays an important role as an orographic barrier that influences the Indian monsoon system since the early Miocene period. Besides, the Himalaya is a place from where major rivers originates, including Ganga, Brahmaputra, and Indus etc. that are lifelines to a major population of the north Indian subcontinent plays a vital role in the growth of the Indian economy. In addition to its great geographical and climatic importance, the Himalaya is much more important in Hindu folklore than just a majestic mountain chain that extends in a 2400 Km arc. The Himalaya is not only the place for rare sanative herbs, or winter sports, it has always been an abode of Hindu saints and Gods. Therefore, the Himalaya is also referred to as devbhomi or God-souled.

The most holy river for Hindus, the Ganga, also originates from the Himalaya, which supplies water to the people of most densely populated Ganga Basin. The Himalaya is therefore as important scientifically as it is societally, culturally and economically to the people of the Indian subcontinent.

The high topography of the Himalaya is a result of Continent–Continent collision where Indian plate subducted beneath the Asian plate. Such type of tectonic activity taken place at convergent plate boundary where two plates collide against each other. In plate tectonics, a convergent plate boundary is an actively deforming region where two (or more) tectonic plates move toward each other. This movement of plates closes and consumes the intervening oceanic plate through the process of subduction of one plate below the other. This results in drifting of continental plates through geological ages and often ending up with collision of continental plates; thus making great mountain chains such as the Himalaya. The sinking of the cold plate, oceanic or continental, deep into the asthenosphere produce partially melted subducting plate and adjoining lithosphere producing extensive magmatism all along the arcuate shaped forefront of the suture zone, referred to as “Arc Magmatism”, which is common phenomenon in the convergent plate boundary (Figure 1.1). Similarly, when a lithospheric plate is subducting at one end, an extension or rifting takes place at the other end and is referred to as divergent boundary. This divergence also causes extensive magmatism through the upwelling of the anthenospheric mantle, e.g. Mid-oceanic ridge.

In convergent tectonic set up, an accretionary prism is developed at the plate boundary in the forearc basin over the subducting plate through ongoing sedimentation and deposition of sediments as well as volcano–clastics derived from both sides of the tectonic plate and accreted onto the overlying plate (Figure 1.1; Mahéo et al., 2006). At the subduction zones, chemical components are cast–off into the mantle through deep subduction and returned to the surface by the arc volcanism. These processes are responsible for the movement of fluids at various stages and levels within subduction zones, which are associated with large volumes of fluid that are dispersed in pulses through seismic activities of larger magnitude (Lallemand and Funicello, 2009). The fluid can be intruded in an accretionary prism due to the seismicity. Most of the fluids are trapped either within hydrous minerals or as pore water in the oceanic crust and superjacent sediments. These entrapments of fluids are expelled within top few tens of kilometers of the subduction zone (Moore and Vrolijk, 1992) and percolate into the wedge–shaped upper–plate of the accretionary prism within the subduction zone. Experimental and observational evidence indicates sedimentary accretionary prism rocks experience dehydration reactions throughout the subduction process (Vrolijk, 1987, 1990; Sample et al., 1993; Jarrard, 2003; Rowe and Sreaton, 2009). These fluids play significant role in development of faulting through both static and dynamic weakening processes during earthquake events at the crustal level (Hubbert and Rubey, 1959; Sibson, 1973; Mase and Smith, 1987; Sibson et al., 1988; Cox, 1995; Ujiie et al., 2007). These processes are usually dominant along the plate boundary thrust and faults

(Yamaguchi et al., 2012). Most of the accretionary prisms are bounded by the weak planes such as faults or thrusts. Records of various stages of movement of fluid history are preserved as veinlets in the development of the mountain chain. The Himalaya is the best example in the world for such type of study, which was developed initially as Alpine-type convergent zones like oceanic–continental subduction followed by continent–continent collision between Indian and Asian plates (Bally, 1981; Meng et al., 2012). Meng et al (2012) suggested that the age and focus of the initial India–Asia collision are at about 50 Ma and 24°N, respectively. These authors further suggest that Tibet stopped India’s northward push during the first 16 Ma of initial impact (~65 Ma) from the collision allowing only little latitudinal displacement. It was little after 34 Ma that Greater India was consumed and thicker Indian Craton subsequently made contact with Asia, resulting in ~6° northward movement of Asia. In this process, Tethys oceanic plate was consumed through subduction first at about 120–100 Ma (Mahéo et al., 2006) beneath the Asian continental plate and shaped an accretionary prism. Subsequently, upon closing of the Tethyan oceanic plate, the Indian continental plate began to subduct beneath the Asian continental plate at about 65–50 Ma (Mahéo et al., 2006; Meng et al., 2012). Due to this continent–continent collision second accretionary prism was formed in the forearc basin of Ladakh magmatic arc along the Indus–Tsangpo suture zone (ITSZ), which is referred to as South Ladakh accretionary prism (SLAP) due to its geographical position and the accretionary prism shaped prior to the SLAP is referred to as paleo accretionary prism (Figure 2.1, modified after Mahéo et al., 2006; Meng et al., 2012). Further,

the subduction of Indian plate is still continuing. Due to these on-going processes, the Indian plate is currently moving at the rate of $\sim 5\text{cm/yr}$ towards the north making the Himalaya as active tectonic region. Such tectonic activity is responsible for thrusting and faulting in the area which can open up pathway for fluid to be entrapped along these weak planes.

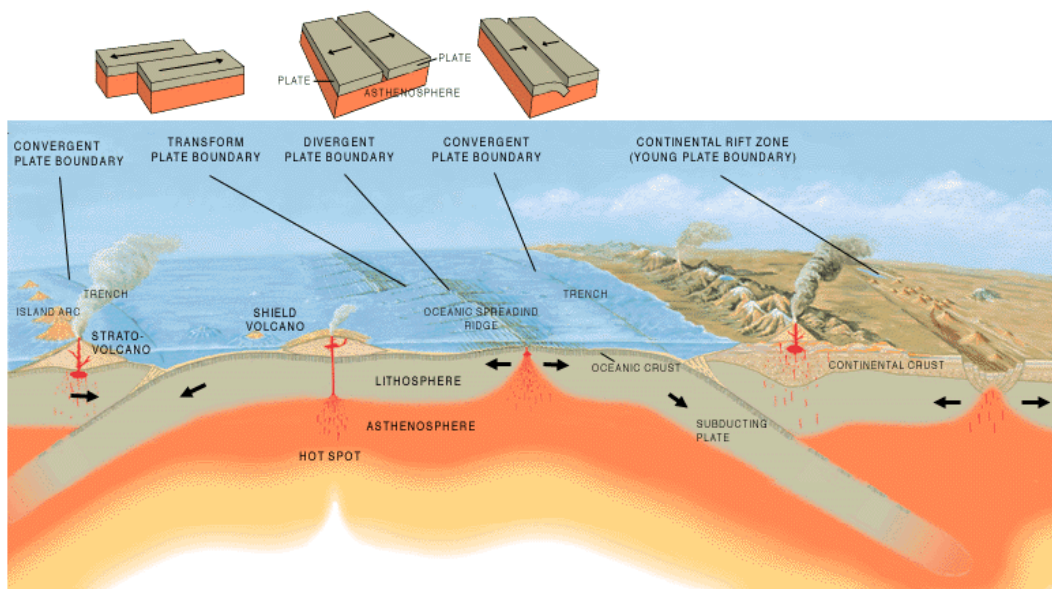


Figure 1.1: A generalized sketch of the plate tectonics model showing different tectonic set-ups. Plate boundary and their deformation process (adopted from http://en.wikipedia.org/wiki/Plate_tectonics).

The Himalaya offers an unique opportunity to study subduction related processes where two accretionary prisms developed at two different time frames as the subduction process is continued. Such type of subduction/tectonic setup is also reported from Japan where two Nankai and Shimanto accretionary prisms are well developed (Byrne et al., 1993; Michiguchi and Ogawa, 2011; and Yamaguchi et

al., 2012). As explained above that the Himalaya is tectonically induced and seismically very active, these seismic or tectonic activities in the Himalaya probably facilitated opening-up of weak planes in the form of faults, thrusts and fractures providing easy pathways for upward migration of warm fluids that were entrapped en-route from deeper part of the Earth's crust. The veining in accretionary prism is common, which took place along the fault and fracture planes. These vein forming fluids may be derived either from deeper sources (magmatic) due to seismic or tectonic activity (discussed above) or locally due to diagenetic and metamorphic processes resulting from continued sedimentation in forearc basin and tectonic processes. Thrusts, and normal and strike-slip faults act as preferred conduits for efficient fluid movement, because they are easier to dilate to make space for emplacement of quartz and calcite veins. Quartz and calcite veins more often occur as mineralized fracture fillings that are ubiquitous in accretionary prism and can serve as valuable monitors of fluid flow. Such type of veining also reported from other accretionary prisms (Michiguchi and Ogawa, 2011; Yamaguchi et al., 2012), such as – Calabrian and Aka Accretionary prism in the Mediterranean Sea; Kodiak accretionary prism in southern Alaska; Nankai and Shimanto accretionary prisms are in Japan; Taiwan accretionary prism located in Taiwan; Barbados accretionary prism of Barbados; and Otago accretionary prism located in New Zealand). Invariable quartz or calcite mineral or both in different proportions constitute a simple mineralogical assemblage of the veins. Till date, very little is known about the role of fluid in the development of the accretionary prism and there was no attempt at all in the past on Ladakh

accretionary prism (LAP) except for the sedimentological, metamorphic and geochemical aspects. This is the first ever attempt in Indian scenario to understand the processes of accretion and subduction through appropriate isotopic fingerprinting and geochemical modeling to aid to our understanding of the formation of accretionary prisms in the Himalayan scenario vis-à-vis the subduction related magmatic activity alongside.

The proposed research work is focused at understanding late stage development of the Himalaya through the detailed study of paleo and South Ladakh accretionary prisms up to the penultimate stage of the mountain building process using Quartz–Calcite veins as the target media. To accomplish this study we select four sections from ITSZ as a case study, covering entire ITSZ from west to east. Out of the four sections, two sections are from paleo accretionary prism, called Shergol and Zildat ophiolitic mélange and two sections from South Ladakh accretionary prism are namely Nimu–Chilling (NC) and Lato–Miru–Upshi (LMU) were chosen for the present investigation. Such types of accretionary prisms are also exposed in Shimanto, Japan and in Chile, between the Nazca and the South American plate which is also known as paleo accretionary prism.

In the Ladakh accretionary prism quartz and calcite veins are generally vertical and at low angle to the bedding plains of the host rock which are also highly tilted and are nearly vertical. This suggests that these veins were intruded in the later stage of deformation of sediments present in the LAP in response to the on-going

Himalayan orogeny. These quartz and calcite veins are common in LAP and elsewhere these are generally said to be derived from metamorphic or diagenetic fluid (Breeding and Ague, 2002 from Otago accretionary prism, New Zealand), marine carbonates or diagenetic process (Vrolijk et al., 1991 from Barbados accretionary prism) from shallow depth. The deeper sources of fluid have not been reported so far. Earlier studies from other accretionary prism suggest that the veins are usually developed in an accretionary complex from shallow marine source or associated host rocks. In the present case, however, this does not seem to be entirely true and there is something beyond this. In this context, it is important to note that the northern margin is entirely composed of granitic and igneous related sediments derived from the Ladakh batholiths. Whereas, the southern margin of LAP is comprised of marine sediments. Some preliminary investigation by the author reveal that potbelly these are not ordinary locally derive veins, but has much deeper origin. If so, that it has important implications in term of continued magmatic activity at the last phase of the Himalayan orogeny. It is normally believed that the quartz and calcite veins under such settings are derived from the marine sediments as in the case of Otago accretionary prism, New Zealand (Breeding and Ague, 2002) and Barbados accretionary prism (Vrolijk et al., 1991), however, the geological setting in the present case strongly argue in favor of an alternative source. Depending upon the nature of the alternative source, a detailed study of these vein networks is likely and most potentially unveil hitherto unknown stories about the processes during the later part of the Himalayan orogeny. Therefore, it is necessary to confirm the

fluid source and to verify if these veins were derived from marine source or not. If not then it becomes important to know the source of fluid in formation of veins. This problem has not been addressed so far and without knowing the exact fluid source in the formation of the veins, the development history of the Himalaya remains incomplete. With this motivation, the present problem was chosen with the prospect that it would add to our current understanding about this gigantic continent-continent collision and subduction related processes.

1.2 LITERATURE REVIEW AND BACKGROUND

The Mesozoic period in the geological history witnessed one of the major mountain building events all over the globe, e.g., Alps in Europe, Andes in south America, Rockies Mountain chain in North America and the Himalaya in Asian continent. The Himalayan orogeny is one of the remarkable events that created most of the highest peaks and deepest gorges of the world spreading over 2500 km across the central Asian continent. Earliest scientific mention and geological reports include those of Hooker (1854), Godwin-Austen (1864), Pilgrim (1906), and Auden (1935) who viewed the Himalaya as a continental fold-thrust mountain chain that came into existence through southward push of the northward drift of the Indian continent. It was still not clear as to where from the enormous force was derived that created such a huge structure on the surface. Contributing to the debate, Wadia (1966) hypothesized that plastic Tethys geosynclines against which Gondwana land juxtaposed and got deformed.

However, the classic reviews by Wadia (1953, 1966), Gansser (1964), and Le Fort (1975) provided a holistic modern view of the Himalayan geology in general and combined with the plate tectonic theory, laid the foundation for the present day concept and research in understanding the complex Himalayan orogeny (Gansser, 1964; McKenzie and Parker, 1967; Isacks et al., 1968; Le Pichon, 1968; Morgan, 1968; Coleman, 1971; Ernst, 1973; and Valdiya, 1981, 1984). Ever since the concept of plate tectonics introduced about 3-4 decades ago, there is a marked improvement in our understanding of the complex tectonic history of the Himalaya. Some of the modern reviews on Himalayan tectonics describing the plate tectonic model, subduction of Tethyan oceanic plate, closing of the Tethyan ocean and ensuing continent-continent collision may be found in Acharyya (1980), Thakur (1981), Singh and Chowdhary (1990), Searle et al (1992), LeFort (1996), Hodges (2000), Yin and Harrison (2000), DeCelles et al. (2002), Johnson (2002), Avouac (2003), Steck (2003), DiPietro and Pogue (2004); and Yin (2006) that includes geological summaries at local as well as in regional scale.

Synthesis and reviews of the geology, structure and tectonics in the Continent-continent collision/subduction zone as exposed in the Ladakh region was presented through studies carried out by Thakur (1981), Honegger et al (1982, 1989), Thakur and Mishra (1984), Schärer et al (1984), Brookfield and Andrews-Speed (1984), Searl et al (1990, 1997), Sinha and Upadhyay (1997), Clift et al (2000), Sinclair and Jaffey (2001), Mahéo et al (2004, 2006), Yin (2006), Ahmad et al (2008), Henderson et al (2010a, 2010b, 2011), Meng et al (2012) and

references therein. These studies mostly focused on reconstructing the structural set-up and collision tectonics and geochronology of events and resulting geomorphologic expressions thereon. However, very little is known about the accretionary prisms that were developed due to the subduction process and more specifically the extensive occurrence of veins within the rocks of accretionary prisms. It is generally believed that the veins within the LAP were emplaced at the end of the cessation of the fore arc basin and completion of suturing, i.e. post 23 Ma. It is therefore envisaged that these veins might reveal some of the hitherto, unknown mysteries of the tectonic activity at this crucial stage of the Himalayan orogeny.

Veining in other accretionary prism was also reported, but few workers trace the source of vein forming fluid as well as their exhumation history. Very few studies have been done so far on the role of fluid source in the formation of veins and the upliftment history. The metamorphic fluids as source of quartz veins were reported from the Otago accretionary prism, New Zealand by Breeding and Ague (2002), where as the marine carbonates or Sea water precipitation were identified in case of the Shimanto accretionary prism, Japan by Yamaguchi et al (2012). Vein formation associated with diagenetic process of associated host rock has been established in case of Barbados accretionary prism at island of Barbados in the North Atlantic Ocean by Vrolijk et al (1991). The tectonic framework of these veins also carried out by few workers such as Byrne et al (1993); Michiguchi and Ogawa (2011) from Nankai accretionary prism, Japan. In no case, the implication

of the quartz-carbonate veins occurring in different levels within the accretionary prisms with the tectonic history has ever been established. This is primarily because the fluid in these cases probably heralds its source from shallower processes as discussed above. The upliftment history of veins was not reported from any accretionary prism so far.

There are two accretionary prism developed in different time frames in Ladakh collision zone, as discussed in section 1.1 of this chapter. A similar set-up has also been reported from the Japanese island arcs from the western Pacific Ocean (Sugimura, and Uyeda, 1973; Vrolijk et al., 1991; Byrne et al., 1993; Taira, A., 2001; Michiguchi and Ogawa, 2011) where two accretionary prisms, Nanki and Shimanto developed separately but are none juxtaposed each other. These accretionary prisms contain numerous veins, which are formed by the metamorphic fluid and sea water/marine carbonates (Vrolijk et al., 1991; Byrne et al., 1993; Michiguchi and Ogawa, 2011).

1.3 OBJECTIVES

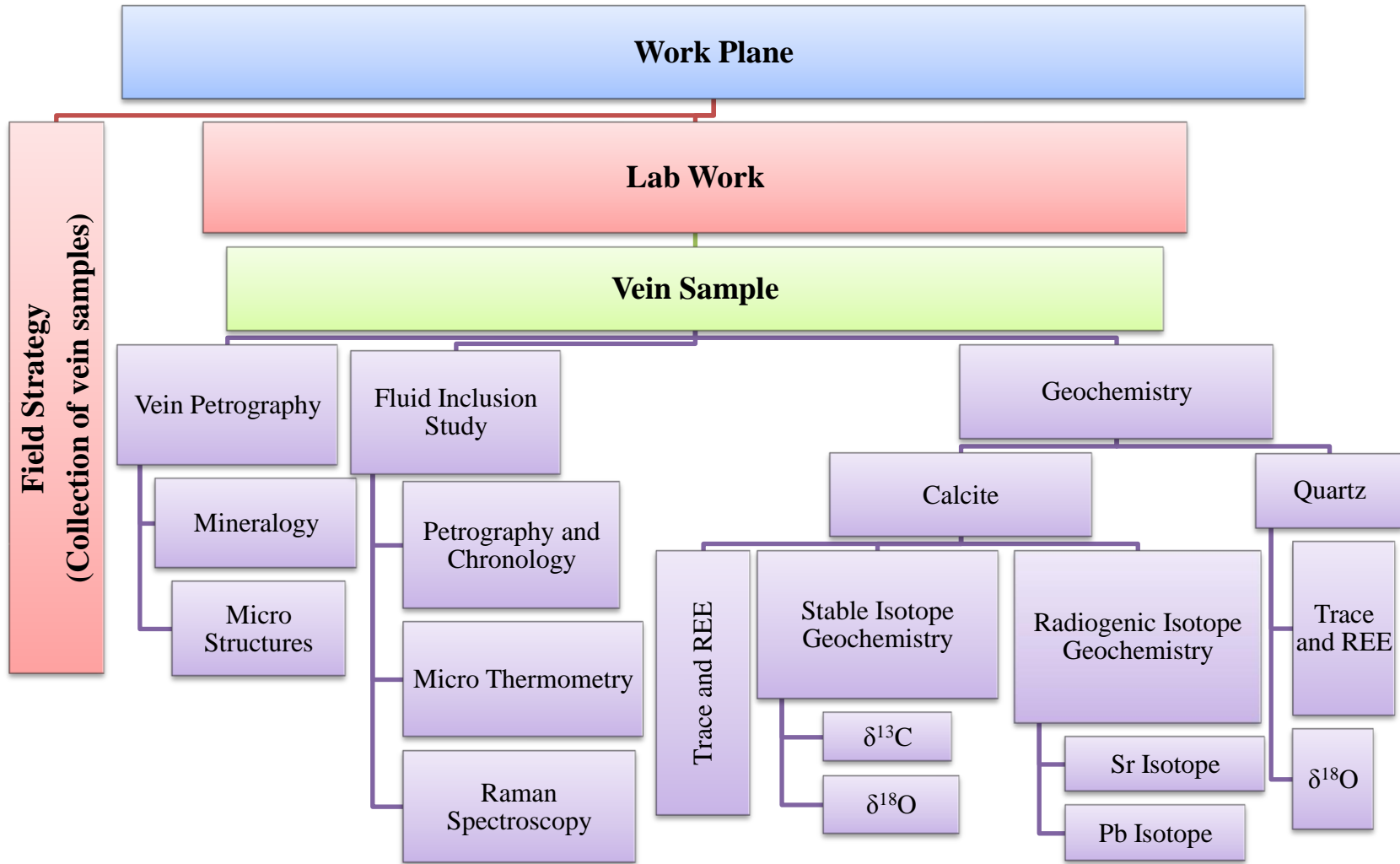
In view of the foregoing discussion and the importance of the quartz calcite veins occurring within the Ladakh accretionary prism of the Himalayan orogeny, an attempt has been made to extract useful inferences from these veins that would likely to throw lights on the subduction processes during the veining stage of the orogen. The objectives of the present study are as follows:

- a) To understand the veining mechanism in accretionary complex.
- b) To know the source of fluid and formation condition of veins and its implication to their tectonics.
- c) To understand the fluid flow on a regional scale in a protracted tectonic event (i.e. formation of accretionary complex) from eastern to western Ladakh in a relation to the Himalayan orogeny.

To achieve these objectives, following research model was adopted.

- a) Rigorous fieldwork to look for quartz–calcite veins along with host rock, spread over accretionary prism (paleo and South–Ladakh accretionary prism).
- b) Intensive Petrographic studies of selected quartz–calcite veins.
- c) Detail Fluid Inclusion Petrography.
- d) Micro thermometric study of fluid inclusions.
- e) Raman spectroscopy of fluid species.
- f) Geochemical study (Trace and REE) of selected quartz–calcite veins.
- g) Isotopic studies of selected quartz–calcite veins.

Petrography of veins helps to know the mineral assemblage and their deformation conditions in the formation of veins. The systematic investigation of fluid inclusions petrography study helps in identification of different generations of fluid movement. Trace and REE elemental compositions together with the



isotopic characteristics is very useful for understanding and identifying the source and put constraints on the exhumation history of accretionary complexes. Isotopic studies will also help to know the source of fluid in the formation of veins and trace their pathways and final entrapment. A snap shot of the methodology adopted for the systematic study of the veins is diagrammatically presented in the flow Chart above.

1.4 THE STUDY AREA

To accomplish the objectives of this study, four sections from both accretionary prisms are selected that are well spread along strike in the ITSZ (Figure 1.2). These are marked in Figure 1.2 from west to east as- [A] Shergol section of paleo-accretionary prism, [B] Nimu–Chilling (NC), [C] Lato–Miru–Upshi (LMU) of South Ladakh accretionary prism and [D] Zildat section of paleo-accretionary prism.

The local detail geological maps of these studied sections are shown in chapter 2. A cross sectional view of study area also shown in the figure 1.3 which suggest that the Ladakh accretionary prism developed in the forearc basin of Ladakh magmatic arc between the Ladakh batholiths and the Lamayuru formation of Indian margin.

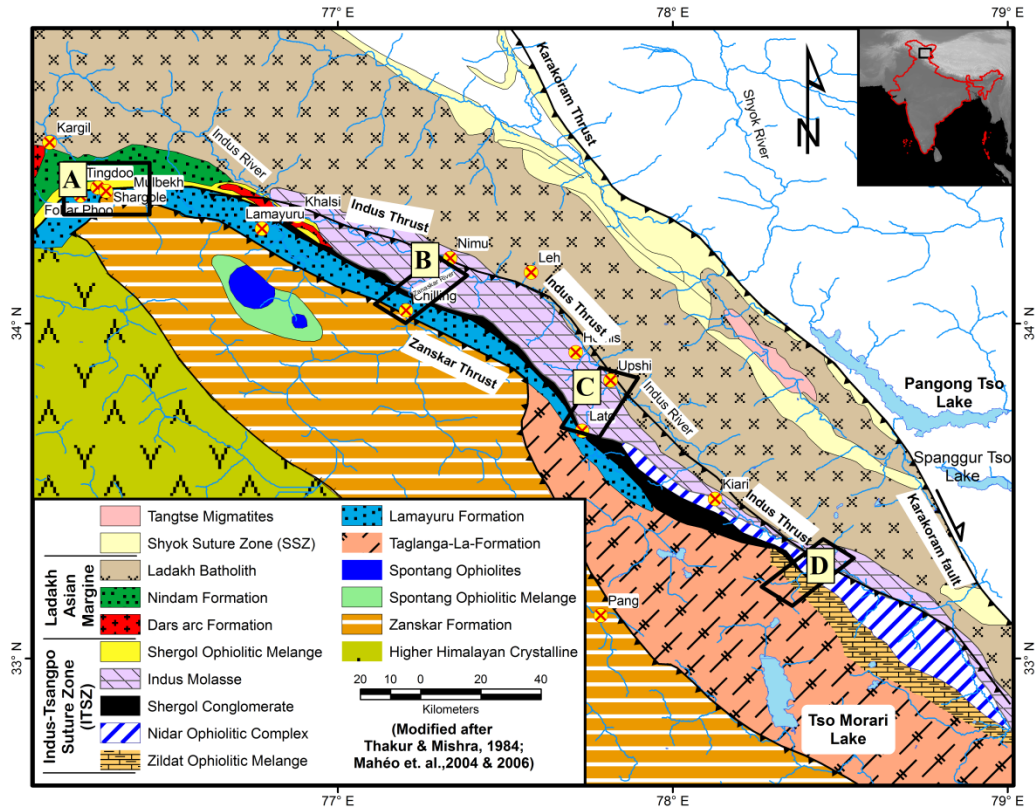


Figure 1.2: Regional Geological Map of the Study area (Ladakh Himalaya) modified after Thakur and Mishra (1984); Mahéo et al (2004, 2006). The rectangular box refers to the investigation sections of this study- [A] represent Shergol area (see Figure 2.4); [B] the Nimu–Chilling (NC) Section (see Figure 2.6 for detail); [C] Lato–Miru–Upshi (LMU) Section (see Figure 2.8 for detail) and [D] the Ziladt Section (see Figure 2.10 for detail).

The Shergol section is well exposed at the western margin of the Ladakh accretionary prism (LAP) whereas, the Zildat section shaped at the eastern margin of LAP which is an extension of ophiolitic mélange. Therefore, the Shergol and Zildat ophiolitic mélange are jointly referred to as the paleo accretionary prism. The NC section lies in the Zaskar Gorge between Nimu and Chilling village at the western margin of the SLAP. While, the LMU section is covered the eastern

part of SLAP and well exposed on Leh–Manali road between Upshi and Lato village.

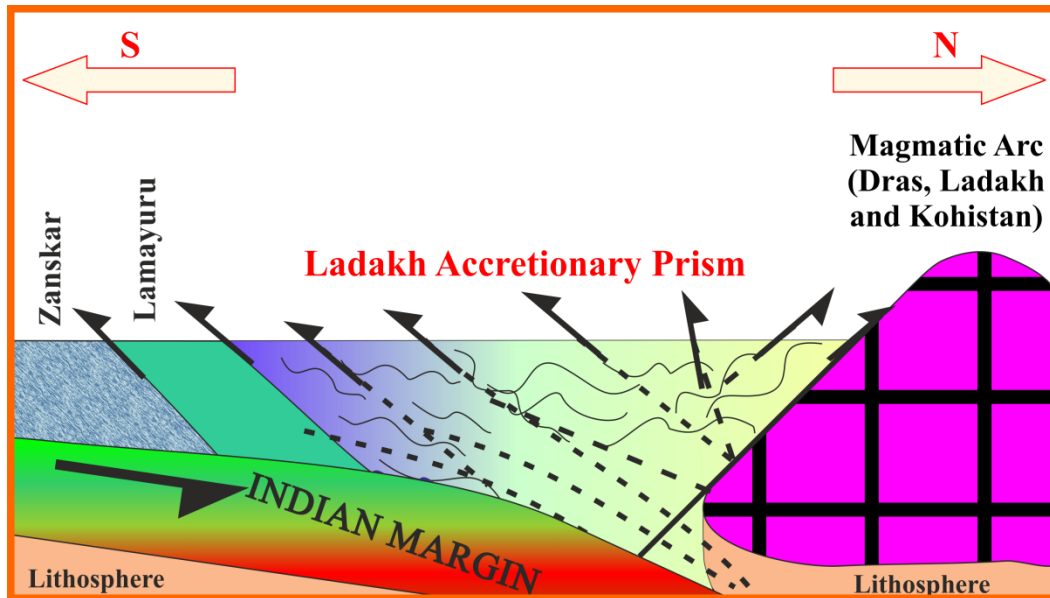


Figure 1.3: Cross sectional view of the Ladakh Accretionary Prism (LAP).

1.5 CONTRIBUTION OF PRESENT RESEARCH

Veining in accretionary prism occurs during the post deformation event of LAP. The accretion prism developed at very last stage of any orogeny process. Therefore, these veins present in accretion prism can be considered as a media to unravel the history of penultimate stage of evolution of the Himalaya. This is the first ever attempt in the Himalayan tectonic set-up to understand the process of accretion and subduction using vein fluid(s) as media. This research work will enhance our understanding of the formation of accretionary complexes and the Himalayan orogeny during the last phase, through the eye of vein fluid. This work

is expected to provide us clues if any magmatic activity along with tectonic activity was involved at the penultimate stage of the development of Himalayan Orogeny. In true sense, the knowledge towards the development history of the Himalayan orogeny will be improved through this research work by adding the penultimate history.

This research work rises following questions that need to be addressed and a justifiable answer would immensely benefit the geoscientific fraternity:

- a. What is the source of vein forming fluid in the development of the Ladakh accretionary prism?
- b. What was the formation temperature of veins?
- c. What was the possible path of emplacement of these veins?
- d. At what depth the vein forming fluid was intruded?
- e. What was the fluid composition?

This thesis report is submitted with the hope that the answers to these questions are quite pertinent to our understanding about the tectono-magmatic regime of the late stage of the subduction and continental collision of the Himalayan orogeny.

CHAPTER 2:

GEOLOGICAL SETTING

CHAPTER 2:

GEOLOGICAL SETTING

The Himalayan orogenic belt is a gigantic feature on Earth that poses toughest challenge to the geoscientific community to unveil geological history of this mountain building process. The mountain chain contains some of the deepest Gorges and highest peaks of the world dividing the Indian subcontinent into a 2400 km arc forming an icy blockade between the tropical India and the Central Asia. For this reason, the Himalaya is also referred to as the 3rd pole on the Earth besides the north and south poles. On both eastern and western ends, there is a marked inward bending of the strike of the orogen, called the NW- and NE- Himalayan Syntaxes. In this chapter, a brief description of the evolutionary history of the Himalayan orogeny, geographical characteristics, regional geology and detailed geology of the suture zone with special emphasis on the geology of the accretionary prisms studied in this investigation is presented.

2.1 EVOLUTION OF THE HIMALAYA

The evolution of Himalaya is a mystery, which remains to be unfolded completely. A working model of evolution of the Himalaya was first introduced by Burrard and Hayden (1907) and Argand (1924). During the early 19th century,

the great mountain chains of the world were viewed as having developed through geosynclinal hypothesis and the Himalaya was considered as a mega geosynclinal entity on Earth's surface. According to this hypothesis, the Himalaya was formed by huge piles of sedimentary succession, deposited in a huge basin called the Tethys Ocean and was uplifted through multi deformational events. However in the mid 19th century, the plate tectonic theory came into light through the pioneering work of McKenzie and Parker (1967), Isacks et al. (1968), Le Pichon, (1968), Morgan, (1968) and others, which gradually picked up momentum and became widely accepted by the geoscientific community (Figure 1.1). Further, in 1970 the plate tectonic theory was arguably used by Dewey and Bird (1970) and put forward a more realistic evolutionary model of the Himalaya. They suggested that the Indian plate collided with the Asian plate resulting in the most spectacular and gigantic event on the Earth, the birth of the Himalayan Mountain chain.

Therefore, to understand the evolution of the Himalaya is a challenging exercise in itself owing to the present and past geographical positions of the Indian plate. The evolution of the Himalaya can only be explained in a proper way by throwing light on the journey of the Indian plate. It becomes necessary to look into the past history and dynamics of the Indian plate since the Proterozoic time. During the Late Paleozoic, the Indian continent was a part of the Pangaea supercontinent. The breakup of Pangaea supercontinent took place at ~200 Ma in three major phases (viz. Early–Middle Jurassic: ~175 Ma; Early Cretaceous: ~145 Ma; and Cenozoic: 65–55 Ma) as suggested by Merali and Skinner (2009). The first phase

of breaking up of Pangaea began ~175 Ma (Early–Middle Jurassic period) that gave rise to two supercontinents namely, Laurasia (to the north) and Gondwana (to the south) due to rifting from Tethys Ocean in the east to the Pacific Ocean at the west. The second phase of breaking of Pangaea took place at ~145 Ma (Early Cretaceous). In this phase, the Gondwana supercontinent separated into two major continents (i) West Gondwana (together with Africa and South America) and (ii) East Gondwana (a group of India, Australia, and Antarctica). Following which, the Indian plate further broke off from the East Gondwana (Australia and Antarctica), and began its journey northward direction to collide with the Asian plate at an estimated rate of 18.5 cm/year (fastest known movement of any tectonic plate), which is responsible to closing the Tethys ocean (Figure 2.1; Meng et al., 2012). The third and final phase of brake-up of Pangaea occurred in Cenozoic period (~60–55 Ma) during which the Laurasia was fragmented into North America and Greenland, collectively referred to as Laurentia.

In the second phase of break-up of Pangaea, the Indian continental plate move towards the Asian plate and is considered to be the beginning of the Himalayan orogeny. In Early Cretaceous period (about 120–100 Ma), the Tethys Ocean began to subduct beneath the Asian plate and resulting in closer of the Neo-Tethys, through northward movement of the Indian plate and ensuing intra-oceanic subduction giving rise to arc magmatism represented now by the Dras arc (Figure 2.1), which was formed at ~120 Ma facilitating formation of an accretionary prism (including Shergol and Zildat ophiolitic mélangé) at its forearc

basin (Figure 2.1; Mahéo et al., 2006). The Indian plate continued to move northward and upon closer of the Tethys Ocean, the two continents, Asian and Indian plates, came face to face and collided at about 55–50 Ma and shaped another accretionary prism south of Shergol Ophiolitic mélange, namely South Ladakh Accretionary Prism (SLAP). In this frame of time, numerous magmatic activities also took place and formed magmatic arcs known as Ladakh, Karakoram and Ladakh–Kohistan, which continued until 13 Ma (Kohistan magmatic arc; Ji et al., 2009). In the development of the Himalayan orogeny, the northward translation of Indian plate was associated with the Tethys oceanic plate subducting beneath the Asian plate in two episodes (see Figure 2.1). Following the completion of subduction of Tethys oceanic plate below the Asian plate, the Indian continental plate began to subduct at about 55 Ma in the second phase (Figure 2.1). The first subduction of Tethys oceanic plate (Neo–Tethys) took place at about 120–100 Ma, whereas the second subduction of Neo Tethys occurred at about 65 Ma (Figure 2.1). Therefore, the subduction of Neo Tethys is also referred to as paleo–subduction, with respect to the second subduction of the Indian continental plate (Gansser et al., 1974; Thakur, 1981; Robertson, 2000; Mahéo, et al., 2006). For this reason, the first accretionary prism which was shaped at ~120–100 Ma is referred to as Paleo Accretionary Prism (PAP), whereas the second accretionary prism (SLAP) developed at about 55–50 Ma. The PAP and SLAP are jointly referred to as the Ladakh Accretionary Prism (LAP), which is well exposed along the Indus Tsangpo Suture Zone (ITSZ).

The geographic as well as the litho-tectonic divisions of the Himalaya is presented below (figure 2.1) and is summarized in Table 2.1.

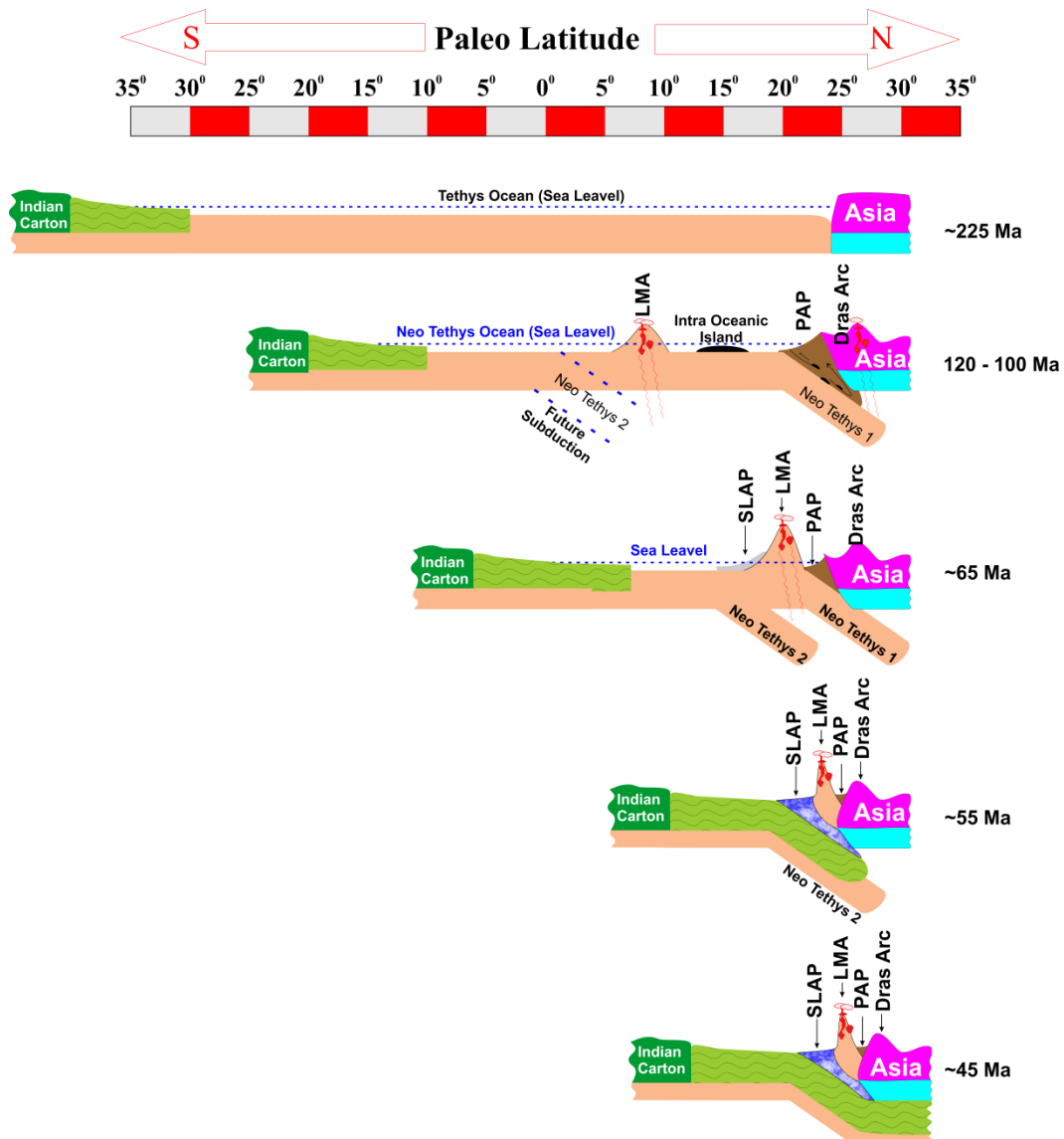


Figure 2.1: Schematic diagram of the Himalayan orogeny and shaping of accretionary prisms, modified after Clift et al (2000); Mahéo et al (2006) and Meng et al (2012).

2.1.1 GEOGRAPHICAL DIVISIONS OF THE HIMALAYA

Geographically, the Himalaya lies between two peaks namely Namche Barwa (at eastern syntaxes) and Nanga Parbat (at western syntaxes). It is bounded in the north by two orogen parallel trans-Himalayan rivers, viz. the east-flowing Yalu Tsangpo (“Tsangpo” meaning “big river” in Tibetan local dialect) and west-flowing Indus River and the southern boundary of the Himalaya is marked by the Main Frontal Thrust (MFT) that delimit the northern limit of the Indo-Gangetic depression. The Hindu Kush Mountains demarcate the boundary of western margin, while the Indo-Burma ranges (Rongklang Range) mark the eastern margin of the Himalayan syntaxes. The Karakorum Mountain chain and the Trans-Himalayan terrain are the northern most margin of the Himalayan orogen (Figure 2.2). The southern political boundary of Tibet (i.e., Xizang in China) follows approximately the crown of the Himalayan range. The difference in political and geographic divisions has led to different naming of the same structures in the Himalayan range (e.g., the north Himalayan normal fault versus south Tibet detachment system; Burg et al., 1984; Burchfiel et al., 1992).

From North to South, the Himalayan orogen is separated into two parts; the North Himalaya and the South Himalaya that are defined by its high crest line (Figure 2.2). The North Himalaya is nearly similar to the Tethyan Himalaya or the Tibetan Himalaya as geographically defined by Heim and Gansser (1939) and LeFort (1975), respectively. The South Himalaya covers rest of the Himalaya,

which is further sub-divided into three main divisions such as, Higher, Lesser, and sub-Himalaya, respectively from north to south (Figure 2.2). The southern boundary of the Higher Himalaya is marked as the base line of the northernmost steepest slope of the southern Himalayan range, whereas the boundary between the Lower Himalaya and sub-Himalaya lies along the axis of the lowest intermontane valley parallel to the range (Yin, 2006).

On the basis of elevation, the Himalayan ranges are divided vertically into three categories (i) the Basal: <1500 m, (ii) Middle: 1500–3500 m, and (iii) Upper Himalaya: >3500 m (Yin, 2006). With this criterion, the Upper Himalaya is mostly absent in northern Pakistan, south of the Indus–Tsangpo suture as reported by DiPietro and Pogue (2004).

From west to east (along the strike direction), the Himalayan orogen is divided into the western (66° – 81°), central (81° – 89°), and eastern (89° – 98°) segments (Yin, 2006). The western Himalayan orogen covers the Salt Range in northern Pakistan, Kashmir (NW India), Zaskar, Spiti, Chamba, Himachal Pradesh, Lahul, Garhwal, and Kumaun. The central Himalayan orogen occupies Nepal, Sikkim, and south-central Tibet, whereas the eastern Himalayan orogen includes Bhutan, Arunachal Pradesh of NE India, and southeastern Tibet.

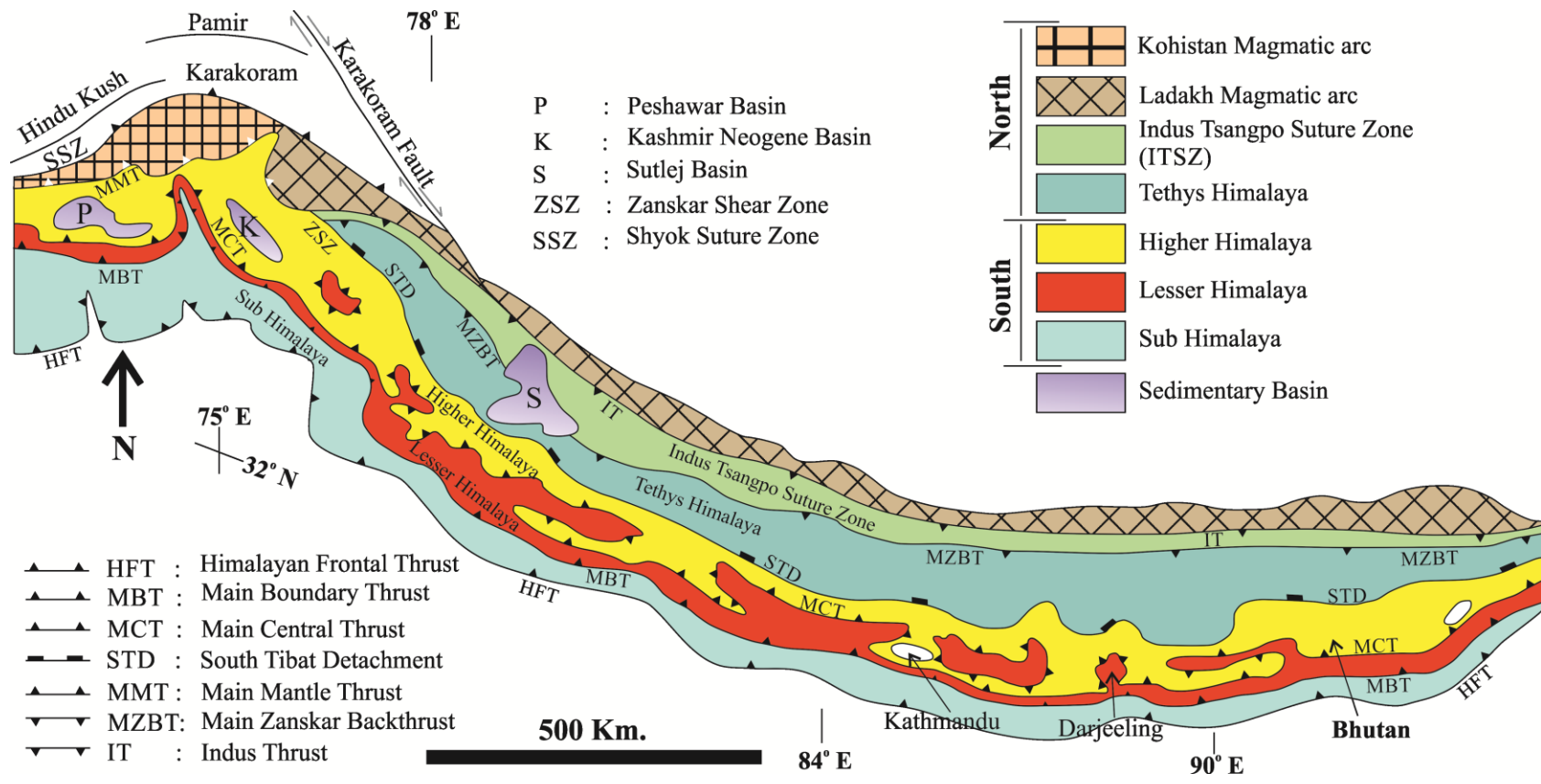


Figure 2.2: A generalized Litho-Tectonic Map of the Himalaya (modified from Searle et al., 2003 and Law et al., 2004).

2.1.2 LITHO- AND TECTONO- STRATIGRAPHICAL DIVISIONS OF THE HIMALAYA

Litho- and Tectono- stratigraphically, the Himalaya is divided into five major classes from south to north (across the strike direction) and are referred to as Sub, Lesser, Higher, Tethyan and Trans Himalaya (Figure 2.2). The Sub Himalaya consists of fine to coarse grained continental foreland basin sediments of Neogene period (23 to 2 Ma) and also known as Siwalik Group. The Proterozoic- Cambrian, Lesser Himalayan Sequence (LHS) is comprised of unfossiliferous low grade metamorphic, metasedimentary and metavolcanic rocks. On the other hand, younger Higher/Greater Himalayan crystalline complex (HHC/GHC) comprised of high grade metamorphic rocks of Cambrian to Early Ordovician period (800- 480 Ma) as reported by Yin, 2006 and others. The Tethyan Himalayan Sequence (THS) is demarcated as the northernmost part of the Indian subcontinent, which consists of Late Precambrian to Eocene (about 650-40 Ma) marine sedimentary rocks intrabedded with volcanics (Yin, 2006). The THS overlies to the Indian continental plate along a normal fault called South Tibet Detachment (STD). The major volcanic and magmatic arcs of the Himalaya were developed in the Trans Himalayan terrain. The major divisions of the Himalaya are structurally and tectonically controlled, in which the thrusts/faults of the Himalayan system are difficult to discriminate because of changes in litho units with the thrust/fault.

The Sub-Himalaya is separated from the Ganga Plain to its southern margin by the Main Frontal Thrust (MFT), whereas the northern margin is demarcated by the Main Boundary Thrust (MBT). In the north of the MBT, Lesser Himalaya is well exposed at its hanging wall. Lesser Himalaya is also referred to as footwall of Main Central Thrust (MCT), which lies at the south of MCT. High grade metamorphic rocks of HHC/GHC are well exposed to the north of MCT on its hanging wall. In turn, the HHC is bounded to the north by the high-angle normal fault, which lies to the south of THS and known as South Tibet Detachment (STD). The STD separates the higher Himalayan crystalline from the Tethyan Himalayan Sequence (THS). Thus, STD is the northern most margin of the Indian tectonic plate, which separates the Asian plate to the north by the Indus-Tsangpo Suture Zone (ITSZ). The ITSZ is actually the zone of collision between Indian and Asian plates where the sediments were accreted from both sides of the tectonic plates. In the north of ITSZ, the trans-Himalaya is well exposed, which is considered in northern margin of the Himalayan orogenic belt.

The divisions of the Himalaya on the geographical/ topographic, litho-, chronostratigraphic and structural basis are tabulated below in table 2.1 (modified after Yin, 2006) for comparison.

Table 2. 1: Geographical, Stratigraphic and Structural divisions of the Himalaya.

	Geographical/ Topographic Division	Litho– and tectono– stratigraphy Division
Across Strike Direction	Tibetan Plateau	Trans Himalaya
	---- Indus/ Tsangpo River ----	----- ITSZ -----
	North Himalaya	Tethyan Himalayan Sequence (THS)
	----- Himalayan Crest -----	----- STD -----
	Higher Himalaya Lower Himalaya Sub Himalaya	Higher Himalayan Crystalline (HHC) ----- MCT -----
Vertical Section	Upper Himalaya (> 3500 m)	Lesser Himalayan Sequence (LHS)
	Middle Himalaya (1500-3500 m)	----- MBT -----
	Basal Himalaya (50-1500 m)	Sub Himalaya/ Siwalik Group
Along Strike Direction	Western Himalayan orogen	----- MFT -----
	Central Himalayan orogen	
	Eastern Himalayan orogen	Gangatic Plane

2.2 REGIONAL GEOLOGY OF THE LADAKH HIMALAYA

A sequence of several magmatic activities is noticed in the Ladakh terrain. These activities are represented by Late Jurassic–Cretaceous intraoceanic arc magmatism (Dras–Nidar volcanics and associated with Ladakh–Kohistan batholith) varying from mafic to intermediate compositions. These magmatic sequences are in turn, invaded by Ladakh–Kohistan granodioritic/granitic intrusives (Ahmad et al., 2008). Numerous ages have been assigned to the

Ladakh–Kohistan batholith starting from 103 ± 3 Ma (U–Pb age: Honegger et al., 1982; Schärer et al., 1984) from Kargil, through 49.8 ± 0.8 Ma (zircon U–Pb: Weinberg and Dunlap, 2000) to cooling ages as younger as 48.7 ± 1.6 Ma (biotite K–Ar: Honegger et al., 1982) and 45.7 ± 0.8 Ma (hornblende Ar–Ar: Weinberg and Dunlap, 2000) for rocks from around Leh, in the central part of Ladakh. This suggests that there are several magmatic phases of Ladakh plutonic complex spanning in time and space from ~ 100 Ma through ~ 45 Ma to the youngest phase of 30–13 Ma as reported from Tibet (Kohistan magmatic arc) by Ji et al (2009).

Present study area belongs to Ladakh terrain in the NW Himalaya along the NW–SE trending ITSZ (Figure 2.3). As described above in section 2.1.2 of this chapter that ITSZ is the zone of collision of Indian and Asian plates, which consists of two accretionary prisms (PAP and SLAP). The western and eastern margin of the study area is bounded by the mélangé zone and ophiolitic rocks of Shergol and Zildat succession, respectively. From north to south across the strike, the Ladakh range may be divided mainly into four groups (map view; Figure 2.3)-

- I. southern margin of Asian plate (Karakoram and SSZ),
- II. Ladakh Asian Margin (Ladakh batholiths, Nindam Formation and Dras arc)
- III. ITSZ (Shergol ophiolitic mélangé, Indus Molasse, Shergol conglomerate, Nidar Ophiolitic Complex and Zildat Ophiolitic Mélangé)

IV. Passive margin of the Indian plate (Lamayuru, Taglanga-La, Spontang ophiolites, ophiolitic mélange, Zanskar formation and HHC/GHC).

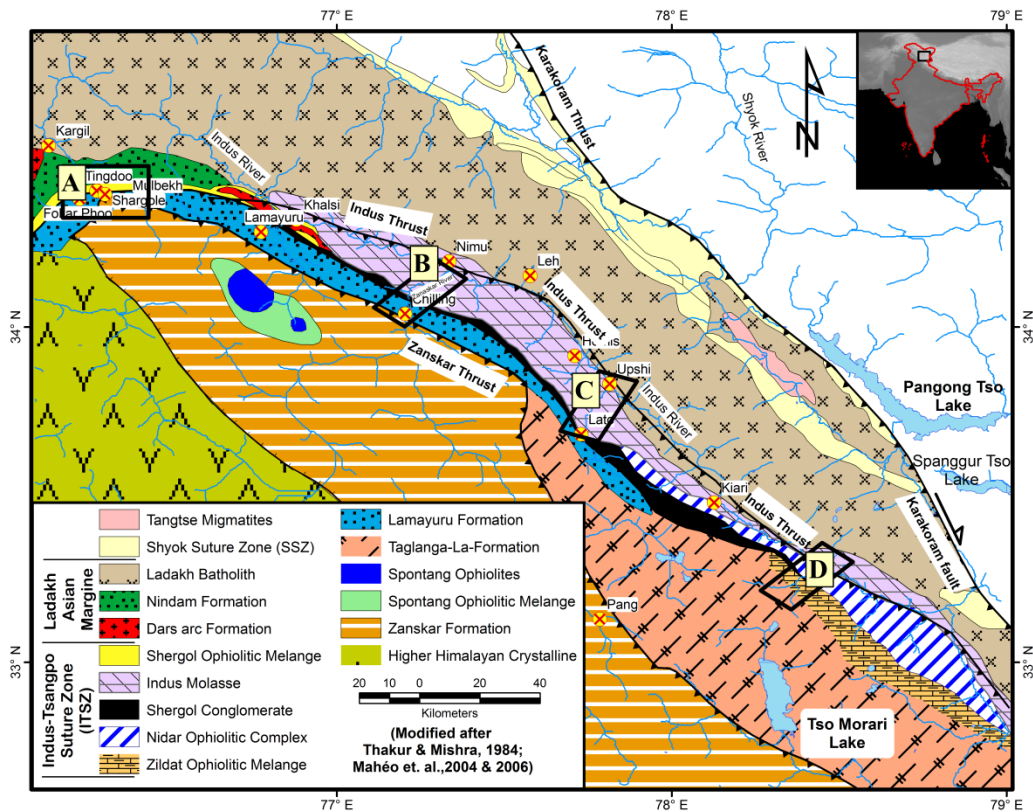


Figure 2.3: Regional Geological Map of the Study area (Ladakh Himalaya) modified from Thakur and Mishra (1984); Mahéo et al (2004, 2006). The rectangular box refers to- [A] Shergol area (see Figure 2.4); [B] the Nimu–Chilling (NC) Section (see Figure 2.6 for detail); [C] Lato–Miru–Upshi (LMU) Section (see Figure 2.8 for detail) and [D] the Ziladt Section (see Figure 2.10 for detail).

(I) **The Southern margin of Asian plate** consists of Karakoram plutonic complex and SSZ. The Karakoram and Lhasa block was a single tectonic unit, which was displaced and separated by the Karakoram

thrust/fault. This Karakoram plutonic complex is a part of the Ladakh Magmatic Arc (LMA) resulting from subduction of the Indian oceanic plate beneath the Asian plate (Thakur, 1981). In the forearc of Karakoram plutonic complex a suture zone developed, which is known as Shyok Suture Zone (SSZ) having the trends similar to that of ITSZ. The SSZ can be divided into four tectono–stratigraphic units, viz. Shyok ophiolite, Luzarum Formation, Diong Formation and Kole molasses. Developed during Cretaceous to Eocene, the Shyok Group consists of sandstone, conglomerate, basic and intermediate volcanics along with chert, gabbro, peridotite and serpentinite, which is interbedded with shale, limestone and quartzite (Thakur, 1981; Thakur and Mishra, 1984). Further, SSZ was displaced from the Karakoram zone by a major fault demarked by the mylonitic gneiss and is referred to as the Karakoram thrust/fault by Thakur and Mishra, (1984), however, recently it has been designated as a strike slip fault (Sen and Collins, 2013).

- (II) **Ladakh Asian Margin** is composed of Ladakh batholith, Nindam Formation and Dras arc (see Figure 2.3). The Ladakh plutonic complex is a NW–SE trending belt of batholithic body, which consists of tonalite, granodiorite and granite and developed in multiphases of magmatic activity and having cross–cut relationship with Dras volcanics (Thakur and Mishra, 1984). The different intrusive phases of Ladakh plutonic complex have been dated by radiometric method, which

indicates three major activities viz. 120 Ma, 60–40 Ma and 20 Ma (Brookfield and Reynolds, 1981; Honegger et al., 1982). Yet another youngest age, 13 Ma of Ladakh plutonic complex is reported from the Tibet (Ladakh–Kohistan magmatic arc) by Ji et al (2009). Closely associated with the Ladakh plutonic complex, the Dras arc was inferred to have formed in the Cretaceous time by the arc type of volcanic activity as Tethys oceanic plate began to subduct and closure of Neo Tethys 1 (Figure 2.1) ensued (Mahéo et al., 2006). The volcanic rocks contain mainly andesitic and basaltic lavas, which is associated with occasional pillow lava, rhyolite, agglomerate and other volcanoclastic rocks (Thakur, 1981; Honegger et al., 1982; Thakur and Mishra, 1984). To the east of the Dras arc formation, flysch sedimentary sequences occur consisting of red and olive–green shales and sandstones in addition to chert, jasper and limestone. The petrochemical property of volcanic rocks indicates that these are mainly tholeiites of calc-alkaline affinity with minor shoshonites (Honegger et al., 1982). The Dras formation as a whole represent an island-arc tectonic set-up resulting from subduction related magmatic eruption (Figure 2.1) through melting of upper mantle or the upper part of subducting Tethys oceanic plate (Thakur, 1981; Honegger et al., 1982; Thakur and Mishra, 1984).

- (III) ITSZ** is a group of NW–SE trending litho-units, which are known as Shergol ophiolitic mélangé, Indus Molasse, Shergol conglomerate, Nidar

Ophiolitic Complex and Zildat ophiolitic mélange (Figure 2.3). As shown in the map (Figure 2.3) the study area is composed of ophiolite and ophiolitic mélange zone of Zildat and Shergol area at the eastern and western part of ITSZ, respectively whereas the central part is comprised of Indus molasse. The southern margin of ITSZ is demarcated by Shergol conglomerate, which separates the ITSZ from the Lamayuru formation. In the north, the ITSZ separates the Ladakh magmatic arc by the deep seated Indus thrust (Kharya et al., 2014), which is also known as Upshi–Bagso thrust (Brookfield and Andrews–Speed, 1984; Tripathy–Lang, 2013).

(IV) Passive margin of Indian plate is represented by various lithounites of Tethys sediments, viz. Lamayuru, Taglang-La, Zaskar formations and associated Spontang ophiolites and ophiolitic mélange, along with high grade metamorphic rocks of HHC/GHC to the south within Indian plate (Figure 2.3). The Lamayuru and Zaskar formations are composed of sediments, which lie on the Indian subcontinent side to the south of ITSZ in which the Spontang ophiolites and ophiolitic mélange were intruded within Zaskar formation (Figure 2.3). Higher Himalaya crystalline (HHC) exposed further south of Zaskar formation, which is comprised of High grade metamorphic rocks.

2.3 GEOLOGICAL SETTING OF THE LADAKH ACCRETIONARY PRISM (LAP)

The Ladakh accretionary prism (LAP) is shaped in the fore arc basin of Dras and Ladakh magmatic arc along ITSZ which mainly consists of sediments (derived from the Asian and Indian plates), conglomerates, ophiolites and ophiolitic mélangé unites and subduction related metamorphic rocks (Blue Schist, Coesite bearing eclogite, etc.) along with numerous mineralized veins. The eastern and western margin of LAP consists of ophiolite and ophiolitic mélangé of Zildat and Shergol, respectively, which was shaped at the same time (Cenozoic). The northern and southern margin of LAP is sandwiched between Ladakh magmatic arc and Lamayuru formation. The LAP is also tectonically bounded by the Indus thrust (at the north) and Zaskar thrust (at the south). It is further subdivided into two accretionary complexes on the basis of their progressive time of formation (Figure 2.1). These are named as paleo- accretionary prism (PAP) and South Ladakh Accretionary Prism (SLAP). The PAP was formed at ~100 Ma (Honegger et al., 1989; Mahéo et al., 2004, 2006) in the forearc basin of Dras arc due to closure of Tethys Ocean (Neo–Tethys 1), by the convergence of Tethys oceanic plate underneath the Asian plate (see Figure 2.1). This closer of Neo–Tethys Ocean took place in two stages at different times (i.e. Neo–Tethys 1 and Neo–Tethys 2) by continued north dipping subduction zone (Figure 2.1). The first subduction of Neo Tethys (Neo Tethys 1) started at ~120 Ma when Tethys oceanic plate was subducting beneath the Asian plate (Thakur, 1981; Pedersen et

al., 2001; Mahéo et al., 2004, 2006), which gave rise to magmatic arcs (Dras volcanic and Ladakh magmatic arc) around the same time. This paleo subduction was subsequently followed by a second northward subduction of Neo-Tethys 2 that began at ~65 Ma and shaped SLAP (Mahéo et al., 2006).

In addition to the formation of LAP in different time periods and development of pertinent litho units, numerous veins are omnipresent present in most of the formations of LAP. These veins cross-cut almost all the litho units present in the accretionary complexes (paleo and South Ladakh accretionary prisms) including even the Shergol conglomerate, which indicates the strong movement of fluid in the formation of veins took place at very last stage. These veins enhance our curiosity to workout, which is still untouched. This is not clear as to where from, these fluids were derived at the waning stage of the Himalayan orogeny, when the magmatic activity seems to have ceased.

These syntectonic mineralized veins are formed by quartz, calcite and/or co-existing quartz-calcite mineral pair, which varies in size from very thin to thick (2mm to few centimeters) and indicate strong movement of fluids during deformation. These veins are randomly distributed in all the direction. On the basis of occurrence, these are further divided into three categories 1) fault/fracture filling veins, 2) network veins and 3) sigmoidal veins (Figure 2.12 to 2.15). The majority ($\geq 98\%$) of the veins are fault/fracture filling type in the study area of LAP, which developed along the weak plane such as fault, fracture, bedding

plane, etc. The occurrence of network and sigmoidal veins are very less (<2%) or negligible. It suggests rapid intrusion in weak planes (fault, fracture, bedding plane). It also indicates that the fault/fracture filling veins were formed during the collapse process of dilatational run within a system (Sibson, 1986). The origin of fault/fracture filling calcite vein preserve the evidence of its source and fluid composition which migrate through faults/fractures (Dietrich et al., 1983; Avigour et al., 1990; Gao et al., 1992) and the co-existing quartz will help to estimate the crystallizing temperature of these veins. The calcite veins are commonly formed with other geological processes such as tectonic deformation, and remagnetization (Kessen et al., 1981; Clauer et al., 1989 and many more).

2.3.1 GEOLOGY OF PALEO ACCRETIONARY PRISM (PAP)

The paleo accretionary prism was shaped in the fore arc basin of Dras arc during the Craterous time. It is mainly comprised of subduction related metamorphic rocks (i.e. Blue schist, Oceanic Island Basalt and Ultra High Pressure metamorphic rocks). The paleo accretionary prism is mainly comprised of cretaceous cherty shale, jasperoid shale, volcanics, sandstone and conglomerate, along with serpentinite, magnesite, peridotite, coesite bearing eclogites, Oceanic Island Basalt (OIB) and blueschist facies metamorphic rocks (Viridi et al., 1977; Thakur, 1981; Thakur and Mishra, 1984; Honegger et al., 1989; Mukherjee and Sachan 2001; De Sigoyer et al., 2004). Rodingite has been observed for the first time to occur in the association with serpentine.

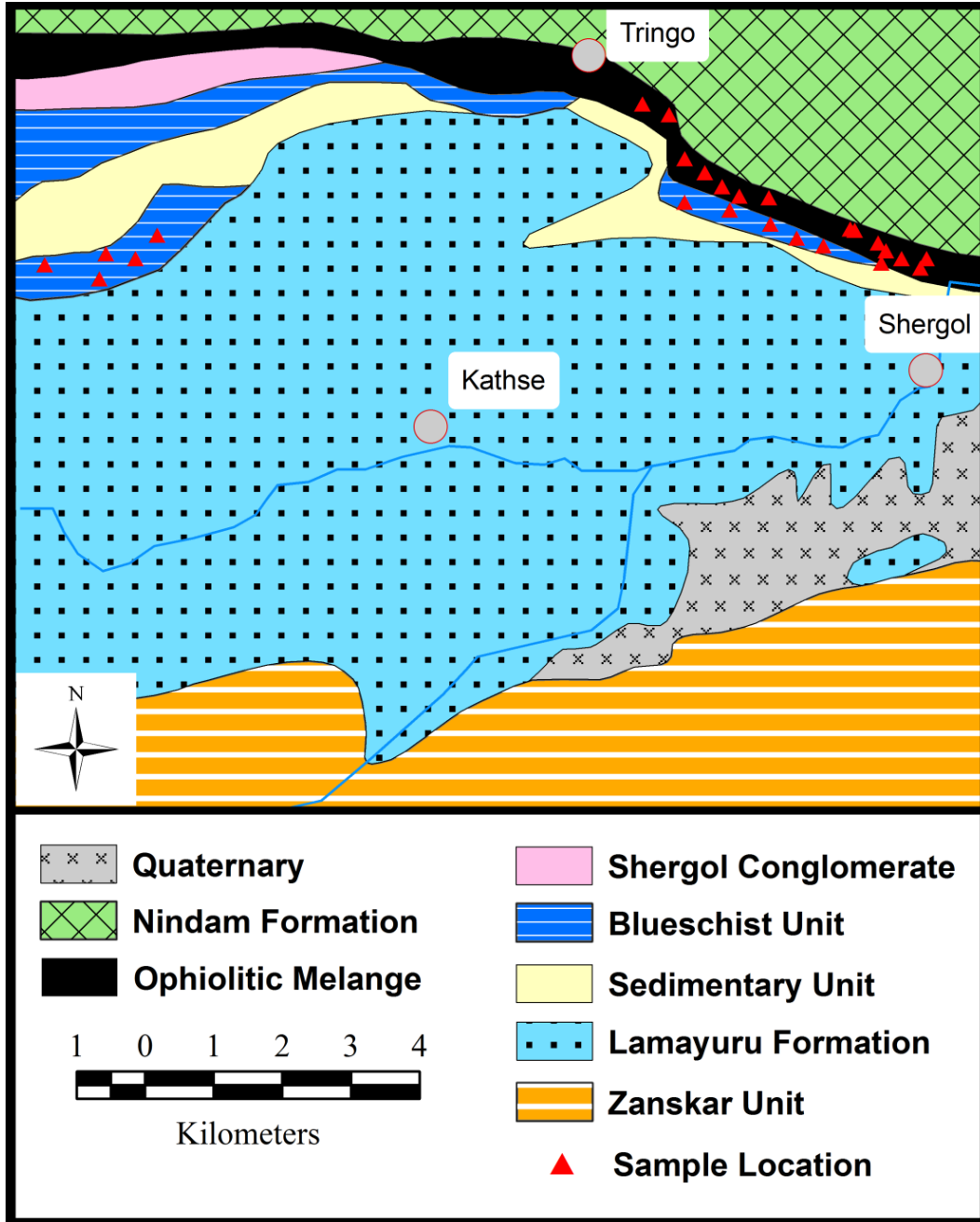


Figure 2.4: Geological Map of the Shergol ophiolitic mélangé (SOM) or western paleo accretionary prism (western PAP), modified from Honegger et al (1989).

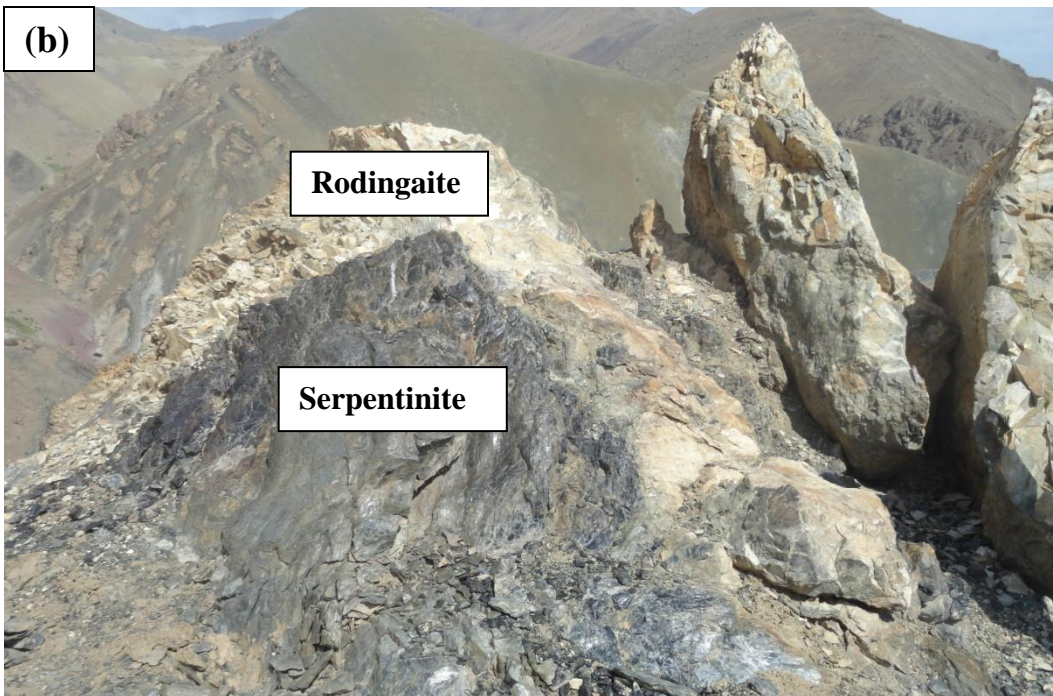


Figure 2.5: Photographs of Shergol Ophiolitic *mélange* (or western PAP). (a) Panoramic view of western PAP, and (b) Contact metamorphism of serpentinite and rodingaite.

This is suggesting of contact metamorphism with the Shergol ophiolitic rocks (Figure 2.5). The SOM is also referred to as western paleo accretionary prism (western PAP) in this study. The Shergol sedimentary units got metamorphosed to various degrees from Green Schist facies to Blueshist facies with intermixing of rocks (Honegger et al., 1989). Conglomerate, Ophiolites and Ophiolitic mélange units are also encountered in this accretionary complex (Figure 2.4). This unit is separated from the Lamayuru formation via a south dipping thrust (Thakur and Mishra, 1984) at its southern margin. The Nindam formation is well exposed to the north of SOM (Figure 2.4).

Numerous veins are present in most of the lithounits of paleo accretionary prism. These veins are encountered in the mélange units and Conglomerates, on the other hand the veining is absent in the Blue schist. It therefore suggests that the veining did not take place during the development of PAP, but are later phenomena. Except for the blue schist rocks, all other litho-units of PAP are invaded by veining.

2.3.2 GEOLOGY OF SOUTH LADAKH ACCRETIONARY PRISM (SLAP)

The South Ladakh Accretionary Prism (LAP) is well exposed along the Indus–Tsangpo Suture Zone (ITSZ) in the forearc basin of the Ladakh magmatic arc, which consists of sediments (alluvial and marine sediments) derived from both

sides of tectonic plates (Indian and Asian plates). These forearc sediments are among the few deposits that have been recognized worldwide as of an intra-oceanic origin (Brookfield and Andrews-Speed, 1984; Einsele et al., 1994; Robertson and Degnan, 1994; Sinha and Upadhyay, 1997; Clift et al., 2000). Two sections from the SLAP have been studied in detail in the present work to understand the development process of SLAP, these are, Nimu–Chilling (NC) and Lato–Miru–Upshi (LMU). The geological settings of these sections are discussed in detail in the forthcoming sections below. The NC and LMU transverse sections of SLAP are formed by the terrestrial and marine sediments derived from both side of tectonic plates and are very much comparable in terms of lithologies and sedimentation process (Henderson et al., 2010a, 2010b, 2011), whereas the Zildat section of SLAP is similar to the PAP.

The NC and LMU sections are tectonically bounded by the Indus thrust to the north (Brookfield and Andrews-Speed, 1984; Tripathy-Lang, 2013; Kharya et al., 2014) and Zaskar thrust in the south. Several local/shallow thrusts or faults are also present in these sections (Clift et al., 2000), which may be inter-connected with deep seated Indus/Zaskar thrust. These sections are bounded by the Ladakh magmatic arc in the north and Lamayuru formation in the south (Figure 2.3, 2.6 and 2.8). In the north of these sections, terrestrial sediments derived from the Asian plate found which are named as Indus group (Henderson et al., 2010a), while the marine sediments encountered at the southern margin which were derived from the Indian plate are named as Tar group (Figure 2.6 and 2.8). The

geology of NC and LMU sections is explained in detail in the next sections (2.3.2.1 and 2.3.2.2). The Zildat and Shergol sections are developed during the Cenozoic time and having similar lithology (subduction related metamorphic rocks). It is probably formed by the same (ophiolitic rocks) fluid of Shergol area. Therefore, Zildat ophiolitic mélangé could be a part of paleo accretionary prism but geographically it is very far off from Shergol area so that many workers do not consider it as a part of paleo accretionary prism. As mentioned above the Zildat was formed by subduction related metamorphic rocks in the Cenozoic time and having the same fluid of Shergol area in the formation of ophiolitic mélangé. For these reasons, Zildat is considered as a part of the paleo accretionary prism in this study (see detail in section 2.3.3).

2.3.2.1 GEOLOGY OF NIMU–CHILLING (NC) SECTION

The NC section is well exposed along the Zanskar Gorge between confluence of the Indus–Zanskar River (near Nimu village) and Chilling village (Figure 2.6, 2.7). The NC section is a transverse section of SLAP, which covers the western part of the SLAP (Figure 2.3). This section is comprised of marine and terrestrial sediments derived from both side of the tectonic plates, Indian and Asian, respectively. Marine sediments are well exposed at the southern side of this section, while the northern part of this section is comprised of alluvial/terrestrial sediments. This section is tectonically bounded by the deep seated Zanskar thrust at the south and Indus thrust at the north. The oldest units of this section mainly

consists of Paleocene–Early Eocene marine sediments along with continent derived sediments in minor quantity, which were deposited prior to the collision in the forearc basin of the Trans Himalaya (Garzanti and Van Haver, 1988; Searle et al., 1990; Steck et al., 1993; Sinclair and Jaffey, 2001). This older sequence is a group of Nummulitic Limestone, Chogdo, Sumdo and Jurutze formations, which are jointly referred to as Tar group (Searle et al., 1990; Sinclair and Jaffey, 2001) and comprised of mudstone, sandstone/siltstone (Figure 2.7) in pre–collision time (Figure 2.6). The Tar group is underlined by the Indus group terrestrial sediments of the Eocene period derived from the Asian plate. These terrestrial sediments were deposited in the forearc basin of LMA after the continental collision i.e. post–collision time and named as Indus Group (Garzanti and Van Haver, 1988; Searle et al., 1990; Sinclair and Jaffey, 2001). The Indus Group is composed of Nurla, Choksti and Nimu formations, which mainly consist of mudstone, silt/sandstone and conglomerate (Figure 2.6 and 2.7). The Indus and Tar Group are jointly referred to as the western part of SLAP, which overlie the Indian northern margin (Cretaceous Khalsi limestone, volcanoclastic sediments of Nindam formation, Triassic–Jurassic deep water sediments of Lamayuru and Ophiolitic mélangé units) and unconformably rest over the Ladakh Batholith/Ladakh–Kohistan island arc (Garzanti and Van Haver, 1988; Searle et al., 1997).

The Tar Group developed at the southern part of NC section (Zanskar Gorge), which is further subdivided into Jurutze, Sumdo, Chogdo and Nummulitic

Limestone litho units (Figure 2.6). It is overlain by the sedimentary rocks of passive Indian margin and underlain by the Indus Group (Indus molasses). The Jurutze formation is mainly comprised of black shale, siltstone/ sandstone (fine to medium grained, gray–green color), gray phyllitic rocks. These fine grain lithologies are commonly associated with silt and laminated mudstone and are profusely invaded by numerous quartz, calcite veining. In this formation shales were metamorphosed to blue–gray phyllites. It is underlain by the Sumdo formation, which consists of Early Eocene sedimentary rocks (mud stone and fine to coarse grain sandstone) along with fossiliferous Nummulitic Limestones (of Ypresian age; Henderson et al., 2010b). The overlying Chogdo formation is composed of fine to medium grained green colored sandstone and maroon shales containing calcareous nodules and conglomerates. The Nummulitic Limestone is the topmost stratigraphic section of the Tar group. The Nummulitic limestone unit of Ypresian age (~48 Ma) consists of interfingering lithologies of clastic and carbonate units. This section contains beds of Nummulitic Limestone along with gritty sandstone, mudstone and conglomerates. The subordinate crystalline nummulites are dominant in the limestone with occasional corals.

The Indus Group sediments are derived from the Asian plate and overlie the Tar Group. These are fashioned on the northern side of NC section. The Indus Group is further subdivided into Nurla, Choksti and Nimu formations (Figure 2.6). Nurla formation is alienated from the nummulitic limestone by a conformable contact, which is marked by the disappearance of carbonates and presence of shale (red

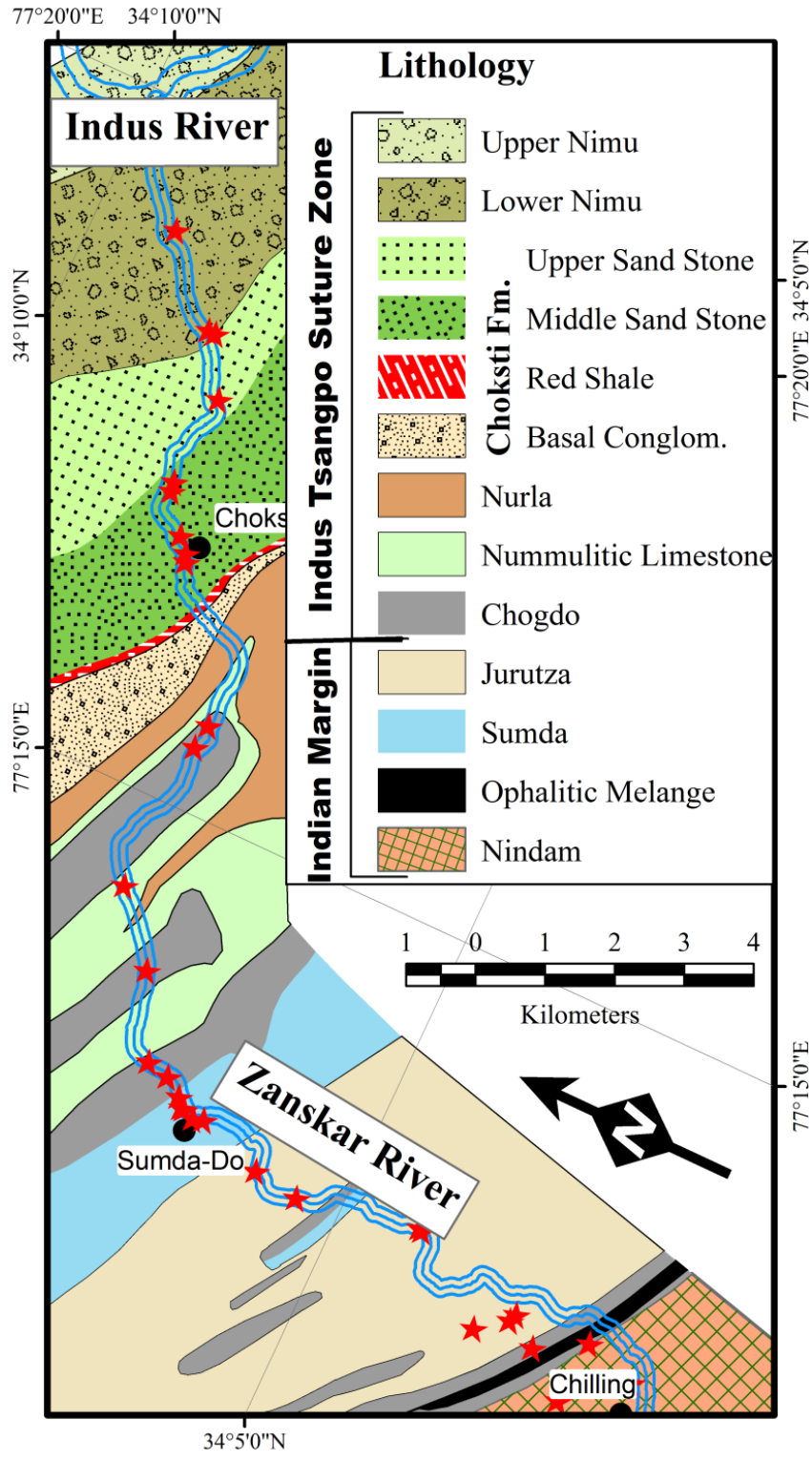


Figure 2.6: Geological Map of the Nimu–Chilling Section modified from Searle et al (1990) and Henderson et al (2010b).

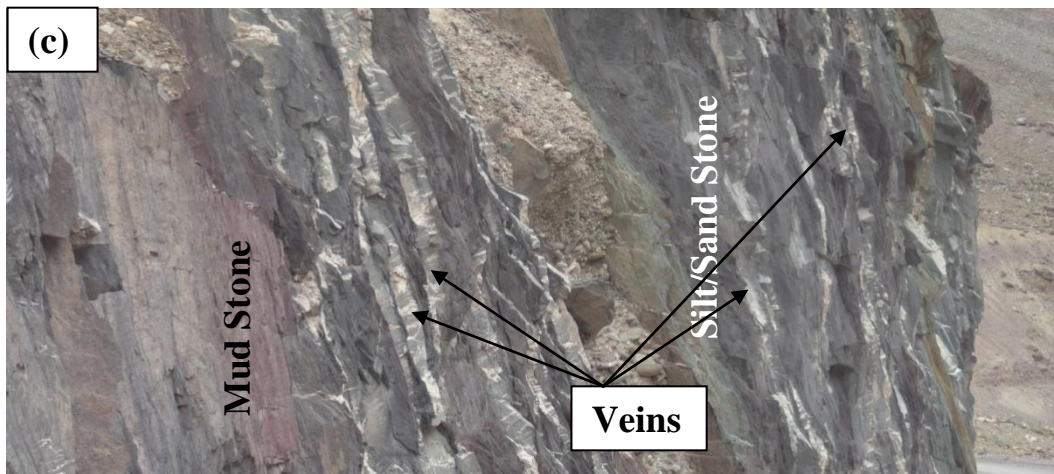
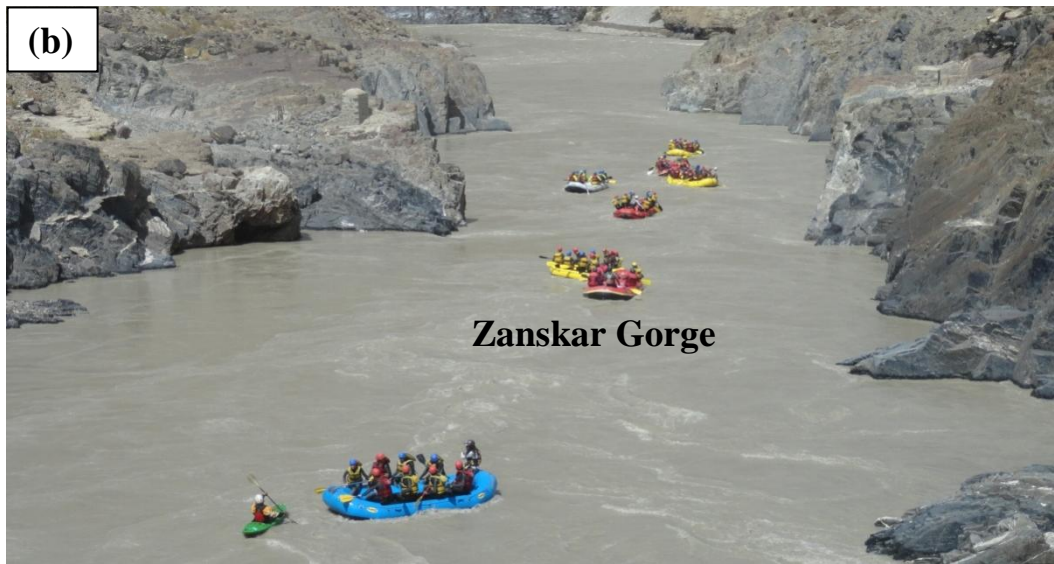


Figure 2.7: Panoramic view of Zanskar Gorge and Nimu–Chilling section. (a) confluence of Indus–Zanskar River; (b) Zanskar Gorge at Choksti bridge; (c) Deposition of Mud stone, Sand/Silt stone and the presence of veins.

and black), sandstone (coarse green to fine red color) and green color conglomerates. A similar facies of succession is noticed in Chogdo formation. The Nurla can be distinguished from the Chogdo by coarser grained deposits of sediments. The red shale contains well developed cleavage. The red shale is dominant in the Nurla formation towards its northern margin, where it has faulted contact with Choksti conglomerate. The Choksti formation is composed of alternative layers of conglomerate, Shale and sandstone, in which conglomerate is dominant member. The lower succession of Choksti formation is mainly composed of Basal conglomerate has faulted contact with the red shale of Nurla formation and Choksti formation at its southern and northern side, respectively. The basal conglomerate is intrabedded with green–yellow color, fine to coarse grained sandstone. The basal conglomerate horizon is underlain by red shale of Choksti formation, which has faulted contact with the conglomerate. It consists of sandstone and shale which show abundant ripple lamination affected by slumping (Henderson et al., 2010b). The uppermost part of Choksti formation is mainly comprised of sandstone, which is further subdivided into two categories Middle and Upper Sandstone. The middle sandstone part starts from the Choksti Bridge where thin sandstone beds are intrabedded by shale and phylite and are similar to the Nurla formation. The middle sandstone is gradually transit into upper sandstone facies having similar lithology. The upper sandstone member is comprised of yellow sandstone, black to grey and red shale. Numerous internal/local dextral faulting is reported by Henderson et al. (2010b). The Choksti formation underlines the Nimu formation at the north, which has faulted

contact (Searle et al., 1990; Sinclair and Jaffey, 2001; Clift et al., 2002). The Nimu formation is mainly comprised of sandstone, red–black Shale and orange–brown color Conglomerate. Further the upper Nimu formation has faulted contact with the lower Nimu formation.

2.3.2.2 GEOLOGY OF LATO–MIRU–UPSHI (LMU) SECTION

The Lato–Miru–Upshi (LMU) section is the central part of SLAP and is well exposed on Leh–Manali road along the Lato nala, a tributary of Indus River (Figure 2.9). This traverse section of SLAP lies between the Lato and Upshi village. The litho units of LMU section are very much comparable to the NC section, in terms of formation and sedimentation (Table 2.2). Sequences in this section are also divided into groups, viz. Tar Group and Indus Group. The Tar group was formed by the marine sediments derived from the Indian plate and overlying the rocks of the Lato Formation, while the Indus Group consists of terrestrial sediments derived sediments from Asian plate, which is overlying the Tar Group (Figure 2.8).

The Tar group in LMU section is represented by the marine sediments of Miru formation and forms a NW–SE trending syncline at the southern part of LMU section. The northern and southern limbs of this syncline are well exposed near the Miru and Lato village, respectively (Henderson et al., 2011).

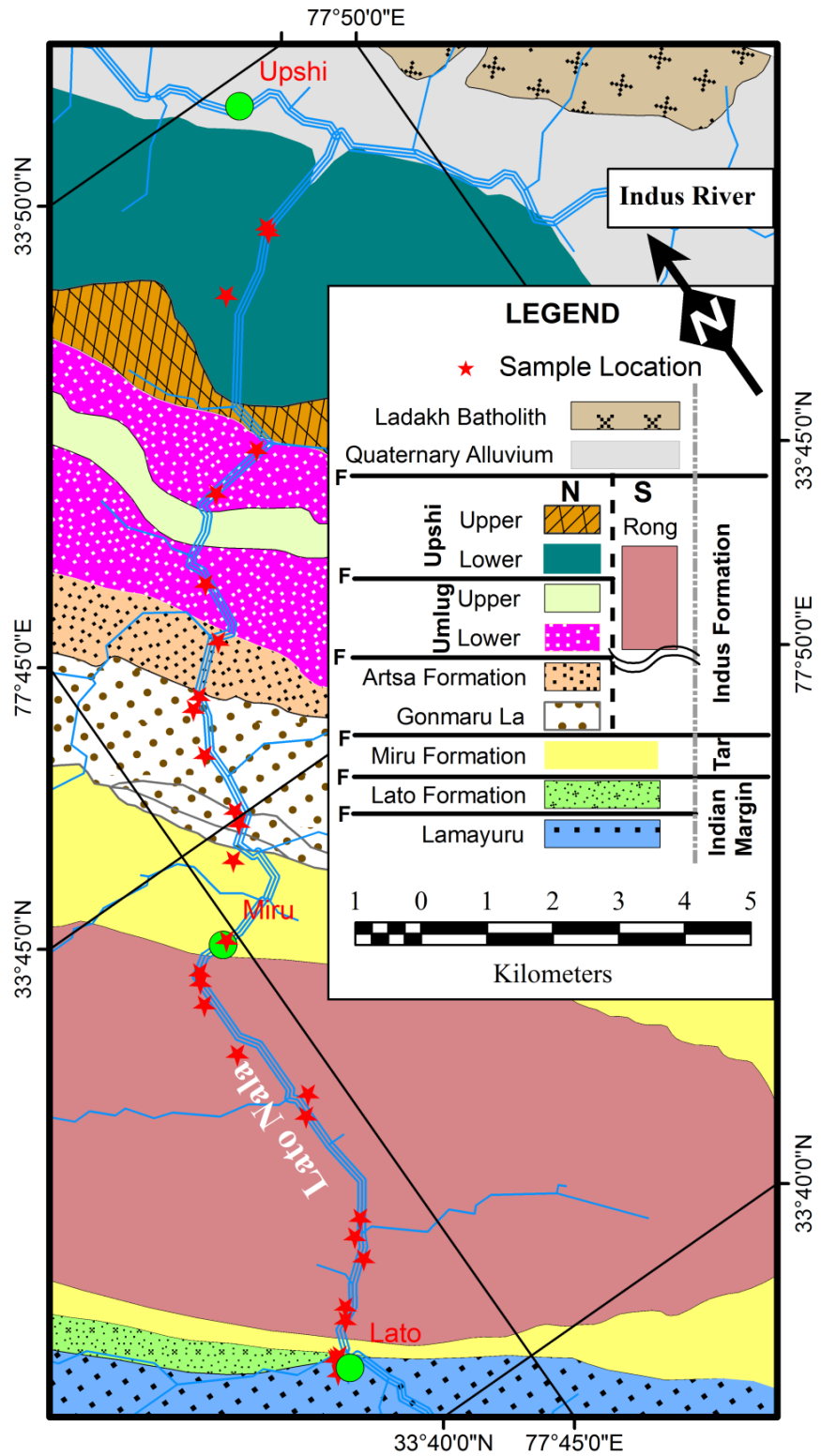


Figure 2.8: Geological Map of the Lato-Miru-Upshi (LMU) section, modified from Henderson et al (2011).



Figure 2.9: Panoramic view of LMU Section.

The Miru formation is mainly comprised of mudstone, sandstone, shale and phyllite (Figure 2.9). Minor occurrence of conglomerate is also noticed in this area.

The Indus group, in contrast, was formed by the alluvial sediments derived from the adjacent Asian plate, north of LMU section. It is further subdivided into five formations, viz. Gonmaru La, Arsta, Umlung, Upshi and Rong formation (Figure 2.8). The Gonmaru La consists of red–brown shale, red fine–medium grain sandstone along with red–blue–green color shale at the southern margin. The southern part of this unit has faulted contact with Miru formation. The Gonmaru La formation underlies the Arsta formation consisting mainly of red shale, purple sandstone and conglomerate. It has confirmable contact with the Gonmura La formation at the south and faulted contact with the Umlung formation at the northern margin. The Umlung formation in turn is structurally bounded by the faults at its both margins that separate the Arsta formation in the south and Upshi formation in the north. The Umlung formation consists of red–green color sandstone and shale along with minor conglomerate that occur near the northern side of this formation. The overlying youngest member of the Indus group, the Upshi formation, is comprised of conglomerate, red–green sandstone and red mudstone. It is separated from the Ladakh batholiths at its north by the deep seated Indus thrust, whereas the southern contact with the underlying Umlung is conformable.

Table 2. 2: Stratigraphical succession/ compression of NC and LMU section.

	Stratigraphica Age	Group	Formations	NC Section	LMU Section	
					North	South
Asian Margin	Early Tertiary	Ladakh Plutonic Complex				
South Ladakh accretionary prism	Miocene	Indus Group	Nimu	Upper Nimu	Upshi	Rong
				Lower Nimu	Umlung	
	Mid Eocene – Late Oligocene		Choksti	Upper Sandstone		Artsa
				Middle Sandstone		
				Red Shale	Gunmaru La	
				Basal Conglomerate		
	Early Eocene		Tar Group	Nurla		Miru
				Nummulitic Limestone		
				Chogdo		
				Sumdo		
Mid Cretaceous– Early Eocene		Jurutze				
Indian Margin	Mid Cretaceous	Khalsi Limestone		Stratigraphically absent		
	Cretaceous	Nindam		Lato		
	Triassic–Jurassic	Lamayuru				

2.3.3 GEOLOGY OF ZILDAT SECTION

The Zildat section is eastern margin of the LAP, which is mainly comprised of ophiolites and ophiolitic mélange rocks. Therefore it is known as Zildat Ophiolitic Mélange (ZOM). As described above in section 2.3.2; the ZOM shaped during Craterous time and are quite similar to the Shergol Ophiolitic mélange in terms of their formation event and lithology. The Zildat Ophiolitic mélange may be an extension of Shergol Ophiolitic mélange. Therefore, ZOM can be consider as a part of PAP and also referred to as the eastern PAP. ZOM is bounded by the Tso–Morari Crystalline (TMC) and Nidar Ophiolitic Complex (NOC) in south and north, respectively (Figure 2.10). The ZOM has tectonic contact with Tso Morari Crystallines and this faulted contact is referred to as the Zildat fault.

The ZOM is comprised of varying litho-units and clasts of rocks different ages, collectively known as Sumdo complex (Steck et al., 1998). The Sumdo complex is further subdivided into Drakkarpo and Ribil units (De Sigoyer et al., 2004) on the basis of lithounites present in the area. The Drakkarpo unit consists of thick (~2 Km.) polygenic conglomerate, which is a mishmash of schists, green color sandstones, and calcareous slates along with lenses of tuffs, basalts, quartzite, serpentine and micaceous schists. These tuffs are highly faulted and are filled by by quartzes, carbonates, chlorites and oxides bearing hydrothermal veins originating due to metamorphism. These alkaline volcanic rocks have similar characteristics to an oceanic island (OIB) as reported by Fuchs and Linner (1997);

De Sigoyer (1998). The white color limestone (Figure 2.11) also noticed in this section, which are said to have platform type origin and probably are of Permian in age (Colchen et al., 1987; Corfield et al., 1999; Sen et al., 2013). Whereas the Ribil units was got metamorphosed under greenschist facies and comprised of agglomeratic slates, dolomitic marbles, basalts, and vesicular basalts. The basalt is alkaline in nature and part of the oceanic island basalts (OIB) (De Sigoyer, 1998). Therefore, the ZOM predominantly consists of volcanogenic litho units with chaotic associations of basic volcanics, carbonaceous and argillaceous sedimentary rocks. The volcanogenic rocks are mainly alkaline basaltic with E-MORB-OIB characteristics and a minor NMORB component (Ahmad et al., 1996; De Sigoyer, 1998; De Sigoyer et al., 2004). The *mélange* has undergone upto blue-schist facies metamorphism (Virdi et al., 1977; De Sigoyer et al., 2004), similar to what is observed in the shergol ophiolitic *mélange* in western Ladakh (Honegger et al., 1989). The coesite bearing eclogites are also reported from this section by Mukherjee and Sachan (2001) suggesting ultra high pressure metamorphism of the Tso-Morari crystallines (Mukherjee and Sachan, 2001; De Sigoyer et al., 2004). The carbonate exotic block and quartz-calcite veining also occur in this area.

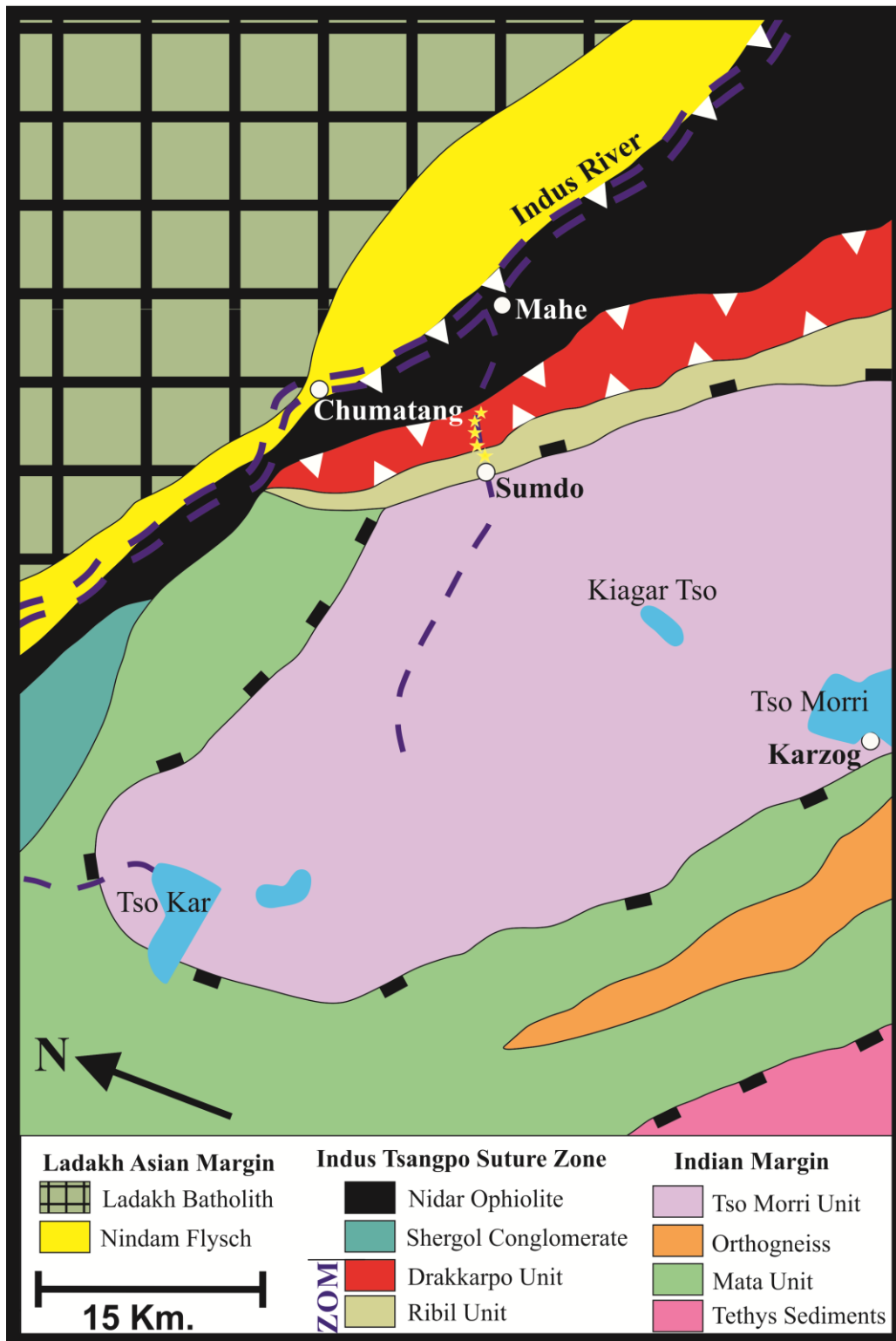


Figure 2.10: Geological Map of the eastern paleo accretionary prism (eastern PAP), modified after De Sigoyer et al (2004).

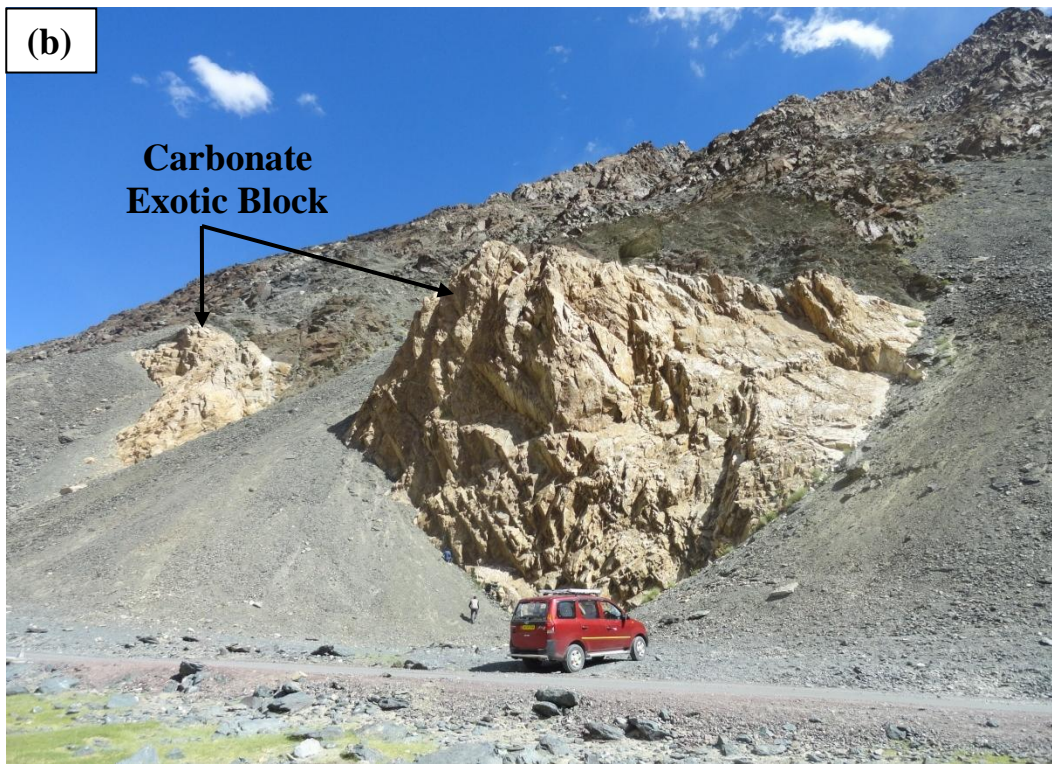
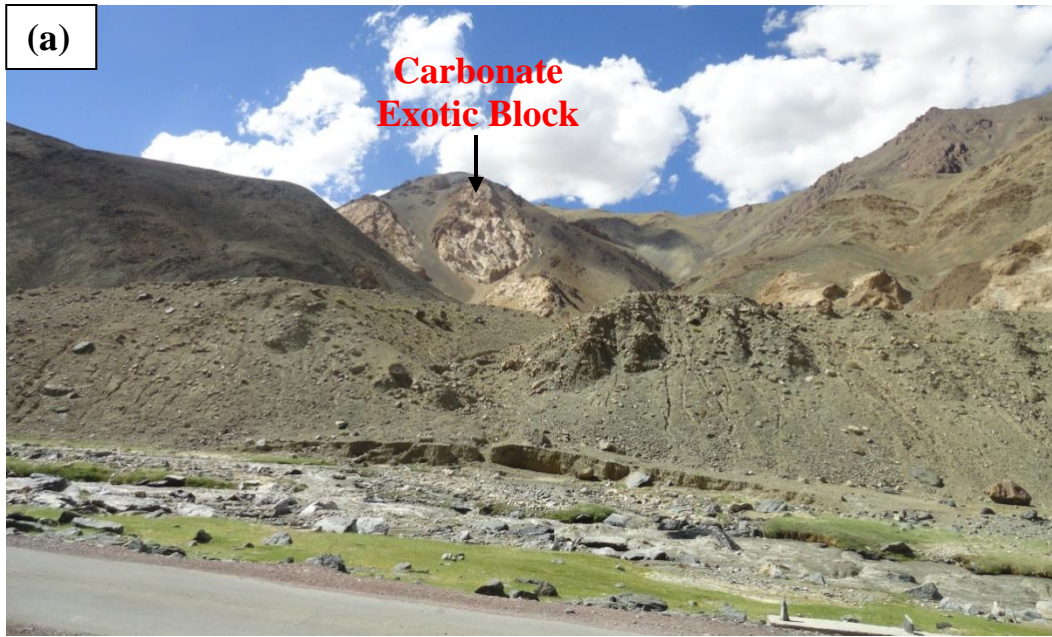


Figure 2.11: Panoramic view of eastern PAP along with the exotic blocks of limestone.

2.4 SAMPLING STRATEGY AND FIELD RELATION

As describe above in section 2.3, the LAP formed in two stages at different time periods giving rise to two separate accretionary prisms. Numerous mineralized veins are omnipresent in both the accretionary prisms. The veins present in LAP are parallel to sub parallel with respect to bedding plane of the associated host rocks, which are dipping nearly vertical (see Figure 2.7, 2.9, 2.12, 2.13, 2.14 and 2.15). This indicates that the veins were intruded in to the LAP during post deformation/tilting of the accretionary sediments along the fault and fractures. Further deformations were not noticed. These fault filling veins are very common in LAP. This veining energy was so strong that it cut the conglomerate strata, suggesting strong fluid movement at the very last stage and are obviously a matter of curiosity to know their role in the upliftment history of LAP. The earlier researchers did not pay attention on these veins. It was generally assumed, though not established, that the veins are locally derived but their presence in entire LAP and nature of occurrence indicates that these are not as simple as were thought to be. These vein samples are most suitable for fluid inclusion studies and can potentially be used to extract information related to fluid source. This is likely to unveil whether or not these veins are locally derived or having affinity to other external sources. The study of veins from LAP would also be expected to throw light to help in better understanding of accretionary processes at the later part of the developmental history of the Himalaya. Thus the veins are selected as the sampling media to unveil the literal source of veining at the accretionary front in

the Ladakh region of the Himalayan orogeny. To accomplish this study, vein samples were systematically collected from each layer of various rock types in a manner that they are representative of the different types and across the stratigraphic sequence in space and time. In view of the importance and objectives of the study, the sampling strategy was devised and adopted as far as possible uniformly in all the four sections, however, tough terrain conditions often restrict sampling to accessible areas only. Nevertheless, the sampling distributions were well representative and satisfactory for the intended purpose.

As discussed in section 2.3 of this chapter the veins types can be classified into three parts on the basis of mineralogy, i.e. (I) Pure Quartz veins, (II) Pure Carbonate veins and (III) Co-paired Quartz–Calcite veins. Apart from the mineralogical division, these veins can also be classified into three categories based on the mode of occurrence and morphology. These are - (I) Fault/Fracture Filling veins, (II) Network Veins and (III) Sigmoidal veins. The representative photographs of these various types of veins from each studied sections are presented in the Figure 2.12, 2.13, 2.14 and 2.15 of Shergol, NC, LMU and Zildat sections, respectively. Most importantly, the stratigraphy and lithology of the host rock were given due consideration. In summary, following points were kept in mind that formed the part of our sampling strategy:

- (I) Sampling has to be done across the accretionary prisms by taking the transverse section, i.e. keeping stratigraphic control of sampling.

- (II) Representative pure quartz, pure calcite and co-paired quartz-calcite vein samples were collected with or without the host rock.
- (III) Few network and sigmoidal type veins samples were also collected wherever possible.
- (IV) Wherever possible, samples from all lithounits in stratigraphic sequence (chronological order) in the proximity were collected.

Description of the lithologies, structural elements and field observations along with photo documentation and GPS locations were recorded and are given in *Appendix A*. Each sample location, thus collected, was prominently numbered and secured in sample bags before transportation to the institute. An inventory was prepared and maintained for all the samples and their field descriptions. A split of all the samples studied is archived for future use and verification. The coordinates of each sample along with other pertinent information are summarized in the *Appendix A*.

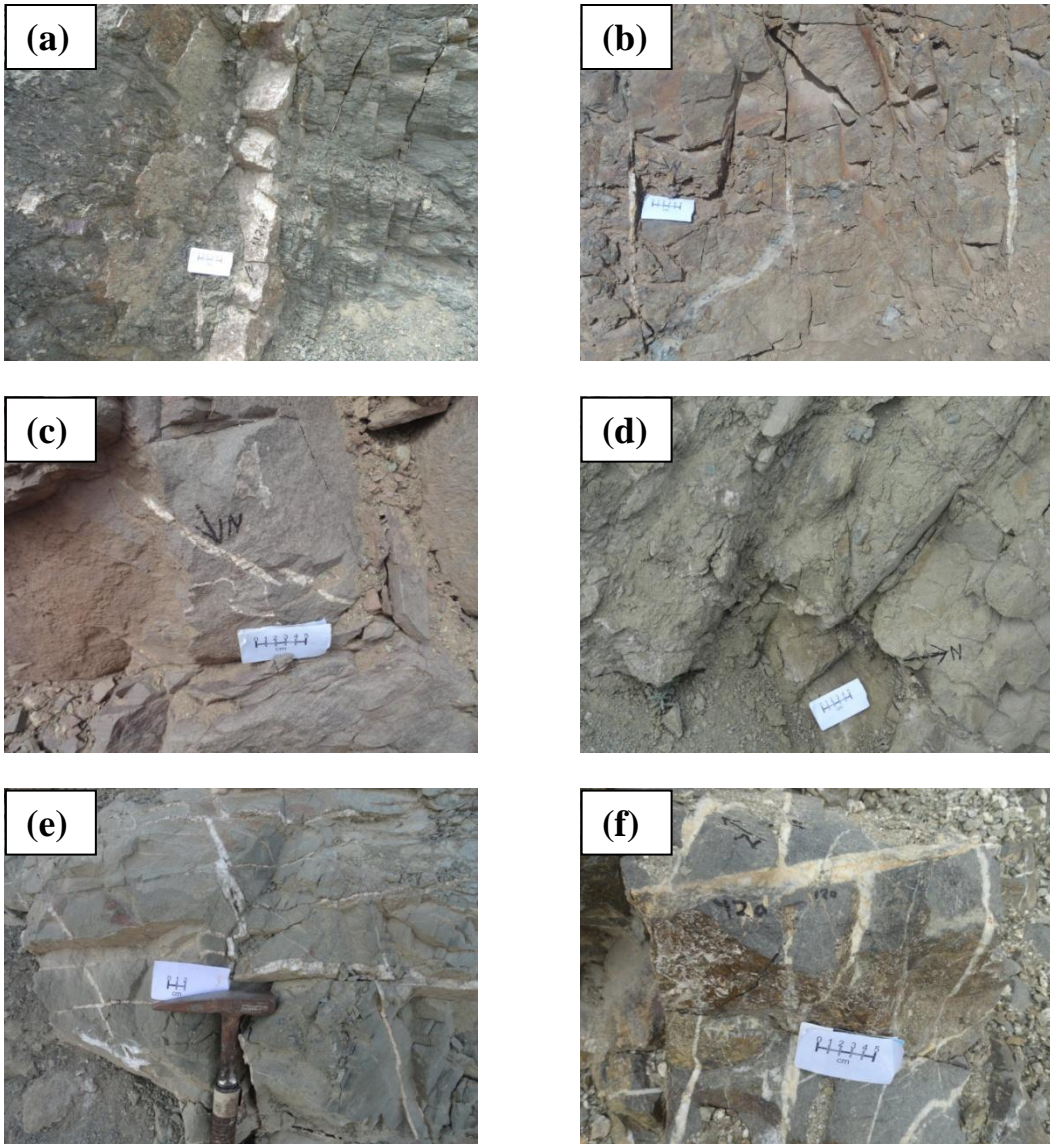


Figure 2.12: Field photographs of various types of veins present in Shergol area. (a-d) Fault/Fracture Filling veins, and (e-f) Network type veins.

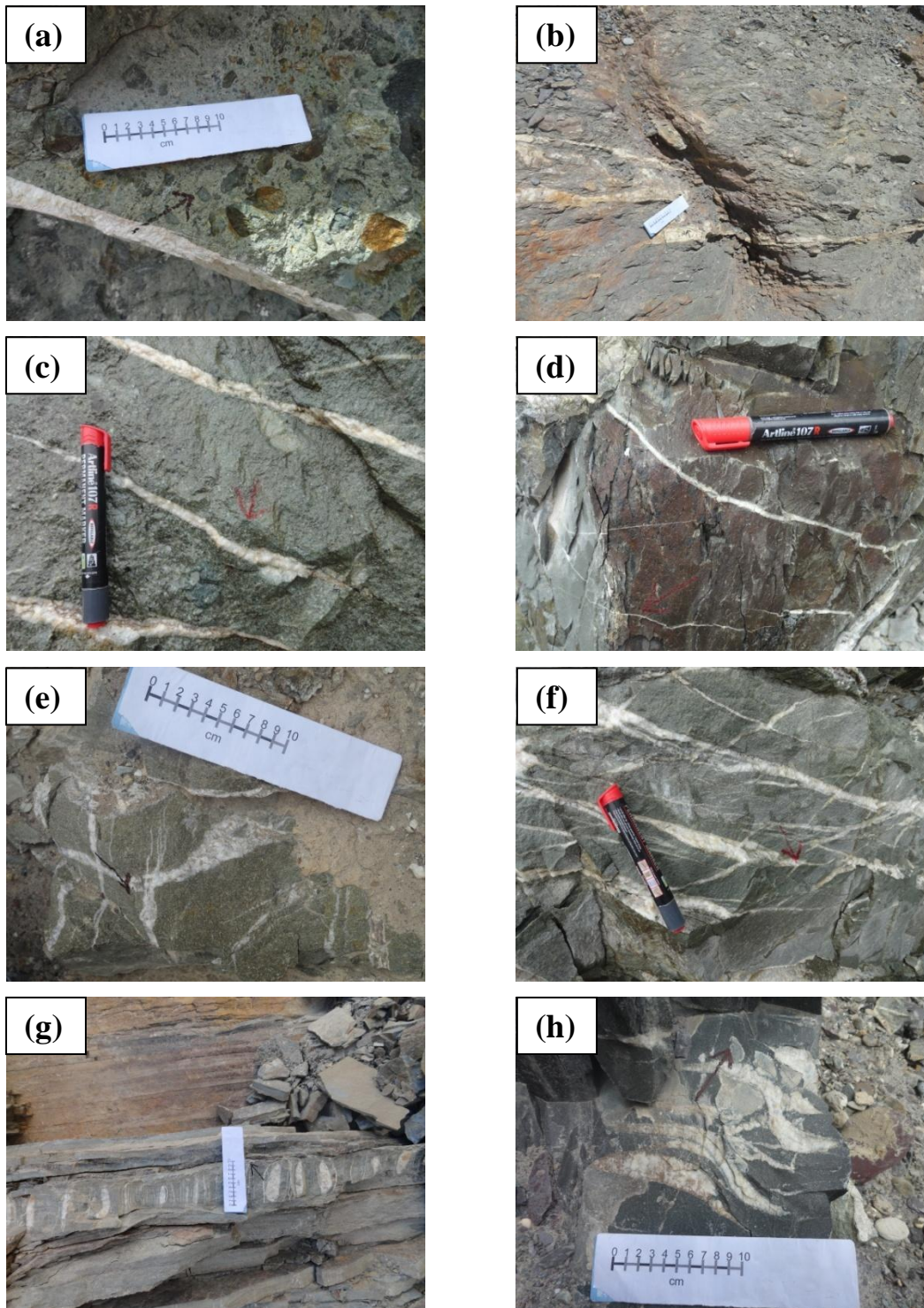


Figure 2.13: Field photographs of veins from NC section. (a-d) Fault/Fracture Filling veins, (e-f) Network type veins, (g) Bounded Neck, and (h) Sigmoidal type veins.

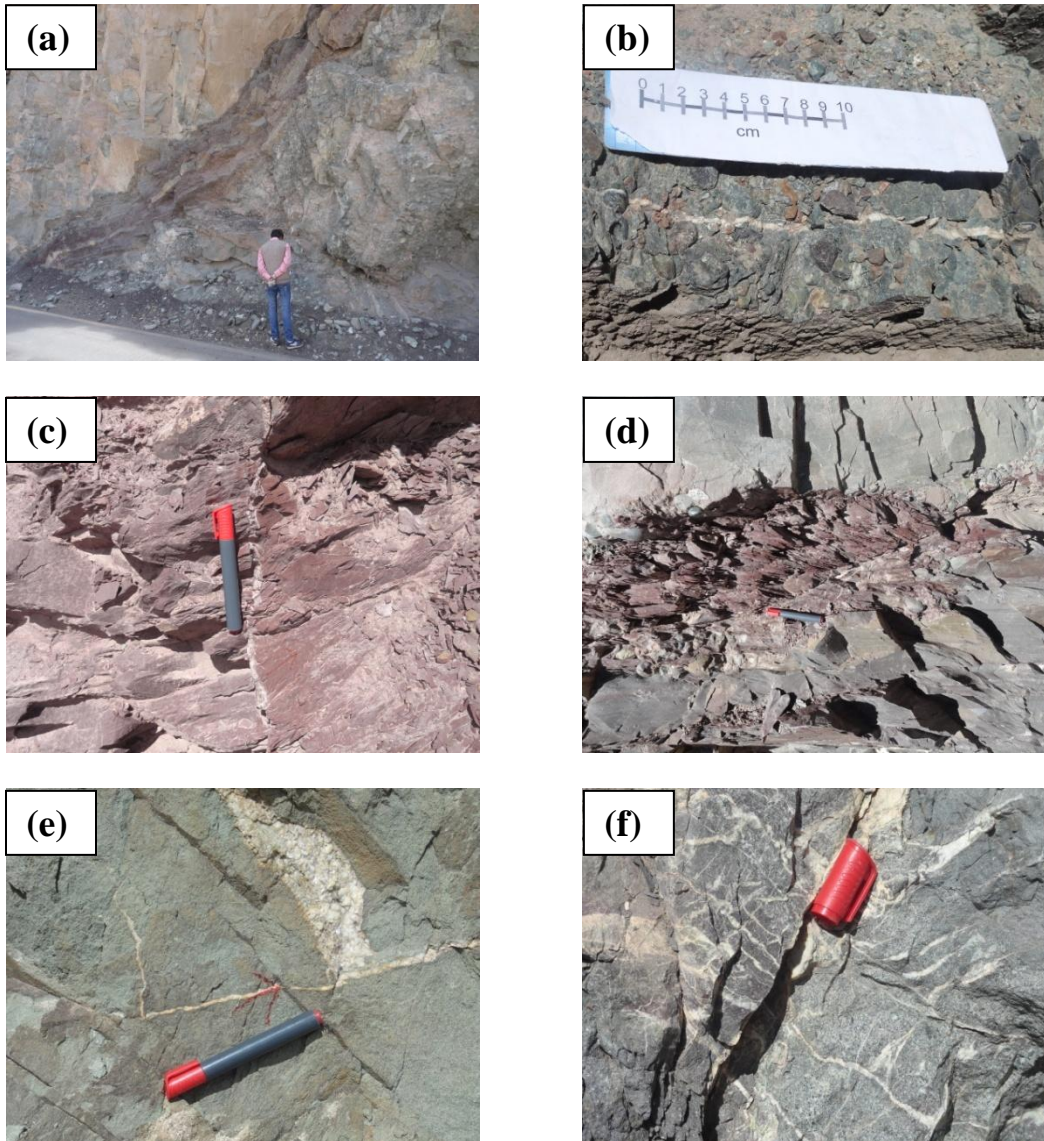


Figure 2.14: Field photographs of veins Intruded in the sediments of LMU section. (a-d) Fault/Fracture Filling veins, (e) Sigmoidal type veins, and (f) Network type veins.

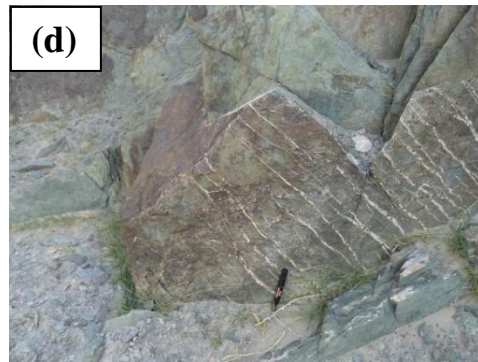


Figure 2.15: Field photographs of veins from Zildat section. (a-c) Fault/Fracture Filling veins, (d) Network type veins, and (e) Bounded Neck type veins.

CHAPTER 3:

PETROGRAPHY AND FLUID

INCLUSION

CHAPTER 3:

PETROGRAPHY AND FLUID INCLUSION

The detailed petrography of veins along with their microstructures is described in this chapter to understand the deformation history of veins. The fluid inclusion study is also included in this chapter to know the P–T emplacement history of the fluids in the study area. The fluid inclusion study covers the fluid inclusion petrography, fluid chronology, microthermometry and micro Raman spectroscopy. The fluid chronology helps to explain the entrapment of various generation of fluid with time. The micro thermometric measurements of fluid inclusions provide the temperature of initial melting/eutectic temperature (*T_{im}*), final melting temperature (*T_{fm}*) and homogenization temperature (*T_h*). These measurements will help understand the fluid composition, salinity, density and exhumation/upliftment history of the study area. The micro Raman spectroscopy deploy on the selected sample to confirm the fluid composition. The analytical procedures of these techniques are described in the forthcoming sections of this chapter.

Two thin sections of each sample were prepared, one for mineral petrography and another one for the fluid inclusion study. The samples are polished on both the

sides using carborundum powder of different mess size (500–2000). The polished samples were mounted on the glass slides using araldite/Canada Balsam. The araldite was used as an adhesive material for petrography and mineral chemistry whereas the Canada Balsam was used for fluid inclusion study.

3.1 ANALYTICAL TECHNIQUES

3.1.1 PETROGRAPHY

The mineral and fluid inclusion petrography has been carried out to examine the minerals, microstructures and the textural relationship of minerals as well as fluid species. Nikon E600 microscope was used for Petrography with the objective lenses of 2X, 5X, 10X (for mineralogy), 20X, 50X and 100X (for fluid inclusion study) magnification. The vein petrography is an authoritative technique to identify the mineral and their textural relation. The fluid inclusion petrography also plays their significance role to trace the history of various generation of fluid according to time of trapping. The size of fluid inclusions can be estimated visibly by the petrography, indicating that whether further measurements can be carried out on those inclusions or not because the small inclusions ($\leq 3 \mu\text{m}$) cannot be measured due to instrument limit.

3.1.2 MICROTHERMOMETRY

The micro thermometric measurements of fluid species were carried out in fluid inclusion laboratory of Wadia Institute of Himalayan Geology, Dehradun. All the

micro thermometric measurements were carried out using the Linkam THMSG 600 heating–freezing (micro–thermometry) stage attached with Nikon E600 microscope. The 20X and 50X magnification objective lenses were used for the measurements. In the heating–freezing stage, liquid nitrogen (LN₂) were used for freezing the inclusion, which helps to know the initial melting and final melting temperature of each individual inclusion. The homogenization temperatures were estimated by heating the inclusions through heating–freezing stage. The precision of heating freezing stage during the measurements was $\pm 1^\circ\text{C}$. The pure CO₂ fluid inclusion standard was used for calibration of the stage.

3.1.3 MICRO–RAMAN SPECTROSCOPY

Raman spectroscopy is a technique based on inelastic scattering of monochromatic light, usually from a laser source (see Figure 3.1). Inelastic scattering means that the frequency of photons in monochromatic light changes upon interaction with a sample. Photons of the laser light are absorbed by the sample and then reemitted. Frequency of the reemitted photons is shifted up or down in comparison with original monochromatic frequency, which is called the Raman Effect. This shift provides information about vibration, rotational and other low frequency transitions in molecules. Raman spectroscopy can be used to study solid, liquid and gaseous samples.

In this technique, most of the light passes through the sample (gas, liquid or solid) without any change using monochromatic light source. However, a small proportion of light will be scattered by the sample. The scattered light measured by a spectrometer, which reveals the scattered incident intensity (10^{-3}) from the sample frequency (ν_0) similar to the incident of light source. The process by which light is scattered from the sample at the same frequency as that of incident light source is called elastic or Rayleigh scattering.

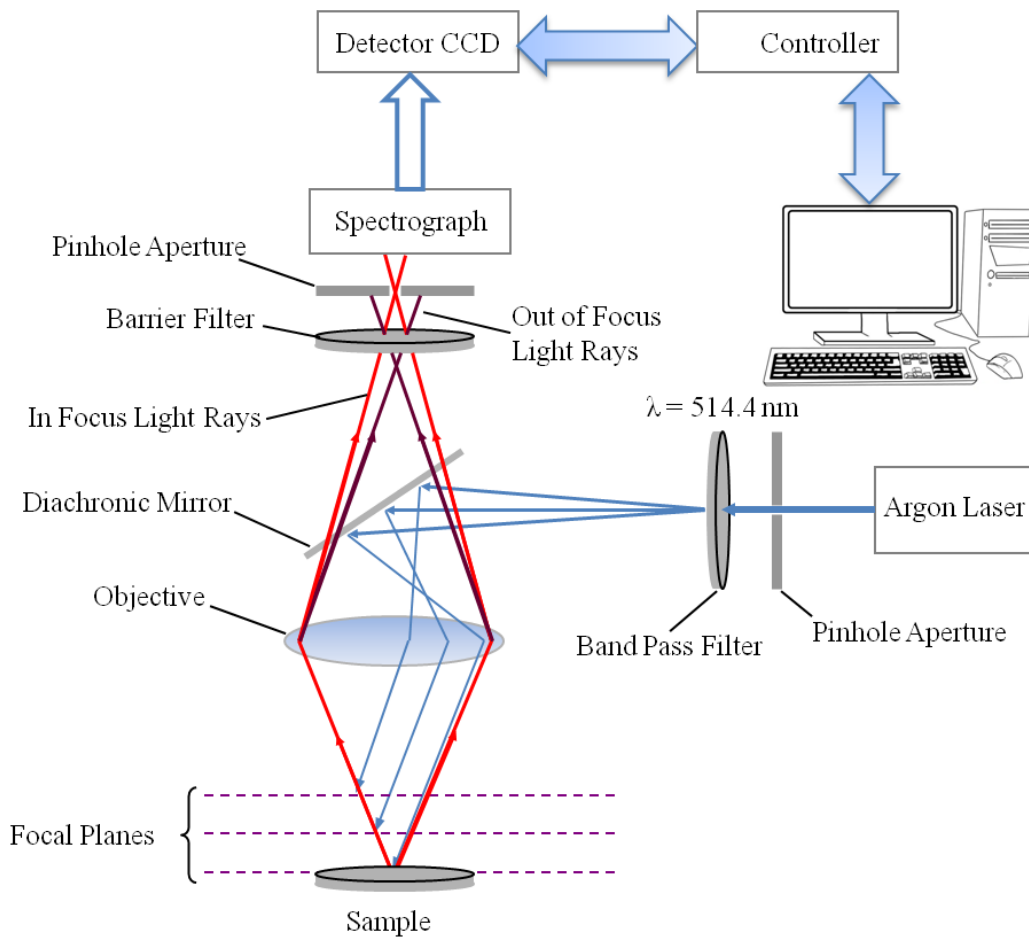


Figure 3.1: A schematic diagram of Raman principle and analytical technique.

In addition to the Rayleigh scattering, a small fraction of the scattered photons (approximately 1 in 10 million or 10^{-6}) get scattered by an excitation, with the scattered photons having a new frequency above ($\nu_0 + \Delta\nu$) and below ($\nu_0 - \Delta\nu$) different from and usually lower than that of the incident photons. It is known as Raman scattering or Raman Effect. This shift in frequency ($\pm\Delta\nu$) from that of photon radiation is independent of the exciting radiation ν_0 and are referred to the species, which give rise to scattering.

Micro Raman investigations were performed on polished fluid inclusion chip samples using a Horiba Jy-Lab HR Raman spectrometer. The device has argon laser operating at 50 mW and 514.4 nm. An Olympus BX-41 microscope was used to focus the laser on the sample, using objective lenses of 50X and 100X magnification. The microscope was equipped with binoculars and a color video camera, allowing to position the sample and to select a specific region for investigation. The backscattered light passes through a holographic notch filter (HNF), which rejects the abundant elastic Rayleigh scattering, to avoid outshining of the weaker Raman signal. The backscattered light is dispersed by using 1800 lines/mm grating and is detected on a Peltier-cooled CCD-detector. This configuration allows to record spectra with a spectral resolution of *ca.* 1 datapoint/ cm^{-1} in the spectral region between 150 and 4000 cm^{-1} . The laser was focused on each fluid inclusion samples for 20–50 seconds. The Laser Raman were calibrated using silicon and CO_2 (Fluid Inclusion) standards.

3.2 RESULTS

3.2.1 MINERAL PETROGRAPHY AND MICROSTRUCTURES

The vein mineralogy is comprised of quartz, calcite and/or its co-existing mineral (Quartz–Calcite) pair (Figure 3.2 to 3.5). The various microstructures were observed in the petrography (see Figure 3.2 to 3.5). The calcite mineral grains show various twining pattern and morphology such as i) very thin to very thick twining pattern (Figure 3.2), ii) oval shaped morphology (Figure 3.3) and iii) laminated twining (Figure 3.3). The micro-fractures in calcite grains were also noticed (see Figure 3.2 and 3.3). The quartz grains show perfect grain boundary along with clear triple junction (Figure 3.5). The sub grains of quartz were also developed along with the large grains (Figure 3.5). The quartz grains exhibited grain boundary migration and bulging and were elongated with calcite in the same manner (Figure 3.5). The quartz inclusions were also present within few calcite grains (Figure 3.4 and 3.5) indicating that calcite and quartz were crystallized together at approximately the same temperature.

The twining patterns in calcite are helpful to know about the deformation pattern controlled by the deformation temperature of the veins (according to Ferrill et al., 2004; Passchier and Trouw, 2005). The thickness of calcite twining in the carbonate veins shows wide variation from very thin to very thick (Figure 3.2 and 3.6) which got oval shape indicating effect of deformation (see Figure 3.3, 3.4 and 3.6).

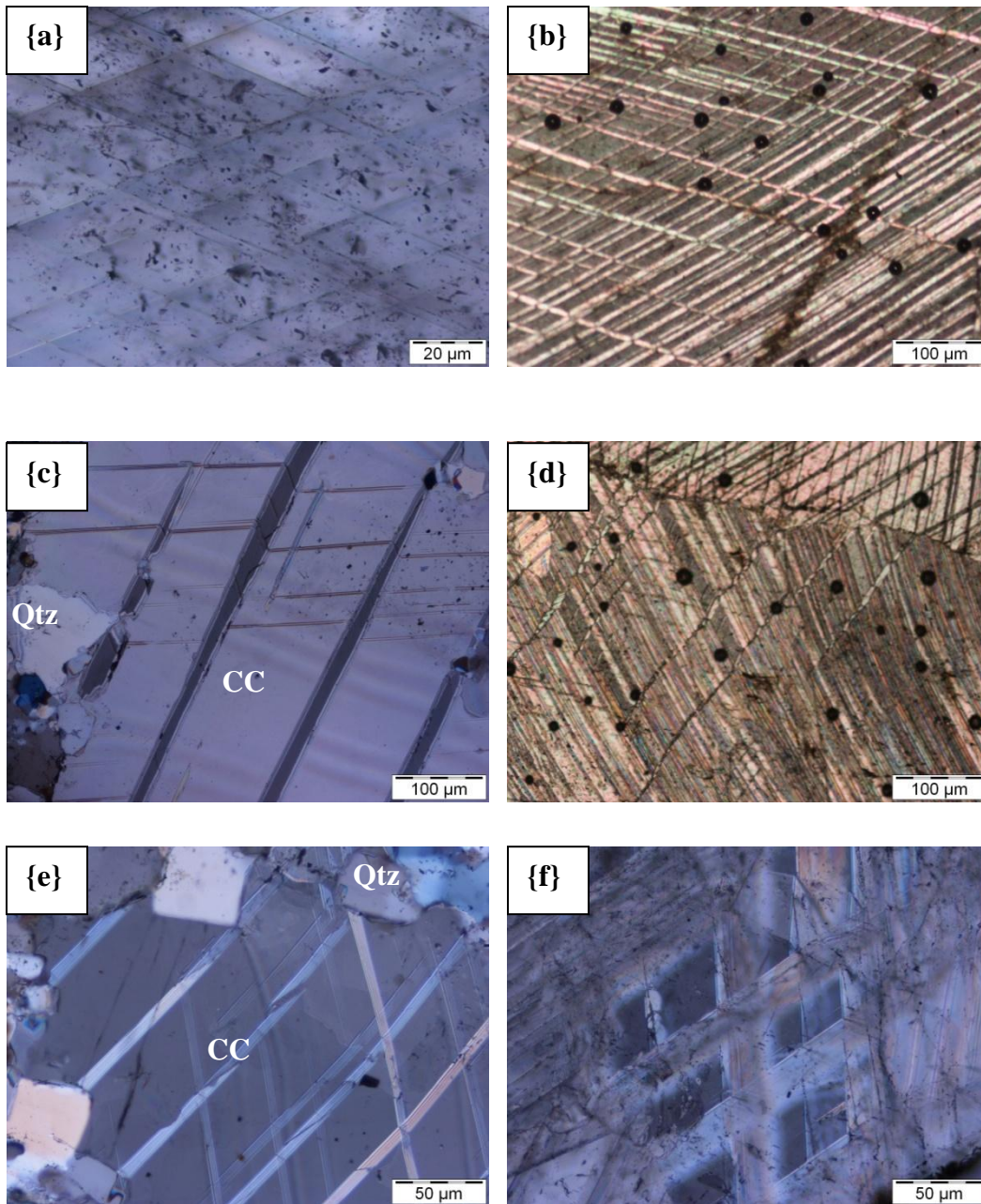


Figure 3.2: Micro photographs of mineralized veins showing various microstructures. a) very thin calcite twinning pattern, b) slightly thick twinning pattern of calcite, c) 3D view of calcite grain along with micro-fracture, d) thin to oval twinning pattern of calcite along with micro fractures, e) thick fractured twinning pattern of calcite, and f) 3D view of thick twinning pattern of calcite. Where CC = Calcite and Qtz = Quartz.

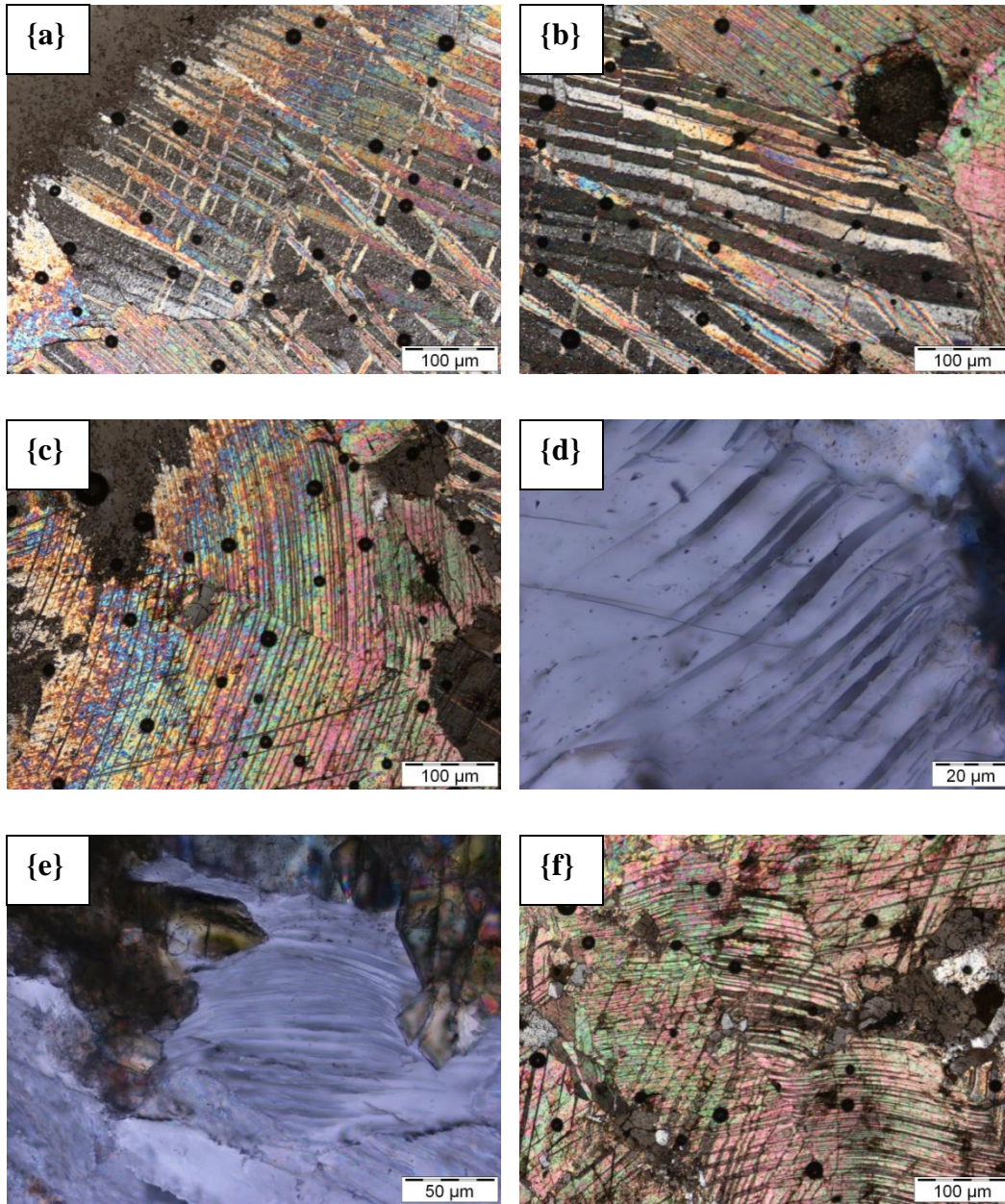


Figure 3.3: Micro photographs of mineralized veins, showing various microstructures. a) oval morphology of fractured calcite, b) thick to oval twinning morphology of fractured calcite grain, c-d) oval shape morphology of calcite mineral, e) pillow like twinning pattern of calcite, and f) highly fractured calcite grains showing thin to thick with oval morphology.

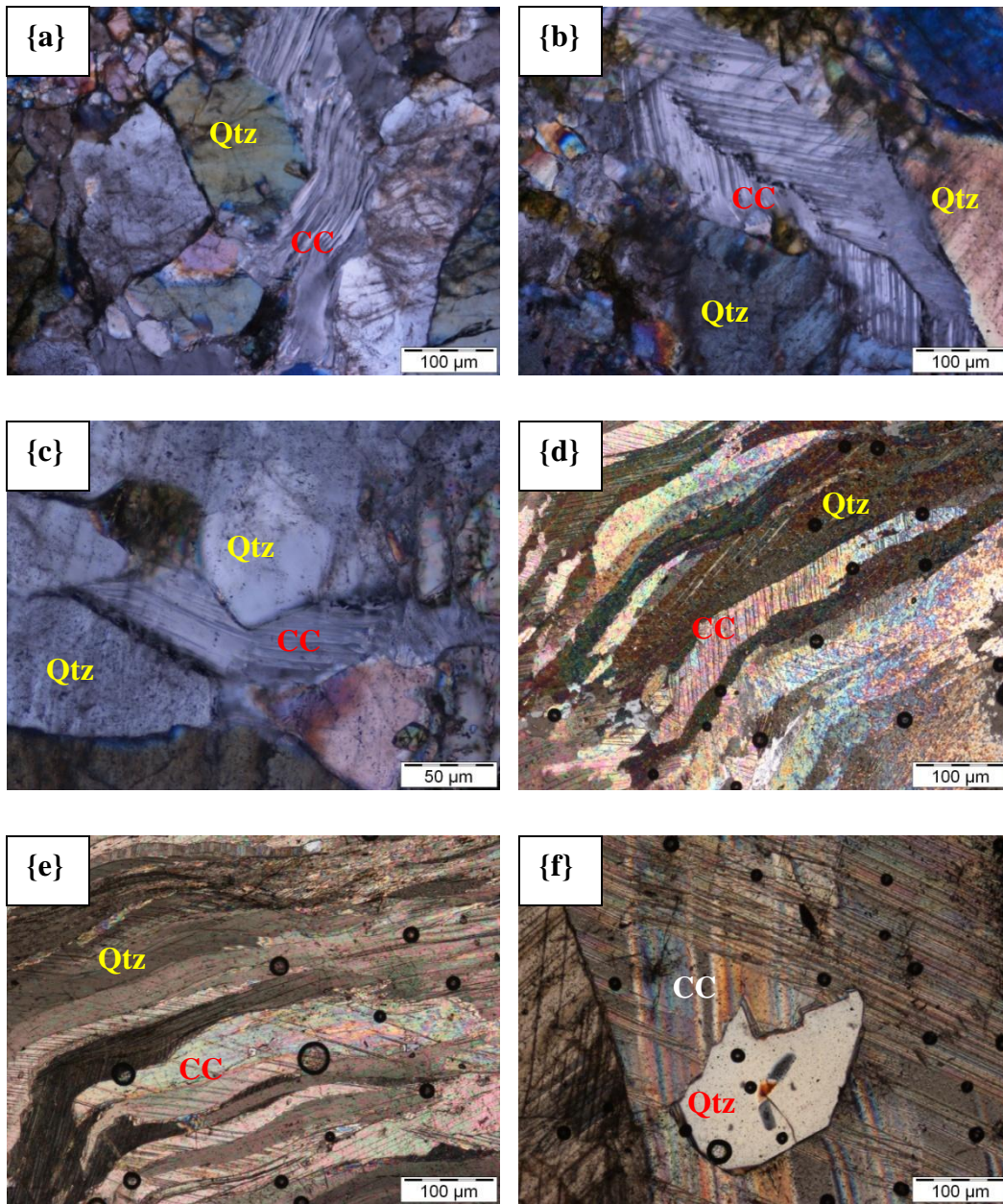


Figure 3.4: Micro photographs of mineralized veins, showing various microstructures. a) Mosaic of quartz grains with flow like calcite twinning pattern, b) co-existing pair of quartz and calcite minerals, c) calcite mineral bracketed by the quartz grains, d-e) elongated quartz and calcite minerals in same manner, and f) Quartz inclusion within the calcite mineral grain. CC = Calcite and Qtz = Quartz.

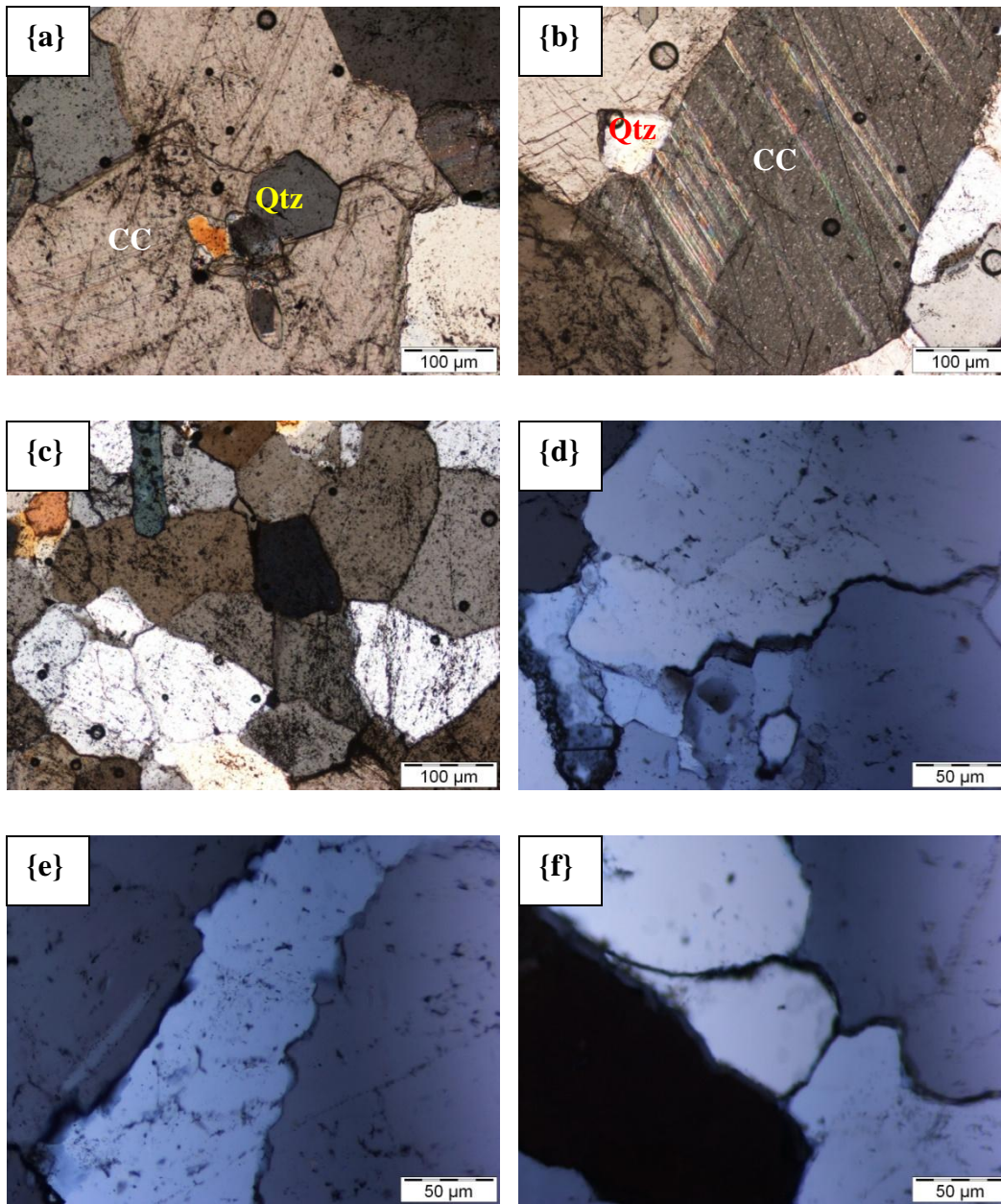


Figure 3.5: Micro photographs of mineralized veins, showing various microstructures. a-b) Quartz inclusion within the calcite mineral grain, c) Mosaic of quartz grains, d) triple point junction and recrystallization of quartz grains, e) elongated quartz grains, and f) triple point junction along with bulging of quartz grain. CC = Calcite and Qtz = Quartz.

As shown in Figure 3.6, the thin twins of calcite adapt thick tabular twinning shape with increasing temperature and further modified to unequal thick twins resulting from dynamic recrystallization (Burkhard, 1993; Ferrill et al., 2004). With increasing strain rate, the twins got curved and tapered to form an oval shaped geometry with the narrow tapering ends (Figure 3.6) as suggested by Vernon (1981). These calcite twins often crisscrossed to each other (Figure 3.2 and 3.6). The secondary micro-fractures are noticed in the calcite grain (Figure 3.2, 3.3 and 3.6) along which micro-displacement. The twin morphology was observed in the calcite grains suggesting a temperature range of 170–300°C (Figure 3.6) for twinning development and deformation (Ferrill et al., 2004).

The microstructure development, as a result of various deformation temperatures in quartz veins, has been used as a potential thermometer (Stipp et al., 2002; 2010). Various deformation patterns were observed in quartz such as sharp grain boundary, bulging, recrystallization, sub-grain development and grain boundary migration (Figure 3.5 and 3.6). The sub grains were developed along the big grain boundary due to micro-crack arrays (Tullis and Yund, 1985). Bulging in quartz grains were also observed along sutured grain boundary with triple junction (Figure 3.5 and 3.6), which also indicates the Grain Boundary Migration (GBM) and a high temperature event. These quartz grains were comprised of elongated porphyroclasts. The sutured grain boundaries with bulge (Figure 3.5 and 3.6) suggest that dynamic recrystallization was driven by local grain boundary bulging (Stipp et al., 2002; 2010) at around temperature of deformation between 300 and

400°C (Figure 3.6). Developments of sub grains within the quartz grains due to recrystallization indicate slightly higher temperature of vein formation ranging from 400 to 500°C.

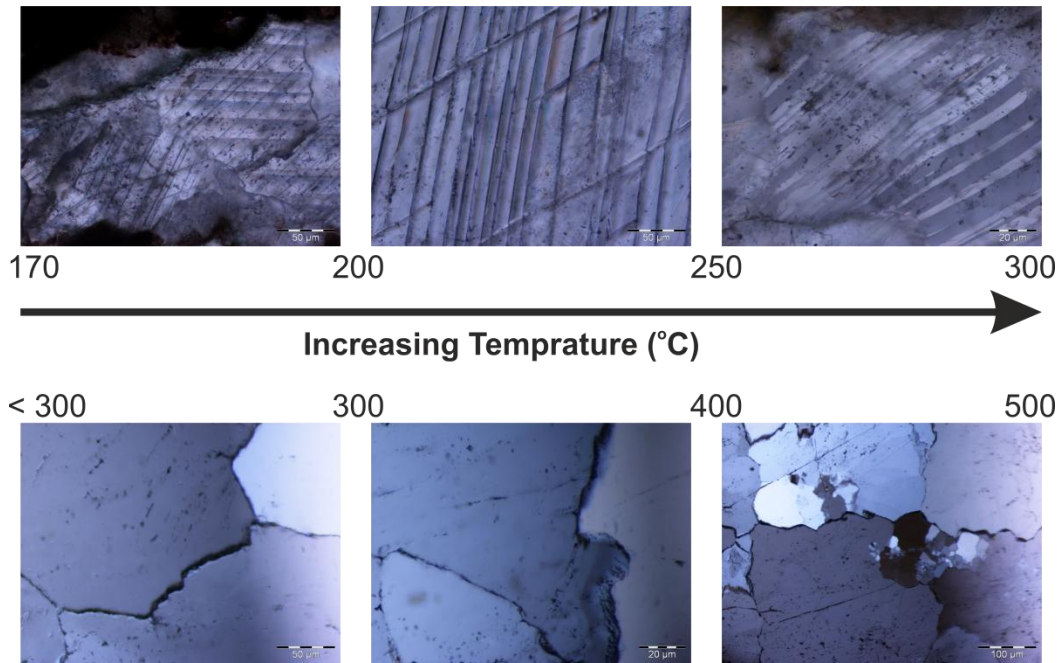


Figure 3.6: *Microstructures and Deformation Temperature of veins adopted after Ferrill et al (2004), Passchier and Trouw (2005), Stipp et al (2002 and 2010).*

As shown in Figure 3.6, the microstructures and deformation pattern of quartz and calcite veins indicate the deformation temperature of veins in the range of 170–500°C (Figure 3.6) based on micro-textural deformation thermometry (Ferrill et al., 2004; Passchier and Trouw, 2005; Stipp et al., 2002, 2010).

3.2.2 FLUID INCLUSION PETROGRAPHY

The fluid inclusion petrography was carried out on all four studied sections. The mono phase carbonic and bi phase aqueous–carbonic inclusions were noticed from all studied sections. The primary fluid inclusions were of 10 to 3 μm in sizes whereas the secondary fluid inclusions are generally $\leq 5 \mu\text{m}$ in size. The fluid inclusions are classified into three categories, viz. (i) primary, (ii) secondary and (iii) pseudosecondary. These inclusions are dominantly either mono–phase or bi–phase and rarely 3–phase type. The fluid inclusion shows various re–equilibration textures from all studied sections, which are the tracer of various fluid movements. The detailed fluid inclusion petrography is summarized in the respective sections below.

Paleo Accretionary Prism (PAP):

The two section Shergol and Zildat studied under the paleo accretionary prism (see detail in chapter 2) and their fluid inclusion microphotographs are shown in Figure 3.7 to 3.9. The mono phase, bi phase inclusions are dominant in PAP. Three phase inclusions were also noticed, rarely (Figure 3.7). The primary, pseudosecondary and secondary inclusions were also recognized during the petrographic observation. The primary inclusions vary in size from 3 to 10 μm whereas the pseudosecondary and secondary inclusions are relatively smaller ($\leq 5 \mu\text{m}$) in size. The three types of primary inclusions are present in this system, namely mono phase, bi phase and three phase (Figure 3.7).

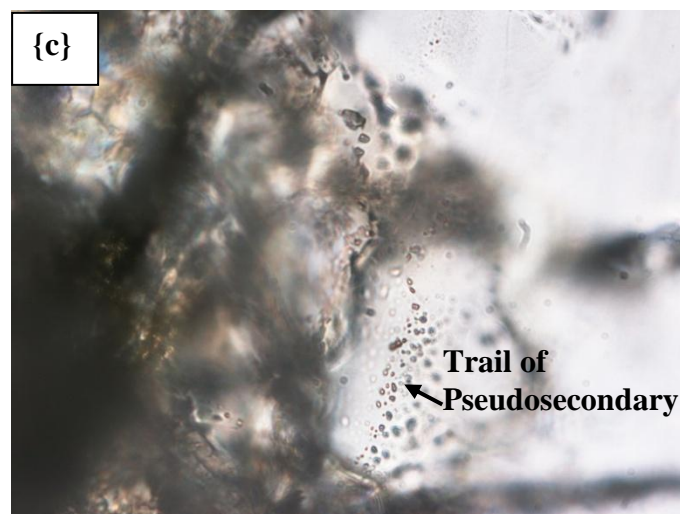
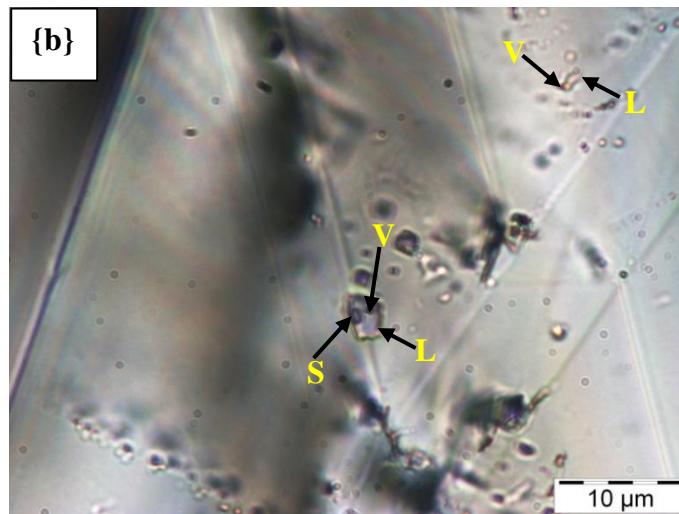
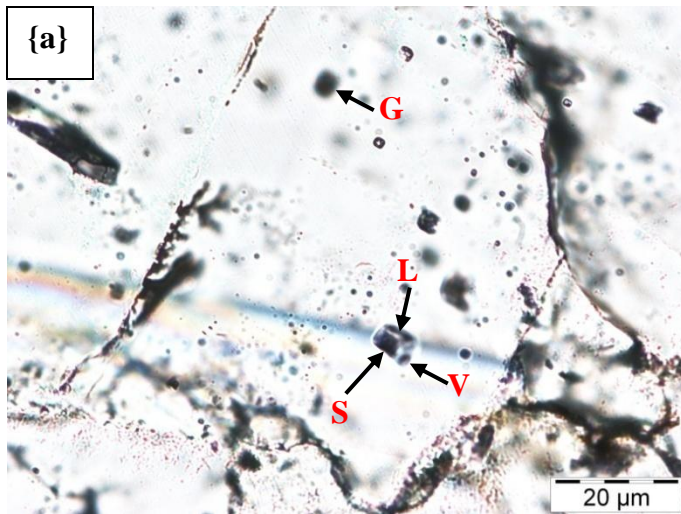


Figure 3.7: Primary mono phase, bi phase and three phase inclusions of PAP.
 Where V = Vapor, L = Liquid, S = Solid and G = Gas.

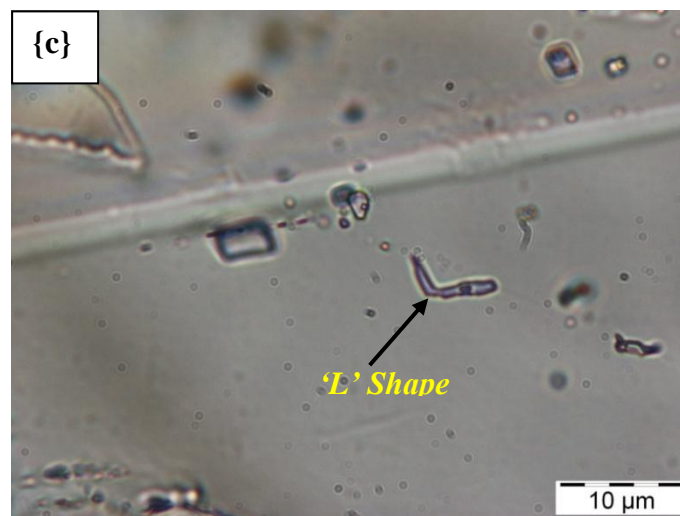
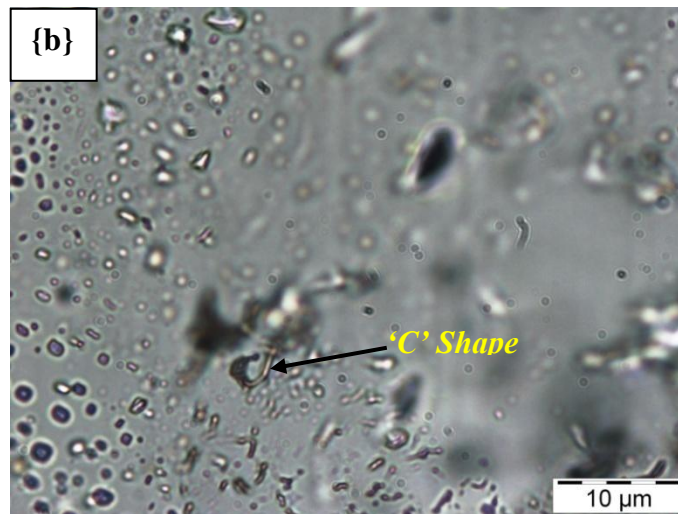
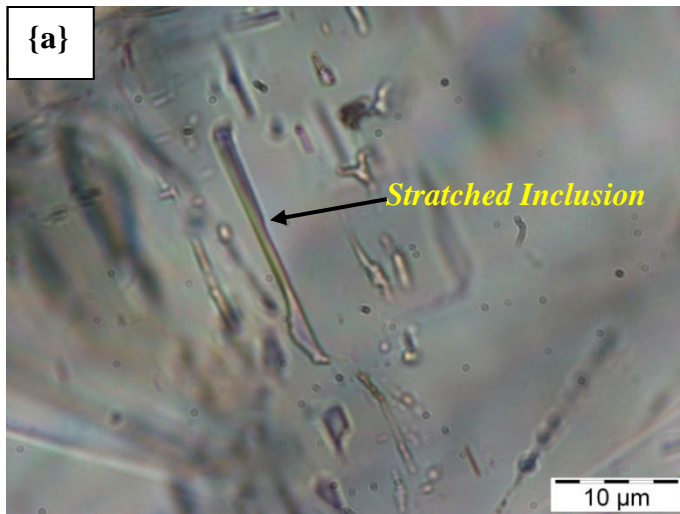


Figure 3.8: Various primary re-equilibration inclusions of PAP.

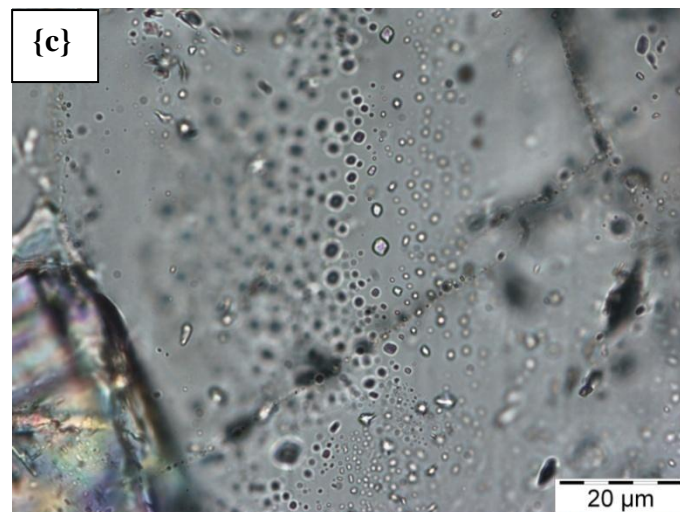
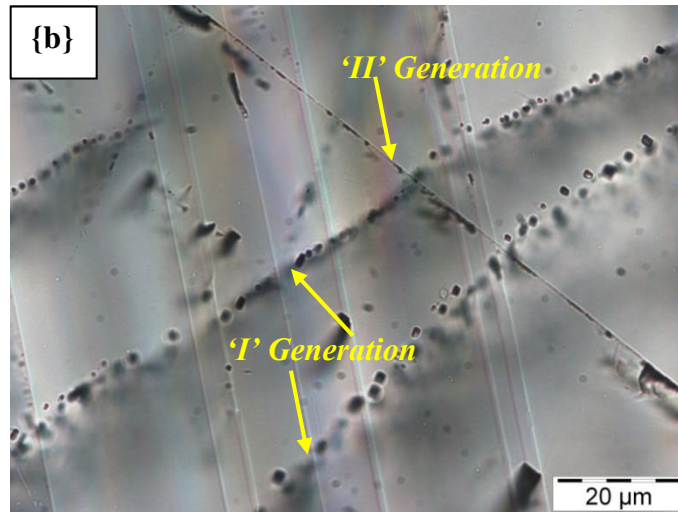
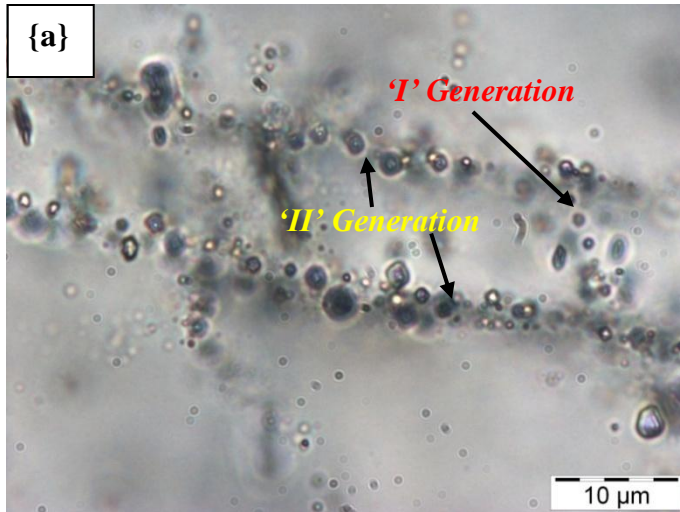


Figure 3.9: Trails of secondary inclusions of PAP.

The pseudosecondary inclusions contain the trail of mono phase and bi phase inclusions (Figure 3.7) and the secondary inclusions comprised of bi phase inclusions only (Figure 3.9). The re-equilibrated primary inclusions are also observed which show various textures such as i) highly stretched inclusions, ii) 'C' shape inclusions and iii) 'L' shape stretched inclusions as shown in Figures 3.8a, 3.8b and 3.8c, respectively.

The fluid chronology of the Paleo accretionary prism (PAP) explains the entrapment features of various types of fluids at different times. The mono phase, bi phase and three phase inclusions occur in isolated as well as in cluster (see Figure 3.7 and 3.8) indicating their simultaneous entrapment at first stage. The pseudosecondary inclusions formed a trail of inclusions at later stage. The secondary (bi phase) inclusions were entrapped in the system at the last stage. The last phase of fluid history was highly tectonized which is evidenced by the presence of the varieties of re-equilibration textures.

South Ladakh Accretionary Prism (SLAP):

The South Ladakh Accretionary Prism (SLAP) is comprised of NC and LMU sections (see detail in chapter 2). The fluid inclusion micro photographs of SLAP are shown in Figures 3.10 to 3.18. The carbonic mono phase and aqueous-carbonic bi phase and three phase inclusions were observed. Some of the primary inclusions show negative crystal shape (Figure 3.13a and 3.13b). The carbonic monophase inclusions are very dense (see Figure 3.10). The bi phase inclusions

are present in various shapes in the system such as i) hexagonal as shown in Figure 3.11a, ii) square/cubic (see Figure 3.11b), and iii) tube shape (Figure 3.12a). The three phase inclusions occur as isolated (see Figure 3.12b and 3.12c). The re-equilibrated fluid inclusions show many unique textural features. The highly stretched fluid inclusions are shown in Figure 3.13c along with continuous series of re-equilibrated textures present in Figure 3.14 and 3.15. The necking (Figure 3.14a), gun shape (Figure 3.14b and 3.14c), large finger nail (Figure 3.15a and 3.15b) and elongated (Figure 3.15c) textures are included in this series of re-equilibrated textures. The similar fluid morphology was also exhibited by mono phase fluid inclusions (see Figure 3.16a and 3.16b). The fluid inclusions sometime got curved and shows 'C' shape (Figure 3.16c). The implosion texture of fluid inclusion was also noticed during the microscopic observation (Figure 3.17a). The trails of pseudosecondary bi phase inclusions are also observed (see Figure 3.17b and 3.17c). The different generation of secondary bi phase inclusions are noticed which indicate multi episodic entrapment of fluid at the ultimate stage.

Fluid Chronology: The mono phase and bi phase are occurring in the form of cluster as well as in isolated form which indicate its primary in nature. Therefore these inclusions were trapped at the early stage. The pseudosecondary inclusion were also noticed which might be entrapped after the primary inclusions. The bi phase inclusions are also occurring in the form of trail cutting across mineral grain boundary.

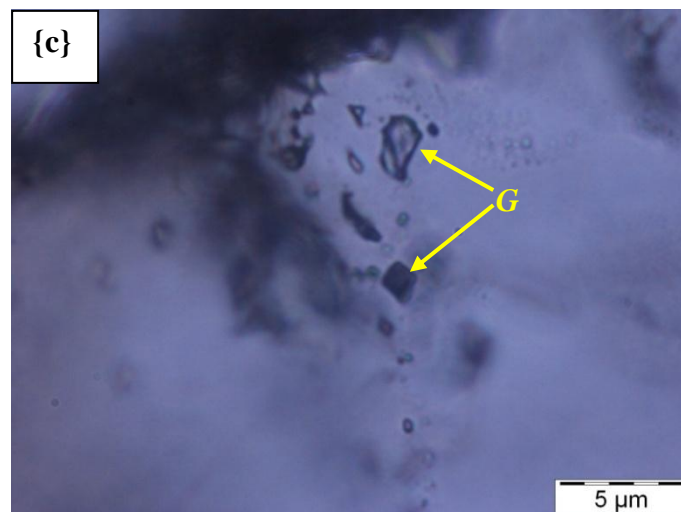
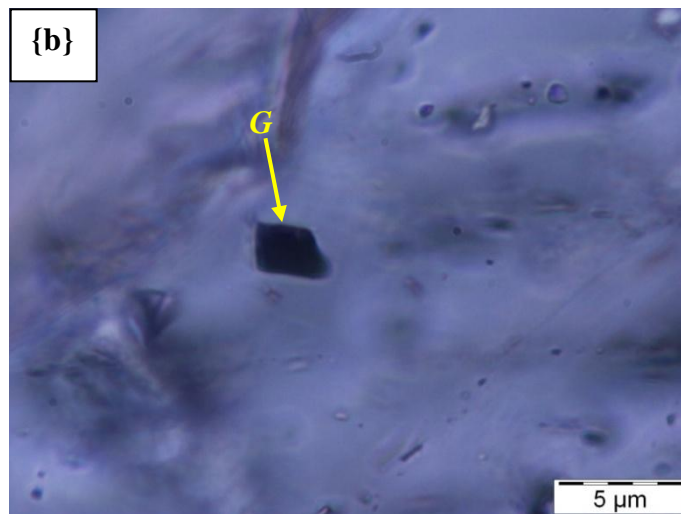
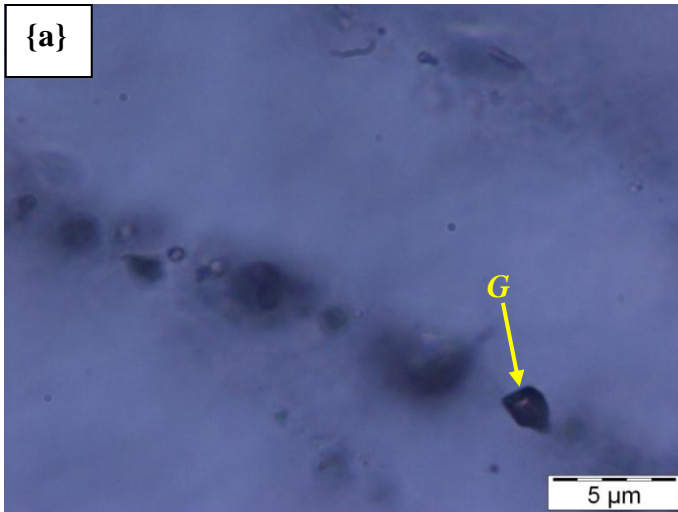


Figure 3.10: Mono phase gas rich primary fluid inclusions of SLAP.

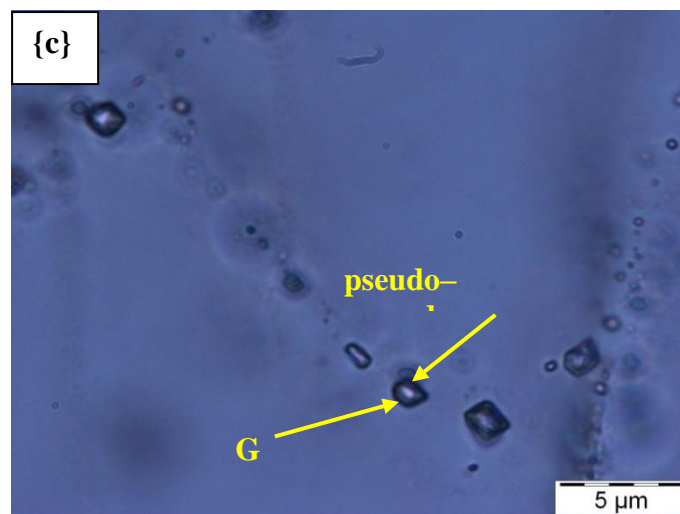
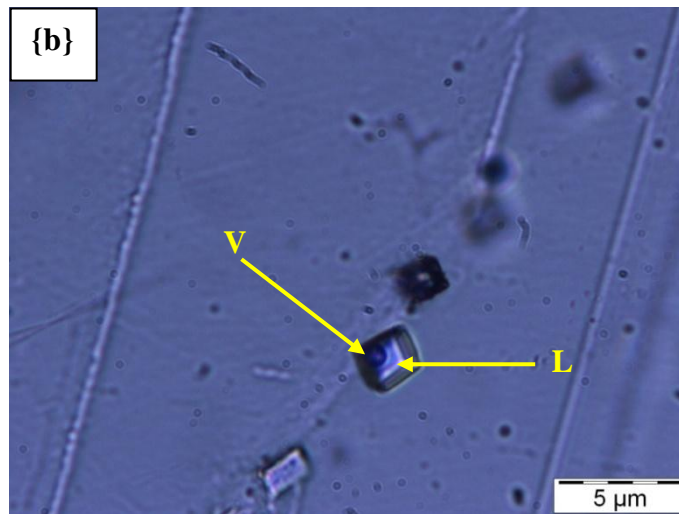
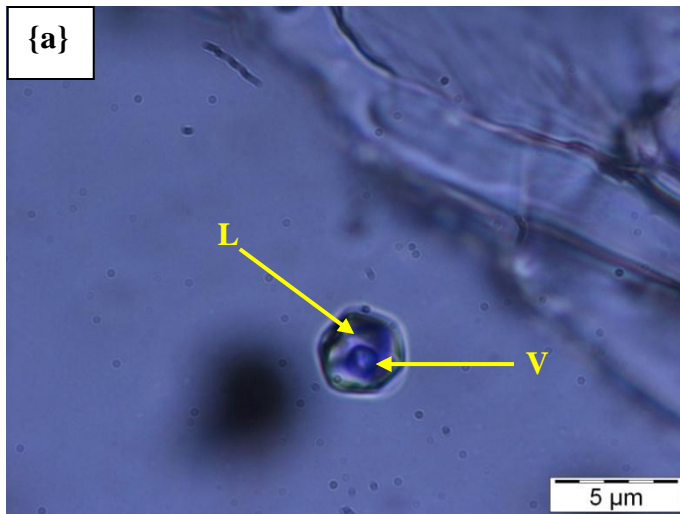


Figure 3.11: Bi phase primary and pseudosecondary fluid inclusions of SLAP.

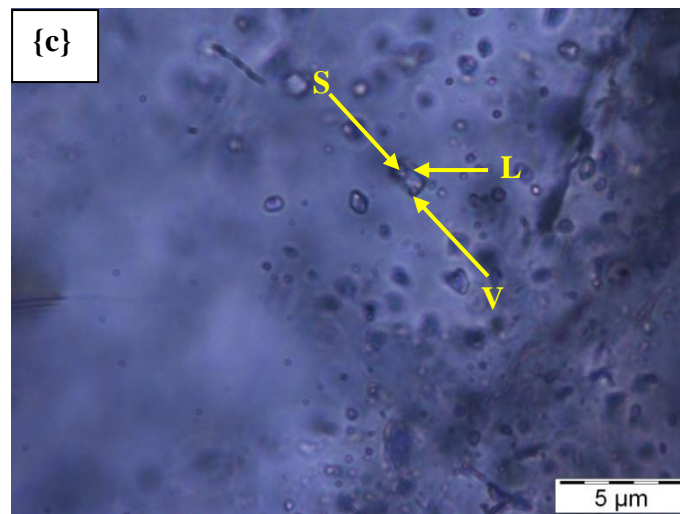
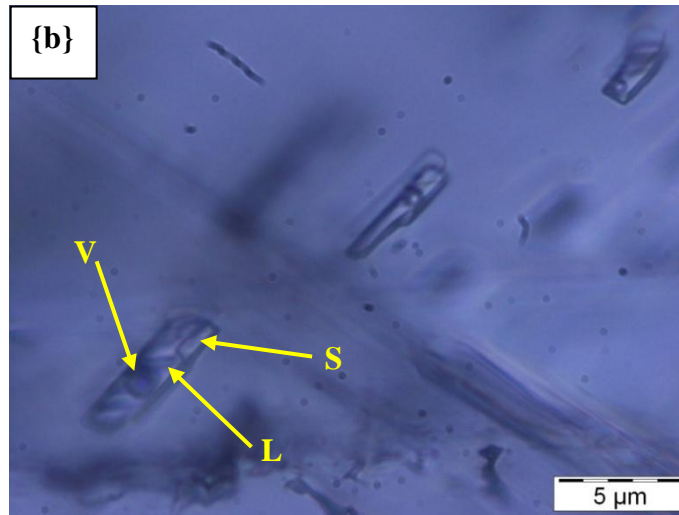
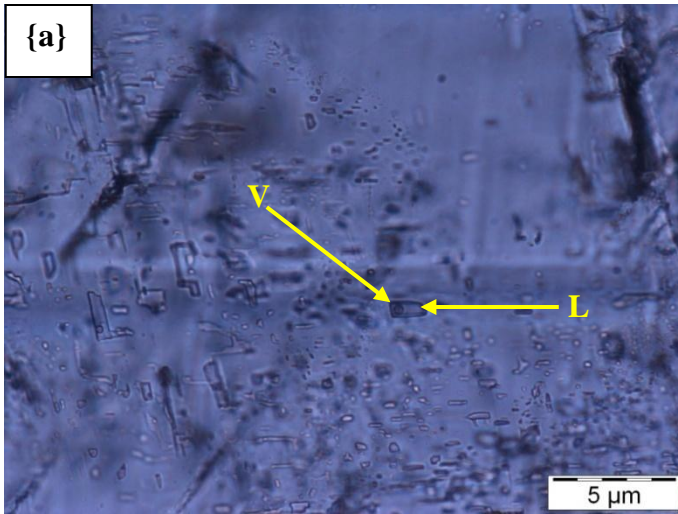


Figure 3.12: Bi phase and Three phase primary inclusions of SLAP.

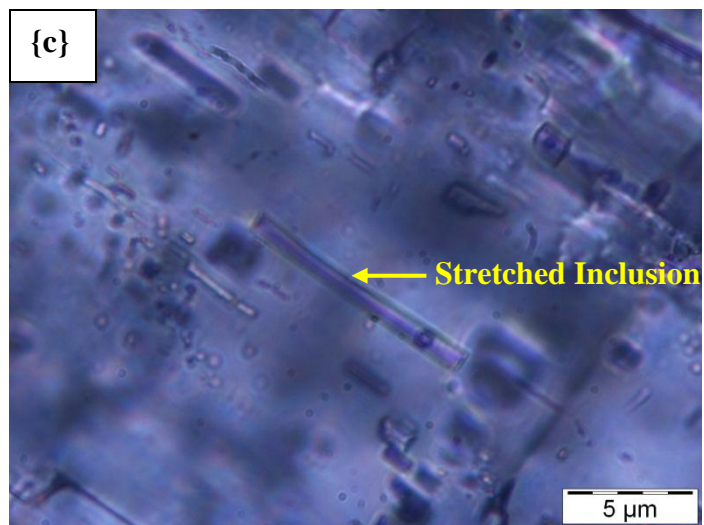
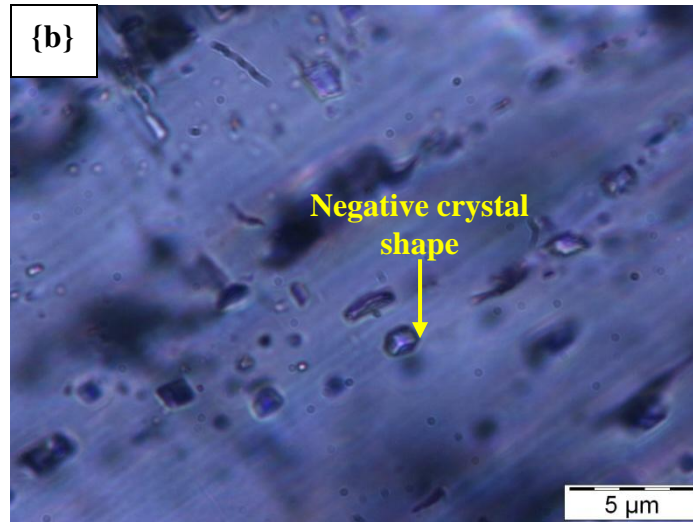
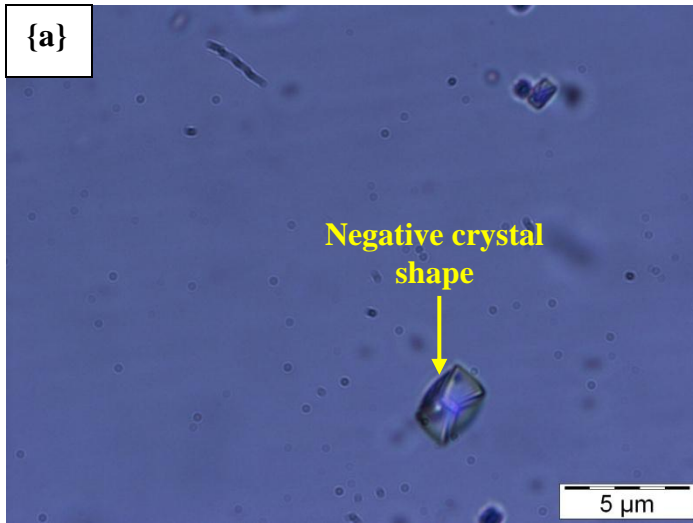


Figure 3.13: Bi phase negative crystal and stretched fluid inclusions of SLAP.

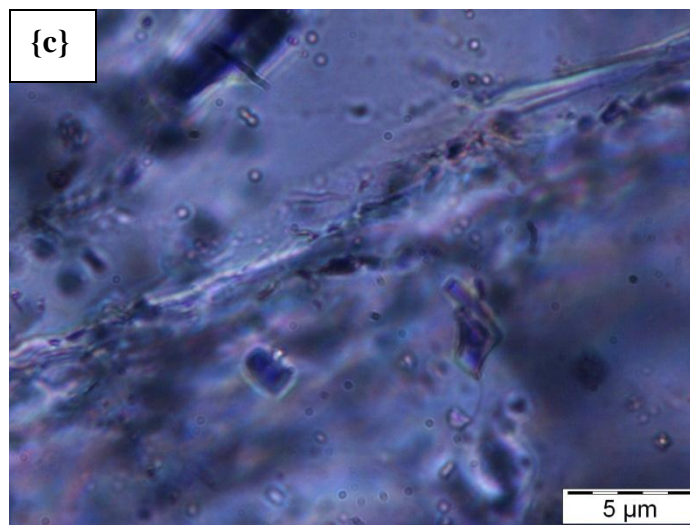
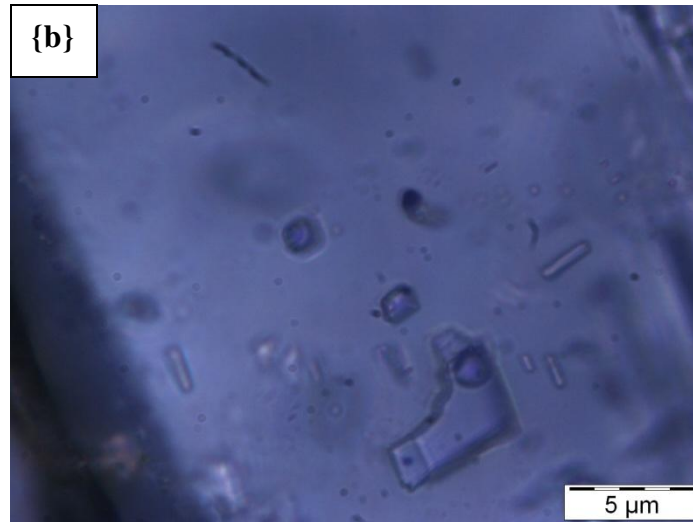
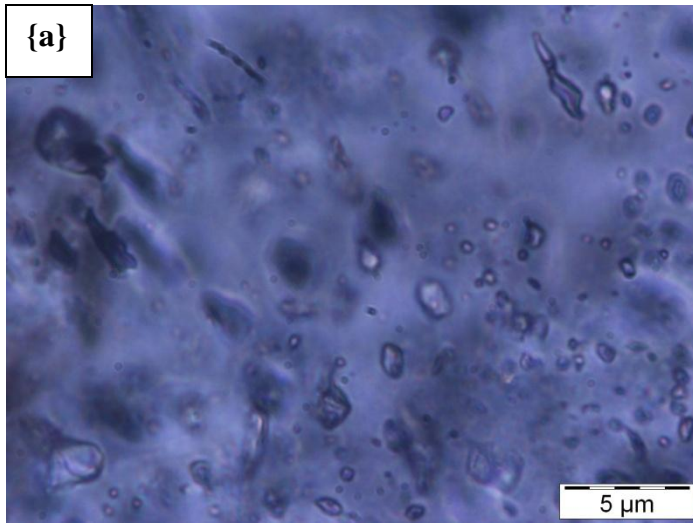


Figure 3.14: Re-equilibration pattern of primary bi phase inclusions of SLAP.

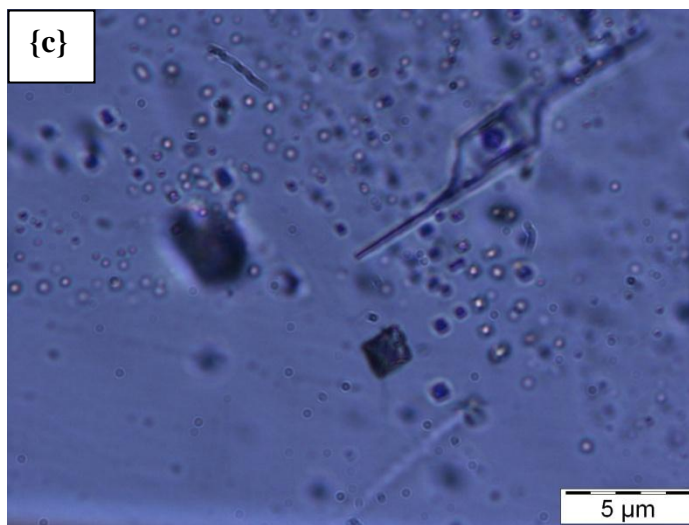
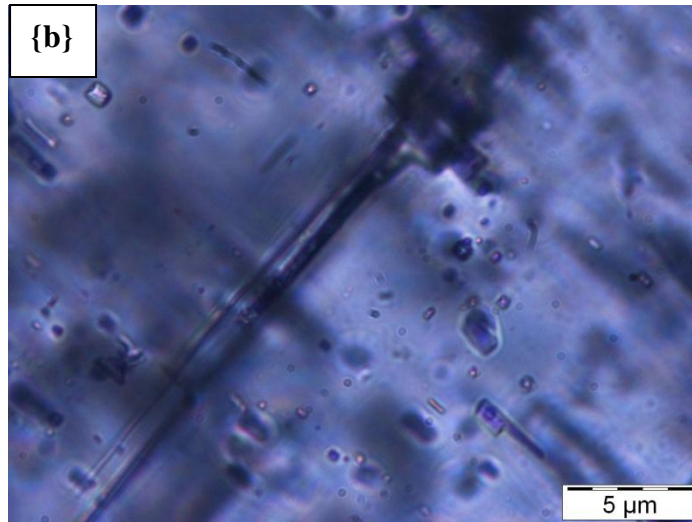
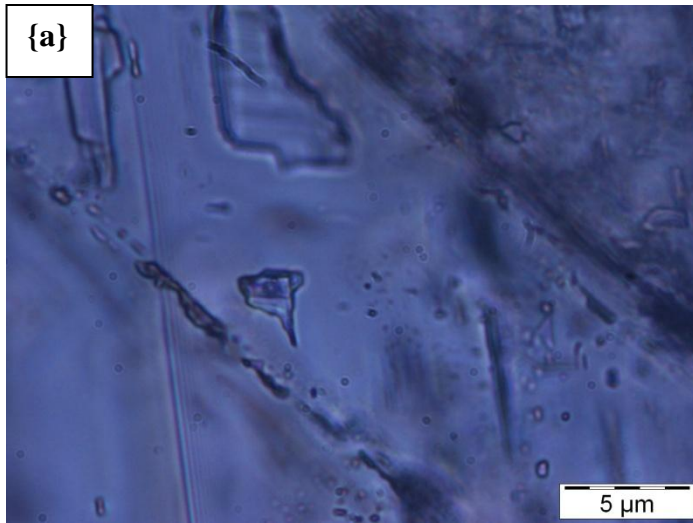


Figure 3.15: Re-equilibration pattern from SLAP indicating the tectonic event.

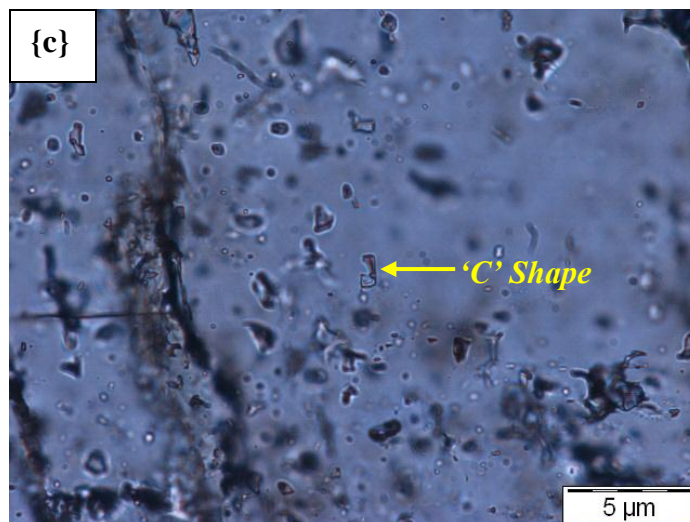
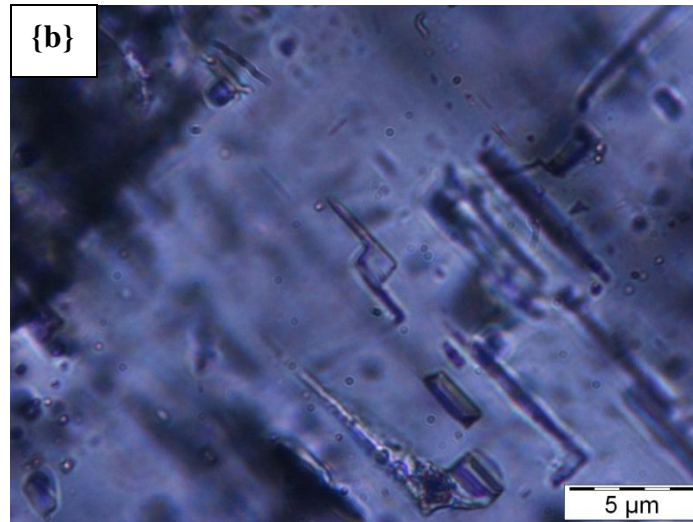
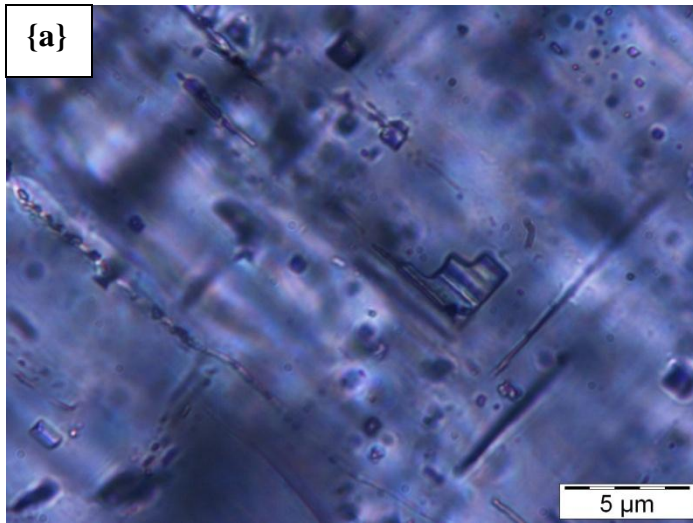


Figure 3.16: Re-equilibrated mono phase and 'C' shape inclusions of SLAP.

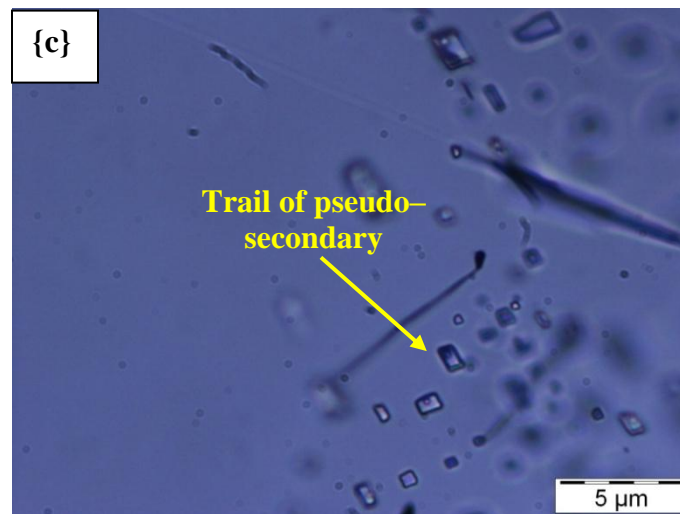
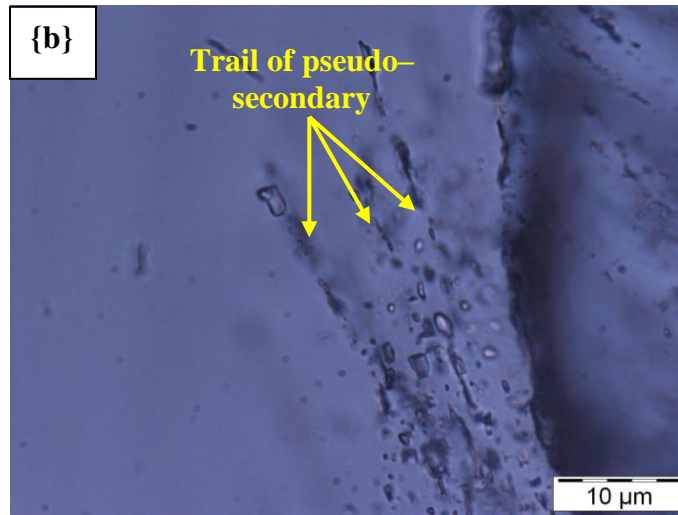
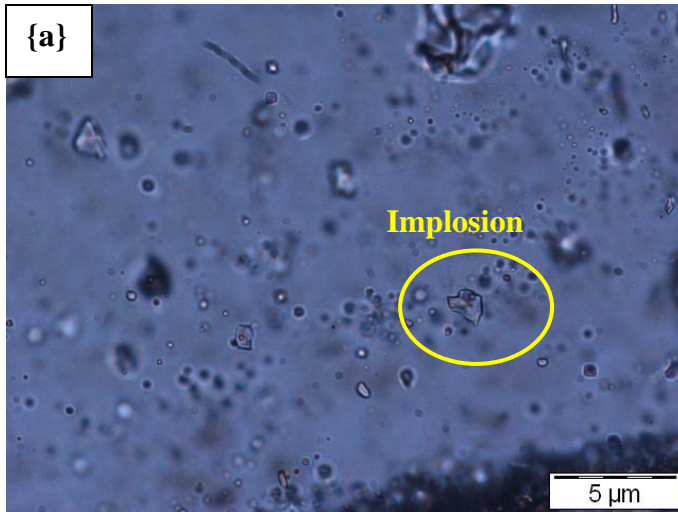


Figure 3.17: Implosion texture and trail of pseudosecondary inclusions of SLAP.

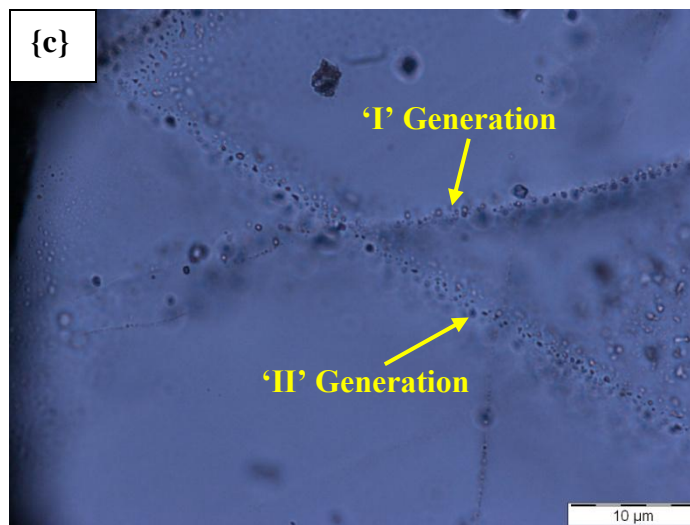
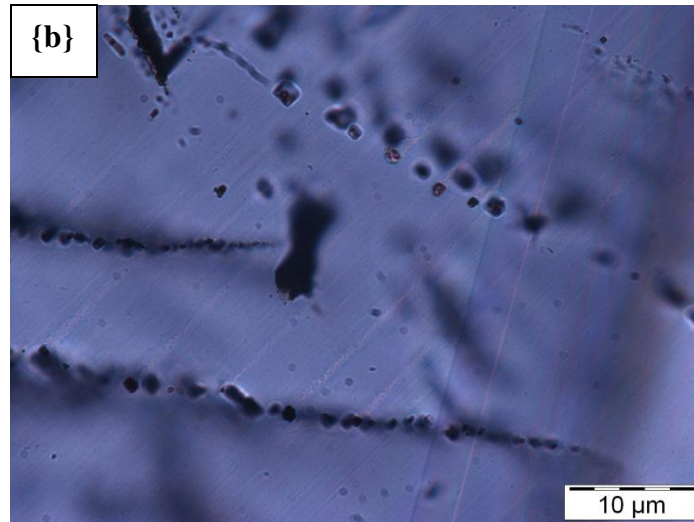
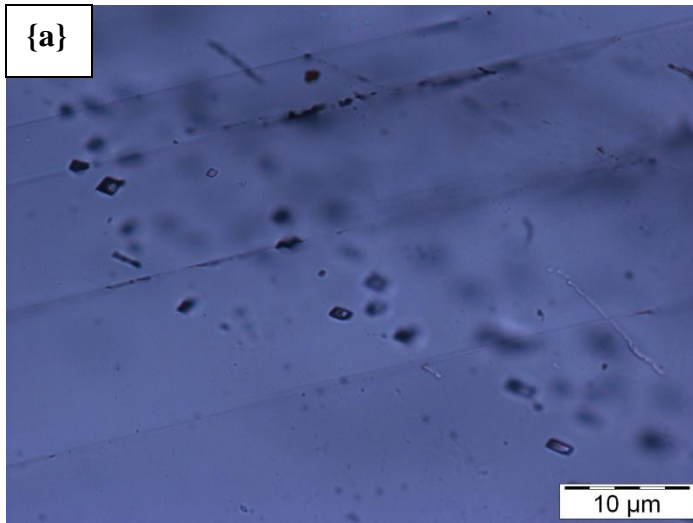


Figure 3.18: Trails of secondary inclusions from SLAP.

The trails of secondary inclusions also crosscut each other which reveal that their entrapment occurs in multi (two to three) episodes (see Figure 3.18).

3.2.3 MICROTHERMOMETRIC MEASUREMENTS

Microthermometric measurements of fluid species help to know the fluid composition, density, salinity and to estimate P–T path. All the measurements were carried out on primary as well as secondary fluid inclusions to know the entrapment condition. The initial melting (*T_{im}*), final melting (*T_{fm}*) and homogenization (*T_h*) temperatures were measured for each fluid inclusion.

Sum of 642 fluid inclusions were measured in quartz and calcite minerals of veins from four studied (NC, LMU, Shergol and Zildat) sections. The primary inclusions help to know the entrapment condition, cooling history and fluid source while the secondary inclusions constraint the upliftment history of Himalaya at penultimate stage. The Liquid Nitrogen (LN₂) was used for freezing the inclusions. The fluid compositions were observed through the initial melting temperatures of these inclusions. The initial melting temperature (*T_{im}*) suggest three type of fluid composition present in the system i.e. CH₄, CO₂ (Mono phase), H₂O-NaCl (Bi phase). The fluid compositions observed in different sections are summarized in table 3.1 whereas the summary of microthermometric measurements of these studied sections are tabulated in table 3.2 (for primary inclusions) and table 3.3 (for secondary inclusions). The detailed dataset for each

measurement is listed in *Appendix B*. Various type of fluids are also grouped as I, II, III which represent the CH₄, CO₂ and H₂O-NaCl, respectively which are ubiquitous in all the studied sections of Ladakh accretionary prism (LAP). The density of each inclusion was calculated through the ‘FILINCORE’ program of Brown (1989) by using the equation of Kerrick and Jacobs (1981) for CH₄ inclusions, Mäder and Berman (1991) for CO₂ inclusions and Zhang & Frantz (1987) for H₂O-NaCl inclusions. Whereas the salinity for H₂O-NaCl inclusions were calculated using the equation 3.1 given by Bodnar (1993).

$$\text{Salinity (wt\% NaCl)} = 0.00 + 1.78\theta - 0.0442\theta^2 + 0.000557\theta^3 \dots\dots\dots\text{Eqn (3.1)}$$

Where, θ is the depression of the freezing point in degrees Celsius (°C).

Table 3.1: Fluid composition of the study area.

Fluid Composition	CH ₄	CO ₂	H ₂ O-NaCl
Group	I	II	III
Shergol	√	√	√
NC	√	√	√
LMU	√	√	√
Zildat	√	√	√

Table 3.2: Summary of micro-thermometric measurements for Primary Inclusions.

	Shergol	NC	LMU	Zildat	Composition
Inclusions Measured (n)	24	28	20	31	CH₄ (Mono Phase) as Suggested by Golstein & Reynolds (1994)
<i>T_{im}</i> (°C)	-183.5 to -182.2	-184.5 to -180.4	-182.4 to -181.5	-183.4 to -181.2	
<i>T_{fm}</i> (°C)	-113.0 to	-163.4 to	-110.0 to	-120.0 to	
<i>T_h</i> (°C)	-92.0	-103.0	-82.6	-90.0	
Salinity (wt % NaCl)	-	-	-	-	
Density (g/cm³)	0.271 to 0.336	0.310 to 0.425	0.172 to 0.329	0.262 to 0.352	
Inclusions Measured (n)	54	24	14	57	CO₂ (Mono Phase) as suggested by Mäder and Berman (1991)
<i>T_{im}</i> (°C)	-58.6 to -56.2	-57.8 to -55.0	-57.1 to -55.0	-58.2 to -56.3	
<i>T_{fm}</i> (°C)	-19.7 to	-22.2 to	-19.8 to	-20.1 to	
<i>T_h</i> (°C)	-8.0	-10.5	-12.2	-4.0	
Salinity (wt % NaCl)	-	-	-	-	
Density (g/cm³)	0.973 to 1.031	0.986 to 1.042	0.995 to 1.031	0.951 to 1.033	
Inclusions Measured (n)	63	24	35	66	H₂O-NaCl (Bi Phase) as criteria given by Knight and Bodnar (1989)
<i>T_{im}</i> (°C)	-21.5 to -21.2	-23.0 to -21.2	-23.7 to -20.8	-23.8 to -21.1	
<i>T_{fm}</i> (°C)	-18.2 to -11.2	-18.9 to -3.5	-18.9 to -0.4	-20.0 to -2.1	
<i>T_h</i> (°C)	222.0 to 298.0	223.0 to 311.6	240.0 to 302.8	212.0 to 325.0	
*Salinity (wt % NaCl)	15.17 to 21.11	5.71 to 21.61	0.64 to 21.61	3.55 to 22.38	
Density (g/cm³)	0.929 to 0.993	0.753 to 0.933	0.717 to 0.933	0.864 to 0.995	

* using the equation 3.1, given by Bodnar (1993)

Table 3.3: Summary of micro-thermometric measurements for Secondary Inclusions.

	Shergol	NC	LMU	Zildat	Composition
Inclusions Measured (n)	54	44	48	56	H₂O-NaCl (Bi Phase) as criteria given by Knight and Bodnar (1989)
<i>Tim</i> (°C)	-21.6 to -21.2	-23.6 to -20.6	-23.4 to -20.8	-23.1 to -21.2	
<i>Tfm</i> (°C)	-10.0 to -2.9	-9.0 to -0.1	-11.9 to -0.1	-8.2 to -2.0	
<i>Th</i> (°C)	150.0 to 217.0	90.0 to 199.0	105.0 to 190.0	148.0 to 200.0	
*Salinity (wt % NaCl)	4.80 to 13.94	0.18 to 12.85	0.18 to 15.86	3.39 to 11.93	
Density (g/cm³)	0.911 to 0.975	0.889 to 1.030	0.908 to 1.027	0.909 to 0.977	

* using the equation 3.1, given by Bodnar (1993)

Shergol Section:

The primary and secondary inclusions were measured which are classified into three groups as shown in table 3.1 and Figure 3.19. The initial melting temperature (*Tim*) of primary inclusion of Group 'I' is in the range of -183.5 to -182.2°C which reveals that these inclusions are comprised of pure CH₄. The CH₄ inclusions were homogenized between -113 to -92°C (Figure 3.19a) having density in the range from 0.271 to 0.336 g/cm³. The Primary Group 'II' inclusion initially melt between -58.6 and -56.2 which give the evidence of presence of CO₂ in the system. The CO₂ inclusions were homogenized between -19.7 and -8.0°C (Figure 3.19b), having density between 0.973 and 1.031 g/cm³.

The Bi phase primary and secondary inclusions are also measured which belong to the group ‘III’ and the initial melting temperatures of these inclusions are in the range of -21.6 to -21.2°C which suggest the presence of H₂O-NaCl inclusions. The final melting temperature (*T_{fm}*) of group ‘III’ primary inclusions varies from -18.2 to -11.2°C and the *T_{fm}* of secondary inclusions are from -10.0 to -2.9°C. Whereas the homogenization temperature of these primary inclusions ranges from 298 to 222°C (Figure 3.19c), the secondary inclusions homogenized between 217 and 150°C (Figure 3.19d).

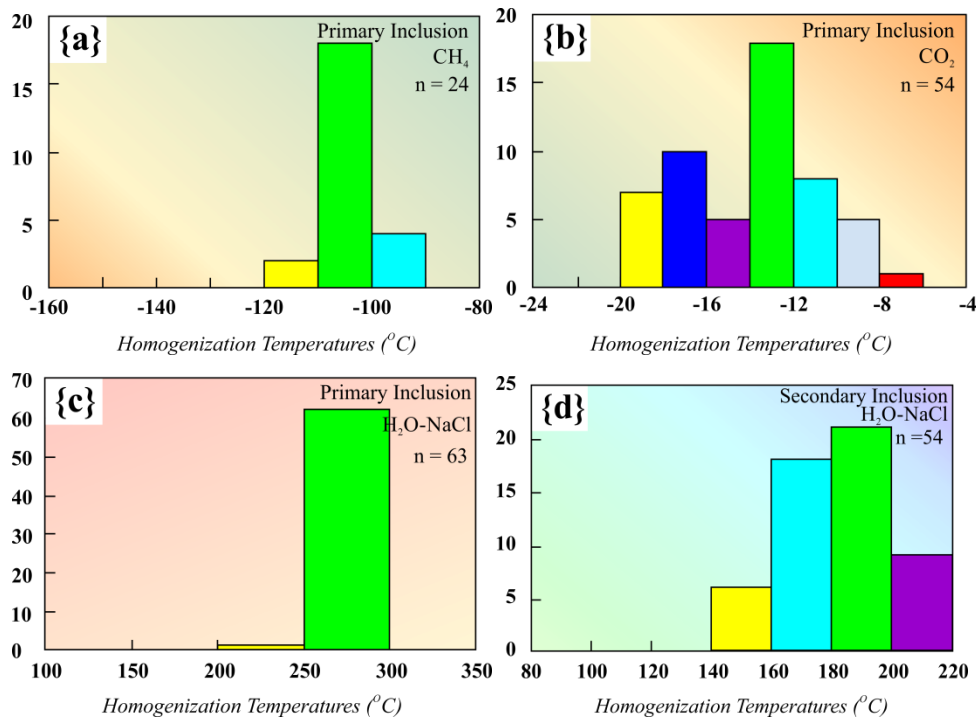


Figure 3.19: Homogenization temperature (*Th*) of various types of fluid inclusions present in the Shergol area. (a) *Th* of Primary CH₄ inclusions, (b) *Th* of Primary CO₂ inclusions, (c) *Th* of Primary H₂O-NaCl inclusions, and (d) *Th* of Secondary H₂O-NaCl inclusions.

The salinity of these group 'III' primary inclusions varies from 15.17 to 21.11 wt% NaCl and the density is in the range of 0.929 to 0.993 g/cm³. The salinity of secondary inclusions varies from 4.80 to 13.94 wt% NaCl and having density in the range of 0.911 to 0.975 g/cm³ as calculated by 'FILINCORE' program using the Zhang and Frantz (1987) equation.

Nimu-Chilling (NC) Section:

Three types of fluid compositions were also recognized from NC section namely group 'I', 'II' and 'III' which are referred to CH₄, CO₂ and H₂O-NaCl, respectively (see table 3.1 for detail) and the histogram of these sections are present in Figure 3.20. The primary fluid inclusions contain all three group inclusions whereas the secondary inclusions are limited to the group 'III'. The Group 'I' primary inclusions initially melted between -184.5 and -180.4 °C suggesting the presence of CH₄ inclusion in the NC section which was homogenized at -163.4 to -103.0°C (See table 3.2) and the histograms are shown in Figure 3.20a. The density of CH₄ primary inclusions of NC section varies in the range of 0.310 to 0.425 g/cm³. The first melting temperature of group 'II' primary inclusions varies from -57.8 to -55.0 °C which infers the existence of CO₂ in the system. These inclusions were homogenized between -22.2 and -10.5°C (see table 3.2) and the histogram present in Figure 3.20b. The density of CO₂ primary inclusion of NC section is in the range of 0.986 to 1.042 g/cm³. The group 'III' primary inclusions were initially melted between -23.0 and -21.2°C indicating H₂O-NaCl fluid composition. The final melting temperature of these H₂O-NaCl

primary inclusions are in the range of -18.9 to -3.5°C which homogenized between 311.6 to 223.0°C (also see in table 3.2) and the histogram shown in Figure 3.20c. Whereas the first melting temperatures (T_{fm}) of group ‘III’ secondary inclusions are between -23.6 and -20.6°C having homogenization temperature between 199 and 90°C (see histogram in Figure 3.20d) and the final melting temperature (T_{fm}) varies from -9.0 to -0.1°C .

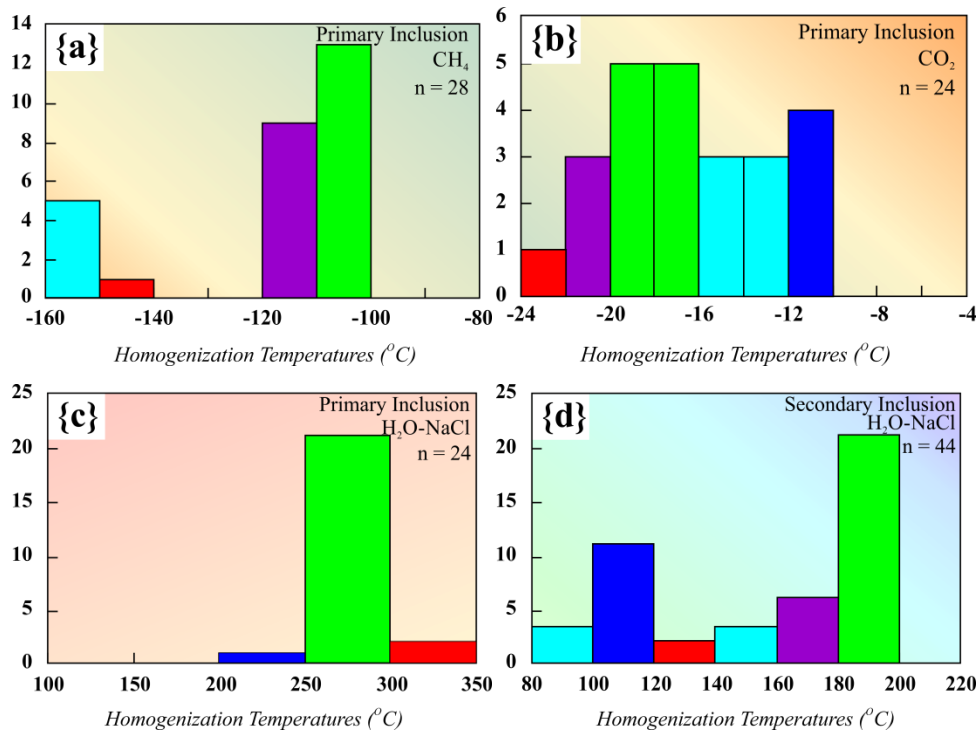


Figure 3.20: Homogenization temperature (T_h) of various types of fluid inclusions present in the Nimu–Chilling (NC) Section (Zaskar Gorge). (a) T_h of Primary CH_4 inclusions, (b) T_h of Primary CO_2 inclusions, (c) T_h of Primary $\text{H}_2\text{O-NaCl}$ inclusions, and (d) T_h of Secondary $\text{H}_2\text{O-NaCl}$ inclusions.

The salinity of $\text{H}_2\text{O-NaCl}$ primary inclusions varies from 5.71 to 21.61 wt% NaCl and the density in the range of 0.753 to 0.933 g/cm^3 . Whereas the salinity of

secondary inclusions are in the range of 0.18 to 12.85 wt% NaCl having density between 0.889 to 1.030 g/cm³.

Lato–Miru–Upshi (LMU) Section:

The LMU section is characterized by three types of fluid compositions which are classified into three categories namely group 'I', 'II' and 'III' for CH₄, CO₂ and H₂O-NaCl fluid composition (see table 3.2). The initial melting temperature (*Tim*) of group 'I' CH₄ primary inclusions are in the range of -182.4 to -181.5°C which are homogenize between -110.0 and -82.6°C temperature (see histogram in Figure 3.21a) and the density is in the range of 0.172 to 0.329 g/cm³. The group 'II' CO₂ primary inclusions first melted between -57.1 and -55.0°C and homogenized at -19.8 to -12.2 °C (see histogram in Figure 3.21b). The CO₂ inclusions show density between 0.995 and 1.031 g/cm³. The group 'III' inclusions having *Tim* between -23.7 to -20.8°C indicate the presence of H₂O-NaCl inclusions which were homogenized at 240.0 to 302.8°C (see histogram in Figure 3.21c) and the *Tfm* varies from -18.9 to -0.4°C. The secondary (bi phase) inclusions initially melted between -23.4 and -20.8°C suggesting H₂O-NaCl fluid composition. These secondary inclusions were homogenized at 105.0 to 190.0°C temperature (see histogram in Figure 3.21d) and the final melting temperature lies between -11.9 and -0.1°C. The salinity of H₂O-NaCl primary inclusions varies from 0.64 to 21.61 wt% NaCl and the density are in the range of 0.717 to 0.933 g/cm³. Whereas the salinity of secondary fluid inclusions are varies from 0.18 to 15.86 wt% NaCl and the density varies from 0.908 to 1.027 g/cm³.

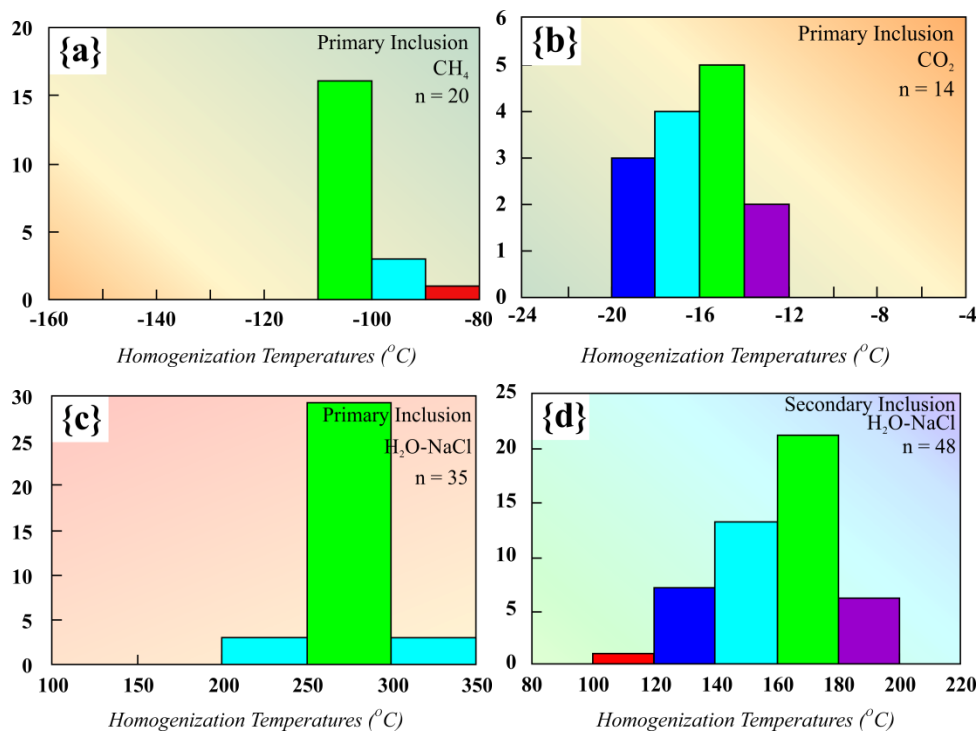


Figure 3.21: Homogenization temperature (T_h) of various types of fluid inclusions present in the Lato–Miru–Upshi (LMU) Section. (a) T_h of Primary CH_4 inclusions, (b) T_h of Primary CO_2 inclusions, (c) T_h of Primary $\text{H}_2\text{O-NaCl}$ inclusions, and (d) T_h of Secondary $\text{H}_2\text{O-NaCl}$ inclusions.

Zildat Section:

The eastern section of LAP is also typified by three types of fluid composition (see table 3.1) which are classified into three groups viz. ‘I’, ‘II’ and ‘III’ for CH_4 , CO_2 and $\text{H}_2\text{O-NaCl}$, respectively (see table 3.1). The initial melting temperature of group ‘I’ primary inclusions vary between -183.4 and -181.2°C indicating CH_4 fluid composition which was homogenized at -120.0 to -90.0°C (see table 3.2 and Figure 3.22a). The density of group ‘I’ inclusions are in the range of 0.262 to 0.352 g/cm^3 . The group ‘II’ type of primary inclusions were first melted between

-58.2 and -56.3°C and homogenized at -20.1 to -4.0°C temperature (see Figure 3.22b) with a density range from 0.951 to 1.033 g/cm³. The group ‘III’ primary inclusions start to melt at -23.8 to -21.1°C temperature and homogenized between 212 and 325°C temperature (Figure 3.22c), with the final melting temperature in range from -18.5 to -2.1°C. The initial melting temperature of secondary fluid inclusion were varies from -23.1 to -21.2°C and homogenized at 148 to 200°C temperature (see table 3.3 and Figure 3.22d), with their final melting temperature between -8.2 and -2.0°C.

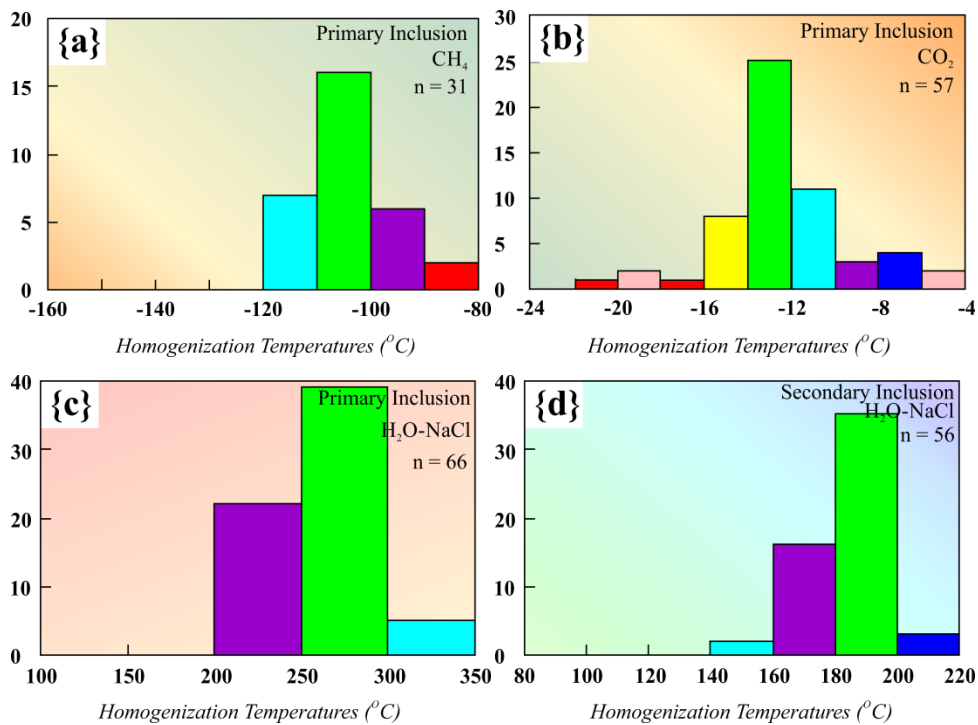


Figure 3.22: Homogenization temperature (T_h) of various types of fluid inclusions present in the Zildat section. (a) T_h of Primary CH_4 inclusions, (b) T_h of Primary CO_2 inclusions, (c) T_h of Primary $H_2O-NaCl$ inclusions, and (d) T_h of Secondary $H_2O-NaCl$ inclusions.

The salinity of H₂O-NaCl primary inclusions varies from 3.55 to 22.38 wt% NaCl and the density is in the range of 0.864 to 0.995 g/cm³. Whereas the secondary type of inclusions range from 3.39 to 11.93 wt% NaCl having density in the range of 0.909 to 0.977 g/cm³.

3.2.4 MICRO-RAMAN SPECTROSCOPY

The Micro Raman spectroscopy was carried out on fluid inclusion of all four studied sections of LAP to identify and confirm the composition of fluid inclusions (especially for CH₄ inclusions) as revealed during the microthermometry. The Raman shifts of fluid inclusions suggest that the pure CH₄ exists in this fluid system. The CH₄ peak encountered at 2917cm⁻¹ (see Figure 3.23) in both quartz and calcite mineral, which indicate that the vein forming fluid, were methane (CH₄) rich.

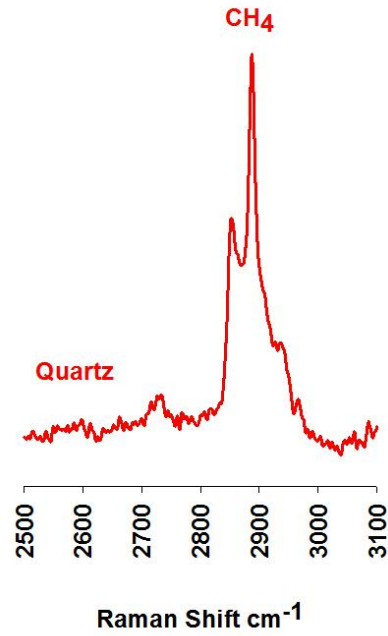
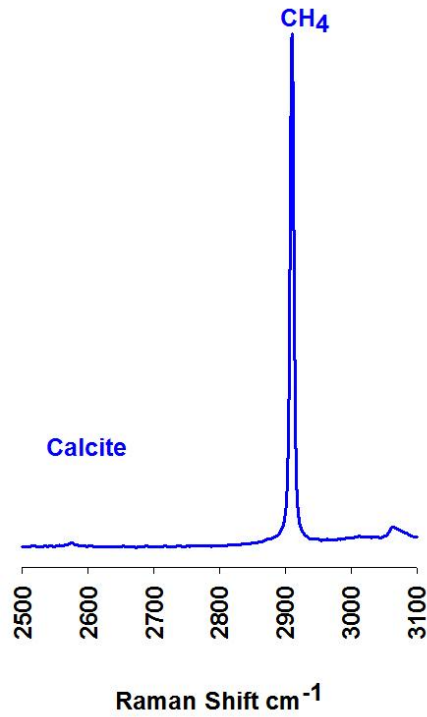
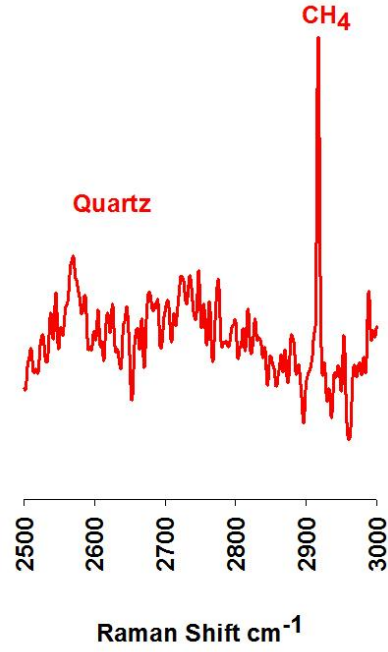
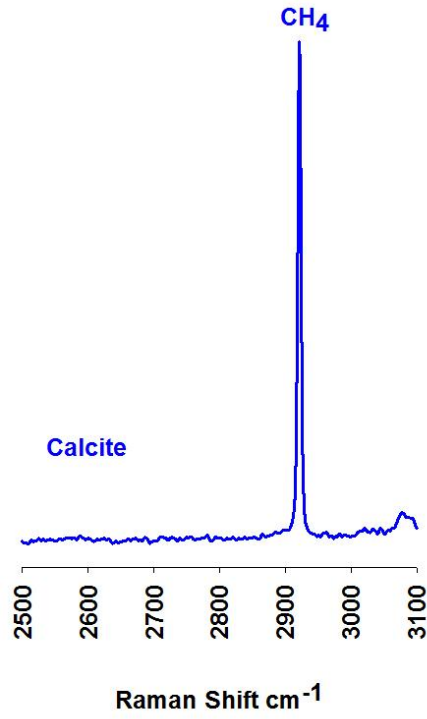


Figure 3.23: Raman shift of fluid inclusions in both quartz and calcite mineral phase.

3.2.5 P-T CONDITIONS FOR THE FORMATION OF VEINS

The representative isochors of the various fluid inclusions and suggested P-T paths of paleo and south Ladakh accretionary prisms are shown in Figures 3.24 and 3.26, respectively. The CH₄ isochors were drawn using the equation of Kerrick and Jacobs (1981) whereas Mäder and Berman (1991) equation used for CO₂ inclusions. The isochors for H₂O-NaCl fluids are drawn using the equation given by Zhang and Frantz (1987). The formation temperature of veins is constrained by microstructure and oxygen isotope thermometry. The area of overlap of the isochors with the thermometric estimates define P-T region of that area.

Table 3.4: Summary of P-T condition of the veins and exhumation depth of the study area at penultimate stage of evolution of the Himalaya.

Studied Section	Temperature (in °C) constrain by		Estimated Pressure (Kbar)	Exhumation depth of veins (Km)
	Microstructures	Oxygen isotope thermometry*		
PAP	200 to 500	-	4.2	12.6
SLAP	170 to 500	152 to 528	7.0	21.0

* Using the criteria of Sharp and Kirschne (1994). Please see Chapter 4 for detail.

Paleo Accretionary Prism (PAP):

As discussed in Chapter 2, Shergol and Zildat sections are jointly referred to as paleo accretionary prisms (PAP). The isochors of primary CH₄, CO₂ and H₂O-NaCl inclusions of PAP are shown in Figure 3.24. The deformation temperature

of mineral veins is approximated through microstructures which reveal higher degree of temperature range from 200 to 500°C. The calcite twining divulges the deformation temperature ranging from 200–300°C (Ferrill et al., 2004). While quartz microstructures suggest the formation temperature ranges from 280–500°C (Passchier and Trouw, 2005).

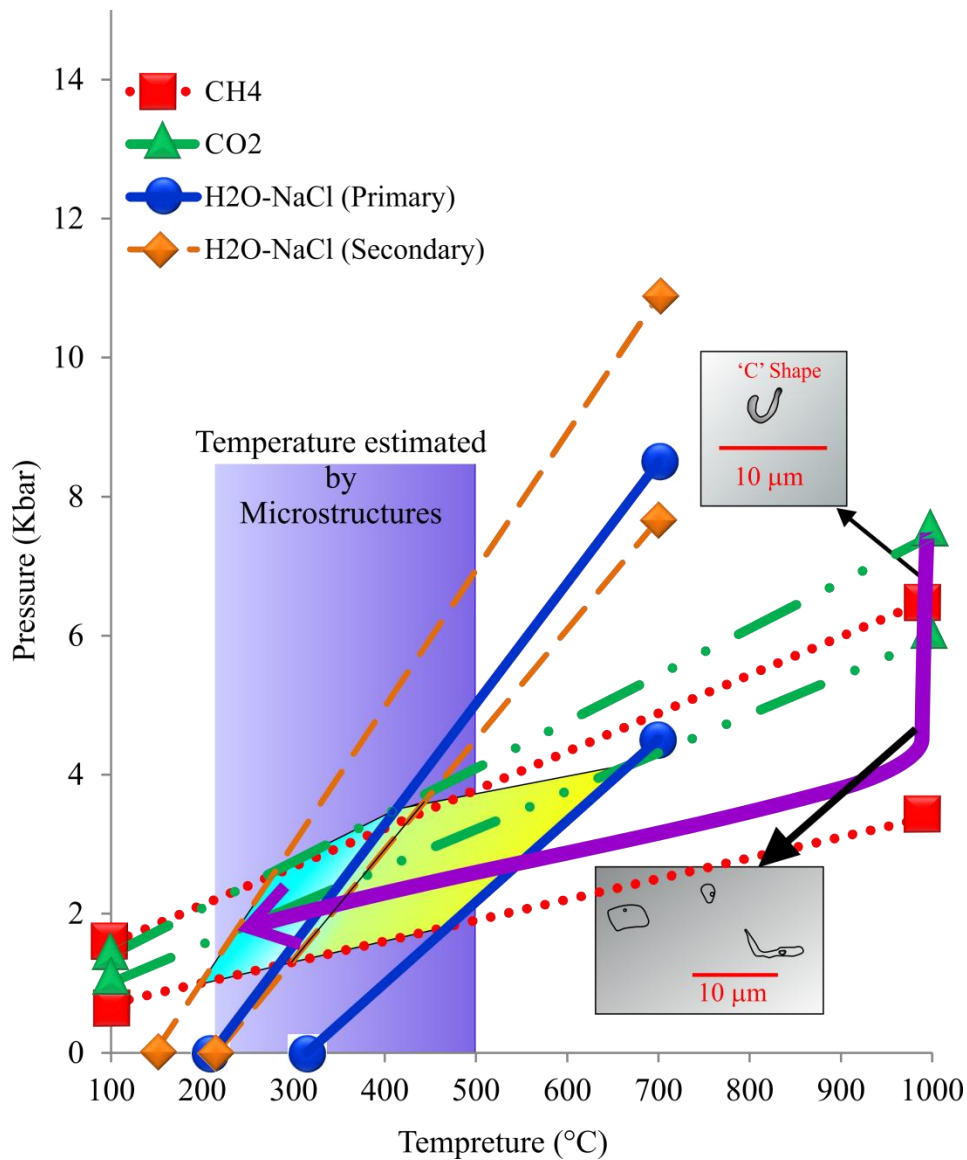


Figure 3.24: Exhumation path with entrapment P-T condition of fluid for paleo accretionary prism (PAP).

The represented isochors of CH₄, CO₂ and H₂O-NaCl inclusions are plotted in Figure 3.24 along with the temperature estimates from microstructures to constrain the P–T entrapment condition of fluid. The area of overlap of the fluid inclusion isochors with the thermometric estimates generally define P–T region, but in the case of PAP the temperature cannot be estimated beyond 500°C with the help of microstructures. Therefore the maximum temperature of initial fluid entrapment is considered by the primary H₂O–NaCl isochors intersection with the primary CO₂ isochors at 670°C and 4.2 Kbar, which were trapped upto 270°C and 1.5 Kbar. The isochors of the secondary H₂O–NaCl fluid inclusion intersect the isochors of primary CH₄ inclusions at 410°C, 3.5 Kbar and 185°C, 1.3 Kbar. This reveals that secondary inclusions entrapped further at lower P–T condition. It is observed from Figure 3.24, that the P–T path for the entrapment of such inclusions was initially isothermal then isochoric at the last stage. This isothermal phenomenon is well illustrated by the presence of ‘C’ shaped fluid inclusion (Figure 3.8 and 3.24) as per the criteria given by Vityk and Bodnar (1995).

Source of Fluid: The gaseous rich (mono phase) inclusions along with some bi phase inclusions having higher salinity are of primary nature whereas the secondary inclusions are of bi phase aqueous only. The rare occurrence of three phase inclusions was also noticed along with other primary inclusions. This suggests that the gas inclusions trapped simultaneously with high saline inclusions. The associated three phase inclusion with gaseous inclusion indicates its derivation from magmatic source (Figure 3.7). These inclusions were trapped

initially during the formation of calcite and quartz grains. The calculated oxygen isotope ratio of fluid for paleo accretionary prism (PAP) varies in between 1.3 and 13.1 ‰ (VSMOW). The calculated oxygen isotope ratios reveal its derivation from mantle/ophicarbonatite fluid source (Figure 4.27). The stable carbon and oxygen isotopic ratio along with strontium and lead isotopes of veins carbonates also suggest the mantle affinity of fluid (see Figure 4.21 to 4.23).

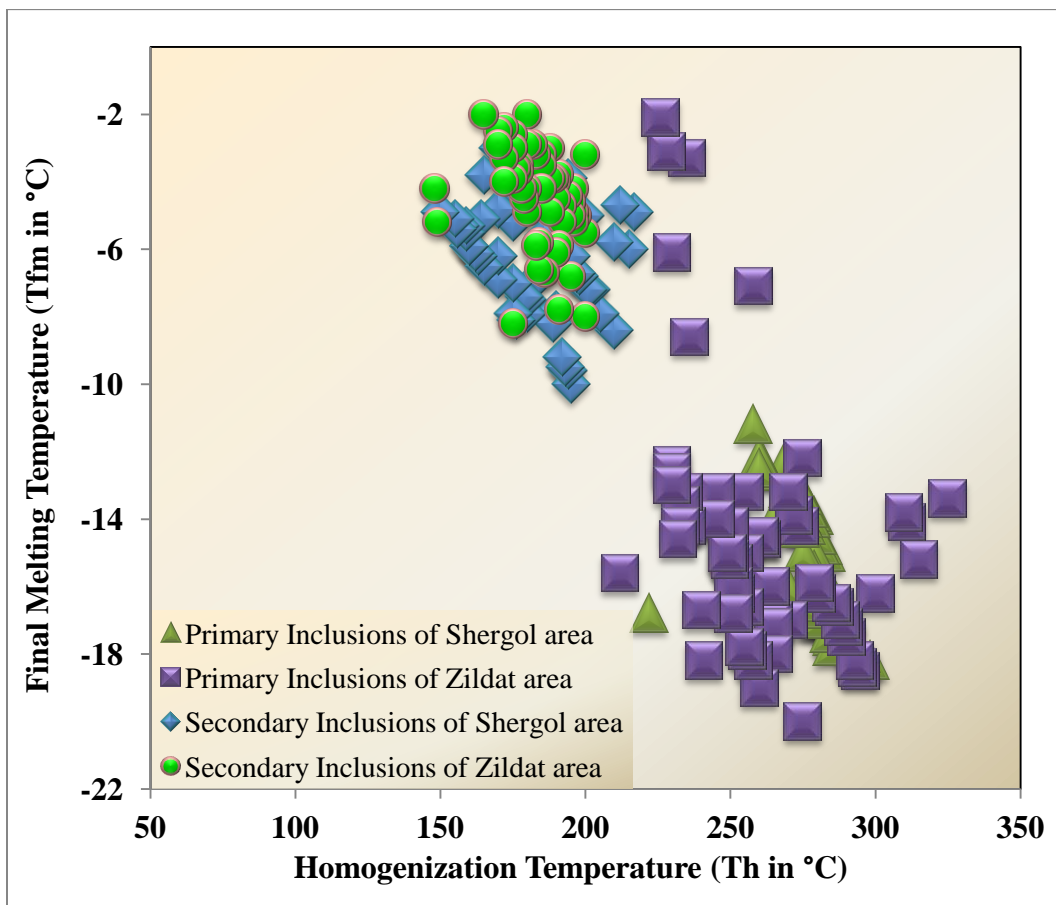


Figure 3.25: Bi variant plot of Th vs Tfm of primary and secondary fluid inclusions for paleo accretionary prism (PAP).

As shown in the figure 3.25, the final melting temperatures (T_{fm}) of primary fluids were decreases simultaneously with the homogenization temperatures (T_h), while the secondary inclusion shows very small variation between T_{fm} and T_h . It suggests that the salinity of fluid increases with the temperature in both primary and secondary fluids.

South Ladakh Accretionary Prism (SLAP):

The represented isochors of primary (CH_4 , CO_2 , $\text{H}_2\text{O-NaCl}$) and secondary ($\text{H}_2\text{O-NaCl}$) inclusions are plotted in Figure 3.26 along with the temperature estimated from the oxygen isotope thermometry and microstructures. The crystallizing temperature of veins is in the range of 170 to 500°C (Figure 3.6) whereas the oxygen isotope thermometry of co-existing quartz and calcite minerals provides the crystallizing temperature range of SLAP between 152 and 528°C. Figure 3.26 suggests that the primary fluid was entrapped between 7.0 and 3.8 Kbar at the temperature range from 500 to 200°C. The upper entrapments of temperature limit for the primary fluid inclusions were constrained by temperature estimated through microstructure of quartz–calcite veins (i.e. 170 to 500°C). The last phase of fluid entrapment obtained through secondary inclusions by the intersection point of secondary isochors between 410°C (intersection point of CO_2 primary and $\text{H}_2\text{O-NaCl}$ secondary isochors) to 110°C (intersection point of CH_4 primary and $\text{H}_2\text{O-NaCl}$ secondary isochors) at the pressure range of 3.5 to 0.5 Kbar. The P–T path as shown in Figure 3.26 is initially isothermal and later on it followed isochoric path. The signature of isothermal exhumation of fluid is also

confirmed by the ‘C’ shape, implosion and stretched fluid inclusions (see Figure 3.13 to 3.17) as the criteria given by Vityk and Bodnar (1995).

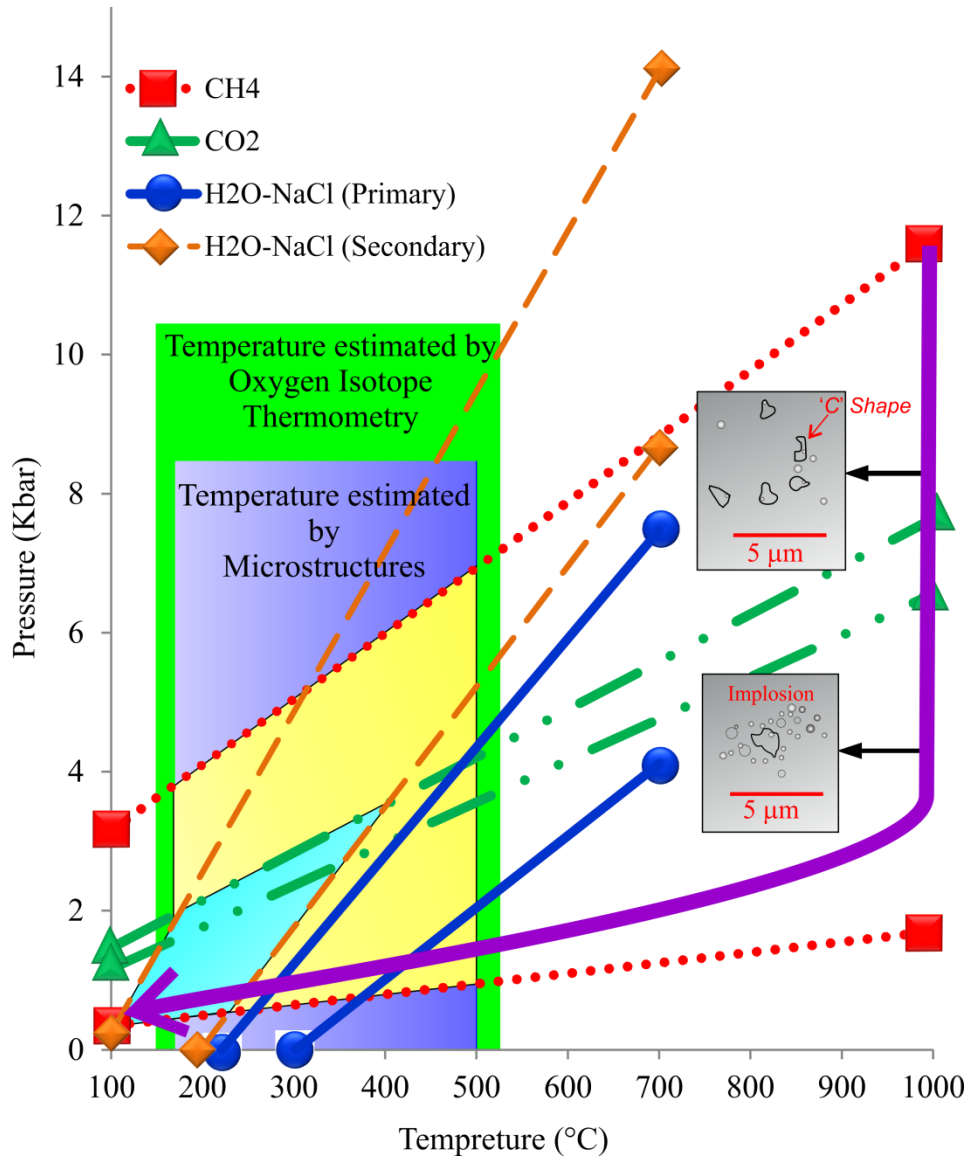


Figure 3.26: Exhumation path with entrapment P-T condition of fluid for South Ladakh Accretionary Prism (SLAP).

Source of Fluid: The CH₄ and CO₂ (mono phase) inclusions are of primary in nature and highly dense in character. The density of CH₄ inclusions is in the range

from 0.172 to 0.425 g/cm³ whereas the density of CO₂ inclusions varies from 0.986 to 1.042 g/cm³. Their mode of occurrence and high dense in nature reveal that they are of deeper origin. The calculated oxygen isotopic ratios of fluid for SLAP are in the range of -4.6 to 12.6 ‰ VSMOW (see Figure 4.27). The calculated oxygen isotope ratio of fluid is plotted in Figure 4.27, which indicates the mantle/ophicarbonatite origin of fluid. The combined carbon, oxygen, Strontium and lead isotopic systematic give the evidence of mantle/ophicarbonatite fluid source (see detail in Chapter 4).

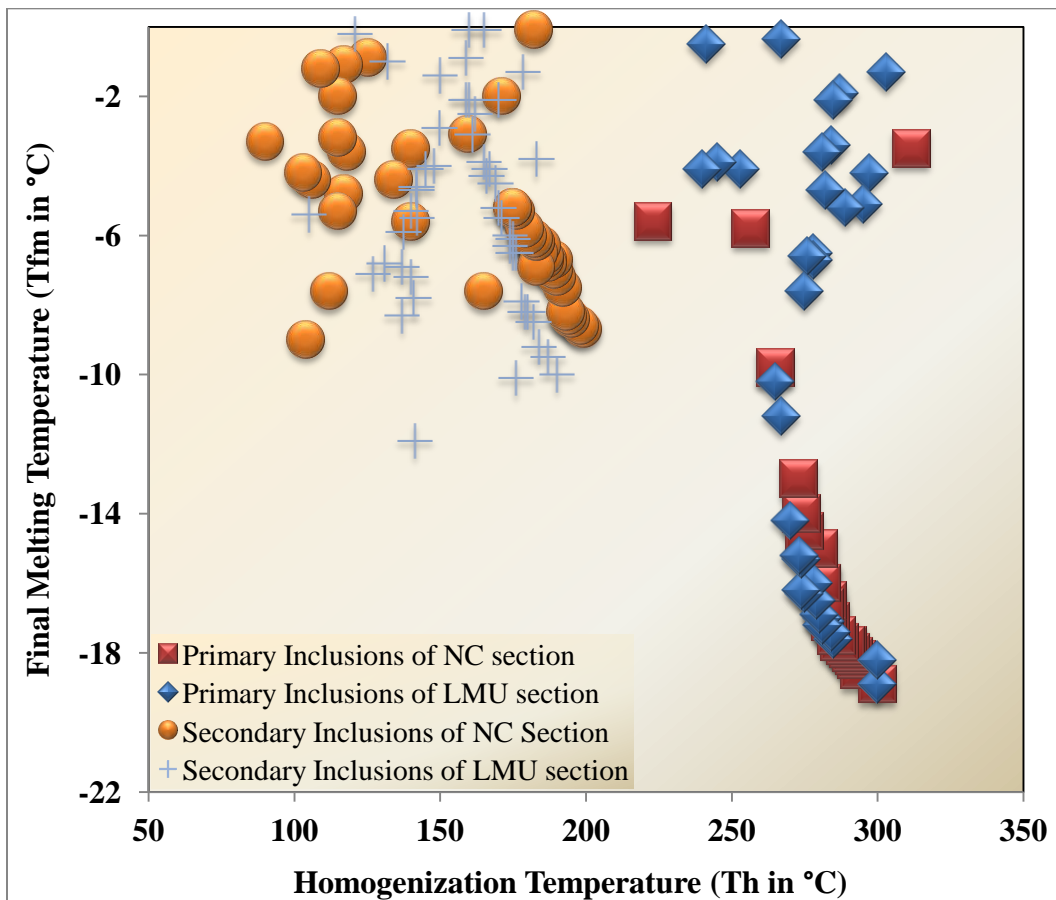


Figure 3.27: Bi variant plot of Th vs Tfm of primary and secondary fluid inclusions for South Ladakh accretionary prism (SLAP).

Notable correlation of primary fluids between final melting temperatures (salinity) and homogenization temperature were observed in figure 3.27, which suggest that the salinity of primary as well as secondary fluid increases with the temperatures.

CHAPTER 4:

ISOTOPIC AND TRACE ELEMENTAL

GEOCHEMISTRY

CHAPTER 4:

ISOTOPIC AND TRACE ELEMENTAL GEOCHEMISTRY

The Isotopic and geochemical studies of the Ladakh Accretionary Prism (LAP) is summarize in this chapter. The stable and radiogenic isotopes are included in the isotopic geochemistry section, whereas trace and REE geochemistry were presented in geochemical sections. The stable isotopic measurements were carried out in the Stable Isotope Laboratory of the Wadia Institute of Himalayan Geology (WIHG), Dehra Dun (India) in both calcite and quartz phases using continues flow Isotopic Ratio Mass Spectrometer (CF-IRMS). The radiogenic Sr and Pb isotopes in carbonate phase were analysed at Physical Research Laboratory (PRL), Ahmadabad (India) and University of Cape Town, Cape Town (South Africa), respectively. The radiogenic isotopic measurements were carried out in the solution phase using Multi Collector Inductively Coupled Mass Spectrometer (MC-ICPMS). The trace and REE geochemistry were carried out on both calcite and quartz minerals at Wadia Institute of Himalayan Geology (WIHG), Dehradun using Inductively Coupled Plasma Mass Spectrometer (ICPMS).

Analytical techniques adopted in this study and the elements and their isotopes measured are summarized in Table 4.1.

Table 4.1: Various analytical techniques used in this study.

Analysis		Instrument		Source	Detector	Laboratory	Sample Introduction Mode	Sample Preparation
Trace and REE Geochemistry		ICPMS (quadrupole): Perkin Elmer: ELAN–DRCe		Inductively Coupled Plasma (ICP)	Analog and Discrete dynode	Spectro Lab of WIHG	Liquid	Sample dissolve by the mixture of HF : HNO ₃
Stable isotope geochemistry	$\delta^{13}\text{C}$ and $\delta^{18}\text{O}$ in carbonate phase	CF–IRMS with Gas Bench (90° magnetic sector with 1–96 g/mol mass range; Thermo scientific; Delta V plus modal)		Ionized by Electron bombardment	Faraday Cup	Stable Isotope Lab of WIHG	Gas	CO ₂ gas produce by putting H ₃ PO ₄ in the sample
	$\delta^{18}\text{O}$ in silicate phase							O ₂ gas produced using laser fluorination system in the fluorination environment of BrF ₅ and the sample burned by CO ₂ monochromatic laser.
Sr isotope geochemistry (⁸⁷Sr/⁸⁶Sr) in Carbonate Phase		MC–ICPMS (magnetic sector)	Thermo Scientific, Neptune modal	Inductively Coupled Plasma (ICP)	Multi Ion Collector (MIC) and Faraday Cup	PRL, Ahmadabad	Liquid	Leaching with 5% acetic acid
Pb isotope geochemistry in Carbonate Phase			Nu Instruments of Nu Plasma HR					University of Cape Town, South Africa

Salient features of the analytical methodology (section 4.1) used are detailed in the following section along with the results (section 4.2) and discussions (section 4.3).

4.1 ANALYTICAL TECHNIQUES

The geochemical studies have been carried out using different Mass spectrometric (MS) techniques as appropriate and applicable in geochemical studies. The complete process involves ionization of constituents of the sample through high temperature dissociation (ICPMS), electronic bombardment (IR-MS) to quantify their abundances and isotopic ratios.

In a MS procedure, it is essential to ionize the sample to be able to discriminate and detect according to their mass to charge ion ratio. A sample, which may be solid, liquid, or gas, is ionized in its molecular form by electron bombarding as in case of IRMS for oxygen and carbon stable isotopic analysis, whereas in case of high temperature ionization using ICP source. Elemental ionization allows measurement of trace elemental abundances using quadrupole ICPMS and isotope ratio measurements by MC-ICPMS.

These ions are further separated according to their mass-to-charge ion ratio, typically by accelerating them through an electric or magnetic field within the mass spectrometer. Ions of the higher mass-to-charge ratio will undergo lesser amount of deflection compared to ions of lower mass which forms the basic principle of mass spectrometric measurements. The charged ions are detected by a mechanism capable of detecting

charged particles, such as an electron multiplier. Results are displayed as spectra of the relative intensity of detected ions as a function of the mass-to-charge ratio. The schematic diagrammatic representation of typical mass spectrometric measurement is shown in figure 4.1.

The Mass Spectrometer has three major components (see figure 4.1):

- i. **Ion Source:** To ionize a portion of the sample (convert into ions).
- ii. **Analyzer:** For resolving the ions into their characteristic mass components according to their mass-to-charge ratio.
- iii. **Detector:** For detecting the ions and recording the frequency of the ions detected per unit time, i.e. relative intensity (counts per second) of each of the resolved ionic species.

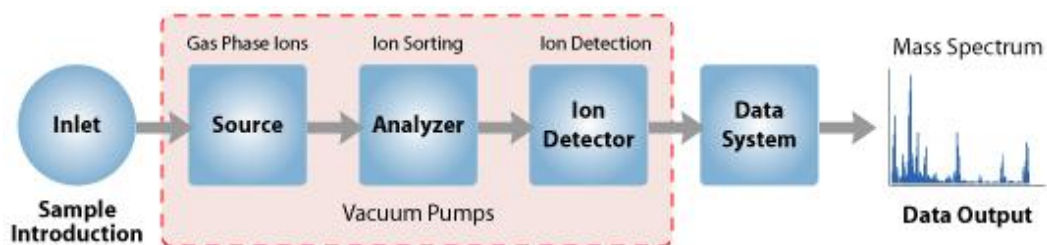


Figure 4.1: A schematic diagram showing the Mass Spectrometric measurement protocol.

All these three major components (Source, analyzer and Detector) of MS are maintained under ultra-high vacuum (10^{-6} to 10^{-9} mm Hg).

4.1.1 ANALYTICAL TECHNIQUE OF TRACE ELEMENTAL GEOCHEMISTRY

The trace elemental geochemistry in calcite and quartz phase has been done in solution phase using Inductively Coupled Plasma Mass Spectrometry (ICPMS) at WIHG (see figure 4.3). The Inductively Coupled Plasma Mass Spectrometry (ICPMS) is a type of mass spectrometry which uses determinations of elemental (metals and several non-metals) abundance in mineral or rock. The very low concentrations elements as low as one part in 10^{12} (part per trillion) can also detected by ionizing the sample with inductively coupled plasma and then using a mass spectrometer to separate and quantify those ions. An ICPMS combines a high-temperature ICP (Inductively Coupled Plasma) source with a mass spectrometer. The ICP source converts the atoms of the elements in the sample to ions. These ions are then separated and detected by the mass spectrometer (see figure 4.2 and 4.4).

ICP Source: Inductively coupled plasma (ICP) source for spectrometer is comprised of a torch that consists of three concentric tubes, usually made of quartz (figure 4.4). The RF load coil wraps around the neck of this torch and is connected to a radio-frequency (RF) generator. As power is supplied to the load coil from the generator, oscillating electric and magnetic fields are generated across the coil within the plasma torch. Seeding of ion is implanted using a few spatters of spark within the torch through which argon gas is flowing. In response to the RF field within the torch, the ion seeds starts oscillating and strikes other argon gas molecules generating heat as high as $>6000^{\circ}\text{C}$ that results in

ionization of the surrounding neutral argon gas atoms forming an argon plasma discharge (figure 4.4). The formation of plasma discharge remains spontaneous as long as continuous supply of plasma gas (argon) is maintained.

Instrumentation: Samples are required to be decomposed to neutral elements and a significant population of these atoms are ionized in high temperature ($>6000^{\circ}\text{C}$) argon plasma. These positively charged ions are introduced into the mass spectrometer and analyzed based on their mass to charge ratios using a quadrupole mass discriminator. An ICPMS technique consists of four main processes, including (i) sample introduction and aerosol generation, (ii) ionization by an argon plasma source, (iii) mass discrimination, and (iv) detection system (see figure 4.4).

Mass discriminator: Positively charged ions from plasma interface are accelerated through the quadrupole rods (figure 4.2), where a strong electrostatic field is applied. In response to the electrostatic field, the ions are deflected according to their mass by charge ratio. By controlling the electrostatic field, specific ions can be made to focus on to the detector allowing their measurements (Figure 4.2).

High ionization efficiency results in high analyte signal (i.e. high sensitivity) making it suitable for measurement of isotope abundances of most elements between mass 6 (Li) and mass 238 (U) with detection limits down to sub ppb level. Though technique suffers from isobaric interferences, but all elements have at least one isotope free of isobaric interference. High sensitivity makes it possible to measure lower abundance isotopes with

reasonable detection limits. There are few molecular interferences and these are well known and corrected through appropriate corrections and use of matrix matching standards. The calibrations are commonly linear up to 7–8 orders of magnitude analytical range (sub ppb to tens of ppm). The detection limits are generally down to parts per trillion for most of the elements and no other geo-analytical technique offer such lower limit of detection with high throughput. However, the technique has limited application for determination of elements at major or minor (i.e. in percentages) abundances in geological samples.

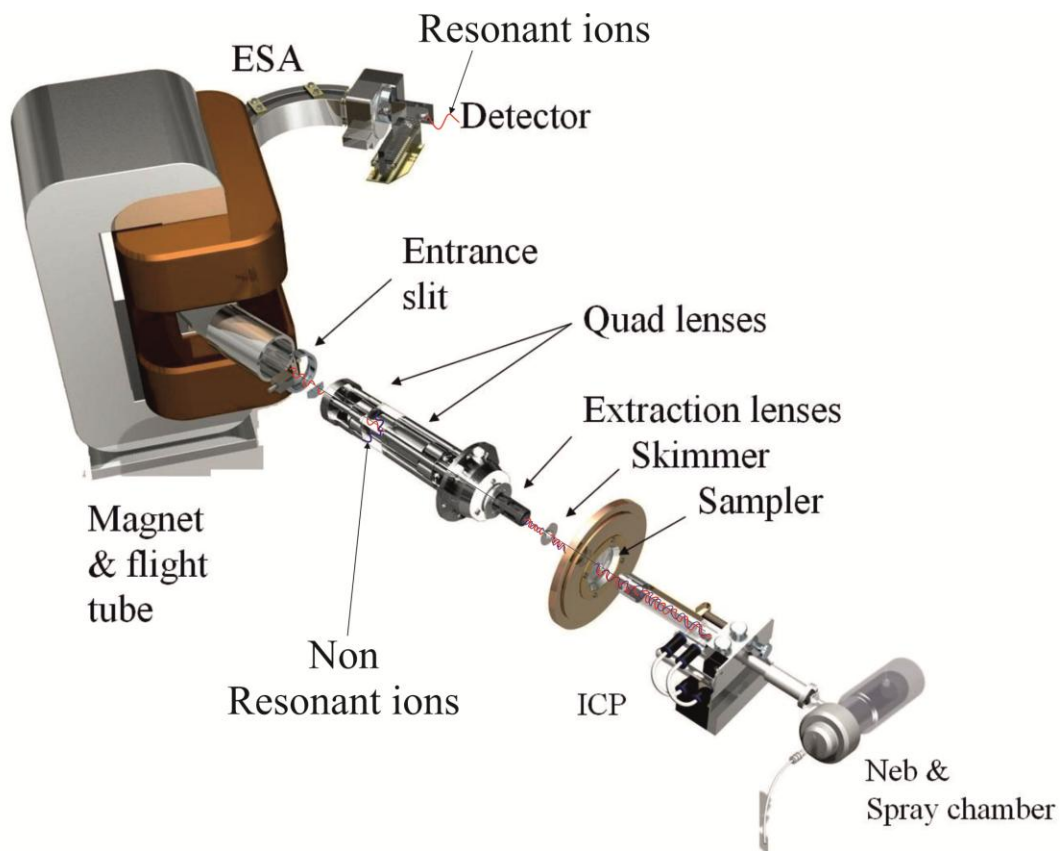


Figure 4.2: Schematic diagram of quadrupole type ICPMS illustrating the working principle of the technique.



Figure 4.3: Author at work on ICPMS in Mass Spectrometer Lab at WIHG, for trace elemental analysis.

Sample Preparation: Analyses were carried out in solution phase through Inductively Coupled Plasma Mass Spectrometry (ICPMS). In this analysis, 1 mg finely powdered sample (clay size) were dissolved at 200 °C using the mixture of HF:HNO₃ :: 2:1 in presence of perchloric acid, until the clear solution appears. After complete dissolution of sample, a clear solution appears, in which 10 ml of 10% HNO₃ is slowly added to dissolve the content and further makeup the volume to 100 ml using de-ionized (Milli Q) water to make 0.1% concentrate sample solution. These solutions were used as such for to determination of the concentration of trace and REE elements. One of each standard and blank were also prepared in the same manner with each batch of about 10 samples.

International carbonate standards used for calibration as well as QA/QC purpose are SGR-1 (Oil Shale of green river from the USGS, USA) and JDo-1 (Dolomite from JGS, Japan) for carbonate; while JG-2 (Granite; JGS, Japan), GH (Granite, Himalaya, WIHG, India) and MAG-1 (Marine sediments from USGS) were used for quartz samples.

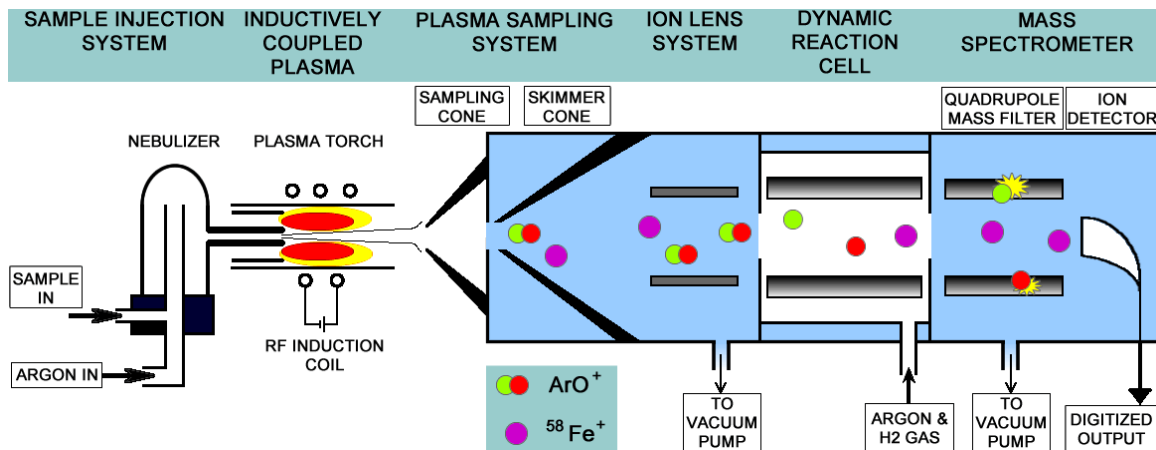


Figure 4.4: A Schematic diagram of Inductively Coupled Plasma Mass Spectrometer (ICPMS).

Analytical Process: The dissolved sample solution is injected into the system by a cross-flow nebulizer. The sample is introduced into the ICP (Inductively Coupled Plasma), where the constituent atoms are ionized at the plasma interface. Once the aerosol sample introduced into the ICP torch, it is completely dissociated and the elements in the aerosol are converted first into gaseous atoms and then ionized. These ions are accelerated into the mass spectrometer by the ion-lenses applying electrostatic field (Figure 4.4). Desired ions (resonant ions) are focused onto the detector by controlling the electric field of the quadrupole mass filters as shown in figure 4.2 and 4.4, while the ions of other isotopes (non-resonant ions) are diverted away from the path. The detected signal is further

processed with the help of a computer and dedicated software. The ion signals (intensities as counts per seconds) are collected and analytical results processed through the software (figure 4.4).

Table 4.2: Physical Parameters of ICPMS used in this study (After Khanna et al., 2009 and Mukherjee et al., 2014).

ICP-MS	
ICP-MS	ELAN DRC-e (Perkin Elmer Corp., Norwalk, USA)
RF Power	1300 W
Carrier gas flow (He)	550ml/min
Nebulizer gas flow	0.64 l/min
Plasma gas flow (Ar)	16 l/min
Auxiliary gas flow	1.20 l/min
Lens voltage	8 V
Detector mode	Dual Pulse counting and Analogue
Pulse Stage Voltage	1250 V
Analogue Stage Voltage	-1950 V
Measurement mode	Peak hopping
Data Acquisition parameters	
Sweeps per reading	1
Replicates	1
Dwell time per isotope	30ms
Points perpeak	1
Measurement mode	Peak hopping

Analytical Strategy: The primary standard SGR-1 is used for the calibration of ICPMS to analyze trace and REE in carbonate phase and further the quality control is cross checked by MAG-1 and JDo-1 standards. Whereas the trace and REE in silicate phase (quartz) is analyzed by calibrating ICPMS using JG-2 which was further cross checked by analyzing reference standard GH for quality control. These standards and blanks are prepared with each batch of samples. The blank, calibration standards and QC standards are run at the interval of each 5-10 samples of respective batches to minimize the error

due to instrumental drift. The sample measurements were bracketed by re-calibration of the instrument. The blank sample is run as a *Blank* which quantifies the zero level of intensity for different elements. The calibration standards are run after the blank to quantifying the intensity of the elements according to their concentration whereas the QC standards are run as unknown to cross check the accuracy and precision of ICPMS for quality control purpose. The physical parameters and analytical protocols used in this study summarized in table 4.2 as described by Khanna et al (2009) and Mukherjee et al (2014).

4.1.2 ANALYTICAL TECHNIQUE OF STABLE ISOTOPE GEOCHEMISTRY

The Stable isotopic analyses of calcite and quartz phases were carried out at Stable Isotope Laboratory of WIHG using Continuous Flow Isotope Ratio Mass Spectrometry (CF-IRMS). The CF-IRMS is configured for precise stable isotopic analysis of light isotopic elements (such as C, O, H and N) in gaseous form (CO₂, O₂, H₂ and N₂) with mass range of 1 to 96 (g/mol) is suitably analyzed by a magnetic sector flight at an angle of 90° (Figure 4.5). The IRMS has three major components (i) *Source*, to generate, accelerate and collimate the ions (ii) *analyser* to generate the strong electric, magnetic field for separation of ion beams according to their mass-by-charged ion ratio and (iii) *collector* to collect, compare or count the different ion beams (see figure 4.1 and 4.5).

- i. The source* is comprised of hot (2000 °C) tungsten filament to produce a small (~2 mA) current of electrons with an energy of 123.631 eV. This electron

energy is sufficient to ionize the gas (CO₂ and O₂) molecules within a high vacuum through electron bombardments.

- ii. **The analyzer**, in which ion beam enter into a strong magnetic field (about 0.75 Tesla) produced by electromagnets. The magnetic field strength varies for different gasses and increases with the molecular weight of gas being analyzed (eqn-4.2). For example, the magnetic strength of CO₂ (molecular weight: 44 g/mol), O₂ (molecular weight: 32 g/mol), N₂ (molecular weight: 28 g/mol) and H₂ (molecular weight: 2 g/mol) is 11804, 9840, 9114 and 1559 Dalton, respectively as is used in the present case. The magnetic field causes the ions to move along circular path that depend on their momentum (eqn-4.1). By the time the beam leaves the magnetic sector, it has been deflected by a significant angle of 90°. These separated beams were then collected in a collector as electronic signals.

$$r = \frac{mv}{qB} \dots\dots\dots \text{Eqn. (4.1)}$$

$$r = \sqrt{\frac{2Vm}{B^2q}} \dots\dots\dots \text{Eqn. (4.2)}$$

- iii. **The collector** is placed at the goal of the ion path, which quantifies the ion beams by detecting and measuring the bantam currents generated by their neutralization. This may typically involve one or several detectors of different types, such as "Faraday cups" electron multipliers, and so on. Precise measurements of isotopic abundances can be habitually made on a few micro-

moles of gas, and even from as little quantity of samples as 200–500 μg in carbonate phase and ~ 0.5 mg in silicate phase (quartz).

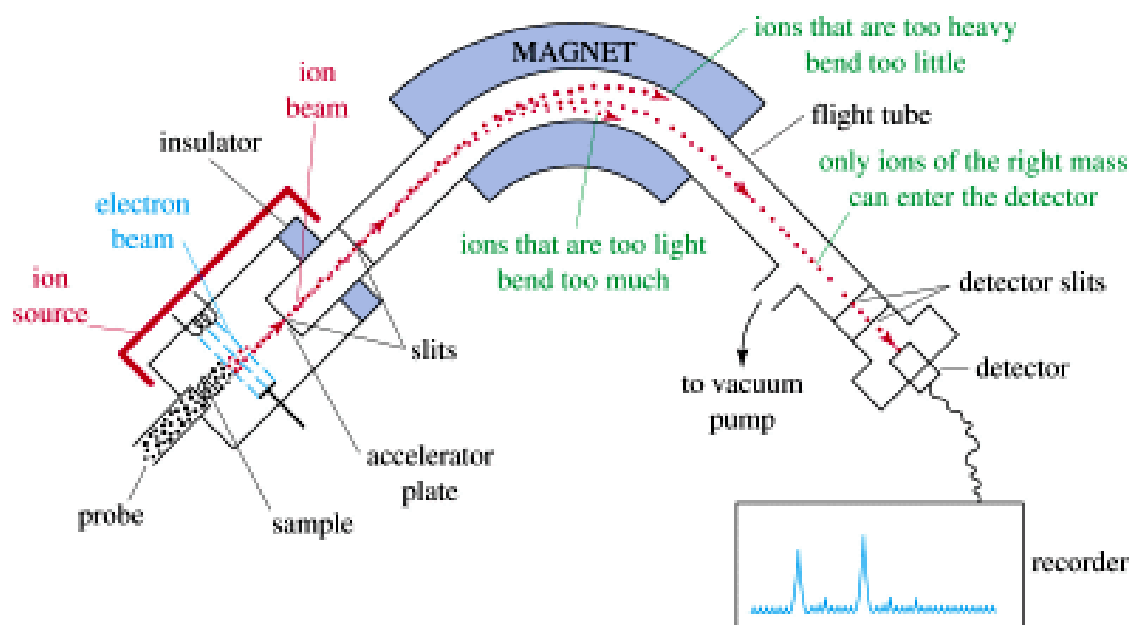


Figure 4.5: A Schematic diagram of isotope Ratio Mass Spectrometer (IRMS) illustrating the working principle and configuration of the instrument used in the study.

The isotopic ration R of the two isotopes of an element is estimated from the measurements in the IRMS. However, it is not used to report stable isotopic data because the variation is numerically too small and is of the order of third/fourth decimal place (e.g., D/H ~ 0.00015). Conventionally, therefore, the ratios are expressed relative to a standard value, i.e. delta notation (δ) and reported as “per mil” unit (‰) as described below. The stable isotopic ratio measurements of C, O, N and H are made electronically through counting and comparing the intensities of the generated beams. The basic assumption here is that the intensities are proportional to their abundance. The intensities at different masses of sample beam are compared with reference to those of known

standardized reference gas intensities at respective masses using standard sample (NBS–18 for carbonates and NBS–28 for silicate). This method allows the isotopic composition of the unknown to be determined by the known intensities from those of the standards (gas tank or sample) with single point/multipoint calibration. For all the above reasons, the stable isotopic data is reported in δ -values (termed "delta-values") as a standard practice.

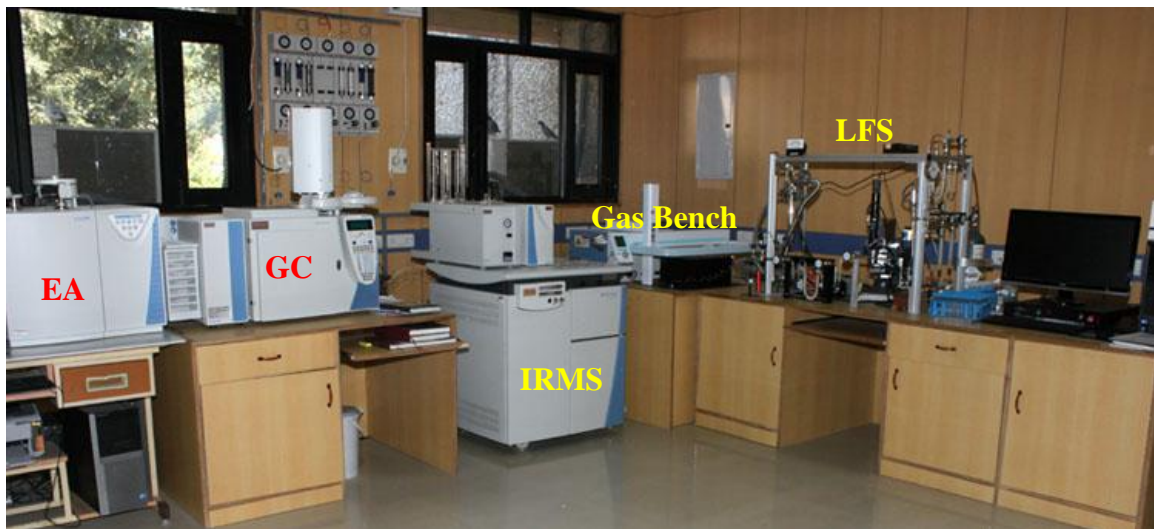


Figure 4.6: Photograph of Stable isotope facility at WIHG, Dehradun.

δ – notation

Relative differences in isotopic ratios can be determined far more precisely than absolute isotopic ratios. McKinney et al. (1950) introduced the delta (δ) notation to report stable isotope data for all materials except extra-terrestrial dust, whose isotopic ratios and variations are frequently so large that absolute ratios are commonly and reasonably used in publications. The delta (δ) value is expressed by–

$$\delta = \left\{ \frac{R_x}{R_{std}} - 1 \right\} \times 1000 \dots \dots \dots \text{Eqn. (4.3)}$$

Where ‘R’ is the ratio of the abundance of the heavy to the light isotope, ‘x’ denotes the sample, and ‘std’ is an abbreviation for standard. For the elements carbon and oxygen, R is given by ¹³C/¹²C and ¹⁸O/¹⁶O, respectively. Delta values are reported in “per mil”, or parts per thousand and the symbol for per mil is ‰.

4.1.2.1 DETERMINATION OF δ¹³C AND δ¹⁸O IN CARBONATE PHASE

The stable isotopic ratios of Carbon (δ¹³C) and Oxygen (δ¹⁸O) in carbonate phase were measured in stable isotope laboratory of WIHG equipped with Gas Bench with CF-IRMS (figure 4.6). In this process, the powdered carbonate samples were put in 12 ml vials. These vials were placed in Gas Bench Tray at 72 °C for flush fill with 99.9995% pure He gas, to remove all atmospheric gasses from the vials. Further, 50–70 μL phosphoric acid (H₃PO₄; ≥99 % Crystalline) were poured into the vials, which reacts with the carbonate sample to produce CO₂ gas (see eqn 4.4). The CO₂ gas is produced for 45 minutes at 72 °C after acid introducing. The CO₂ thus produced is ionized and analyzed by IR-MS and isotopic ratios of Carbon (δ¹³C) and Oxygen (δ¹⁸O) are obtained using the SSH correction following Santrock et al (1985). The blank, in-House Standard (Merck-CaCO₃) and an International Standard (NBS-18) were also run with each set of batch as QA/QC measure. Precision of these measurements are better than ±0.1‰. The schematic diagram of Carbon (δ¹³C) and Oxygen (δ¹⁸O) isotopes in carbonate phase is shown in figure 4.7. The primary standard NBS-18 was run for the calibration whereas the in-House standard

Merck–CaCO₃ was run at the interval of 10 samples to verify precision and quality of the measurement.

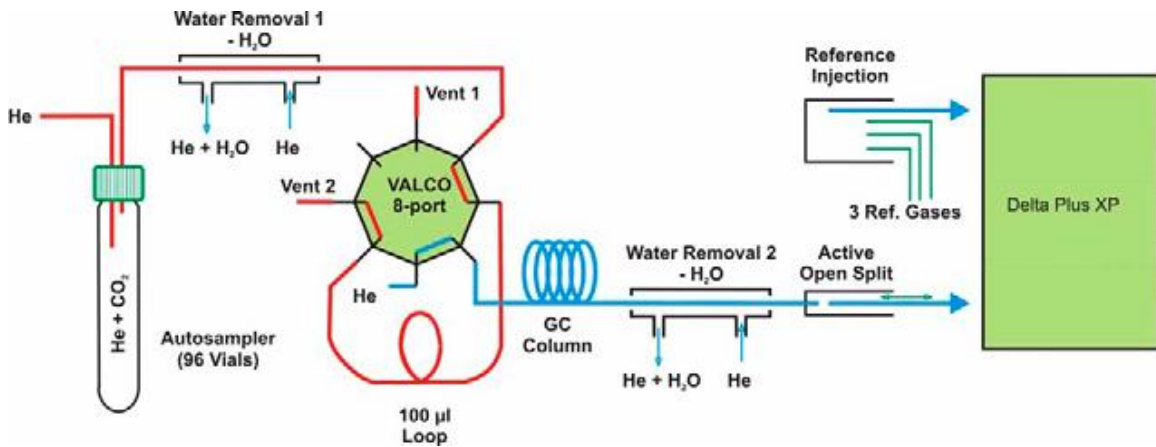
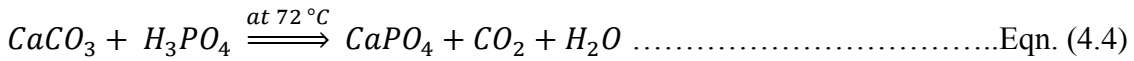


Figure 4.7: A Schematic diagram of stable isotopic analysis in carbonate phase.

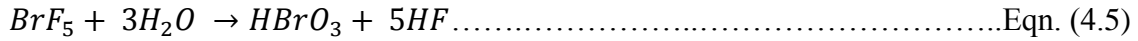
4.1.2.2 DETERMINATION OF δ¹⁸O IN SILICATE PHASE

Realizing the importance of oxygen isotopic systematics in the silicate system, the Oxygen isotopic (δ¹⁸O) ratio measurements in silicate phase was first introduced as early as in early 19th century (Groot, 2009 and Sharp, 2007). Extraction of oxygen species from silicate phase is not so straight forward. Many techniques were developed since then and have gone through many improvisations with time to get more precise oxygen isotopic results in silicate minerals. These techniques require very high temperature (1000 °C – 2500 °C) to analyze and cannot be adopted at microscopic level or individual grain scale because it required high amount of sample powdered (50–60 mg). At that time whole rock was analyzed in place of individual mineral grain and precision was also very low ±2.5‰ (Groot, 2009). The isotopic analysis of silicate minerals/rocks is time consuming

and expensive too. Various techniques devised and commonly adopted techniques include:

- (a) Reduction with carbon method;
- (b) Potassium hydrogen fluoride reaction
- (c) BrF_3 , KBrF_4 , and BrF_2SbF_6 fluorination technique
- (d) Fluorination systems using Ni reaction vessels
- (e) Laser fluorination method.

Now a day's, *Laser fluorination technique* (Sharp, 1990) has received much popularity and is used worldwide to measure the oxygen isotopic ratio in the silicate phase. In this technique individual separate grain of mineral or very small amount of sample can be analyzed with very high precision down to $\pm 0.2\%$. The basis for the fluorination technique, as mostly used for oxygen isotope in silicates and oxides, was described by earlier workers used in different fluorination agents like (i) BrF_5 (Clayton and Mayeda, 1963); (ii) F_2 and HF mixture (Baertschi and Silverman, 1951); and (iii) F_2 (Taylor and Epstein, 1962). IF_5 was also tested for this application, but it was decomposed above 400°C producing I_2 deposits (Borthwick and Harmon, 1982), so that this method didn't receive much attention. The BrF_5 and ClF_3 both are the strong fluorination reagent for oxygen isotope in silicate phase with high precision. The BrF_5 is used as a fluorination agent for this study due to the availability. Although all the fluorination reagents are highly explosive and hazardous (see eqn-4.5) but the $\text{O}=\text{Si}=\text{O}$ bond can break at high temperature ($\geq 700^\circ\text{C}$) only in fluorination environment. Therefore, it is necessary to use suitable fluorination reagent (BrF_5 or ClF_3) as per the availability in this system.



The Technique presented here highlights the analytical methodology developed for Oxygen isotope measurement in silicate minerals using continuous flow IRMS. This is a modified Laser Fluorination technique of Sharp (1990). The novelty of this modification is that, with this technique we can analyze the evolved oxygen directly (without converting it into CO₂) as described by Sharp (1990).

4.1.2.2.1 The Laser Fluorination Technique

Sharp (1990, 1992) described a laser fluorination system for oxygen isotope analysis of silicates. In this approach, the laser is used as a rapid and powerful heat source in lieu of the resistance furnace used in the conventional fluorination method. Laser systems allow performing analyses on small quantities of samples, including single grains or in situ grains on rock slabs or sections at microscopic scale. With the classical Ni tube reaction method, analytical precision decreases dramatically for sample size between 0.5 and 1.0 mg. In the laser system, possible interactions with, or contributions from absorbed water attracted by hygroscopic NiF₂ are excluded, since no NiF₂ is formed in the reaction chamber (Sharp, 1990). Therefore, blanks in the laser system are lower than in the classical fluorination systems (Sharp, 1990; Matthey and Macpherson, 1993). The laser heats samples to >2000 °C in few seconds and reaction time is very short. The energy of the laser can be absorbed by framework anions/cations or by defects in the crystal lattice (Kyser, 1995) whereby vibrational modes of the crystal lattice causes heating of the mineral (Farquhar and Rumble, 1998). The high reaction temperatures enable to analyze

the most resistant minerals, e.g. forsterite, kyanite, coesite, corundum, epidote, which are otherwise difficult to react with the conventional approach. The main difference between the laser system and the classical technique is in the oxygen extraction from the silicates. The basic procedure of oxygen isotopic analysis following Sharp (1990) is presented below. This is followed by more specific analytical evaluations of this laser technique.

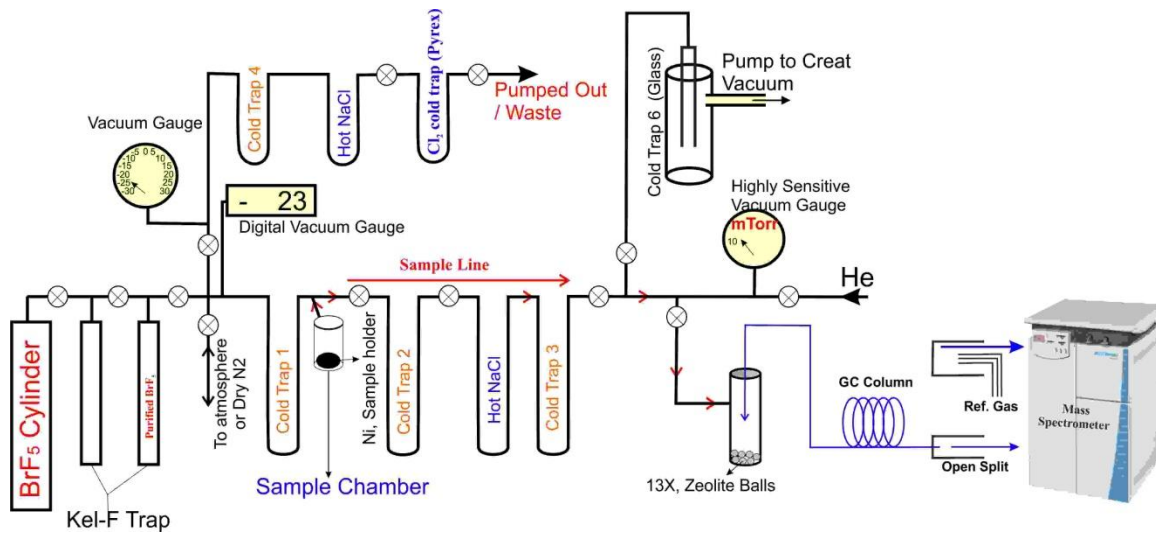


Figure 4.8: A Schematic flow sheet diagram of Laser fluorination system for oxygen isotope measurement in silicate phase.

The fluorination technique is limited by the sample size. Very small size, sample will give large errors related to the blanks (which ‘pollute’ the small quantity of gas produced). Another limit is related to the nature of few silicate or oxide mineral structures, such as Mg–olivine, garnet, kyanite, epidote and spinel group minerals (Taylor and Epstein, 1962; Garlick and Epstein, 1967; Taylor, 1967; Kyser et al., 1981; Sharp and O’Neil, 1989; Vennemann and Smith, 1990; Matthey and Macpherson, 1993).

Fluorination agent and Distillation Process

Most laser fluorination devices use BrF_5 or ClF_3 as fluorination agent. In our laboratory, we are using BrF_5 as a fluorination agent due to its availability. The BrF_5 distillation process requires high quality trap tube, which has zero moisture absorption and the working temperature varies from very low ($-240\text{ }^\circ\text{C}$) to very high ($+240\text{ }^\circ\text{C}$). The Kel-F is the best material for such type of work. Kel-F is homopolymer of chlorotrifluoroethylene has the lowest vapor transmission rate of any plastic and zero moisture absorption, non-wetting. The compression, impact and tensile strength are high over wide temperature ranges which make it important.

It is mandatory to purify BrF_5 fluorination reagent before using through doubly distilled by passing it between two adjacent ('A' and 'B') Kel-F tubes (see figure 4.8). For distillation of BrF_5 must be trapped in 'B' Kel-F tube. Now all non-condensable gases by liquid nitrogen are removed from the line except for BrF_5 in 'A' Kel-F tube. The purified BrF_5 slowly turns into yellowish color in 'B' Kel-F trap which indicates that only BrF_5 remains in 'B' Kel-F trap, which can be used for analysis. The BrF_5 can be trapped below its melting temperature (i.e. $-61.30\text{ }^\circ\text{C}$), therefore liquid nitrogen used for this purpose due to its melting temperature (i.e. $-210\text{ }^\circ\text{C}$) and boiling point (i.e. $-196\text{ }^\circ\text{C}$).

Instrument and attachments

The instrument (Laser Fluorination system) comprised of two parts: a metal part and a glass part. The metal part is made up of monel (Ni-Cu alloy), silver-soldered to copper fittings. Other materials used for tubing are stainless-or Inconel steel, copper or nickel.

Fittings of the Sawgelok type, preferably with metal ferrules (although Teflon ferrules or combined metal–Teflon ferrules can be considered) can also be used. The glass part is made out of pyrex glass to withstand a wide temperature range from $-400\text{ }^{\circ}\text{F}$ to $+400\text{ }^{\circ}\text{F}$.

Laser: There are several types of moderately high power lasers that are applicable to stable isotope geochemistry. These are CO_2 , Nd–YAG or Nd–glass, Ar, monochromatic lasers for use of geochemistry. The characteristics of each laser are different, so that no laser may be ideal in all respects. In this system CO_2 monochromatic laser is used, which is a 55–watt, RF–excited, sealed system with a modulation capability of 55 kHz, having 63 mm focal length beam delivery system with power stability within 2%. This CO_2 laser required cooling either water cooling or magnet cooling. In our laboratory, high power magnets were used for cooling of laser. This laser beam has a wavelength of $10.6\text{ }\mu\text{m}$, which is absorbed by all oxygen bearing compounds. As a result, all silicates and oxides can be heated up rapidly to very high temperature with a moderate power of CO_2 laser. The laser is mounted on stacked translation stages that are controlled by computer. In order to align the laser over the sample, the lightweight laser is moved over the sample chamber. This greatly simplifies the construction of high vacuum system. The CO_2 laser beam is invisible for the human eye. The laser can be operated in different modes such as- focused, defocused, continuous and pulsating. Powders and small chips must be heated slowly in defocused pulsating mode, to prevent a violent reaction and ejection of material out of the sample holder—a disaster for holders containing several samples, which must all be considered contaminated after such an event.

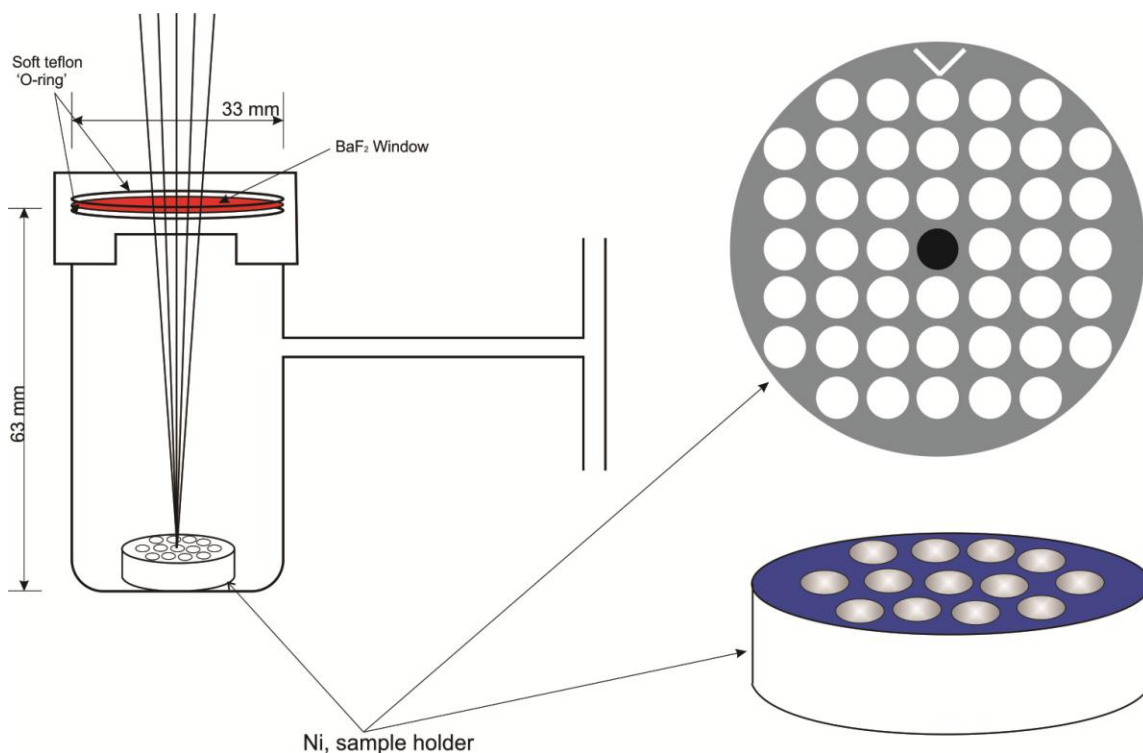


Figure 4.9: A Schematic diagram of sample chamber and Ni sample holder used in the laser fluorination system.

Sample Chamber consists of double side electro polished 314 stainless steel tubes with a window to admit the laser radiation, a quick-disconnect flange for sample insertion and removal. The laser radiation passes through a BaF₂ window, a material that is transparent in the visible, infrared regions and is also non-reactive with fluorine. BaF₂ is recommended for use as a vacuum ultraviolet window, where high radiation resistance is required.

The BaF₂ window has transmission range of 0.265 to 10 μm, with 5.27 g/cm³ density along with the melting temperature of 1525 °C. BaF₂ window compressed between two soft Teflon O-rings (Kal-Rez) to make vacuum-tight seal. A nickel block with 44 tapered

holes is used as a sample holder. Each of the tapered holes is used for an individual sample, so that 44 samples can be loaded and degassed simultaneously (Figure 4.9). The long length minimizes accumulation of fluorinated debris on the underside of the BaF₂ window.

Sample Preparation: To analyze the silicate minerals using laser fluorination technique, minerals must be separated from whole rock by crushing and make ~200 µm Dia or treated chemically. No 'best' grain size of the sample required. The small sample grain and large in surface area of the sample is best for measurements. The larger surface area is used for completing reaction within short time (~1 Minute). Whole rock samples may contain fluorination-resistant components, and therefore it is desirable, although there is risk of more adsorbed water, to use fine grained cuts for analysis. Often a split of the sample, powdered for other geochemical analytical purposes, is used. For mineral separates, the grain size depends on the mineral structure and composition. In case of refractory minerals, fine grained samples are definitely a better choice. For the more reactive minerals relatively larger grain sizes, like sand size or even larger, are preferable.

After preparation, all samples were placed in a dry place, e.g. in a desiccators, until they were analyzed. Prior to the measurements sample were placed in an oven at 100°C–200°C for overnight (Yeh and Savin, 1977). Small sample size ~200 µm dia (silt/fine sand size) and 0.5–1.0 mg is suitable for the measurements, depending on the oxygen content in the sample.

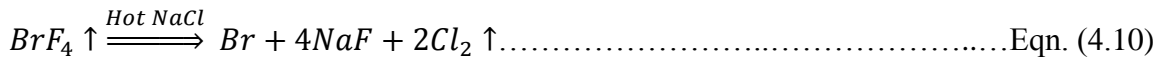
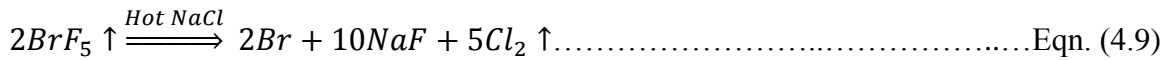
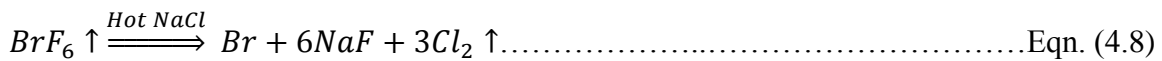
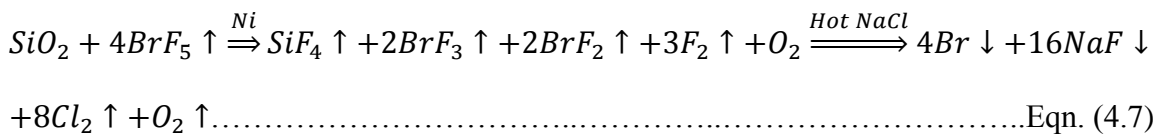
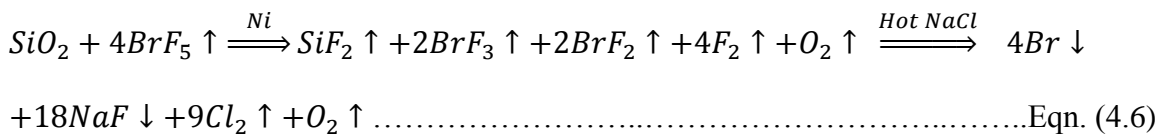
Purification process of O₂

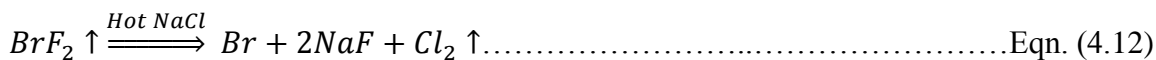
Samples are first loaded in a Ni sample holder with 44 trapped holes (groves). Samples were cleaned of all traces of epoxy, glue or oil products and are heated in an oven for 2-3 hours to remove absorbed moistures. After cleaning, samples were not touched with hand to avoid any pollution (Rumble et al., 1997). The sample holder is placed in the sample chamber and the chamber is evacuated. The reaction chamber was flushed by dry nitrogen/He gas (Fouillac and Girard, 1996) to avoid moisture to enter in the chamber during loading.

Sample was placed in the sample chamber at low vapor pressure vacuum (<30 mTorr) for about 48 hrs. Then a small amount of fluorination agent is allowed in the reaction chamber at a low pressure (<30 mTorr) to pre-fluorinate the chamber and samples for ~15 hrs (or overnight) to remove any adsorbed greasy, oily material and water vapor.

The pre-heating step is important to prevent formation of significant quantities of HF, a product frosting the BaF₂ window in CO₂ monochromatic laser systems (Spicuzza et al., 1998). The residuals of the pre-fluorination treatment were removed from line and discarded by passing through '*HOT NaCl*'. The sample chamber is further placed under low vapor pressure vacuum (<30 mTorr) for ~1 hr. Now the system is ready to analysis, and a small amount of fluorination agent (BrF₅) is introduced into the reaction chamber for the measurement.

In the fluorination environment, CO₂ monochromatic laser is operated by defocused beam pulsed at 10% of its total power, with pulse spacing of 1 kHz and pulse width of 100 ms. The power of the laser was slowly increased by decreasing the pulse spacing and increasing the pulse width until the sample began to glow. The reaction was complete when the sample was no longer incandescent. Most materials leave a residue of solid fluorides, which are transparent to the laser radiation but may prevent efficient heating of sample material when abundant. For large samples, restoring of the laser beam over the sample may be needed for a complete reaction. Total reaction time varies between 1 and 5 minutes typically to produce O₂ from silicate minerals in fluorination environment of BrF₅ (eqn 4.6, 4.7). In this system, possible interactions with, or contributions from absorbed water attracted by hygroscopic NiF₂ are excluded, since no NiF₂ is formed in the reaction chamber (Sharp, 1990). Therefore, blanks in the laser system are lower than in the classical fluorination systems (Sharp, 1990; Matthey and Macpherson, 1993).





After pre fluorination of quartz samples a small amount of BrF₅ was introduced into the sample chamber to make fluorination environment. In the fluorination environment of BrF₅ samples were heated rapidly using CO₂ monochromatic laser and evolved O₂ gas for analysis (eqn 4.6, 4.7). As shown in the eqn 4.6 and 4.7, that O₂ gas is produced along with other gasses and little amount of untreated BrF₅ may also remain in the line, which must be purified prior to the analysis of O₂. After complete reaction, the untreated fluorination agent and condensable gasses were frozen back in the cold trap 1 of the vacuum system (Figure 4.8). The evolved O₂ is passed through the cold trap 2 to trap all untreated fluorination agent (if remains in the system). Further, O₂ gas is slowly admitted into the Hot NaCl (diffusion chamber) to react with any fluoride or halogen oxy-fluoride components that may have formed during the reaction procedure, where it converts the F₂ gas into the Cl₂ (eqn 4.8 – 4.12). A cold trap (using liquid Nitrogen) placed behind the Hot NaCl to trap Cl₂ gas (if produced). The F₂ is formed in small quantities by interaction of ClF₃/BrF₅, and to the lesser extent of BrF₅, with the laser beam in the reaction chamber. The F₂ is not properly trapped by liquid nitrogen (due to its melting point - 220°C, which is lower than boiling point of nitrogen, -196 °C) in the cold traps and was removed by reacting with NaCl, which produce NaF and Cl₂ (See eqn 4.8 – 4.12). The Cl₂ gas was trapped by liquid nitrogen in cold trap 3 (Figure 4.8). Now, it is confirmed that the oxygen gas is purified by passing through three cold traps followed by diffusion chamber of Hot NaCl and no other gases remain in the line. As discussed above that the oxygen gas is passed through the liquid nitrogen but not trapped due to the melting

temperature of oxygen i.e. -222.6°C which is lower than the liquid nitrogen. Therefore, a special treatment is required to trap the oxygen gas using liquid nitrogen for this region 13X zeolite balls are used. The zeolite balls contain depression on its surface which holds the gas molecules (Oxygen) by liquid nitrogen (LN_2). The trapped O_2 gas analyzed using CF-IRMS through GC Column.

Cleaning processer of sample holder: All samples loaded in the sample holder are reacted in this manner, one after the other. The sample holder was cleaned thoroughly using deionized water (Milli Q) followed by dilute acid solution, prior to the next set of samples. The BaF_2 window re-polished using diamond suspension of $1\ \mu\text{m}$ and holder should be ultrasonically cleaning in de-ionized water and acetone. Spicuzza et al. (1998) describe the cleaning procedures in which Ni holder is cleaned using 5M HCL, followed by rinsing in 95% ethanol and drying in oven at $\sim 100^{\circ}\text{C}$.

Precision of the technique is $\pm 0.2\%$, and often better than $\pm 0.1\%$, typically for a sample size in the range of 0.5–1 mg.

4.1.3 ANALYTICAL TECHNIQUES FOR MEASUREMENT OF RADIOGENIC ISOTOPIC COMPOSITIONS

To constrain the source of fluid, it was felt necessary to carryout radiogenic isotope geochemistry of vein mineral (calcite). Sr and Pb radiogenic isotope geochemistry was included in the present study, which is established to be very powerful proxy to trace the

fluid source. The Sr isotopic compositions were measured at the Physical Research Laboratory, Ahmadabad, whereas the Pb isotopic system was done at the University of Cape Town, South Africa in solution phase using Multi Collector Inductively Coupled Plasma Mass spectrometer (MC–ICPMS).

A MC–ICPMS is a hybrid mass spectrometer with wide ranging applications in geochemistry, geochronology, and cosmochemistry. The instrumentation consists of inductively coupled plasma (ICP) plasma source to ionize atoms in the sample aerosol. With an electrostatic energy filter and magnetic sector analyzer of the mass spectrometer, the accelerated charged ions very efficiently are separated according to their charge–mass ratio and the ions were measured in the multi ion collectors (MIC) detector array which gives us isotopic ratio of element(s) of interest. The sample solution is introduced into the ICP which strips off electrons thereby creating positively charged ions. These ions are accelerated across an electrical potential gradient (up to 10 KV) and focused to form a beam via a series of slits and electrostatically charged plates. These ion beams pass through a magnetic field to separate the ions on the basis of their mass to charge ratio followed by passing through an energy filter, to make consistent energy spectrum in the ion beam. These charged ions are directly collected in the collectors where each ion impact generates electric pulses. Isotope ratios are calculated by comparing voltages from the different collectors.

The Modern MC–ICPMS composed of three major components:

- (i) **Source:** an inductively coupled plasma (ICP) ion source were used in this instrument, where ions are produced, accelerated, and focused;
- (ii) **Analyzer:** In which the ions are focused and filtered to produce a beam where the ions have the same approximate energy and can be separated based on their mass/charge ion ratios; and
- (iii) **Detector:** a series of collectors (Multi ion collector) and faraday cups, where the ion beams are measured simultaneously.

All these three major components of MC–ICPMS must be maintained under high vacuum along the path of the ion beam in order to avoid scattering of the ions due to interaction with air molecules. The major advantage is the high resolution of such magnetic sector mass spectrometers allowing speciation and measurement of different isotopes of Sr without isobaric interference from isotopes of Rb.

4.1.3.1 STRONTIUM ISOTOPIC MEASUREMENTS

The Sr isotopic ratios ($^{87}\text{Sr}/^{86}\text{Sr}$) of carbonate minerals were analyzed at the Physical Research Laboratory, Ahmadabad using Neptune MC–ICPMS. The isotopic ratios were measured on unspiked leached carbonate samples by following the chemical process of Rai and Singh (2007) and are briefly mentioned below. The Sr isotopic ratios were measured in static multi–collection mode (Goswami et al., 2012). Instrumental mass fractionation was corrected using an exponential law with 0.1194 for $^{86}\text{Sr}/^{88}\text{Sr}$. The Rb contribution was corrected by the natural abundance of $^{85}\text{Rb}/^{87}\text{Rb}$, though the amount of

^{85}Rb was negligible in all samples. SRM987 standard was run with every set of samples which yielded $^{87}\text{Sr}/^{86}\text{Sr}$ ratio of 0.710270 ± 0.000018 (1σ , $n=7$). The procedural blank for Sr during measurement was less than 1 ng and the total Sr analyzed for the samples were always 3–4 orders of magnitude higher than the blank. In general, the internal precision ($2\sigma_{\mu}$) of these measurements was better than 0.0024 %.

Column Chemistry for Sr isotope Geochemistry

It is essential to separate pure Sr species quantitatively from the rest of the ions. This is done by liquid chromatographic technique. The chemical process for Sr isotope separation in the liquid phase is outlined below adopting the procedure established by Rai and Singh (2007).

- (i) Firstly, carbonate samples were cleaned by leaching with 5% acetic acid.
- (ii) The leached samples were dried and separated from the residual.
- (iii) Residuals were dissolved in 3N HNO_3 .
- (iv) Eichrom Sr specific resin was preconditioned by passing 3N HNO_3 .
- (v) The dissolved residual were passed through the pre conditioned Eichrom Sr specific resin.
- (vi) The Eichrom Sr specific resin having the capacity to hold the Sr only.
- (vii) Pure Sr fraction was collected after addition of Milli-Q water as eluent to the column.
- (viii) This Sr fraction was then dried and re-dissolved in 0.4N HNO_3 for isotopic measurements by MC-ICPMS under standard instrumental conditions.

4.1.3.2 LEAD ISOTOPE GEOCHEMISTRY

The lead isotopic analysis has been carried out at Department of Geological Sciences, University of Cape Town, Rondebosch, South Africa using a Nu Plasma multi-collector inductively coupled plasma mass spectrometer (Nu Plasma HR, see figure 4.10).



Figure 4.10: Photograph of MC-ICPMS facility (Nu Plasma) used in this study for Lead (Pb) isotope systematic at University of Cape Town, Cape Town, South Africa.

Details of the chemical procedures are given in Fölling et al. (2000) and the same procedure was adopted for Pb isotopic determination by MC-ICPMS. The Pb isotopic ratio was corrected for ^{204}Hg interference at ^{204}Pb and mass fractionation (Galer and Abouchami, 1998; Will et al., 2010). The correction for instrumental mass fractionation was carried out using the exponential law and a $^{205}\text{Tl}/^{203}\text{Tl}$ value of 2.3889. The lead

isotope ratios of $^{206}\text{Pb}/^{204}\text{Pb}$, $^{207}\text{Pb}/^{204}\text{Pb}$ and $^{208}\text{Pb}/^{204}\text{Pb}$ were analyzed against the NIST SRM981 standard. All the Pb isotopic measurements are reported here within error of 2σ .

Column Chemistry for Pb isotope Geochemistry

It is essential to separate the pure fraction of lead from matrix using column chromatography. The chemical procedure used in this study given by Fölling et al (2000) is given below.

- (i) About 1 g powder carbonate sample were weighed into a Teflon beaker.
- (ii) Dissolved with 1N acetic acid by adding 3–5 ml in multi steps until a slight stoichio–metric excess (ca. 20 ml) was reached.
- (iii) The samples were left on hotplate at 30–50 °C for about 48 hrs until reaction was completed.
- (iv) The residue fractions were washed and centrifuging minimum three times with de–ionized (Milli Q) water to separate the carbonate fractions.
- (v) The residue fractions were dried, weighed and then dissolved in a 4:1 HF:HNO₃ mixture on a hot plate at 70 °C for 2–4 weeks.
- (vi) Both carbonate and residue fractions were dried down after dissolution and taken up in 5 ml 6.2M HCl.
- (vii) Unspiked aliquots were again dried down and taken up in 0.5 M HBr.
- (viii) Unspiked aliquots were passed twice through 2.5 ml Teflon ion exchange columns containing 0.5 ml anion exchange resin (BioRad AG 1–X8 resin) to extract the Pb, which was eluted with 0.5M HNO₃.

- (ix) The extracted Pb from the unspiked aliquots was contained in a 10–ml drop of phosphoric acid, which was split immediately prior to analysis by MC–ICPMS.

4.2 RESULTS

The analytical results of geochemistry are summarized in this section. Trace element, REE geochemistry of quartz and calcite along with the stable isotope ($\delta^{13}\text{C}$ and $\delta^{18}\text{O}$), radiogenic isotope ($^{87}\text{Sr}/^{86}\text{Sr}$, $^{208}\text{Pb}/^{204}\text{Pb}$, $^{207}\text{Pb}/^{204}\text{Pb}$ and $^{206}\text{Pb}/^{204}\text{Pb}$) geochemistry of calcite and oxygen isotope ($\delta^{18}\text{O}$) geochemistry of quartz are explained in this section. This geochemical study helped to trace the source of vein fluid in the development of Himalayan orogeny at penultimate stage. All the geochemical results explain here, presented in graphical form and also tabulate in the *appendix 'C'*. The geochemical results are discussed in section 4.3.

4.2.1 TRACE AND REE GEOCHEMISTRY OF QUARTZ AND CALCITE

Trace elemental geochemistry of quartz and calcite minerals were carried out on pure mineral separates. The trace elemental abundances in calcite phase shows remarkable mutual correlation among HFSEs in Shergol sections, whereas other sections show moderate correlation. Many trace elements including REE infer the mantle signature for the fluid. However the marine components cannot be ruled out as a cause for the high concentration (~400 ppm) of Na in carbonate phase from all studied sections excluding ZOM, where Na content shows extreme enrichment by an order of magnitude up to (5080

ppm) compared to other sections. The high concentration of Na indicate that carbonate rich fluids might have interacted with the NaCl rich marine components which were also substantiated by fluid inclusion studies (see table 3.2, 3.3 and figure 3.19 to 3.22). The bi-phase H₂O-NaCl primary and secondary inclusions are dominant with other mono phase primary inclusions in the system and rarely three phase inclusions are observed, which indicate high salinity of fluid (at least 25 wt% NaCl). The carbonate veins contain significant concentration of Na, which is highly incompatible mantle element. The variable concentration of Na (up to few hundred ppm) is expected in vein carbonate derived from magmatic activity. However, exceptionally high Na content of some samples may be attributed as a result of marine interaction. Other trace elements including HFSEs are too low (sub ppm) in their abundance and are very close to the detection limits. HFSEs are heavy nuclides elements and sparingly soluble in aqueous fluids. The distribution coefficients or solubility are too low for these elements to be incorporated and transported by the fluids unless in presence of specific carrier species in hydrothermal fluids, e.g. fluoride, phosphates and hydroxide etc (Wood, 1990; Haas et al., 1995) and at high temperature (Bau, 1991). Thus high HFSEs and REEs in hydrothermal solutions may suggest their origin under magmatic conditions in presence of suitable anionic carrier.

Though there are palpable mutual correlations observed that may have petrogenetic implications, but are not consistent across the different sections and are potentially may be doubtful as the concentrations are close to the detection limits of their determination.

However, some notable features are worth mentioning here that may have important implications.

The Sr, Sc, Hf, Y, U and Th shows excellent positive mutual correlation in carbonate samples of SLAP (NC and LMU sections of SLAP, see Figure 4.11 to 4.13). But are too scattered in case of PAP (Shergol, Zildat sections of PAP, see Figure 4.14). In particular, these correlations are more prominent in case of SLAP. The tectonic set-up of PAP is markedly different from the SLAP. This suggests a progressive development through ongoing mantle magmatic processes at the source region from which these fluids were derived or are fractionated en-route to final emplacement. In other words, the vein calcites consists of early formed veins with more pristine source signatures as well as later fractionates including marine interaction.

Strontium (Sr) content of these vein calcites widely varies from as low as <100ppm to as high as >1500 ppm. Sr content of the calcites may be used as an index of fractionation. The Sr is likely to be incorporated more in early formed calcites and the residual fluid become progressively depleted in Sr content and later fractionates of the vein calcites become depleted in Sr. normally diagenetic carbonates are depleted in Sr (Banner, 1995) content (<200 ppm). However, high Sr content of the vein calcite discounts the possibilities of being derived locally through diagenetic or low grade metamorphism.

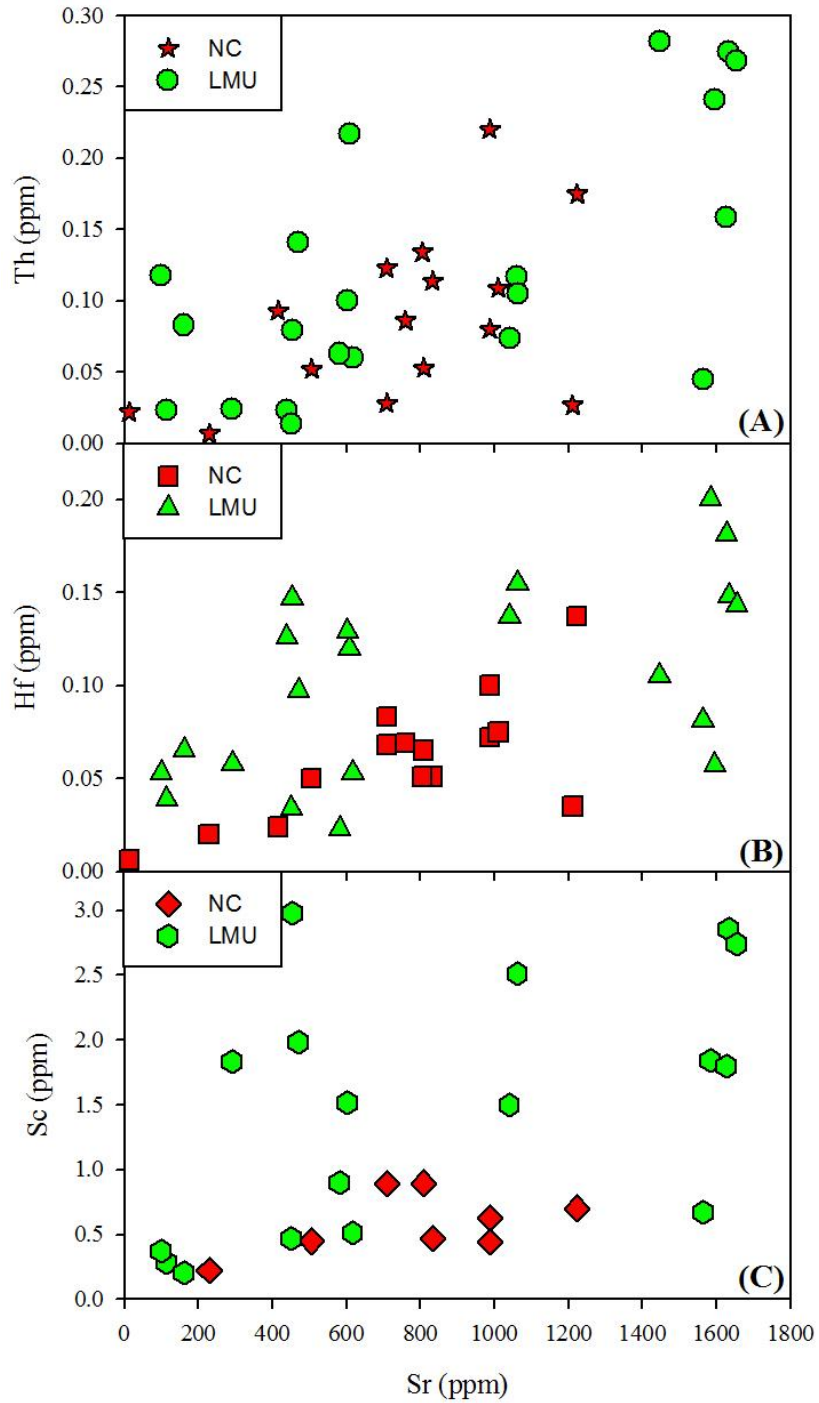


Figure 4.11: Trace element plots of SLAP with Sr concentration. (A) Sr vs Th, (B) Sr vs Hf, and (C) Sr vs Sc.

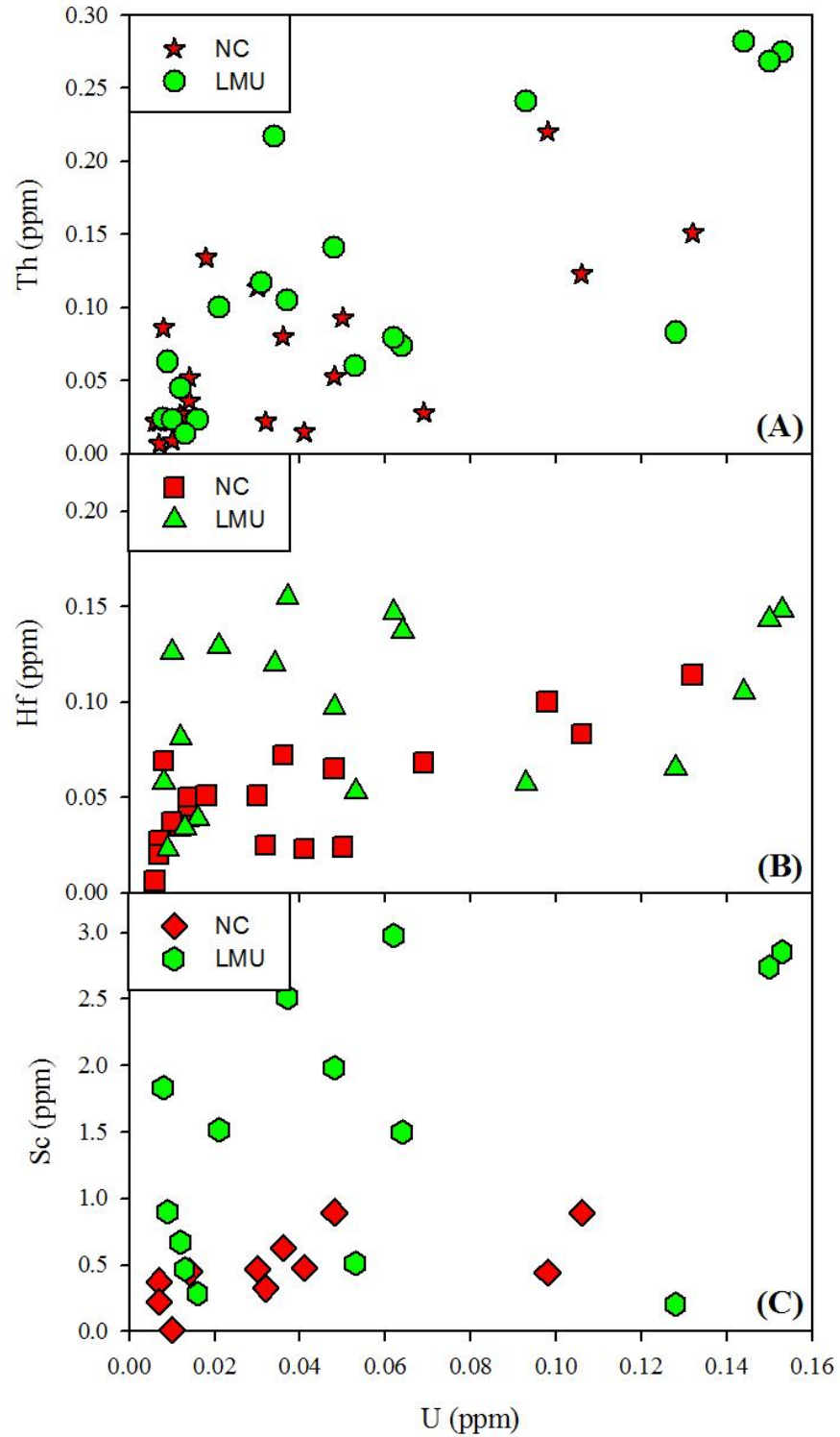


Figure 4.12: Trace element plots of SLAP with U concentration. (A) U vs Th, (B) U vs Hf, and (C) U vs Sc.

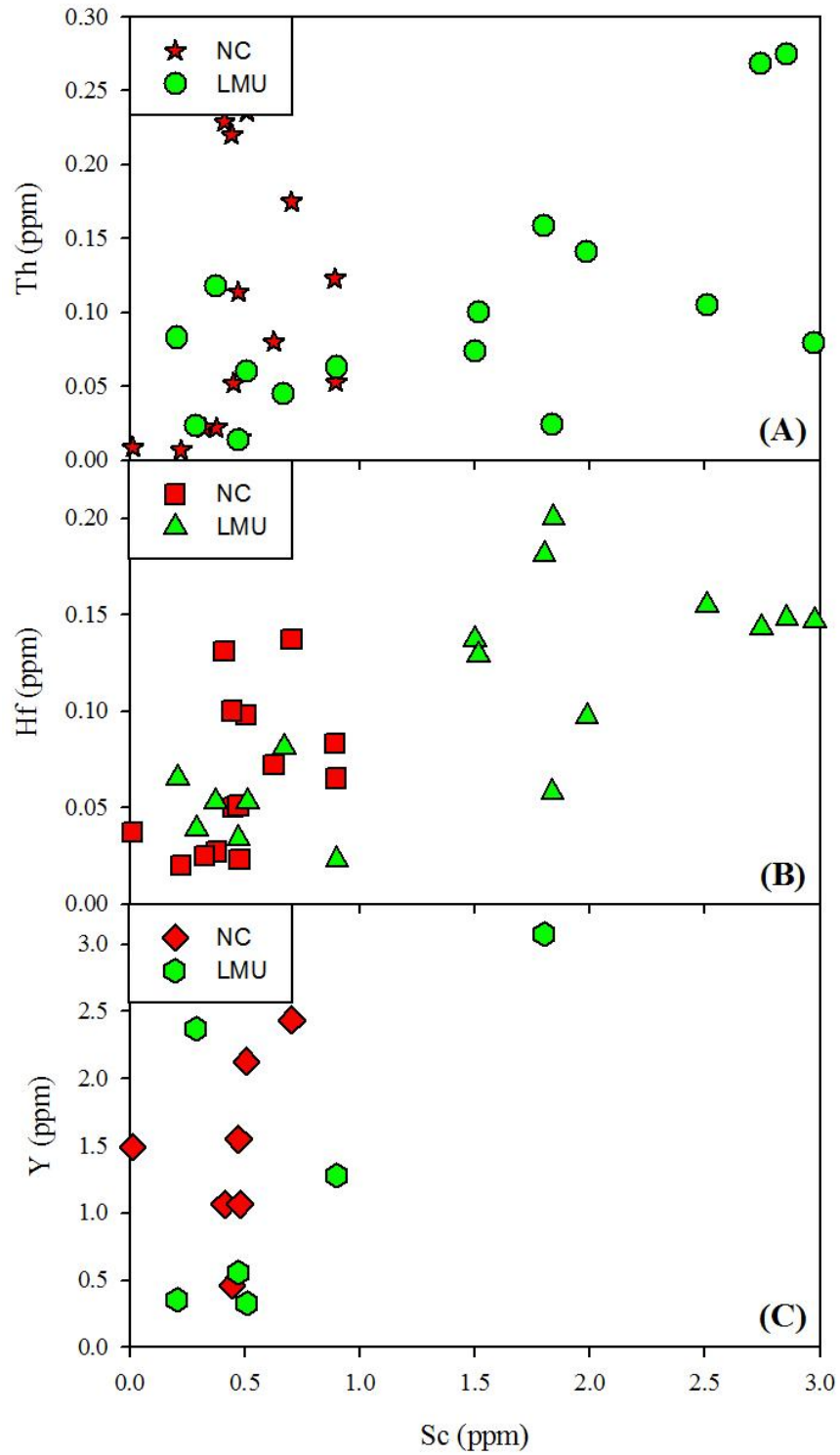


Figure 4.13: Trace element plots of SLAP with Sc concentration. (A) Sc vs Th, (B) Sc vs Hf, and (C) Sc vs Y.

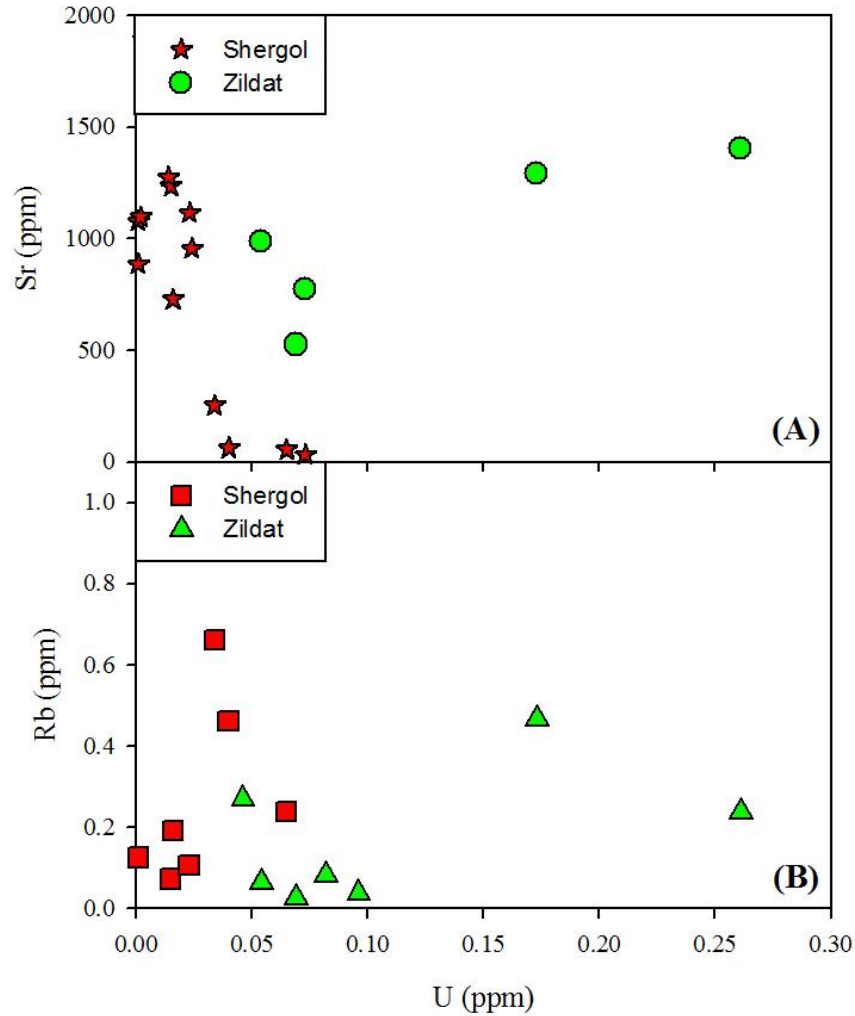


Figure 4.14: Trace element plots of PAP with U concentration. (A) U vs Sr, and (B) U vs Rb.

The above observations are consistent with the oxygen isotopic studies where these samples plot on oxygen isotopic fractionation trends. Several parallel trends in this diagram may suggest different pulses of the fluid generation with different initial isotopic compositions and were fractionated as a function of temperature.

REE Geochemistry of Co-paired quartz and calcite minerals:

The ionic radii of REEs vary from 0.93°A (Lu) to 1.15°A (La) and they commonly occur in +3 oxidation state in nature. The ionic radius of Ca²⁺ is 0.99°A, which is very close to that of the REEs (within 15%) in particular to the MREEs having a charge difference of only one. On the other hand, the ionic radius of Silicon (0.41°A) is much smaller than the REEs. It is therefore obvious that REEs can likely be found in Ca-carbonate phase as substitution in notable amount but are unlikely to be incorporated in quartz and can only be incorporated as structural defects. The distribution coefficient for REEs between calcite and quartz (CC/Qtz) is, therefore, very high and are of the order of >40-100, suggesting their very strong preference to calcite phase in relation to quartz. It is worthwhile to mention that the partition coefficients for CC/Qtz are much higher for MREEs compared to the HREEs and LREEs (Table 4.3). This is in general agreement with the fact that due to similar ionic radii of Ca and MREEs the MREEs are more readily incorporated compared to other REEs.

The REE pattern of quartz and calcite minerals from all four studied sections are shows high LREE and Low HREE or nearly flat REE pattern with positive (+ ve) Eu anomaly, which indicate relatively reducing environment of fluid source, i.e. mantle magmatic system, where Eu²⁺ is more readily incorporated in calcite compared to other REEs in +3 state, giving rise to +ve Eu anomaly. The REE of co-existing quartz and calcite minerals were analyzed separately and when compared on pair basis, it shows high distribution coefficient (>40) of REEs for calcite/quartz (see table 4.3 and Figure 4.15, 4.16); irrespective of net REE budget of the initial hydrothermal solution.

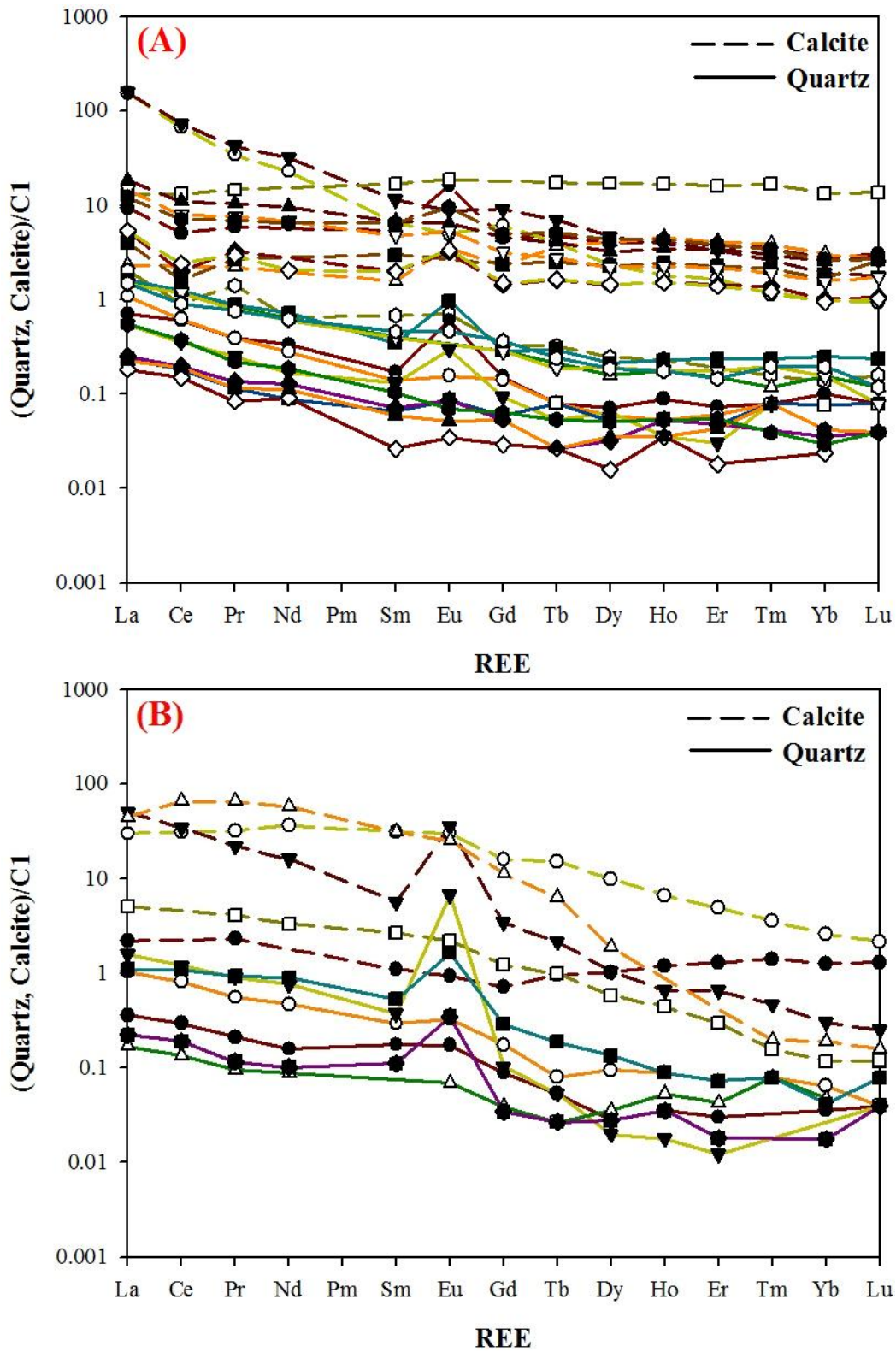


Figure 4.15: Co-paired Quartz and Calcite vein REE plots of PAP. (A) Represent the data set of Shergol area, (B) Shows the REE trend of Zildat section.

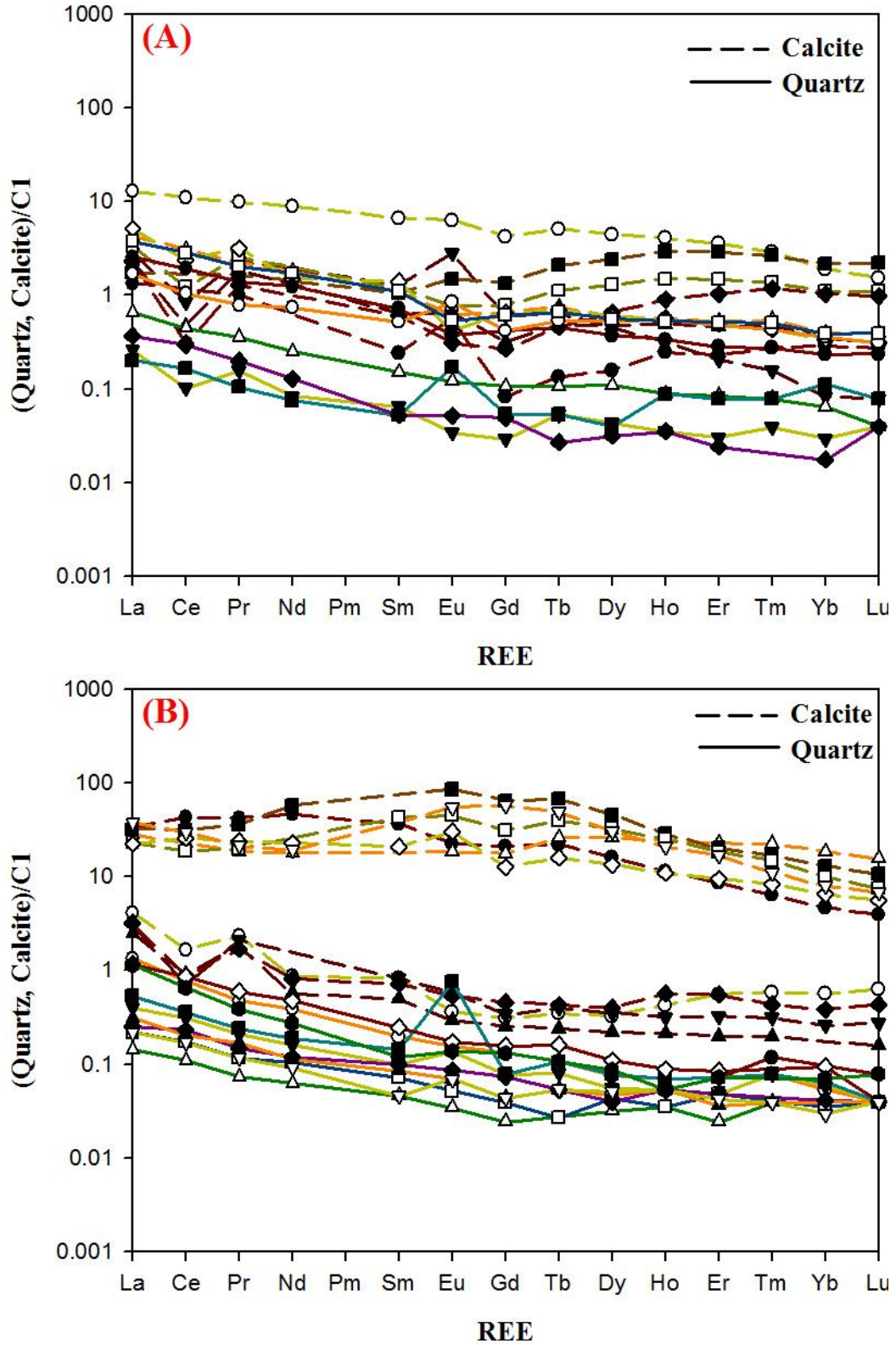


Figure 4.16: Co-paired Quartz and Calcite vein REE plots of SLAP. (A) Represent the data set of NC section, (B) Shows the REE trend of LMU section.

The co-paired quartz and calcite minerals pair of PAP and SLAP (Figure 4.15 and 4.16) reveal Eu^{+ve} anomaly with primitive mantle like REE pattern (high LREE and low HREE or flat REE pattern). The majority of the REE pattern in carbonate phase lacks fractionated crustal signature, e.g. negative (-Ve) Eu anomaly or high (La)_N/(Lu)_N value. The distribution coefficient for REEs between carbonate and silicate (CC/Qtz) is very high and are of the order of >40 to as high as >100 magnitude (table 4.3), suggesting their very strong preference to carbonate phase in relation to quartz. These results are consistent with the experimental results for magmatic siliceous-carbonate immiscibility system by Martin et al (2013) under water saturated conditions.

Table 4.3: Distribution coefficient (K_D CC/Qtz) of REEs between calcite and quartz.

Average distribution coefficient for REEs (Calcite/Quartz)													
<i>La</i>	<i>Ce</i>	<i>Pr</i>	<i>Nd</i>	<i>Sm</i>	<i>Eu</i>	<i>Gd</i>	<i>Tb</i>	<i>Dy</i>	<i>Ho</i>	<i>Er</i>	<i>Tm</i>	<i>Yb</i>	<i>Lu</i>
48	46	62	64	131	102	93	123	103	95	88	52	61	54

The Eu/Eu* values of all four studied sections are mostly around unity, suggesting very little Eu fractionation with respect to other REEs and most of Eu species were in it 3+ state. Further, the absences of Eu anomaly in conjunction with presence of Ce negative anomaly in many samples indicate a more oxidizing condition for the derivation of the fluid from its source. In this context, the negative Ce anomaly is typical of marine fluids (Lottermoser, 1992) and its presence in some samples may suggest interaction with marine components.

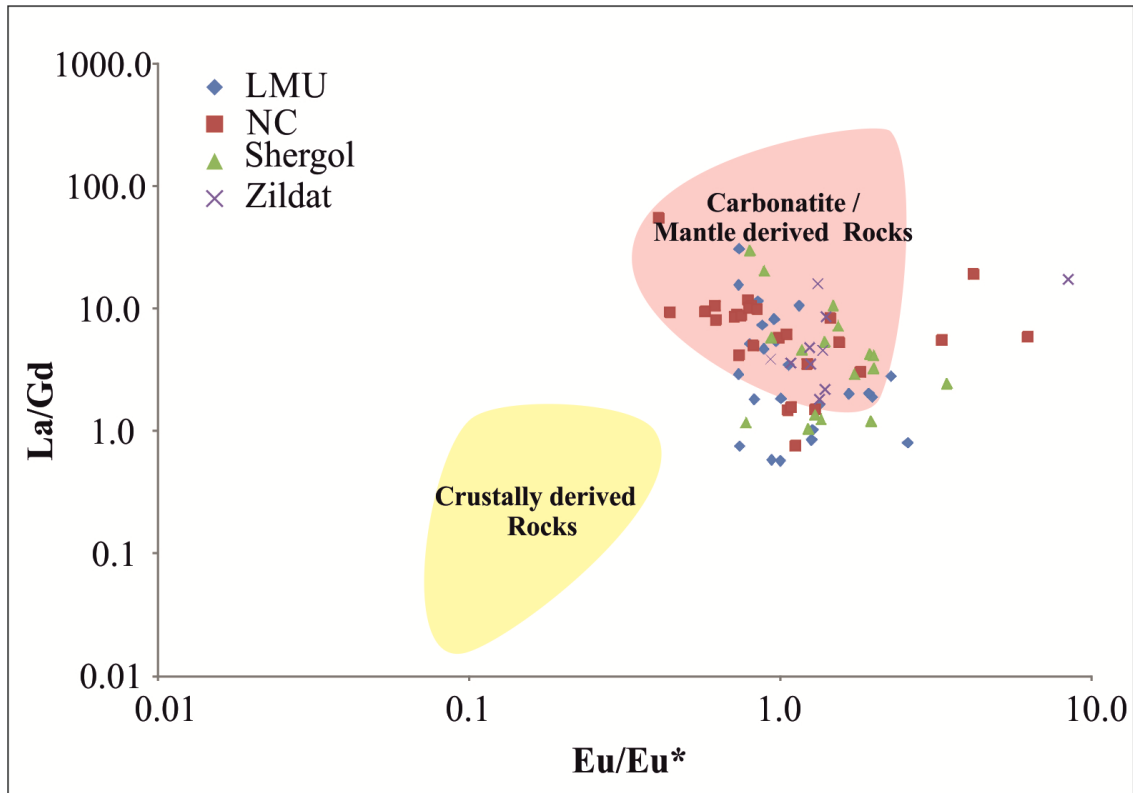


Figure 4.17: Bi-variant plot of La/Gd vs Eu/Eu^* .

The LREE/MREE is a good measure of extent of REE fractionation and their origin (crustal versus mantle). Similarly, Eu/Eu^* is also useful indicator of source that is plagioclase bearing (Crustal) or plagioclase free (Mantle) from which the fluids are derived (Castor and Hedrick, 2006). The bi-variant plot of La/Gd with Eu/Eu^* is illustrated in figure 4.17, where La and Gd represents LREE and MREE, respectively. It may be noted that the vein carbonate samples from the study area plot well with the magmatic carbonatite field. It is inferred that many of the veins are derived from deeper mantle like magmatic systems. But there crustal/marine affinity is too low or negligible, although their interaction cannot deny completely.

4.2.2 ISOTOPE GEOCHEMISTRY IN CARBONATE PHASE

The isotope geochemistry of carbonate phase from all four studied sections is summarized here, which include stable and radiogenic isotope geochemistry. The stable C and O isotope compositions are susceptible to primary and secondary geological processes and are fractionated leaving imprints of the operative process. However, they leave distinct signature of source from which they are originated and is traceable if the nature of interaction process is precisely known. This is often very different to know or assume the original C and O isotopic ratio of the fluid, rendering the inferences as tentative or plausible only. On the other hand, the heavier nuclide isotopic ratios are relatively insensitive to even extreme geological process and therefore, preserve the signature of the source, unless it is contaminated or assimilated. The radiogenic isotope geochemistry of Sr and Pb were also carried out together with the stable isotopic signatures to constrain the fluid source of vein carbonates.

4.2.2.1 $\delta^{13}\text{C}$ AND $\delta^{18}\text{O}$ OF CALCITE

The stable isotopic results of C ($\delta^{13}\text{C}$) and O ($\delta^{18}\text{O}$) are conventionally reported in V-PDB and V-SMOW, respectively and the range of the values obtained for different sections are summarized in table 4.4 (see results of each sample in the appendix C). The $\delta^{13}\text{C}$ values of calcite veins from the Shergol (paleo accretionary prism) varies in range from -7.5 to 1.3‰ VPDB (Figure 4.18a), whereas the $\delta^{18}\text{O}$ values are in the range of 12‰ to 19‰ VSMOW (Figure 4.18b).

Table 4.4: Stable C and O isotopic distributions of calcite veins from LAP.

	Shergol	NC	LMU	Zildat
$\delta^{13}\text{C}$ ‰ (VPDB) ± 0.1 ‰	-7.5 to +1.3	-14 to -1	-13 to -8	-2 to +2
$\delta^{18}\text{O}$ ‰ (VSMOW) ± 0.2 ‰	+12 to +19	+5.8 to +20	+8 to +19	+14.2 to +21.8

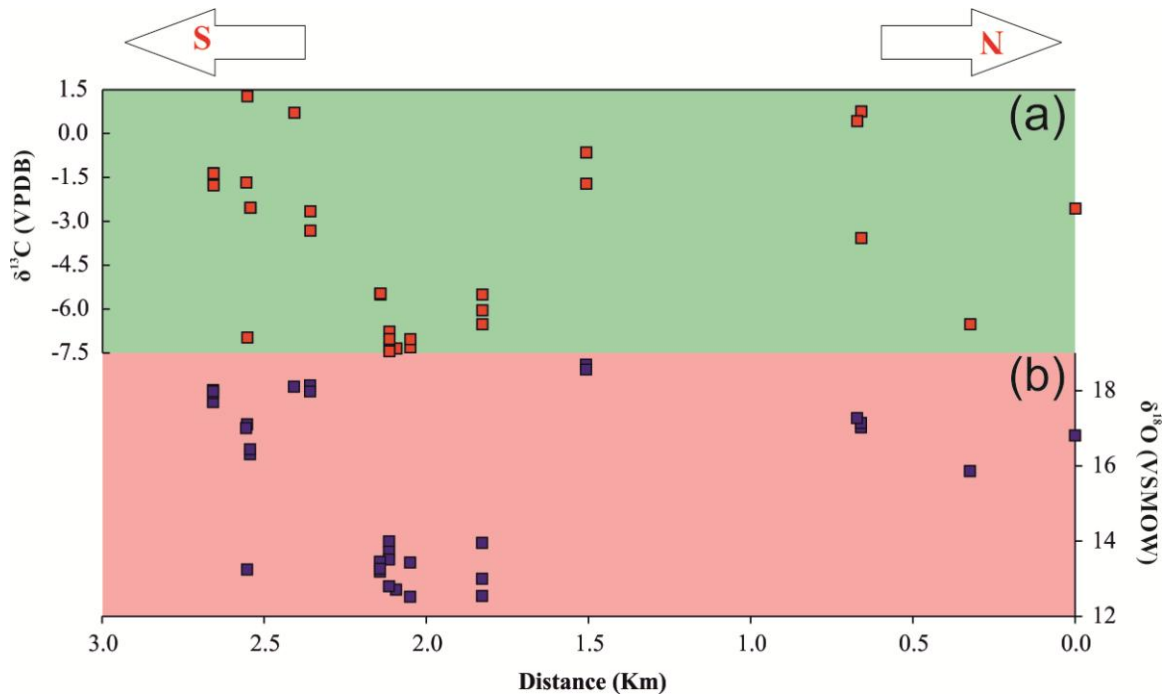


Figure 4.18: Stable C and O isotopic distribution of vein calcite from Shergol section. (a) Systematic distribution of $\delta^{13}\text{C}$, and (b) Systematic distribution of $\delta^{18}\text{O}$.

The $\delta^{13}\text{C}$ values of calcite veins from NC section (North ward section of SLAP) vary in range of -14‰ to -1‰ (Figure 4.19a). Where the $\delta^{18}\text{O}$ values of calcite veins are lie in the range of 5.8‰ to 20‰ (Figure 4.19b).

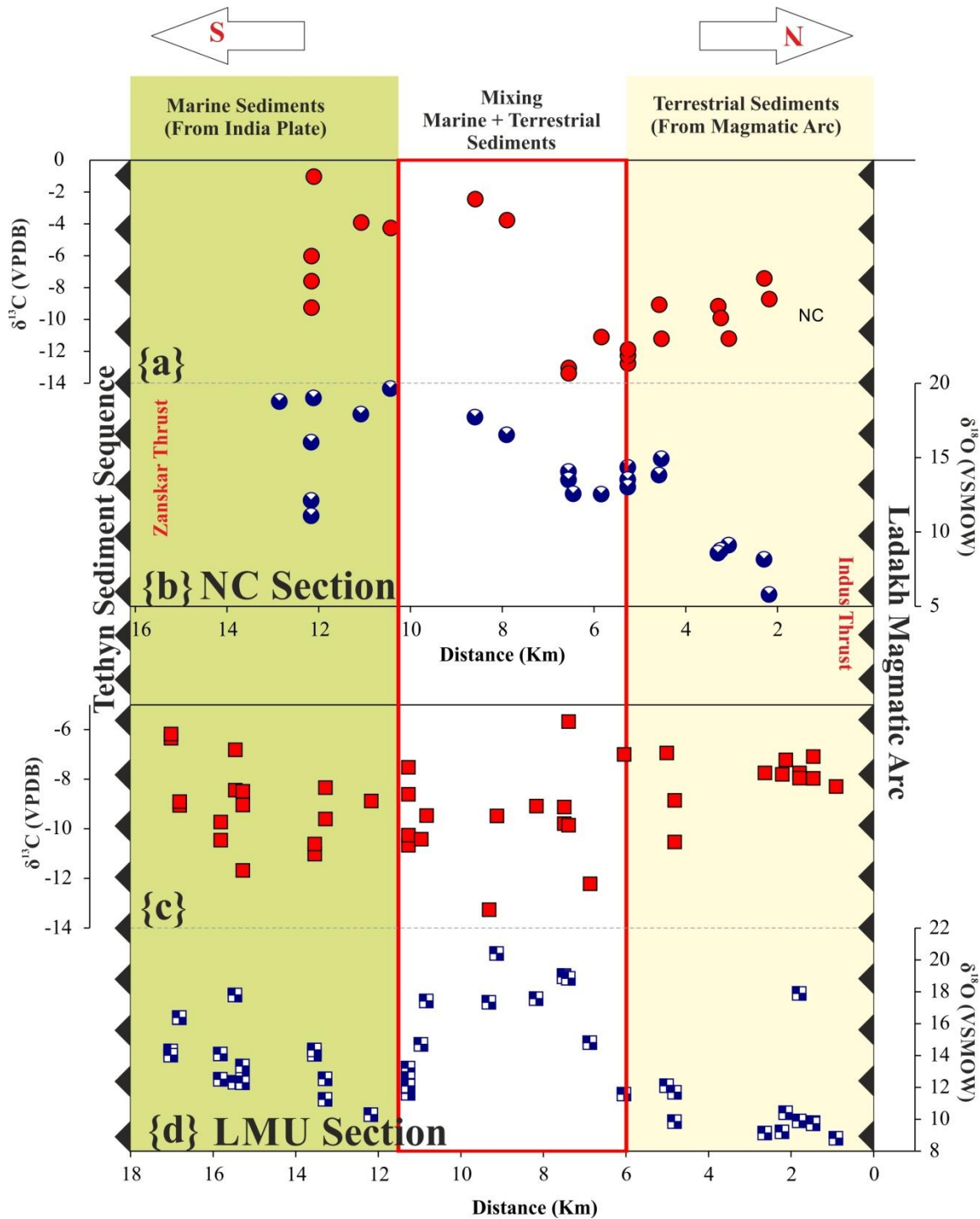


Figure 4.19: Stable C and O isotopic distribution of calcite veins between two (Indus and Zanskar) thrust in NC and LMU sections of South Ladakh Accretionary Prism (SLAP). (a) Systematic distribution of $\delta^{13}\text{C}$ in NC Section, (b) Systematic distribution of $\delta^{18}\text{O}$ in NC Section, (c) Systematic distribution of $\delta^{13}\text{C}$ in LMU Section, and (d) Systematic distribution of $\delta^{18}\text{O}$ in LMU Section.

The stable isotopic composition of vein calcite from LMU section (Middle section of SLAP) varies from -11.0 to -8‰ in $\delta^{13}\text{C}$ (Figure 4.19c) having $\delta^{18}\text{O}$ values in the range from 8.0‰ to 19‰ (Figure 4.19d). As Shown in figure 4.19, the $\delta^{13}\text{C}$ and $\delta^{18}\text{O}$ values of vein calcite are depleted near the Indus Thrust in terrestrial sedimentary setting, whereas the $\delta^{13}\text{C}$ and $\delta^{18}\text{O}$ values were enriched in the marine deposits (where the nummulitic limestone is also present) towards the Zanskar thrust. On the other hand, there is no such type of isotopic trend observed in $\delta^{13}\text{C}$ of LMU section from terrestrial to marine sediment deposits. But there is a very little isotopic dissimilarity in $\delta^{18}\text{O}$ of LMU section, which is enriched towards the marine setting from the terrestrial deposition.

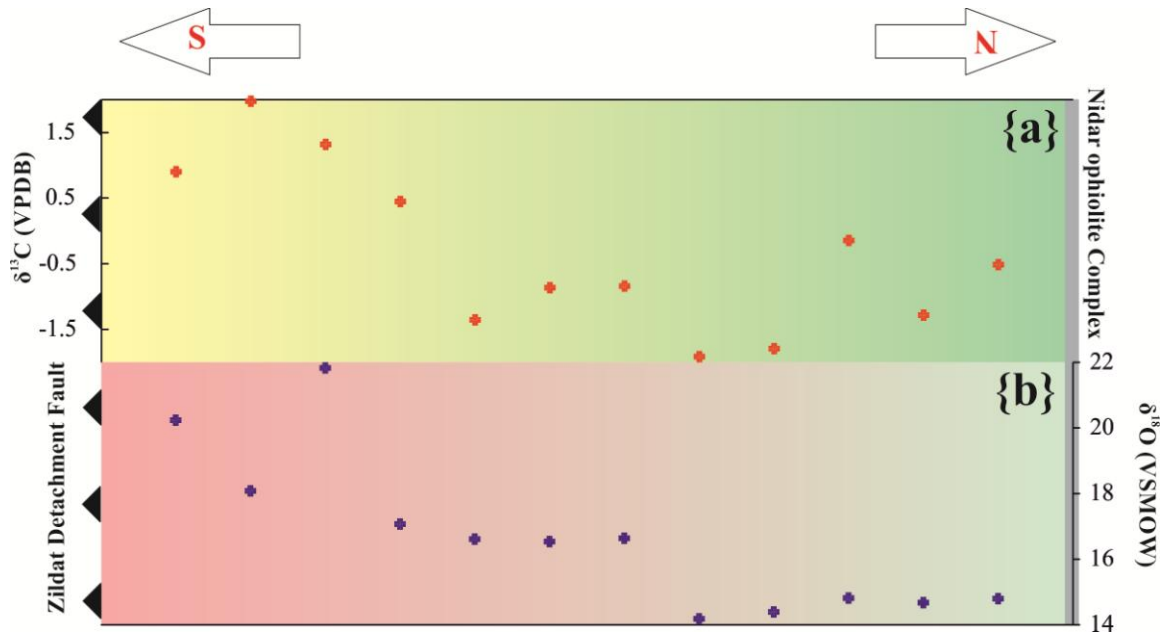


Figure 4.20: Systematic Stable C and O isotopic distribution of calcite veins between Zildat Detachment Fault (ZDF) and Nidar Ophiolite Complex (NOC) in Zildat section of PAP.

The $\delta^{13}\text{C}$ values of calcite veins from the Zildat area (Southern section of SLAP) vary in the range of -2‰ to 2.0‰ (Figure 4.20a), whereas $\delta^{18}\text{O}$ values are in the range of 14.2‰ to 21.8‰ (Figure 4.20b). As shown in the figure 4.20, the $\delta^{13}\text{C}$ and $\delta^{18}\text{O}$ values of vein calcite in Zildat section are relatively enriched near to the Zildat detachment fault (ZDF) and are depleted towards the Nidar Ophiolite Complex (NOC).

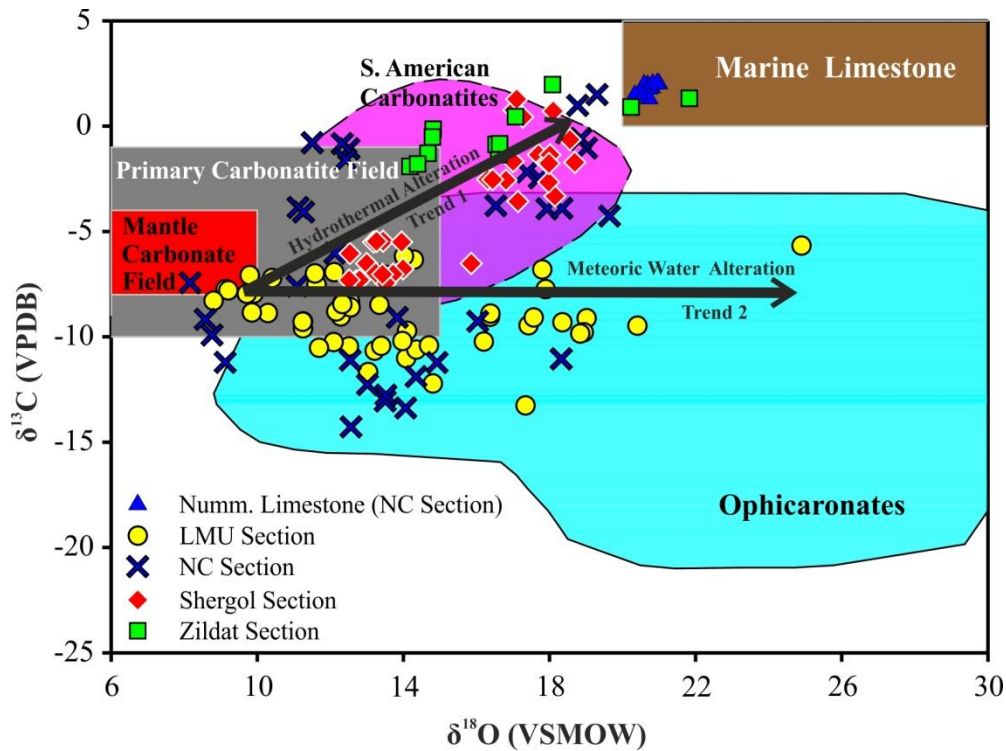


Figure 4.21: Two Isotope $\delta^{13}\text{C}$ and $\delta^{18}\text{O}$ plot of calcite veins from the Ladakh Accretionary Prism. Data Source for Mantle Carbonate Field (Taylor et al., 1967); Primary Carbonatite field (Ray and Ramesh, 2006); Ophicarbonates (Perkins et al., 2006); South American carbonatite (Bell and Simonetti, 2010).

To understand the stable isotopic systematics and trace the source of vein fluid of these studied section; the C and O isotopic compositions are plotted against each other (Figure 4.21) showing two discernible trends of the data plot. In this bi-variant plot most of the

data lies in the Primary carbonatite Field (Plyusnin et al., 1980; Deines, 1989; Ray and Ramesh, 2006) or mantle carbonate field (Taylor et al., 1967) with a sizeable number also plotted within ophicarbonatite field (Perkins et al., 2006). However, only an insignificant number of vein carbonate samples are plotted with the marine limestone field but are co-linear to the hydrothermal alteration trend (Trend-1) which is drawn through the South American Carbonatite compositional field (Bell and Simonetti, 2010). The implications of these results shall be discussed in a latter section of this chapter (section 4.3).

4.2.2.2 $^{87}\text{Sr}/^{86}\text{Sr}$ RATIO OF CALCITE

There are some ambiguity still remaining in spite of a good insight into the genesis of the fluids of the veins in LAP through the stable isotopic systematics of the vein calcites and quartz. The fluid source was not so clear through the study of the stable C and O isotopes as these isotopic ratios were probably fractionated at low temperatures. The atomic mass of Sr is much heavier than the C and O. Due to its heavy atomic mass the Sr isotopes are not easily fractionated by the geological processes and retain their original signatures. Therefore, $^{87}\text{Sr}/^{86}\text{Sr}$ is regarded as a good proxy to trace the fluid source and was aptly used in the present study. The Sr isotopic values of all studied sections are summarized in table 4.5. The Sr isotopic composition, in terms of $^{87}\text{Sr}/^{86}\text{Sr}$ ratios, of calcite veins from the South Ladakh Accretionary Prism (SLAP) vary from 0.7050 to 0.7095 in NC section (Figure 4.22a) while that of the of LMU section are in the range of 0.7060 to 0.7102 (Figure 4.22b). A distinct and systematic spatial variation is observed with $^{87}\text{Sr}/^{86}\text{Sr}$ values increasing southward. As shown in figure 4.22, the Sr isotopic composition near

to the Indus Thrust at the northern margin are depleted and ranges between 0.7050 and 0.7077 within the terrestrial sedimentary setting from SLAP (NC and LMU sections).

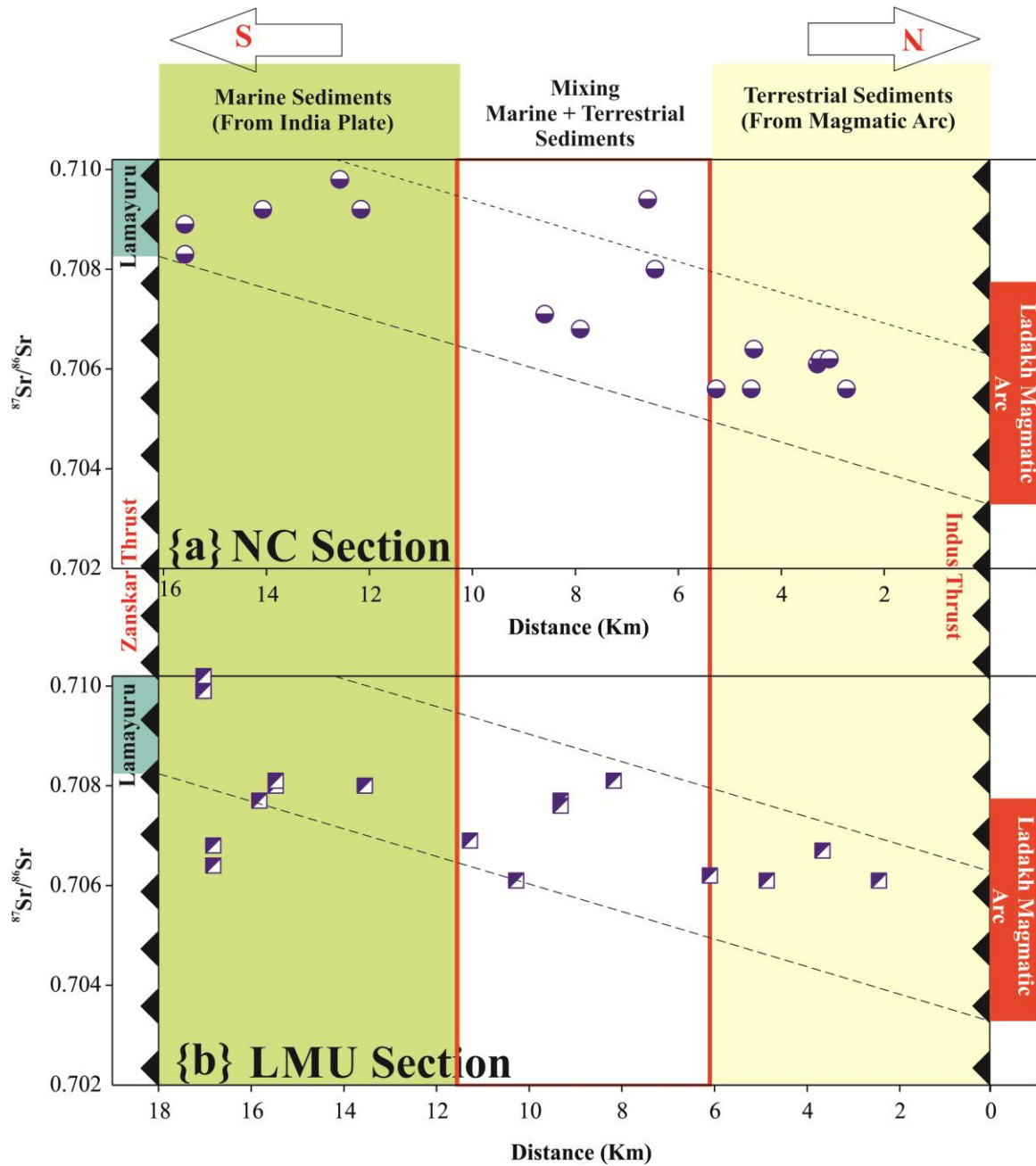


Figure 4.22: Distribution of $^{87}\text{Sr}/^{86}\text{Sr}$ ratio between two (Indus and Zanskar) thrust in NC and LMU sections of SLAP. (a) Systematic distribution of $^{87}\text{Sr}/^{86}\text{Sr}$ in NC Section, and (b) Systematic distribution of $^{87}\text{Sr}/^{86}\text{Sr}$ in LMU Section. Data source for Ladakh Magmatic arc is Honegger et al., 1982; Weinberg and Dunlap, 2000.

Notable these values in turn, are found to be similar to the reported Sr isotopic values of the rocks of Ladakh Magmatic Arc (Honegger et al., 1982; Weinberg and Dunlap, 2000). On the other hand, the Sr isotopic compositions of vein calcite are found to be enriched towards the Zaskar thrust (southern Margin) with the values ranging from 0.7080 to as high as 0.7102, for the veins occurring within the marine sedimentary setting. In order to compare this, few samples from the carbonate rocks of the marine Lamayuru formation in the proximity were also investigated which yielded similar high Sr isotopic compositions (0.7085 to 0.7105).

Table 4.5: Distribution of $^{87}\text{Sr}/^{86}\text{Sr}$ ratio in calcite veins from NC and LMU sections of SLAP.

	Shergol	NC	LMU	Zildat
$^{87}\text{Sr}/^{86}\text{Sr}$ ± 0.00003	–	0.7050 to 0.7095	0.7060 to 0.7102	–

4.2.2.3 LEAD ISOTOPIC RATIO OF CALCITE

The lead isotopic measurements were initially carried out to determine the age of carbonate veins. However, the isotopic results of veins from same lithounites were too tightly clustered to be used for geochronological purpose and could not be used for determination of age of these vein calcites. Nevertheless, the lead isotopic systematics is also a powerful tool and has been used to trace the fluid source. The results are utilized here to constrain the fluid source. The results of Pb isotopic systematics of vein calcite are presented in this section, which include ratios of $^{208}\text{Pb}/^{204}\text{Pb}$, $^{207}\text{Pb}/^{204}\text{Pb}$ and

$^{206}\text{Pb}/^{204}\text{Pb}$. The Pb isotopic ratios of vein calcites from each individual section do not vary much and are tightly clustered suggesting that these are not fractionated and are supposed to bear its source signatures. It is considered to be very powerful proxy to trace the source of fluid in the formation of veins. The Pb isotopic compositions of all four studied sections are summarized in the table 4.6.

Table 4.6: Stable C and O isotopic distribution of vein calcite from the Ladakh Accretionary Prism.

	Shergol	NC	LMU	Zildat
$^{208}\text{Pb}/^{204}\text{Pb}$ ± 0.005	38.788 to 39.160	38.831 to 39.037	38.972 to 39.222	40.037 to 40.180
$^{207}\text{Pb}/^{204}\text{Pb}$ ± 0.002	15.485 to 15.703	15.640 to 15.681	15.665 to 15.715	15.665 to 15.701
$^{206}\text{Pb}/^{204}\text{Pb}$ ± 0.002	18.303 to 18.757	18.578 to 18.663	18.644 to 18.754	20.072 to 20.722

Since the Pb and Sr isotopes are heavy nuclides and are least effected by secondary alterations, allowing them to be used as tracers from which these fluids are derived. A set of bi-variant plots are commonly used with various fields of potential sources marked on it for ready comparison. These binary plots of $^{87}\text{Sr}/^{86}\text{Sr}$ vs $^{206}\text{Pb}/^{204}\text{Pb}$, $^{208}\text{Pb}/^{204}\text{Pb}$ vs $^{206}\text{Pb}/^{204}\text{Pb}$, and $^{207}\text{Pb}/^{204}\text{Pb}$ vs $^{206}\text{Pb}/^{204}\text{Pb}$ are shown in figure 4.23.

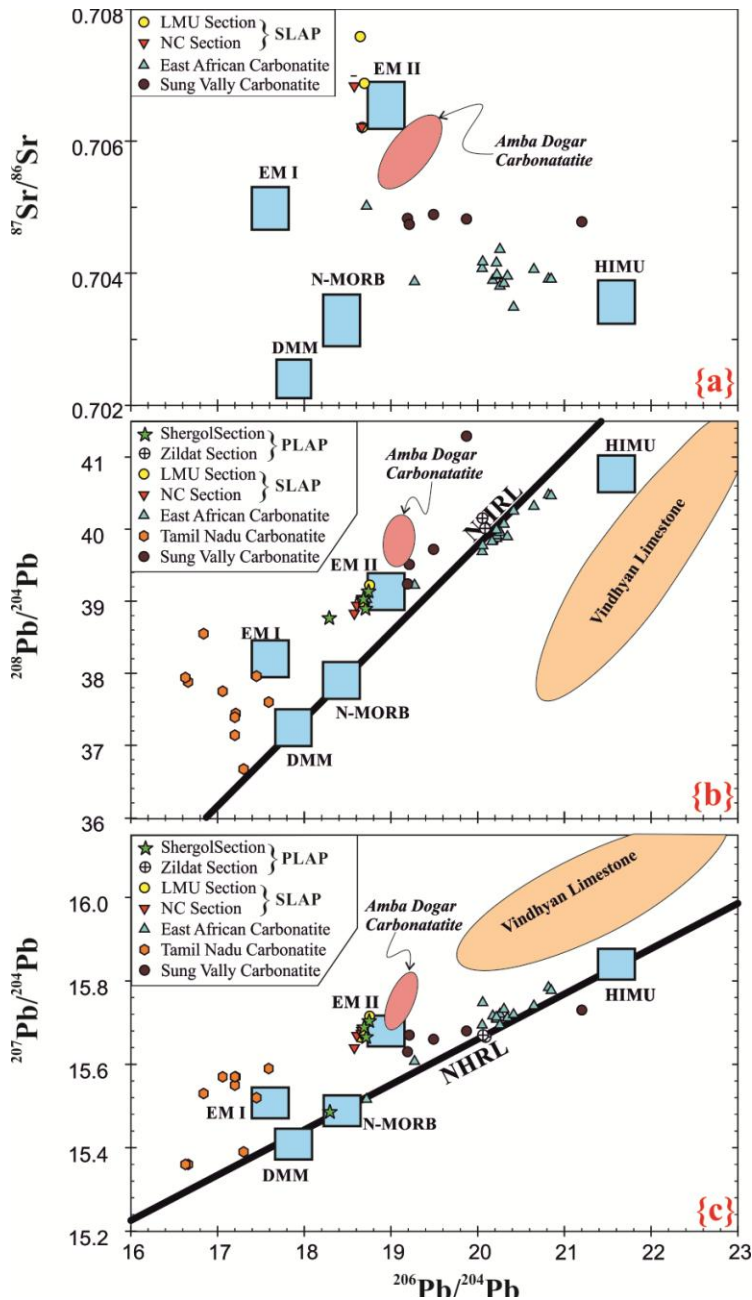


Figure 4.23: Bi-varient plots of a) $^{206}\text{Pb}/^{204}\text{Pb}$ vs $^{87}\text{Sr}/^{86}\text{Sr}$, b) $^{206}\text{Pb}/^{204}\text{Pb}$ vs $^{208}\text{Pb}/^{204}\text{Pb}$, and c) $^{206}\text{Pb}/^{204}\text{Pb}$ vs $^{207}\text{Pb}/^{204}\text{Pb}$ of LAP (all four studied sections). Data source for OIBs: N-MORB, normal MORB; EM I, Enrich Mantle I; EM II, Enrich Mantle II; DMM, Depleted MORB Mantle and HIMU, high U/Pb Mantle are Hart et al (1986); Hart (1988); NHRL, Northern Hemisphere Reference Line (Hart, 1984). Data source for carbonatites and limestone: AmbaDogar Carbonatites (Simonetti et al., 1995); East African Carbonatites (Kalt et al., 1997); Tamil Nadu Carbonatites (Schleicher et al., 1998); Sung Vally Carbonatites (Veena et al., 1998); and Vindhyan Limestones (Ray et al., 2003).

As shown in figure 4.23a, the vein calcites from Shergol, NC and LMU plot in the proximity of the Enriched Mantle II (EM II) field, which in turn are also close to the Amba Dongar Carbonatite compositional field (Simonetti et al., 1995). This is consistent in the Pb-Pb isotopic plots (Figure 4.23b and 4.23c) where Pb isotopic compositions of the vein calcites plot in the proximity of the Enriched Mantle II (EM II) field, while few samples plotted on the NHRL reference line.

The Pb-Pb isotope plots (Figure 4.23) show more close affinity of carbonate veins with Amba Dongar carbonatites rather than the East African carbonatites. However, the samples from Zildat section lies on NHRL reference line and are close to the East African carbonatite field (Kalt et al., 1997).

4.2.2.4 ISOTOPIC CORRELATIONS OF CALCITE

To integrate the results and inferences drawn from stable isotopic systematics of C and O and that of heavy nuclides including radio isotopic ratios, a combined plot was used to deduce the source affiliations of these vein fluids. The combined plot of two different isotopes can probably constrain our proxy more precisely.

The binary variation plots of $^{87}\text{Sr}/^{86}\text{Sr}$ with respect to $\delta^{18}\text{O}$, $\delta^{13}\text{C}$ and $^{206}\text{Pb}/^{204}\text{Pb}$ are shown in figures 4.24a, 4.24b and 4.23a, respectively. The bi-variant plots of $^{87}\text{Sr}/^{86}\text{Sr}$ vs $\delta^{18}\text{O}$ and $^{87}\text{Sr}/^{86}\text{Sr}$ vs $\delta^{13}\text{C}$ illustrate that $^{87}\text{Sr}/^{86}\text{Sr}$, most of the values for samples are well within mantle/magmatic field but $\delta^{13}\text{C}$ and $\delta^{18}\text{O}$ for few samples are shifted. In contrast,

$^{87}\text{Sr}/^{86}\text{Sr}$ values are enriched in few samples, especially those that occur within marine sediments. The high $^{87}\text{Sr}/^{86}\text{Sr}$ values vein samples in marine sediments having $\delta^{13}\text{C}$ and $\delta^{18}\text{O}$ values similar to the mantle/magmatic field. Therefore, enriched $^{87}\text{Sr}/^{86}\text{Sr}$ values do not lie in the marine field as well (see figure 4.24).

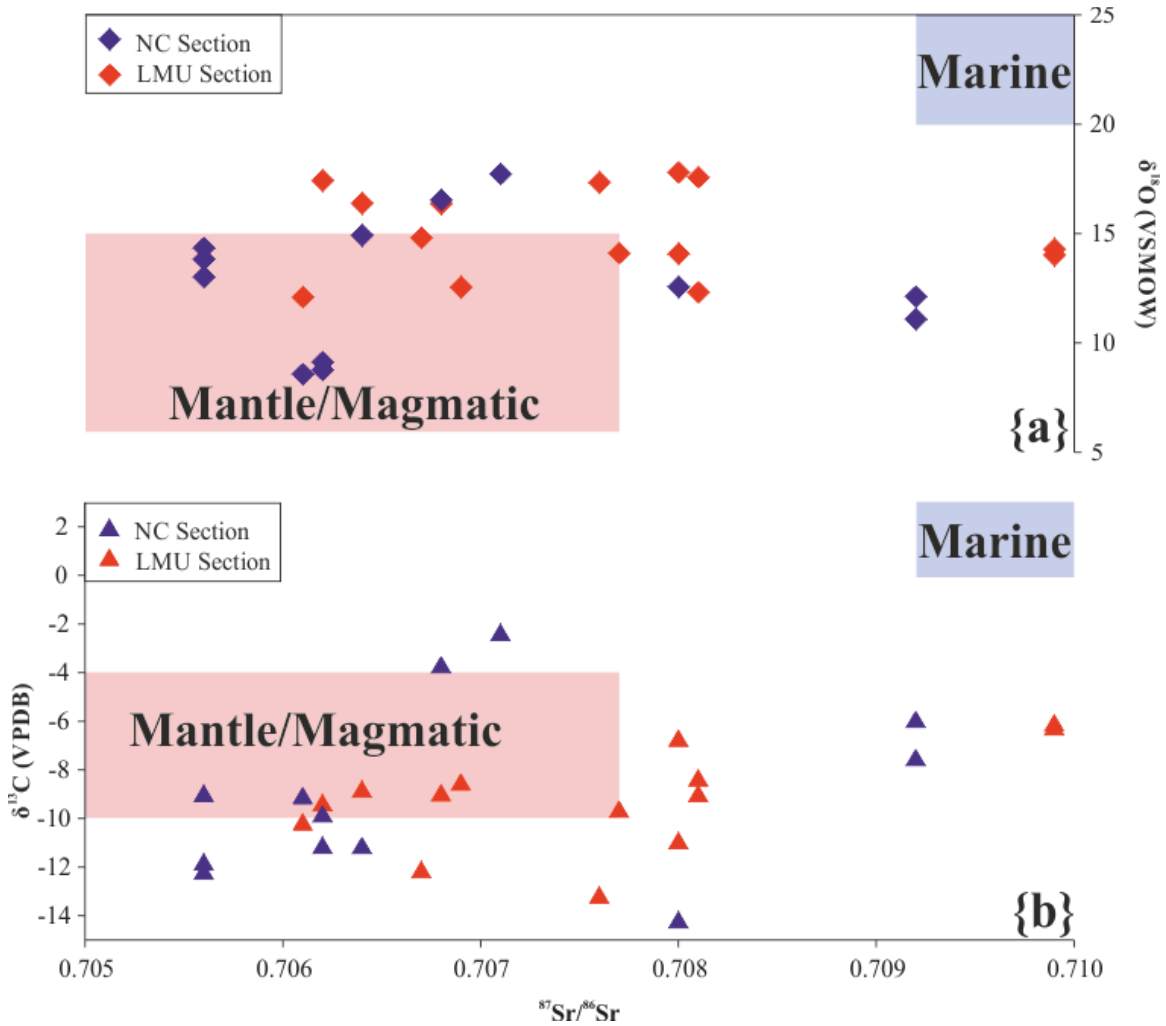


Figure 4.24 : Bi-variant plot of two isotopes in SLAP to trace the fluid source. (a) $^{87}\text{Sr}/^{86}\text{Sr}$ vs $\delta^{18}\text{O}$, and (b) $^{87}\text{Sr}/^{86}\text{Sr}$ vs $\delta^{13}\text{C}$. The Sr isotope value of Mantle/Magmatic field obtained from the Ladakh magmatic area.

4.2.3 ISOTOPE GEOCHEMISTRY IN SILICATE PHASE

The stable oxygen isotope geochemical results of quartz minerals from the veins are presented in this section, which are useful petrogenetic indicators for the source of vein fluid.

4.2.3.1 $\delta^{18}\text{O}$ OF QUARTZ

Determination of the stable oxygen isotope ratio ($\delta^{18}\text{O}$) of quartz or silicate phase is time taking cumbersome process as describe in section 4.1.2.2 of this chapter therefore, few represented quartz samples were analyzed for oxygen isotopic ($\delta^{18}\text{O}$) composition.

In addition to its petrogenetic importance, $\delta^{18}\text{O}$ of quartz and co-paired calcite together provides a very reliable crystallizing temperature and used as powerful thermometer. The $\delta^{18}\text{O}$ value in silicate phase of NC and LMU sections are very similar ranging from 13 to 23.4‰ and 12.9 to 21.9‰, respectively (see table 4.7).

Table 4.7: $\delta^{18}\text{O}$ Distribution of quartz veins from the South Ladakh Accretionary Prism.

	Shergol	NC	LMU	Zildat
$\delta^{18}\text{O}$ (VSMOW) $\pm 0.2\text{‰}$	–	13.0 to 23.4	12.9 to 21.9	–

As shown in figure 4.25, $\delta^{18}\text{O}$ value of the quartz is depleted at the northern and southern margins, i.e. near the Indus and Zansker thrusts, while it is enriched at the central part. Therefore the $\delta^{18}\text{O}$ value of quartz shows the bell shaped telling ends in both NC and

LMU sections; while in the central part of these sections the $\delta^{18}\text{O}$ value becomes more enriched (Figure 4.25).

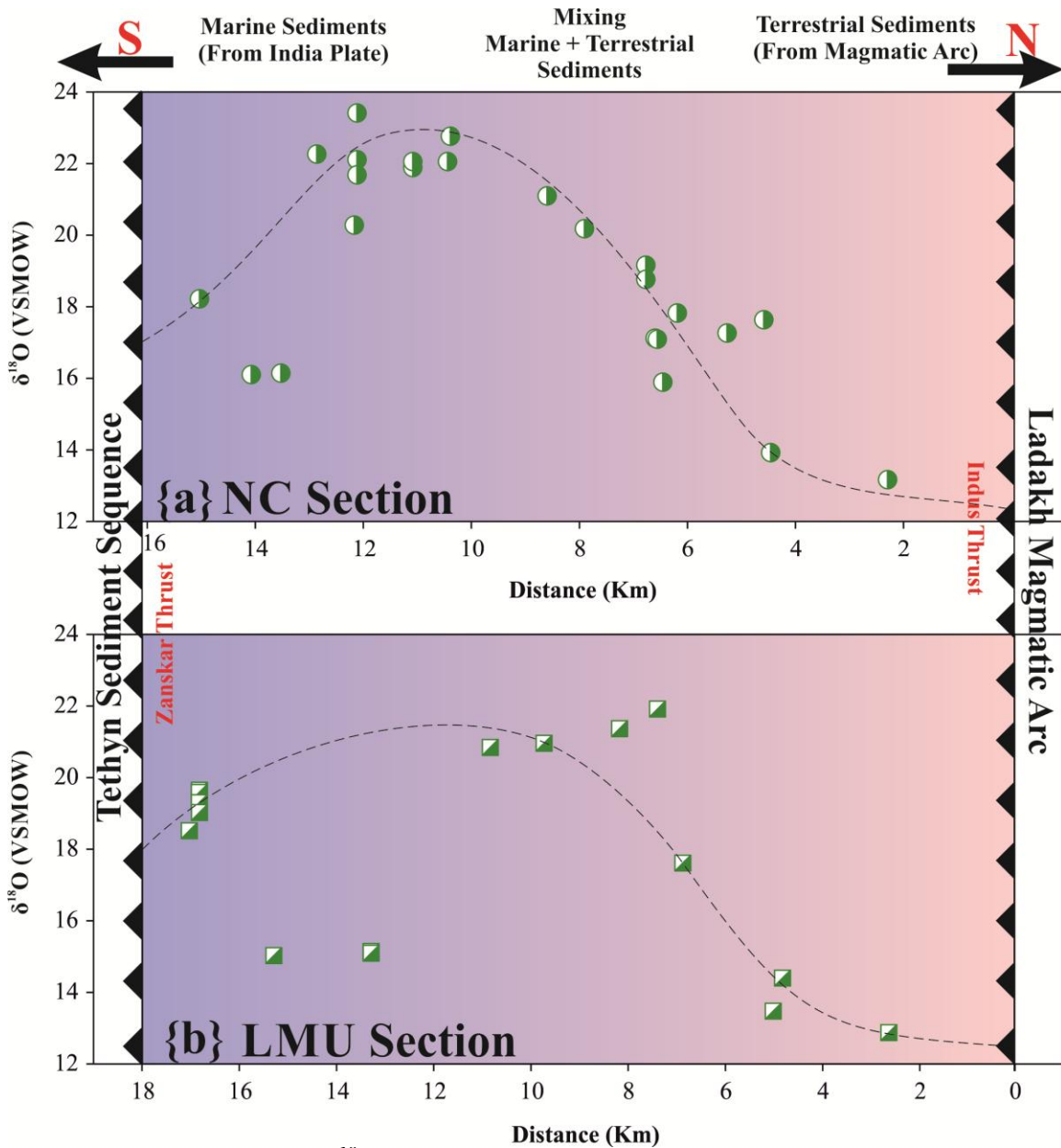


Figure 4.25: Systematic $\delta^{18}\text{O}$ distribution of quartz veins between two (Indus and Zanskar) thrusts in NC and LMU sections of SLAP. (a) Systematic distribution of $\delta^{18}\text{O}$ in NC Section, and (b) Systematic distribution of $\delta^{18}\text{O}$ in LMU Section.

4.2.3.2 OXYGEN ISOTOPE THERMOMETRY

Oxygen isotopic analyses of co-existing quartz–calcite mineral pair from two of the studied sections were used for thermometric applications. To implement this, pure mineral fractions were obtained by physical separation and chemical cleaning. The calcite minerals were analyzed by conventional Gas Bench (See section 4.1.2.1 for analytical technique) and while quartz grains were analyzed by Laser Fluorination technique as detailed in section 4.1.2.2.

Oxygen isotopic fraction in carbonate system is sensitive to temperature and is frequently used as thermometer. But this requires a crucial assumption of the oxygen isotopic composition of the original fluid from which the carbonate phase is precipitating, which is difficult to know. However, the fractionation of oxygen isotopes among coexisting minerals can be used as a geothermometer. When two oxygen bearing phases are in equilibrium (co-existing phases) and have precipitated from a common fluid, it is possible to estimate the temperature by solving the oxygen isotopic fractionation equation for the respective phases to get a unique temperature of equilibration or temperature of crystallization as was refined by Sharp and Krischner (1994) through experimental verification. It must be assumed that (i) the minerals were crystallized at the same time, (ii) were at equilibrium, and (iii) were not subsequently altered. In the present case the co-existing calcite-quartz were used for this purpose which can be assumed to be in equilibrium and thus application of co-existing mineral pair oxygen isotopic thermometry (Sharp and Krischner, 1994) would yield temperature of crystallization of the veins.

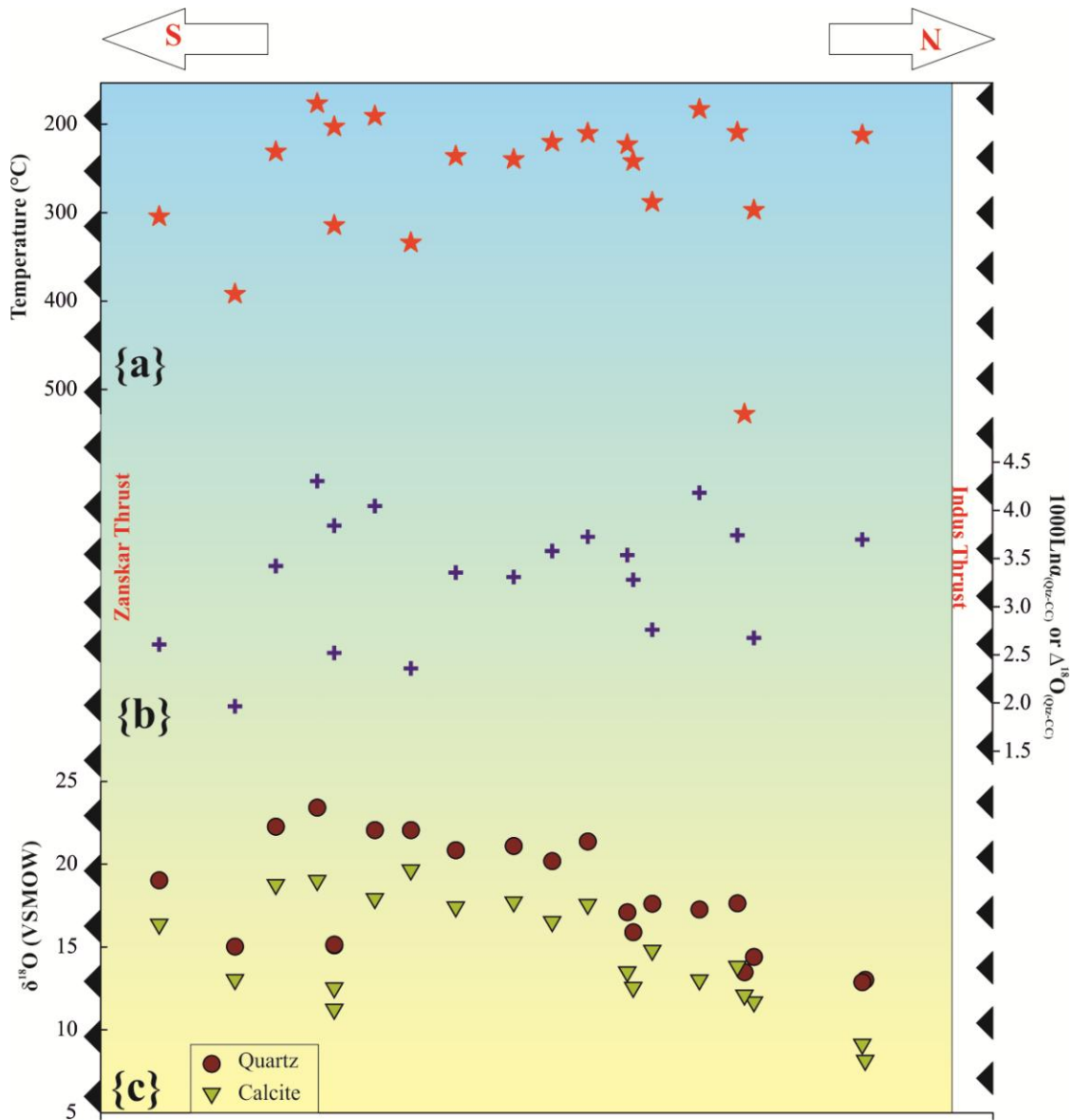


Figure 4.26: The crystallizing Temperature of veins from Indus to Zanskar thrust using oxygen isotope thermometry in NC and LMU sections of SLAP. (a) variation in crystallizing temperatures of veins between Indus and Zanskar thrust, (b) difference in $\delta^{18}\text{O}$ composition between two mineral (quartz and calcite) phase, and (c) Systematic distribution of $\delta^{18}\text{O}_{(\text{Qtz})}$ and $\delta^{18}\text{O}_{(\text{Calcite})}$ in NC and LMU Sections between Indus and Zanskar thrusts.

The crystallizing temperature of veins was estimated using the thermometric calibration equation (eqn no. 4.13) given by Sharp and Krischner (1994).

$$1000\ln\alpha_{(Qtz-calcite)} = 0.87 (\pm 0.06) \times 10^6 / T^2 \dots\dots\dots \text{Eqn. 4.13}$$

Where Temperature (T) in °K and

$$1000\ln\alpha_{(Qtz-calcite)} = \Delta^{18}O_{(Qtz-calcite)} = \delta^{18}O_{(Qtz)} - \delta^{18}O_{(calcite)} \dots\dots\dots \text{Eqn. 4.14}$$

The temperatures (T) thus obtained are in °K, which is further converted into °C and the results are summarized in Table 4.8.

Table 4.8: Crystalline Temperature of veins of NC and LMU sections using Oxygen Isotope Thermometry.

Sample No	$\delta^{18}O_{(Qtz)} \text{‰}$ (VSMOW)	$\delta^{18}O_{(Calcite)} \text{‰}$ (VSMOW)	$1000\ln\alpha_{(Qtz-Calcite)}$	$\Delta^{18}O_{(Qtz-Calcite)}$	T (°C)
NC12/8	15.8	13.1	2.7	2.7	295
NC/12/21	22.3	18.8	3.4	3.5	231
NC/12/23	23.4	19.0	4.3	4.4	176
NC/12/25	22.1	17.9	4.0	4.1	191
NC/12/26	22.1	19.6	2.4	2.4	334
NC/12/28	21.1	17.7	3.3	3.4	240
NC/12/29	20.2	16.5	3.6	3.6	220
NC12/31	17.1	13.5	3.6	3.6	220
NC/12/33	17.1	13.5	3.5	3.6	223
NC/12/35	15.9	12.6	3.3	3.3	242
NC12/36	17.8	13.5	4.3	4.4	177
NC/12/39	17.3	13.0	4.2	4.2	183
NC/12/45	17.6	13.8	3.7	3.8	209
NC/12/53	13.0	8.2	4.8	4.9	152
LMU/12/7	19.0	16.4	2.6	2.7	304
LMU/12/15	15.0	13.0	2.0	2.0	392
LMU/12/20-1	15.1	11.2	3.8	3.9	203
LMU/12/20-2	15.1	12.5	2.5	2.6	314
LMU/12/27	20.8	17.4	3.4	3.4	236
LMU/12/34	21.4	17.6	3.7	3.8	210

LMU/12/39	17.6	14.8	2.8	2.8	288
LMU/12/41	13.5	12.1	1.4	1.4	528
LMU/12/43	14.4	11.7	2.7	2.7	297
LMU/12/45	12.9	9.1	3.7	3.7	212

The oxygen isotope composition of co-existing quartz and calcite minerals along with their formation temperature are illustrated in figure 4.26, which reveals wide range of crystallizing temperature of veins ranging between 152°C and 528°C from two of the studied sections (LMU and NC).

4.2.4 $\delta^{18}\text{O}$ OF FLUID SPECIES

The oxygen isotopic composition of the fluids ($\delta^{18}\text{O}_{\text{fluid}}$) for the veins was calculated using the fractionation equation of quartz–water system (eq 4.15) and calcite–water system (eq 4.16) as given by Shiro and Sakai (1972) and O’Neil et al. (1969), respectively. In this case only those samples were used, for which oxygen isotopic composition known from analysis and temperature of formation is independently estimated. We used micro-thermometric homogenization temperatures obtained from fluid inclusion studies (see chapter 3) in conjunction with the $\delta^{18}\text{O}$ values of the same quartz and calcite samples to deduce the oxygen isotope ratio of fluid using the following equations-

Quartz–water fractionation equation derived by Shiro and Sakai (1972)

$$1000\ln\alpha_{(\text{Qtz-Water})} = 3.55 (10^6/T^2) - 2.57 \dots\dots\dots \text{Eqn. 4.15}$$

Calcite–water fractionation equation derived by O’Neil et al. (1969)

$$1000\ln\alpha_{(Calcite-Water)} = 2.78 (10^6/T^2) - 3.39 \dots\dots\dots \text{Eqn. 4.16}$$

Where, Temperature (T) is in °K.

The oxygen isotopic composition of vein forming fluids thus estimated was found to be in the range of $-7.0\text{‰}_{\text{VSMOW}}$ to $+15.9\text{‰}_{\text{VSMOW}}$ and the results are summarized in table 4.9. The individual oxygen isotopic compositions of fluid as a function of homogenization temperatures are illustrated in figure 4.27.

Table 4.9: Oxygen Isotope values of Fluid from LAP.

	Calcite	Quartz	
Homogenization Temperature (°C)	90 to 325	105 to 182	241 to 303
$\delta^{18}\text{O}_{(\text{Mineral})}\text{‰}$ (VSMOW)	10 to 21.8	15.3 to 15.7	
$\delta^{18}\text{O}_{(\text{fluid})}\text{‰}$ (VSMOW)	-4.6 to 15.9	-7.0 to 0.2	4.4 to 7.1

The bi–variant plot of homogenization temperature (measured from fluid inclusion thermometry) and $\delta^{18}\text{O}_{(\text{fluid})}$ depict a curvilinear trend in accordance with the equation 4.15 and 4.16. The estimated fluid compositions plotting mostly within the Mantle fluid fields with some fluids trends plot in the intermediate zone between mantle and marine hydrothermal compositional fields or is encompassed by the ophicarbonatite field (i.e. altered fluid from mantle related rocks) as shown in figure 4.27.

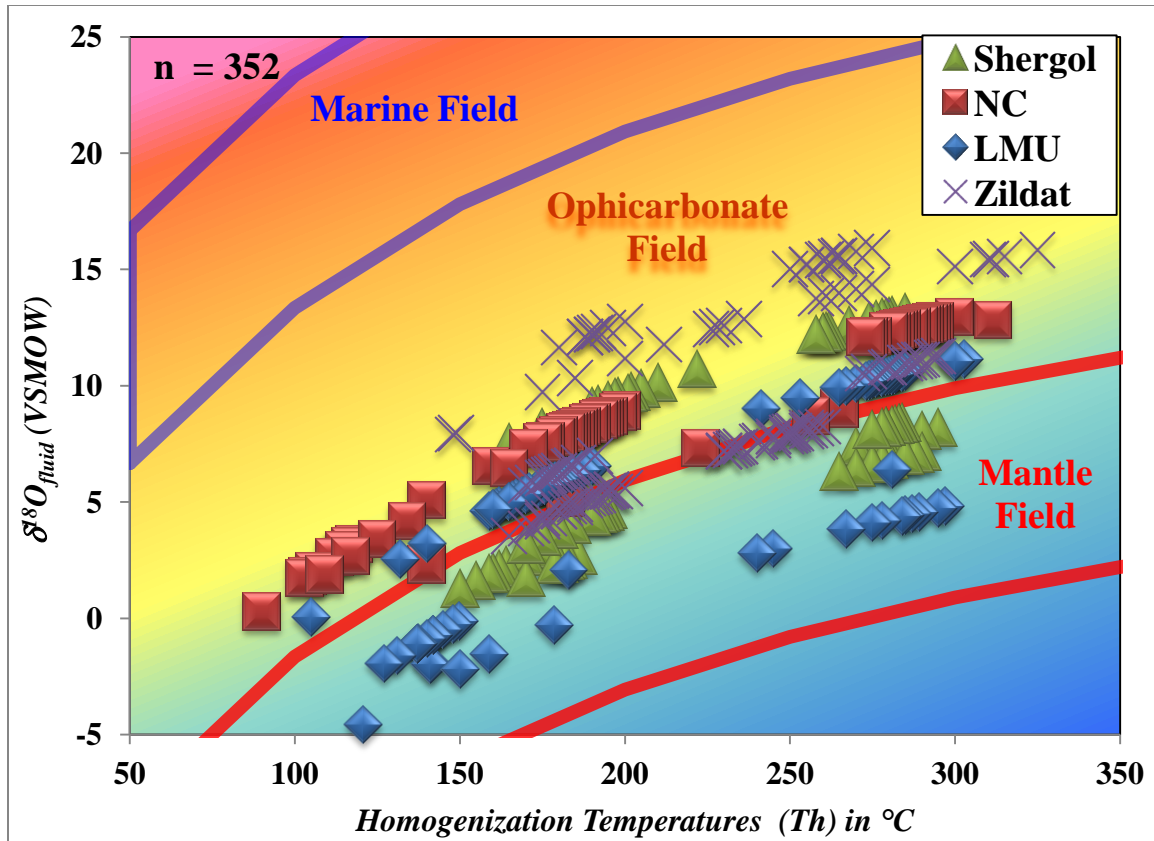


Figure 4.27: $\delta^{18}\text{O}$ of vein fluid from NC and LMU sections of SLAP. The mantle field has been plotted by using the $\delta^{18}\text{O}$ value from Mantle carbonate field (Taylor et al., 1967) and the $\delta^{18}\text{O}$ value of marine carbonate field were used from Sharp (2007). The homogenization temperatures were assumed 50, 100, 150, 200, 250, 300 and 350°C.

4.3 DISCUSSION

The carbon and oxygen isotopic compositions ($\delta^{13}\text{C}$ and $\delta^{18}\text{O}$) of calcite from all of the four studied sections of paleo and south Ladakh accretionary prism lies mostly within the broader primary carbonatite field (Ray and Ramesh, 2006), whereas few data sets lie in the mantle carbonate field (Figure 4.21) as defined by Taylor et al (1967). This is suggestive of having mantle affinity for the source from which these fluids were derived and emplaced as veins in Ladakh Accretionary Prism. Further, the plot of samples in $\delta^{13}\text{C}$ vs $\delta^{18}\text{O}$ compositional space (Figure 4.21) illustrates two distinct fractionation trends

marked as Trend-I and trend-II. (i) The Trend-I shows a positive correlation with enrichment in both $\delta^{13}\text{C}$ and $\delta^{18}\text{O}$ values and follow a trend starting from Mantle carbonatite through Primary carbonatite to South African carbonatite compositional space (Bell and Simonetti, 2010). The limit of Marine compositional field is delimited by the isotopic ratios of nummulitic limestone studied and analyzed from NC sections of SLAP. Only two samples from Zildat section plot in this extended marine field may be considered as outlier and are ignored from further discussion. This trend is termed as hydrothermal alteration trend. (ii) Trend-II shows enrichment of $\delta^{18}\text{O}$ at more or less constant $\delta^{13}\text{C}$ values. Such trends are commonly developed as a result of meteoric water alteration (Ray and Ramesh, 2006; Srivastava and Taylor, 1989). The data defining trend-II also corresponds to Ophicarbonatite field (Perkins et al., 2006), suggesting an additional possibility of altered mantle related rocks as source for derivation of ophicarbonatite like fluids. The enrichment in $\delta^{13}\text{C}$ and $\delta^{18}\text{O}$ values of calcite as shown in Trend-I of figure 4.21 may be due to the hydrothermal alteration. While, the trend-II, enrichment in $\delta^{18}\text{O}$ values is either due to the meteoric water alteration (Shrivastav and Taylor, 1989; Ray and Ramesh, 2006) or fluid derived from the methane rich oceanic crust, i.e. ophicarbonatite (Perkins et al., 2006). Notable amounts of methane gas are omnipresent in the fluid inclusion studies of vein calcite and quartz (see chapter 3). This is further confirmed by Raman Spectroscopic studies of these fluid inclusions (Figure 3.23). Therefore, the contribution of ophicarbonatites in fractionating the isotopic compositions of the fluids, at least in part, is an important mechanism explaining the observed isotopic fractionation in the development of veins of LAP.

The systematic distribution of $\delta^{13}\text{C}$ and $\delta^{18}\text{O}$ values from any of the four studied sections does not show any remarkable variation throughout the marine and terrestrial sedimentary sequences in LAP. Local contamination from the host rocks is unlikely to have affected the isotopic compositions. But the enrichment in $\delta^{13}\text{C}$ and $\delta^{18}\text{O}$ values of the vein carbonates within the marine sequences of NC section toward the Zaskar thrust (as shown in fig 4.19) may be attributed to the presence of nummulitic limestone in this area through fluid rock interaction. This probably caused modified the isotopic composition of vein carbonate to some extent. The effect is more pronounced in veins occurring further south in the proximity of the Zaskar thrust beyond nummulitic limestone. Although, there is a humble possibility of mixing of marine component contributing to the formation of veins causing shift in the $\delta^{13}\text{C}$ or $\delta^{18}\text{O}$ values of the vein fluid in the studied sections.

In addition to the stable isotope geochemistry ($\delta^{13}\text{C}$ and $\delta^{18}\text{O}$) of carbonate, oxygen isotopes ($\delta^{18}\text{O}$) in quartz were also analyzed to elucidate the fluid source. The high $\delta^{18}\text{O}$ of quartz ($>12\text{‰VSMOW}$) suggests their magmatic origin similar to what is advocated by Smith et al (1991). Systematic spatial distribution of $\delta^{18}\text{O}$ in quartz is shown in figure 4.25. The North-South variation, which has telling ends near the thrusts giving a bell shaped variation trend. The $\delta^{18}\text{O}$ is enriched at the central part probably due to interaction with mantle related magmatic rocks of the oceanic plate rather than the marine carbonate components.

As discussed above that there is a very little possibility of in-situ contamination of vein fluids from the marine sediments in which it is emplaced. It is, therefore, pertinent to examine the possibility if at all contamination might have taken place at the deep source area from where the vein forming fluid was generated, through interaction with the marine carbonate component of the deeper part of the down-going slab of oceanic plate. It is thus, necessary to verify the origin of the fluid source of veins using other proxies.

The $^{87}\text{Sr}/^{86}\text{Sr}$ measurements have been made on selected carbonate samples to confirm and add more evidence to the debate related to the fluid source in the formation of veins and constrain our stable isotope ($\delta^{13}\text{C}$ and $\delta^{18}\text{O}$) geochemistry proxy. The Sr isotopic composition varies in the range of 0.7050 to 0.7077 in terrestrial sedimentary setting near the Indus thrust at the northern margin. The strontium isotopic composition of the vein carbonates is gradually enriched southward towards the Zaskar Thrust reaching up to a value of 0.7080 to 0.7102 in marine sedimentary deposits near the southern margin. Near the Indus thrust the Sr isotope values (0.7050 to 0.7077) of vein calcites are similar to the magmatic arc of Ladakh region (0.7033 to 0.7077) as reported by Honegger et al. (1982) and Weinberg and Dunlap (2000). On the other hand, the Sr isotope values of the calcite veins near the Zaskar thrust are found to be highly radiogenic in nature and closely match with that of the marine carbonate of Lamayuru Formation (0.709 to 0.710) and current sea water (0.7092). We infer from this that vein forming fluid bear pristine mantle/magmatic signature near the Indus thrust which is gradually enriched towards the Zaskar thrust as a result of marine mixing. The clear mantle/magmatic signature of Sr isotope near the Indus Thrust also suggest that the mantle related fluids were not

contaminated at the deeper source area. This discounts the possibility of contamination at source as inferred above from the results of $\delta^{13}\text{C}$ and $\delta^{18}\text{O}$ variations. The Sr isotope systematics also suggests that the isotopic variation may be due to marine mixing or other processes, such as hydrothermal alteration or derivation of fluid from ophicarbonates-like sources. The mantle versus marine signature of the fluid can be better understood by using Sr isotopic compositions in combination with oxygen and carbon isotopic ratios rather than individually. To solve this puzzle and know about the fluid source in the development of veins at penultimate stage two combined isotopic binary plots ($^{87}\text{Sr}/^{86}\text{Sr}$ vs $\delta^{18}\text{O}$ and $^{87}\text{Sr}/^{86}\text{Sr}$ vs $\delta^{13}\text{C}$) were used (figure 4.24) with different fields of fluid sources plotted comparison. Most of the vein carbonate sample $^{87}\text{Sr}/^{86}\text{Sr}$ vs $\delta^{18}\text{O}$ and $^{87}\text{Sr}/^{86}\text{Sr}$ vs $\delta^{13}\text{C}$ plot within or in close proximity of the mantle fluid field (figure 4.24) and none plot anywhere close to the marine field. Thus, it can be concluded that vein forming fluid were derived from the mantle source. However, this does not explain enrichment of Sr isotopic composition towards the Zaskar Thrust (in the marine deposits) though it is confirmed by $^{87}\text{Sr}/^{86}\text{Sr}$, $\delta^{13}\text{C}$ and $\delta^{18}\text{O}$ isotope geochemistry that vein forming fluids were derived from the mantle source.

The Pb isotope systematics ($^{208}\text{Pb}/^{204}\text{Pb}$, $^{207}\text{Pb}/^{204}\text{Pb}$ and $^{206}\text{Pb}/^{204}\text{Pb}$) were, therefore, studied on selected carbonate vein samples to further establish if the fluids from the veins in the southern margin were actually contaminated or not. Lead isotopic ratios are sensitive to such contaminating and are very useful too. Different Pb isotopic ratios are plotted in figure 4.23 against each other and also against $^{87}\text{Sr}/^{86}\text{Sr}$ along with the compositional ranges of mantle end members. Compositional fields of other important

carbonatite occurrences in India, such as Amba Dongar carbonatite, Sung Vally carbonatite and Tamil Nadu carbonatite and also that of an East African carbonatite are also shown for comparison. The Vindhyan limestone is also plotted for comparison with carbonatite and our data set. As shown in figure 4.23, the Pb isotopes from this study are more akin to the Enrich Mantle II (EM II) field and which in turn are also similar to the Amba Dongar carbonatites, whereas the Pb isotopic ratios of Zildat section lie on the NHRL and are similar to the East African carbonatites. In both the cases, the carbonatites are said to have mantle magmatic origin. The $^{206}\text{Pb}/^{204}\text{Pb}$ ratio in combination with the $^{87}\text{Sr}/^{86}\text{Sr}$ of the carbonate samples are plotted in figure 4.23a, which also suggest an enriched Mantle (EM–II) like source for the derivation of the fluids in the LAP. Therefore, the combined Pb and Sr isotope systematics from this study confirm the mantle origin of vein forming fluid. It also suggests that the fluid were highly radiogenic in nature from lower crust or upper mantle without any contamination from the marine components through the down going slab of the Indian plate. Thus, it is reconfirmed that the vein forming fluids were not contaminated in the source area. This has very important tectonic implications as it suggests that the late phase once again after a longer quiescence.

CHAPTER 5:

PROPOSED EVOLUTIONARY

MODEL OF THE LADAKH

ACCRETIONARY PRISM

CHAPTER 5:

**PROPOSED EVOLUTIONARY MODEL OF THE
LADAKH ACCRETIONARY PRISM**

An evolutionary model has been projected through this study to understand and further elucidate the subduction process, evolution and geodynamics of the Himalaya during the late phase of the orogeny (~late Miocene period). Well established subduction process of the Indian plate by earlier workers such as Mahéo et al (2006) and Meng et al (2010) is used here as base model and modified to incorporate the finding of this study to put forward the developmental history of the Himalayan orogeny and accretion process of sediments in the forearc basin of magmatic arcs (i.e. PAP and SLAP) in different time frame. The development of accretionary prism and accretion process are well defined by earlier workers but the veining in accretionary prism remained untouched. This necessitates to work on the veins of LAP which have important implications at the waning penultimate stage of evolution of the Himalaya. The age of the SLAP formation is said to be between 55 and 23 Ma (Henderson et al., 2010b, 2011 and reference therein). Based on this, the earlier hypothesis also suggests that all the major tectonic events took place prior to the accumulation of sediments in the fore







arc basin of magmatic arc (i.e. Ladakh Accretionary Prism) before beginning of the Miocene period (Thakur and Mishra, 1984; Searle, 1997; Yin, 2006). In case of the PAP, the age of the sediments are still older, i.e. 120-100 Ma (Honegger et al., 1982, 1989).

An evolutionary model has been proposed on the basis of results and inferences drawn from the present study, which stressed the role of mantle related fluid through various proxies such as $\delta^{13}\text{C}$, $\delta^{18}\text{O}$, $^{87}\text{Sr}/^{86}\text{Sr}$, $^{208}\text{Pb}/^{204}\text{Pb}$, $^{207}\text{Pb}/^{204}\text{Pb}$ and $^{206}\text{Pb}/^{204}\text{Pb}$ ratios. Most of the veins contain pristine isotopic signature at the northern side of accretionary complex which is further modified towards the southern margin throughout the accretionary complex due to various processes, i.e. mixing, alteration etc. (see Chapter-4 for detail). The fluid inclusion and micro textures suggest that the LAP was highly tectonically disturbed and the vein forming fluids were derived from the deeper part of the Earth's crust. The oxygen isotopic ratios of vein forming fluid suggest the mantle related fluid or ophicarbonates as a source (figure 4.21). This is further supported by the fluid inclusion studies which also indicate the magmatic fluid source. Table 5.1 summarizes results of isotopic compositions of the vein carbonate and quartz in relation to their source and forms the major basis for the proposed evolutionary model described below.

It is clear from the isotopic studies that the source characteristic of these vein fluids has strong affinity with the mantle magmatic activity. There is a systematic

spatial variation of isotopic signatures from north to south with more pristine mantle signatures of fluids in the north that gradually grading shift towards more marine signatures. The trace elemental characteristics of the carbonates phases also corroborated probable mantle signatures. If this is true then it has far reaching consequences and tectonic implications. In view of the fact that the tectonic activities ceased at the collision zone (shifted southward at MCT) well before the veins fluid activity.

Table 5.1: Source of vein forming fluid(s).

Proxy Used	Paleo Accretionary Prism		South Ladakh Accretionary Prism		Cross reference for detail
	Shergol	Zildat	NC	LMU	
C and O isotopes of Calcite					
O isotope of Quartz					
O isotope of fluid(s)					
Sr isotope of calcite					
Pb isotope of calcite					
Fluid Inclusion study					

It is therefore pertinent to question in light of the tectonic set-up of the accretionary prism and Himalayan tectonics –

- 1) What triggered the discharge of such huge quantity fluids?
- 2) What could be a mechanism of transport of these fluids from such deeper sources and emplacement in accretionary prism?
- 3) What are the tectonic implications of the magmatic activity at the waning stage of the development of accretionary prism?
- 4) What was the interaction of these mantle derived fluids with the host rock sediments of the accretionary prism?

An attempt has been made to evolve a model to address the above-mentioned questions pertaining to the evolution of the Himalaya at the penultimate stage through integration of the results of our study. We, therefore, envisage a working model to find a rational answer to the above-mentioned questions through a series of schematic diagrams (Fig. 5.1, 5.2 and 5.3) drawn to illustrate the development at different stages of development of the accretionary prism and veining within.

The progressive developmental stages of accretionary prism along with the subduction processes of the Indian plate in the context of the Himalayan orogeny is shown in figure 5.1 as a function of paleo latitude. It is depicting the development of two accretionary prisms in the forearc basin of magmatic arc(s) at different time frames as a consequence of two subduction processes as is also generally believed (Gansser et al., 1974; Thakur, 1981; Robertson, 2000;

Mahéo et al., 2006). The first accretionary prism shaped in the forearc basin of Dras arc at 120–100 Ma due to the subduction of Neo Tethys–1 (figure 5.1b). This accretionary prism is termed as paleo accretionary prism (PAP). The subduction ceased as the Ladakh Magmatic Arc (LMA) crashed with the Dras arc to the north and a second subduction initiated at the forefront of the LMA (figure 5.1c). Due to this subduction phenomenon, the Tethys Ocean was completely consumed by subduction process beneath the Asian plate and favored formation of a second accretionary prism called SLAP (5.1d). The Indian continental plate came in the contact with Asian plate at about 55 Ma and the accretionary prism thus formed in the fore arc basin of Ladakh Magmatic Arc (LMA). This accretionary prism shaped at the south of PAP in the fore arc basin of LMA, therefore, is known as South Ladakh Accretionary Prism (SLAP). The PAP and SLAP are jointly referred as Ladakh Accretionary Prism (LAP).

The present study proposes a new modified hypothesis about the tectonic process during the Miocene. It is hypothesized and established that the tectonic activity propagated southward with the progressing development of the Himalayan orogeny. Therefore, the tectonic activity in ITSZ is supposed to have ceased at the beginning of the Miocene with the tectonic activities gradually shifting towards south resulting in exhumation of HHC and in-sequence thrusting gave rise to MCT, MBT and MFT, respectively. Therefore, it is generally assumed that there was no tectonic activity within the suture zone after the formation of LAP.

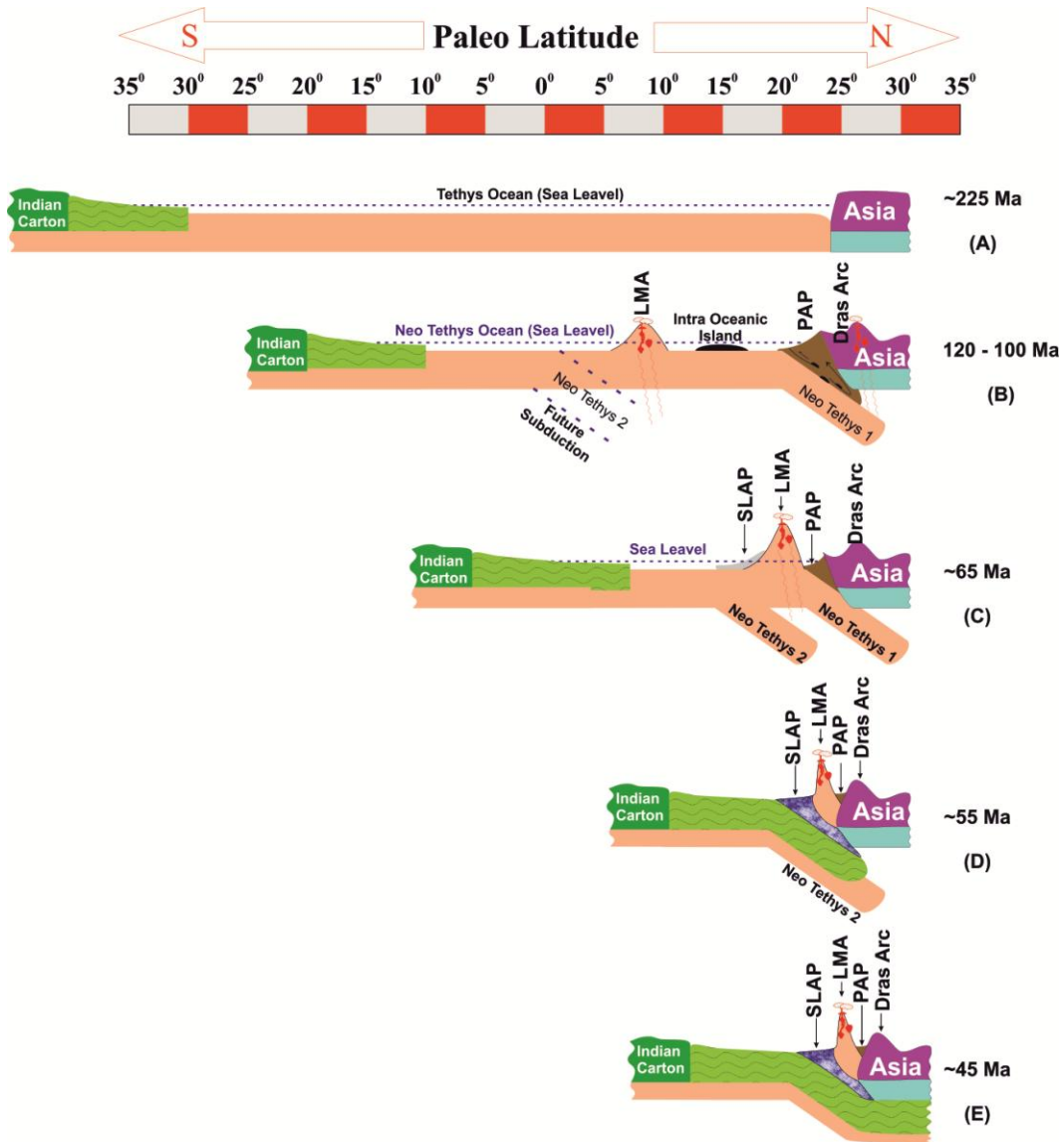


Figure 5.1: Generalized schematic sketch diagram showing stage wise progressive development of accretionary prism in Himalayan orogeny, modified after Mahéo et al (2006); Meng et al (2012). Where LMA referred to Ladakh Magmatic Arc; PAP for Paleo Accretionary Prism and SLAP for South Ladakh Accretionary Prism.

This study did not discard the general concept completely but results of our study do suggest that there were some disturbances in the deep mantle beneath the collision zone such that profuse fluid fluxing took place that invaded the entire

accretionary sedimentary sequences. This warrants for a serious attention to these quartz-calcite veins of common occurrence as proxies to have a better insight into the activities happening in the deeper part. As discussed in the previous chapter, the fluid for the veining in LAP were sourced from the deeper part of the earth; this further requires rational mechanism and causative factors for derivation and transportation of fluids from deeper part i.e. mantle source.

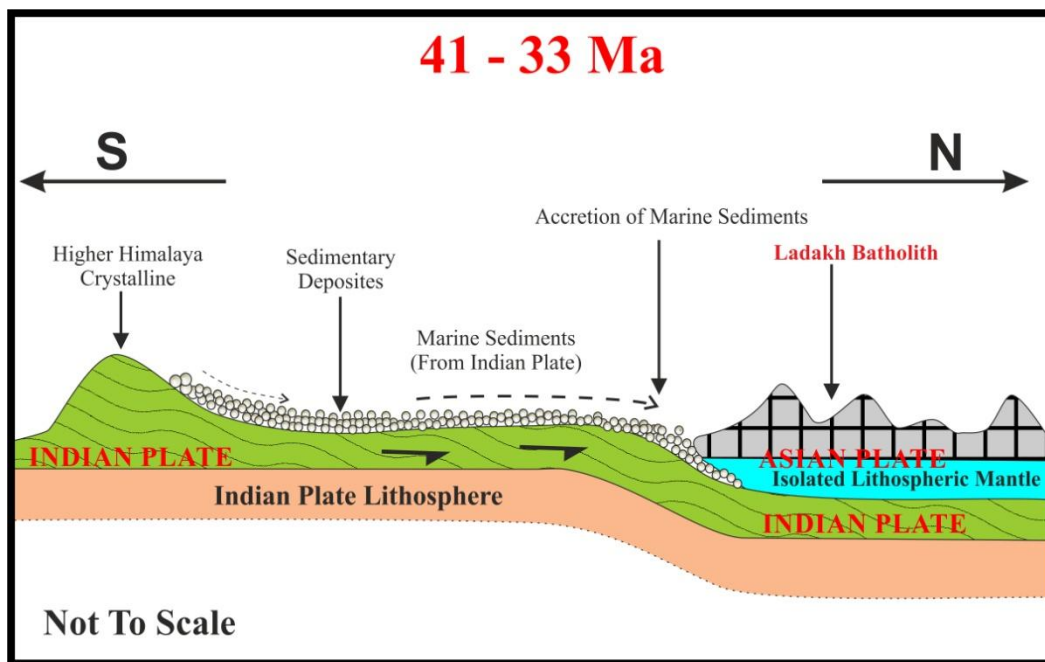


Figure 5.2: Deposition of sediments for shaping LAP and locking of Indian plate, modified after Clift et al (2000); Ji et al (2009); Henderson et al (2011).

As shown in figures 5.1 and 5.2, the Indian continental crust subducted beneath the Asian land mass between 44 and 33 Ma (Clift et al., 2000; Ji et al., 2009) following the complete consumption of Tethys oceanic plate. The observation of Clift et al (2000) supports the submission that there is no noticeable tectonic

activity during the Miocene time. Since these veins cut across even the youngest members of LAP, there must be some event beyond this lock-in stage. Further, the mantle signatures inherited in these veins discount the possibility for their source entirely from local hydrothermal activities. The present study, therefore, provides an important evidence and insight into the probable mantle activity, which was otherwise not known hitherto in the context of the Himalayan orogeny during the Miocene.

Figures 5.1 and 5.2 is constructed on the basis of the hypothesis proposed by Clift et al (2000) and views of many important synthesis and reviews published from time to time. However, none of these models including that of more commonly accepted model of Clift et al. (2000) are able to explain the origin and transportation of mantle derived fluid for veins as discussed above (table 5.1) during the late stage of the Himalayan Orogeny. Therefore, a revised model is proposed that incorporates generating of fluids and possible pathway for the migration of mantle related fluid(s) in the formation of veins in LAP is proposed in this study (Figure 5.3).

Scenario –I: Locking up of the Indian plate beneath the Asian Plate:

As shown in figure 5.2 which is based on the model proposed by Ji et al (2009), the Indian plate is placed beneath the Asian plate through continued subduction during 41–33 Ma (see also Clift et al., 2000). It is hypothesized that the Indian plate got locked up with the Asian plate during this period and subduction ceased.

This leads to migration of deformation southward as the rocks from deeper portion exhumed in the form of HHC and ensues in–sequence thrust tectonic activities further south.

Scenario – II: Breaking-off of the subducted Indian Plate and mantle upwelling:

However, continued northward push of the Indian plate and increasing strain, the subducted Indian plate succumbed ultimately and broke off (See figure 5.2b) at about 33 Ma (Chemenda et al., 2000, Ji et al., 2009). This is supposed to be a major catastrophic event that must have noticeable consequences and surface manifestations. The breaking off of the Indian continental plate would produce upwelling of asthenosphere and would rise up through the broken gaps (figure 5.3); as a consequence of sinking of broken piece of continental plate downward.

Scenario – III: Decompressional melting and Fluid fluxing:

The consequence of mantle upwelling would lead to partial melting by decompression of mantle rocks as well as the subducted oceanic crust. In addition, a huge amount of fluid is also expected to be discharged. Whereas the partial melting is manifested in the form of the younger magmatic phases of the Ladakh-Kohistan magmatic arc (Ji et al., 2009); the fluid thus discharged migrated upward and fluxed into the entire accretionary prism finding passage through the down

going slab and emplaced as veins in the forearc basin of LMA (i.e. Ladakh Accretionary Prism).

The accretionary prism was highly disturbed by this tectonic event. Presence of several local shallow thrust/faults (Searle et al., 1990, 1997; Clift et al., 2000, 2002; Sinclair and Jaffey, 2001; Henderson et al., 2010a, 2010b, 2011, etc.) that are probably interlinked with deep seated thrusts (Indus and Zaskar) may be provided easy pathway for the fluid to form veins. In the study area there are two major thrusts (i) Indus thrust at the northern margin associated with the Ladakh magmatic arc which is also known as Upshi–Bagso thrust (Brookfield and Andrew–Speed, 1984; Tripathy-Lang et al., 2013) and (ii) Zaskar thrust at the southern margin of the accretionary prism. As described here and in Chapter 2 that Indus and Zaskar thrusts are deep seated which have also been confirmed by recent Magnetotelluric (MT) studies by Arora et al. (2007).

Based on the results of isotopic studies (Chapter 4), it was noticed that there is a systematic variation in Sr isotopic compositions of these vein carbonates with the $^{87}\text{Sr}/^{86}\text{Sr}$ ratios increasing systematically from north ($^{87}\text{Sr}/^{86}\text{Sr} = 0.7055$ to 0.7066) to south (Fig. 5.2c).

The veins close to the Ladakh batholith are depleted in $^{87}\text{Sr}/^{86}\text{Sr}$ isotopic composition resembling pristine mantle signature, while the veins toward the south are gradually enriched in Sr isotopic ratios ($^{87}\text{Sr}/^{86}\text{Sr} = 0.0767$ to 0.7080). The veins at southern most margin of the LAP are highly enriched with value as high as 0.7101 and are more akin to be of marine origin. The marine sediments at the southern margin are expected to be highly radiogenic in term of Sr isotopic ratios as these are crustally derived. We infer that this enrichment trend in Sr isotopic composition is due to increasing interaction of the fluid with the crustally derived marine sediments as it moves away. The systematic distributions of fluvial and marine sediments are shown in figure 5.3. As attempted has been made to incorporate these results of the study in the proposed working model, which is illustrated in figure 5.3. The fluvial sediments where the interaction is least are illustrated by yellowish color at the northern margin. The marine sediments where the interaction is intense, are shown in blue color whereas the intermediate part of LAP showing moderate mantle–marine mixing.

Geophysical surveys at local as well as in regional scale are the only means to peep into the present day sub-surface conditions and structures. With the help of inverse MT (also known as TM) survey carried out by Arora et al. (2007), a model has been proposed for the present day disposition of thrust systems (Figure 5.4) across the Himalayan collision zone. Based on the results of TM profile they deduced that the Indus thrust is about 40-60 Km deep whereas the depth of Zaskar thrust is about 40-50 Km. The model incorporates the depth of

the Indian Moho at about 70–80 Km below the Ladakh accretionary prism (or Indus Tsangpo Suture Zone) based on the seismic studies by Rai et al (2007). If the depth of present day Indus thrust is 50–60 Km (Arora et al., 2007) at present, then it must have been much deeper during the Miocene Period (~23 Ma) and were arguably interconnected with the downgoing slab of the Indian plate as shown in figure 5.3b. This provides an important clue that these deep-seated faults served as the pathways for the upward migration of fluids alongside the downgoing Indian slab. We further infer that these deep seated faults were triggered as a consequence of this breaking off event of the Indian plate. This provides important supporting evidence for our proposed model explaining the mechanism for generation and emplacement of mantle related fluids within LAP.

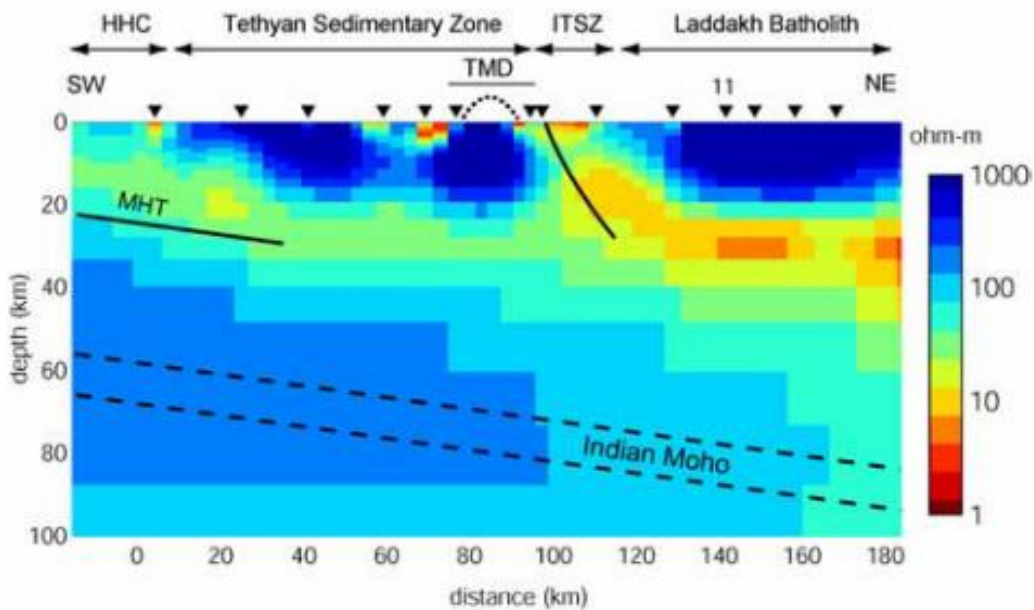


Figure 5.4: Inversion model obtained by inverting TM mode and magnetic field transfer functions (Arora et al., 2007). The location of Indian Moho obtained from Rai et al (2006). MHT, Main Himalayan Thrust; HHC, Higher Himalayan Crystalline; TMD, Tso Moriri Dome; ITSZ, Indus Tsangpo Suture zone.

As discussed in Chapter 4 that the carbon, oxygen (figure 4.18 to 4.20) and strontium isotopic compositions show systematic variation (Figure 4.22 and 5.3b) from north to south in the LAP. These isotopes preserve their pristine mantle signature near the Indus thrust (at the northern margin of LAP) which were fractionated through increasing interaction towards the Zaskar thrust (at the Southern margin of LAP) and akin to the marine carbonates field. These isotopic variations or fractionations are discussed in Chapter 4 and only the salient features are described here in the context of the proposed model of this study in figure 5.3b.

The south dipping Indus thrust was a deep thrust system and associated with the downgoing slab of the Indian plate (Figure 5.3b). Under the situation, as described above, the initiation of this thrust may be linked to the breaking off event of the down going slab of the Indian crust (Chemenda et al., 2000 and Ji et al., 2009). If so, then it would also serve as pathways for the fluid exhaled due to pressure release leading to generation of mantle related fluid that swept through the fluvial sediment in the proximity to the Indus thrust (i.e. the northern margin of LAP). This also explains the reasons that these fluid(s) preserved their pristine isotopic signatures in the veins that emplaced within fluvial sediments. Further, the carbon, oxygen and strontium isotopic compositions of the fluids were altered as it spread southward through interaction (Hydrothermal alteration) with the marine litho-units containing contrasting isotopic signature. This resulted in a shifting of isotopic compositions of the fluids from more pristine mantle signature

at the northern margin towards marine values at the central part of LAP, where the marine sediments were mixed with fluvial sediments. Further south, the veins contain more marine isotopic signatures. An important conclusion can be drawn that the isotopic ratio of the vein calcite and quartz were fractionated as it interacts with marine litho unites further south, causing the observed isotopic spatial variation throughout the accretionary prism.

CHAPTER 6:

CONCLUSIONS AND FUTURE PROSPECTIVES

CHAPTER 6:

CONCLUSIONS AND FUTURE PROSPECTIVES

6.1 CONCLUSIONS

The study area, Ladakh Accretionary Prism (LAP), was developed in two different subduction events, i.e. (i) at the beginning, the Tethys Oceanic plate subducted below Continental Asian plate giving rise to a magmatic arc called Dras and development of an attendant accretionary Prism, called Paleo Accretionary prism (PAP) at the fore arc basin as the Dras arc collided with the Asian Plate (Honegger, 1982, 1989; Thakur, 1981; Mahéo et al., 2004, 2006 and many more). (ii) The continued northward push of the Indian plate caused complete consumption of the Tethyan oceanic plate that ensued Indian and Asian continental plate collision (Figure 2.1). This second phase gave rise to the Ladakh magmatic arc along the Indus–Tsangpo Suture Zone (Honegger, 1989; Mahéo et al., 2004, 2006; Henderson, 2011) and shaped the South Ladakh Accretionary Prism (SLAP). The first phase of the collision began at ~120 Ma while the second phase of the collision took place sometimes at ~65 Ma. Further, the extension of a part of Paleo accretionary prism (PAP) occurs to the NE section of Ladakh Himalaya, which is referred to as Zildat Ophiolitic Mélange (ZOM).

The southern margin of SLAP is dominated by the marine sediments derived from the Indian plate while at the northern margin; the sediments are deposited under fluvial condition consisting chiefly of terrestrial sediments derived from Ladakh magmatic arc (LMA). The PAP and SLAP is jointly referred to as the Ladakh Accretionary Prism (LAP) which is bounded by deep seated thrusts at the northern and southern margins namely, the Indus thrust and the Zaskar thrust respectively. The fault/fracture filling veins comprised of quartz and calcite minerals are omnipresent in the LAP, which intruded and emplaced during the Miocene time (Kharya et al., 2014). These cut across all the formations of the LAP and are therefore much younger than the last phase of the deposition in the LAP. These veins are the subject matter of this study as it is expected to contain vital archives of the tectono-magmatic activities during waning phase of Himalayan orogeny. Following are the salient conclusions that can be drawn from the present study:

The petrographic study of these mineralized veins indicates that the veins were formed by quartz and calcite minerals which were present either in the pure form or in co-existing pair. Fluid inclusion micro-thermometric results predict minimum temperature of fluid entrapment in the range of 212 to 325 °C. This is found consistent with the oxygen isotope thermometric results ranging from 152 to 528 °C. We assign these temperatures to be the crystallization temperatures of the hydrothermal veins of SLAP (Figure 4.26). The re-equilibration textures of

fluid inclusions (Figure 3.8 and 3.13 – 3.17) indicate an enhanced tectonic activity in SLAP (as criteria given by Boullier, 1999).

The fluid inclusion study suggests that the P–T path for the entrapment of fluid inclusions was initially isothermal then become isochoric at the last stage (Figures 3.24 and 3.26). It also indicates that the veins were rapidly exhumed from about 12.6 km and 21.0 km depth in PAP and SLAP, respectively. Re-equilibration textures such as ‘C’ shape ‘L’ shape, implosion and dense CO₂ fluid inclusions were noticed during petrography and microthermometry which point toward the deep seated magmatic origin of fluid from the deep part of the earth.

High REE abundance having nearly flat trend (Figure 4.15 and 4.16) with or without positive Eu anomaly ($\text{Eu}/\text{Eu}^* \geq 1$), which are quite unlikely of crustally derived materials, and were probably have mantle or magmatic kinship. High partition coefficient of REEs in coexisting calcite/quartz, high La/Gd ratios (Figure 4.17) and high $\sum\text{REEs}$ in calcites are also suggestive of magmatic affinity of the fluids.

The stable isotope geochemistry of calcite suggests strong affinity for mantle or ophicarbonatite like fluid source, which was probably fractionated to some extent at the later stage due to various mixing or alteration processes, such as- marine mixing, hydrothermal alteration and meteoric water alteration (Figure 4.21).

Furthermore, the Sr isotopic ratio also suggests that the fluid was initially derived from mantle sources and were fractionated by various processes at later stage as the fluid travelled further southwards. The Pb isotopic compositions are in agreement with other proxies and offers strong evidence of mantle fluid source. The Pb isotopic systematics propose that fluid were derived from the Enrich Mantle II type of deeper sources (upper mantle), that are relatively more radiogenic in nature compared to other mantle sources (Figure 4.23). Low Sr isotopic compositions are also relatively enriched but are within the range of enriched mantle composition (EM II). Sr isotopic ratios together with Pb isotopic signatures suggest derivation of fluid from deeper source in the mantle domain and are more radiogenic than other mantle end members such as normal-MORB, depleted MORB mantle (DMM) etc. The oxygen isotopic ratio of quartz shows affinity very similar to those of the fluids of magmatic origin. Moreover, the oxygen isotopic composition of vein forming fluid $\delta^{18}\text{O}_{(\text{fluid})}$ estimated from the $\delta^{18}\text{O}$ values of quartz and calcite veins at known temperatures of formation is also fall within the mantle and ophicarbonates field (Figure 4.27).

In the spatial distribution of $^{87}\text{Sr}/^{86}\text{Sr}$ ratios in the vein carbonates reveal a more pristine enriched mantle value in veins that occur at the northern side of LAP. This is further enriched gradually towards the southern margin (Figure 4.22). It suggests that the vein forming fluids were initially intruded from the northern margin of LAP, but gradually became enriched through mixing and interaction with the crustally derived marine components (with higher $^{87}\text{Sr}/^{86}\text{Sr}$ values) as it

moved further south along the down going slab (Kharya et al., 2014; also see in Figure 5.3). It is notable that the southern margin of SLAP consists of mostly marine sediments.

The mantle related magmatic activity in the Miocene also reported from the Kohistan part of magmatic arc between 30 and 13 Ma from Tibet (Ji et al., 2009). This arguably is an evidence of mantle related fluid activity in the Himalayan orogeny took place until as late as ~13 Ma (Ji et al., 2009). Ji et al (2009) further proposed that the late stage Kohistan arc magmatism is related to few pulses of mantle melting, which is coeval with the break-up of the locked-in Indian plate beneath the Asian plate. Based on the new results from this study, a modified tectonic model of the late stage of the Himalayan orogeny is proposed here. This comfortably explains a rationale for the mechanism of derivation of mantle fluids flux and revival of mantle activity during the Miocene time and attendant tectonic activity (Figure 5.3, Kharya et al., 2014). The proposed break-off of Indian plate during the Miocene epoch (Chemenda et al., 2000; Ji et. al. 2009) resulted in upwelling of asthenospheric mantle promoting partial melting by decompression and exaltation of fluid fluxes that swept all across the LAP. Therefore, it can be concluded that the presence of mantle signature in the fluid for the formation of veins in LAP is a crucial evidence and is one of the manifestations of the breakoff of the Indian plate underneath at the penultimate stage of the Himalayan Orogeny within accretionary complexes (Figure 5.2 and 5.3).

6.2 FUTURE PROSPECTIVES

The results of this study establishes link between fluid fluxing and mantle magmatic activity at the late stage and its connection with the unlocking through breakoff of Indian plate underneath. This has important tectonic bearing in understanding the changing course of geodynamic processes thereafter. It would be essential therefore, that the ages of the fluid activity be precisely constrained. More definitive proxies and geochronological tools such as Hf, Os and Nd, isotopic studies of the veins would better constrain the source region of fluid generation and tectonic implications in the Himalayan context. The stable isotopic ratio of veins were fractionated with the lithology, therefore a detail work on fluid rock interaction and their mechanism has to be known for better understanding of isotopic fractionation in the study area.

The tectonic activities resulting from this mantle activity are rather poorly understood. Therefore, in the light of the results of this study, a new thought process is expected to be generated, opening up new opportunities and scope of research in the quest for a better unravelling of the history of collision zone of the Himalaya during the Miocene epoch.

CHAPTER 7:

REFERENCES

CHAPTER 7:

REFERENCES

- Acharyya, S. K. (1980). Structural framework and tectonic evolution of the eastern Himalaya. *Himalayan Geology*, 10, 412-439.
- Ahmad, T., Islam, R., Khanna, P. P., & Thakur, V. C. (1996). Geochemistry, petrogenesis and tectonic significance of the basic volcanic units of the Zildat ophiolitic melange, Indus suture zone, eastern Ladakh (India). *Geodinamica Acta*, 9(5), 222-233.
- Ahmad, T., Tanaka, T., Sachan, H. K., Asahara, Y., Islam, R., & Khanna, P. P. (2008). Geochemical and isotopic constraints on the age and origin of the Nidar Ophiolitic Complex, Ladakh, India: Implications for the Neo-Tethyan subduction along the Indus suture zone. *Tectonophysics*, 451(1), 206-224.
- Argand E. (1924) *La tectonique de l'Asie*. Comptes-rendu du XIIIe Congrès géologique international, 170–372.

- Arora, B., Unsworth, M., & Rawat, G. (2007). Deep resistivity structure of the northwest Indian Himalaya and its tectonic implications. *Geophysical Research Letters*, *34*, L04307.
- Auden, J. B. (1935). Traverses in the Himalaya. *Rec. Geol. Surv. India*, *69*(2), 123-167.
- Avigour, A., Magaritz, M., Issar, A., & Dodson, M. H. (1990). Sr isotope study of vein and cave calcites from southern Israel. *Chemical Geology*, *82*, 69-81.
- Avouac, J. P. (2003). Mountain building, erosion, and the seismic cycle in the Nepal Himalaya. *Advances in Geophysics*, *46*, 1-80.
- Baertschi, P., & Silverman, S. R. (1951). The determination of relative abundances of the oxygen isotopes in silicate rocks. *Geochimica et Cosmochimica Acta*, *1*(4), 317-328.
- Bally, A. W. (1981). Thoughts on the tectonics of folded belts. *Geological Society, London, Special Publications*, *9*(1), 13-32.
- Banner, J. L. (1995). Application of the trace element and isotope geochemistry of strontium to studies of carbonate diagenesis. *Sedimentology*, *42*(5), 805-824.
- Bau, M. (1991). Rare-earth element mobility during hydrothermal and metamorphic fluid-rock interaction and the significance of the oxidation state of europium. *Chemical Geology*, *93*(3), 219-230.

- Bell, K., & Simonetti, A. (2010). Source of parental melts to carbonatites—critical isotopic constraints. *Mineralogy and Petrology*, 98(1-4), 77-89.
- Bodnar, R. J. (1993). Revised equation and table for determining the freezing point depression of H₂O-NaCl solutions. *Geochimica et Cosmochimica Acta*, 57(3), 683-684.
- Borthwick, J., & Harmon, R. S. (1982). A note regarding CIF₃ as an alternative to BrF₅ for oxygen isotope analysis. *Geochimica et Cosmochimica Acta*, 46(9), 1665-1668.
- Breeding, C. M., & Ague, J. J. (2002). Slab-derived fluids and quartz-vein formation in an accretionary prism, Otago Schist, New Zealand. *Geology*, 30(6), 499-502.
- Brookfield, M. E., & Reynolds, P. H. (1981). Late Cretaceous emplacement of the Indus suture zone ophiolitic melanges and an Eocene-Oligocene magmatic arc on the northern edge of the Indian plate. *Earth and Planetary Science Letters*, 55(1), 157-162.
- Brookfield, M. E., & Andrews-Speed, C. P. (1984). Sedimentology, petrography and tectonic significance of the shelf, flysch and molasse clastic deposits across the Indus suture zone, Ladakh, NW India. *Sedimentary Geology*, 40(4), 249-286.

- Brown, P. E. (1989). FLINCOR; a microcomputer program for the reduction and investigation of fluid-inclusion data. *American Mineralogist*, 74(11-12), 1390-1393.
- Burchfiel, B. C., Zhiliang, C., Hodges, K. V., Yuping, L., Royden, L. H., Changrong, D., & Jiene, X. (1992). The South Tibetan detachment system, Himalayan orogen: Extension contemporaneous with and parallel to shortening in a collisional mountain belt. *Geological Society of America Special Papers*, 269, 1-41.
- Burg, J. P., Brunel, M., Gapais, D., Chen, G. M., & Liu, G. H. (1984). Deformation of leucogranites of the crystalline Main Central Sheet in southern Tibet (China). *Journal of Structural Geology*, 6(5), 535-542.
- Burkhard, M. (1993). Calcite twins, their geometry, appearance and significance as stress-strain markers and indicators of tectonic regime: a review. *Journal of Structural Geology*, 15(3), 351-368.
- Burrard, S. G., & Hayden, H. H. (1908). *A Sketch of the Geography and Geology of the Himalaya Mountains and Tibet: The high peaks of Asia* (Vol. 1). Superintendent government printing, India.
- Byrne, T., Maltman, A., Stephenson, E., Soh, W., & Knipe, R. (1993). Deformation structures and fluid flow in the toe region of the Nankai accretionary prism. In *Proc. Ocean Drill. Program Sci. Results* (Vol. 131, pp. 83-101).

- Castor, S. B., & Hedrick, J. B. (2006). Rare earth elements. Industrial Minerals volume, 7th edition: Society for Mining, Metallurgy, and Exploration, Littleton, Colorado, 769-792.
- Chemenda, A. I., Burg, J. P., & Mattauer, M. (2000). Evolutionary model of the Himalaya–Tibet system: geopoem: based on new modelling, geological and geophysical data. *Earth and Planetary Science Letters*, 174(3), 397-409.
- Clauer, N., Chaudhuri, S., & Subramaniam, R. (1989). Strontium isotopes as indicators of diagenetic recrystallization scales within carbonate rocks. *Chemical Geology: Isotope Geoscience section*, 80(1), 27-34.
- Clayton, R. N., & Mayeda, T. K. (1963). The use of bromine pentafluoride in the extraction of oxygen from oxides and silicates for isotopic analysis. *Geochimica et cosmochimica acta*, 27(1), 43-52.
- Clift, P. D., Degnan, P. J., Hannigan, R., & Blusztajn, J. (2000). Sedimentary and geochemical evolution of the Dras forearc basin, Indus Suture, Ladakh Himalaya, India. *Geological Society of America Bulletin*, 112(3), 450-466.
- Clift, P. D., Carter, A., Krol, M., & Kirby, E. (2002). Constraints on India-Eurasia collision in the Arabian Sea region taken from the Indus Group, Ladakh Himalaya, India PETER D. CLIFT¹, ANDREW CARTER², MICHAEL KROL³ & ERIC KIRBY⁴. *The tectonic and climatic evolution of the Arabian Sea region*, (195), 97.

- Colchen, M., Reuber, I., Bassoullet, J. P., Belier, J. P., Blondeau, A., Lys, M., & De Wever, P. (1987). Données biostratigraphiques sur les mélanges ophiolitiques du Zaskar, Himalaya du Ladakh. *CR Acad. Sci*, 305, 403-406.
- Coleman, R. G. (1971). Plate tectonic emplacement of upper mantle peridotites along continental edges. *Journal of Geophysical Research*, 76(5), 1212-1222.
- CORFIELD, R. I., SEARLE, M. P., & GREEN, O. R. (1999). Photang thrust sheet: an accretionary complex structurally below the Spontang ophiolite constraining timing and tectonic environment of ophiolite obduction, Ladakh Himalaya, NW India. *Journal of the Geological Society*, 156(5), 1031-1044.
- Cox, S. F. (1995). Faulting processes at high fluid pressures: an example of fault valve behavior from the Wattle Gully Fault, Victoria, Australia. *Journal of Geophysical Research: Solid Earth (1978–2012)*, 100(B7), 12841-12859.
- De Groot, P. A. (Ed.). (2009). *Handbook of stable isotope analytical techniques*(Vol. 2). Elsevier.
- De Sigoyer, J. B. D. (1998). *Mécanismes d'exhumation des roches de haute pression basse température en contexte de convergence continentale: Tso Morari, NO Himalaya* (Doctoral dissertation, Université Claude Bernard-Lyon I).

- De Sigoyer, J., S. Guillot, and P. Dick (2004), Exhumation of the ultrahigh-pressure Tso Moriri unit in eastern Ladakh (NW Himalaya): A case study, *Tectonics*, 23, TC3003.
- DeCelles, P. G., Robinson, D. M., & Zandt, G. (2002). Implications of shortening in the Himalayan fold-thrust belt for uplift of the Tibetan Plateau. *Tectonics*, 21(6), 12-1.
- Deines, P. (1989). Stable isotope variations in carbonatites. *Carbonatites: Genesis and evolution*, 301-359.
- Dewey, J. F., & Bird, J. M. (1970). Mountain belts and the new global tectonics. *Journal of Geophysical Research*, 75(14), 2625-2647.
- Dietrich, D., McKenzie, J. A., & Song, H. (1983). Origin of calcite in syntectonic veins as determined from carbon-isotope ratios. *Geology*, 11(9), 547-551.
- DiPietro, J. A., & Pogue, K. R. (2004). Tectonostratigraphic subdivisions of the Himalaya: a view from the west. *Tectonics*, 23(5).
- Einsele, G., Liu, B., Dürr, S., Frisch, W., Liu, G., Luterbacher, H. P., Ratschbacher, L., Ricken, W., Wendt, J., A Wetzel, Yu, G., & Zheng, H. (1994). The Xigaze forearc basin: evolution and facies architecture (Cretaceous, Tibet). *Sedimentary Geology*, 90(1), 1-32.
- Ernst, W. (1973). Blueschist metamorphism and PT regimes in active subduction zones. *Tectonophysics*, 17(3), 255-272.

- Farquhar, J., & Rumble III, D. (1998). Comparison of oxygen isotope data obtained by laser fluorination of olivine with KrF excimer laser and CO₂ laser. *Geochimica et cosmochimica acta*, 62(18), 3141-3149.
- Ferrill, D. A., Morris, A. P., Evans, M. A., Burkhard, M., Groshong Jr, R. H., & Onasch, C. M. (2004). Calcite twin morphology: a low-temperature deformation geothermometer. *Journal of Structural Geology*, 26(8), 1521-1529.
- Fölling, P. G., Zartman, R. E., & Frimmel, H. E. (2000). A novel approach to double-spike Pb–Pb dating of carbonate rocks: examples from Neoproterozoic sequences in southern Africa. *Chemical Geology*, 171(1), 97-122.
- Fouillac, A. M., & Girard, J. P. (1996). Laser oxygen isotope analysis of silicate/oxide grain separates: Evidence for a grain size effect?. *Chemical geology*, 130(1), 31-54.
- Fuchs, G. & Linner, M. (1997). Multiphase tectonics in the Indus suture zone of eastern Ladakh. *12th Himalayan Karakorum Tibet International Workshop, Acad. Naz. dei Lincei and Soc. Geogr. Ital., Rome, Italy.*
- Galer, S. J. G., & Abouchami, W. (1998). Practical application of lead triple spiking for correction of instrumental mass discrimination. *Mineral. Mag. A*, 62, 491-492.

- Gansser, A. (1964). *Geology of the Himalayas*.
- Gansser, A., Gansser, A., Geologist, S., Gansser, A., & Gansser, A. (1974). *The ophiolitic mélangé, a world-wide problem on Tethyan examples*.
- Gao, G., Elmore, R. D., & Land, L. S. (1992). Geochemical constraints on the origin of calcite veins and associated limestone alteration, Ordovician Viola Group, Arbuckle Mountains, Oklahoma, USA. *Chemical geology*, 98(3), 257-269.
- Garlick, G. D., & Epstein, S. (1967). Oxygen isotope ratios in coexisting minerals of regionally metamorphosed rocks. *Geochimica et Cosmochimica Acta*, 31(2), 181-214.
- Garzanti, E., & Van Haver, T. (1988). The Indus clastics: forearc basin sedimentation in the Ladakh Himalaya (India). *Sedimentary Geology*, 59(3), 237-249.
- Godwin-Austen, H. H. (1864). Geological notes on part of the North-Western Himalayas. *Quarterly Journal of Geological Society of London*, 20, 383-387.
- Goldstein, R. H., & Reynolds, T. J. (1994). Systematics of fluid inclusions in diagenetic minerals: SEPM Short Course 31. *Society for Sedimentary Geology*, 199.

- Goswami, V., Singh, S. K., Bhushan, R., & Rai, V. K. (2012). Temporal variations in $^{87}\text{Sr}/^{86}\text{Sr}$ and ϵNd in sediments of the southeastern Arabian Sea: Impact of monsoon and surface water circulation. *Geochemistry, Geophysics, Geosystems*, *13*(1).
- Haas, J. R., Shock, E. L., & Sassani, D. C. (1995). Rare earth elements in hydrothermal systems: estimates of standard partial molal thermodynamic properties of aqueous complexes of the rare earth elements at high pressures and temperatures. *Geochimica et Cosmochimica Acta*, *59*(21), 4329-4350.
- Hart, S. R. (1984). A large-scale isotope anomaly in the Southern Hemisphere mantle. *Nature*, *309*, 753-757.
- Hart, S. R., Gerlach, D. C., & White, W. M. (1986). A possible new Sr-Nd-Pb mantle array and consequences for mantle mixing. *Geochimica et Cosmochimica Acta*, *50*(7), 1551-1557.
- Hart, S. R. (1988). Heterogeneous mantle domains: signatures, genesis and mixing chronologies. *Earth and Planetary Science Letters*, *90*(3), 273-296.
- Heim, A., & Gansser, A. (1939). Central Himalaya.
- Henderson, A. L., Foster, G. L., & Najman, Y. (2010a). Testing the application of in situ Sm-Nd isotopic analysis on detrital apatites: A provenance tool for

constraining the timing of India–Eurasia collision. *Earth and Planetary Science Letters*, 297(1), 42-49.

Henderson, A. L., Najman, Y., Parrish, R., BouDagher-Fadel, M., Barford, D., Garzanti, E., & Andò, S. (2010b). Geology of the Cenozoic Indus Basin sedimentary rocks: Paleoenvironmental interpretation of sedimentation from the western Himalaya during the early phases of India-Eurasia collision. *Tectonics*, 29(6).

Henderson, A. L., Najman, Y., Parrish, R., Mark, D. F., & Foster, G. L. (2011). Constraints to the timing of India–Eurasia collision; a re-evaluation of evidence from the Indus Basin sedimentary rocks of the Indus–Tsangpo Suture Zone, Ladakh, India. *Earth-Science Reviews*, 106(3), 265-292.

Hodges, K. V. (2000). Tectonics of the Himalaya and southern Tibet from two perspectives. *Geological Society of America Bulletin*, 112(3), 324-350.

Honegger, K., Dietrich, V., Frank, W., Gansser, A., Thöni, M., & Trommsdorff, V. (1982). Magmatism and metamorphism in the Ladakh Himalayas (the Indus-Tsangpo suture zone). *Earth and Planetary Science Letters*, 60(2), 253-292.

Honegger, K., Le Fort, P., Mascle, G., & ZIMMERMANN, J. L. (1989). The blueschists along the Indus suture zone in Ladakh, NW Himalaya. *Journal of Metamorphic Geology*, 7(1), 57-72.

- Hooker, J. D. (1854). Notes of a Naturalist in Bengal, the Sikkim and Nepal Himalayas, the Khasia Mountain etc. *Himalayan Journals*, 2.
- Hubbert, M. K., & Rubey, W. W. (1959). Role of fluid pressure in mechanics of overthrust faulting I. Mechanics of fluid-filled porous solids and its application to overthrust faulting. *Geological Society of America Bulletin*, 70(2), 115-166.
- Isacks, B., Oliver, J., & Sykes, L. R. (1968). Seismology and the new global tectonics. *Journal of Geophysical Research*, 73(18), 5855-5899.
- Jarrard, R. D. (2003). Subduction fluxes of water, carbon dioxide, chlorine, and potassium. *Geochemistry, Geophysics, Geosystems*, 4(5).
- Ji, W. Q., Wu, F. Y., Chung, S. L., Li, J. X., & Liu, C. Z. (2009). Zircon U–Pb geochronology and Hf isotopic constraints on petrogenesis of the Gangdese batholith, southern Tibet. *Chemical Geology*, 262(3), 229-245.
- Johnson, M. R. W. (2002). Shortening budgets and the role of continental subduction during the India–Asia collision. *Earth-Science Reviews*, 59(1), 101-123.
- Kalt, A., Hegner, E., & Satir, M. (1997). Nd, Sr, and Pb isotopic evidence for diverse lithospheric mantle sources of East African Rift carbonatites. *Tectonophysics*, 278(1), 31-45.

- Kerrick, D. M., & Jacobs, G. K. (1981). A modified Redlich-Kwong equation for H₂O, CO₂, and H₂O-CO₂ mixtures at elevated pressures and temperatures. *American Journal of Science*, 281(6), 735-767.
- Kessen, K. M., Woodruff, M. S., & Grant, N. K. (1981). Gangue mineral ⁸⁷Sr/⁸⁶Sr ratios and the origin of Mississippi Valley-type mineralization. *Economic Geology*, 76(4), 913-920.
- Khanna, P.P. Saini, N.K., Mukherjee, P.K. and Purohit, K.K. (2009). An appraisal of ICP-MS technique for determination of REEs: Long term QC assessment of Silicate Rock analysis. *Himalayan Geology*, 30(1), 95-99.
- Kharya, A., Sachan, H. K., Singh, S. K. & Gupta, A.K. (2014) Isotopic Evidence of mantle contribution to Ladakh Accretionary Prism (India). *Goldschmidt Conference*, 1240.
- Knight, C.L. & Bodnar, R.J. (1989). Synthetic fluid inclusions: IX. Critical PVTX properties of NaCl-H₂O solutions. *Geochimica et Cosmochimica Acta*, 53(1), 3-8.
- Kyser, T. K., O'Neil, J. R., & Carmichael, I. S. (1981). Oxygen isotope thermometry of basic lavas and mantle nodules. *Contributions to Mineralogy and Petrology*, 77(1), 11-23.
- Kyser, T. K. (1995). Micro-analytical techniques in stable isotope geochemistry. *Canadian Mineralogist*, 33, 261-261.

- Lallemand, S., & Funiciello, F. (2009). *Subduction zone geodynamics*. Springer.
- Law, R. D., Searle, M. P., & Simpson, R. L. (2004). Strain, deformation temperatures and vorticity of flow at the top of the Greater Himalayan Slab, Everest Massif, Tibet. *Journal of the Geological Society*, 161(2), 305-320.
- Le Fort, P. (1975). Himalayas: the collided range. Present knowledge of the continental arc. *Am. J. Sci*, 275(1), 1-44.
- Le Fort, P. (1996). Evolution of the Himalaya. *WORLD AND REGIONAL GEOLOGY*, 95-109.
- Le Pichon, X. (1968). Sea-floor spreading and continental drift. *Journal of Geophysical Research*, 73(12), 3661-3697.
- Lottermoser, B. G. (1992). Rare earth elements and hydrothermal ore formation processes. *Ore Geology Reviews*, 7(1), 25-41.
- Mäder, U. K., & Berman, R. G. (1991). An equation of state for carbon dioxide to high pressure and temperature. *American Mineralogist;(United States)*, 76.
- Mahéo, G., Bertrand, H., Guillot, S., Villa, I. M., Keller, F., & Capiez, P. (2004). The South Ladakh ophiolites (NW Himalaya, India): an intra-oceanic tholeiitic arc origin with implication for the closure of the Neo-Tethys. *Chemical geology*, 203(3), 273-303.

- Mahéo, G., Fayoux, X., Guillot, S., Garzanti, E., Capiez, P., & Mascle, G. (2006). Relicts of an intra-oceanic arc in the Sapi-Shergol melange zone (Ladakh, NW Himalaya, India): Implications for the closure of the Neo-Tethys Ocean. *Journal of Asian Earth Sciences*, 26(6), 695-707.
- Martin, L. H., Schmidt, M. W., Mattsson, H. B., & Guenther, D. (2013). Element Partitioning between Immiscible Carbonatite and Silicate Melts for Dry and H₂O-bearing Systems at 1–3 GPa. *Journal of Petrology*, egt048.
- Mase, C. W., & Smith, L. (1987). Effects of frictional heating on the thermal, hydrologic, and mechanical response of a fault. *Journal of Geophysical Research: Solid Earth (1978–2012)*, 92(B7), 6249-6272.
- Mattey, D., & Macpherson, C. (1993). High-precision oxygen isotope microanalysis of ferromagnesian minerals by laser-fluorination. *Chemical Geology*, 105(4), 305-318.
- McKenzie, D. P., & Parker, R. L. (1967). The North Pacific: an example of tectonics on a sphere. *Nature*, 216, 1276-1280.
- McKinney, C. R., McCrea, J. M., Epstein, S., Allen, H. A., & Urey, H. C. (1950). Improvements in mass spectrometers for the measurement of small differences in isotope abundance ratios. *Review of Scientific Instruments*, 21(8), 724-730.

- Meng, J., Wang, C., Zhao, X., Coe, R., Li, Y., & Finn, D. (2012). India-Asia collision was at 24 [deg] N and 50 [emsp14] Ma: palaeomagnetic proof from southernmost Asia. *Scientific reports*, 2.
- Merali, Z., Skinner, B. J., Strahler, A. H., & Strahler, A. H. (2009). *Visualizing Earth Science*. Wiley.
- Michiguchi, Y., & Ogawa, Y. (2011). Implication of dark bands in Miocene–Pliocene accretionary prism, Boso Peninsula, central Japan. *Geological Society of America Special Papers*, 480, 247-260.
- Moore, J. C., & Vrolijk, P. (1992). Fluids in accretionary prisms. *Reviews of Geophysics*, 30(2), 113-135.
- Morgan, W. J. (1968). Rises, trenches, great faults, and crustal blocks. *Journal of Geophysical Research*, 73(6), 1959-1982.
- Mukherjee, B. K., & Sachan, H. K. (2001). Discovery of coesite from Indian Himalaya: a record of ultra-high pressure metamorphism in Indian continental crust. *CURRENT SCIENCE*, 81(10), 1358-1360.
- Mukherjee, P. K., Khanna, P. P., & Saini, N. K. (2014). Rapid Determination of Trace and Ultra Trace Level Elements in Diverse Silicate Rocks in Pressed Powder Pellet Targets by LA-ICP-MS using a Matrix-Independent Protocol. *Geostandards and Geoanalytical Research*.

- O'Neil, J. R., Clayton, R. N., & Mayeda, T. K. (1969). Oxygen isotope fractionation in divalent metal carbonates. *The Journal of Chemical Physics*, 51(12), 5547-5558.
- Passchier, C. W., & Trouw, R. A. J. (2005). *Microtectonics*.
- Pedersen, R. B., Searle, M. P., & Corfield, R. I. (2001). U–Pb zircon ages from the Spontang ophiolite, Ladakh Himalaya. *Journal of the Geological Society*, 158(3), 513-520.
- Perkins, G. B., Sharp, Z. D., & Selverstone, J. (2006). Oxygen isotope evidence for subduction and rift-related mantle metasomatism beneath the Colorado Plateau–Rio Grande rift transition. *Contributions to Mineralogy and Petrology*, 151(6), 633-650.
- Pilgrim, G. E. (1906). Notes on the geology of a portion of Bhutan. *Records of Geological Survey of India*, 34, 22-30.
- Rai, S. K., & Singh, S. K. (2007). Temporal variation in Sr and $^{87}\text{Sr}/^{86}\text{Sr}$ of the Brahmaputra: Implications for annual fluxes and tracking flash floods through chemical and isotope composition. *Geochemistry, Geophysics, Geosystems*, 8(8).
- Rai, S. S., Priestley, K., Gaur, V. K., Mitra, S., Singh, M. P., & Searle M. (2006). Configuration of the Indian Moho beneath the NW Himalaya and Ladakh, *Geophysical Research Letters*, 33, L15308.

- Ray, J. S., Trivedi, J. R., & Dayal, A. M. (2000). Strontium isotope systematics of Amba Dongar and Sung Valley carbonatite-alkaline complexes, India: evidence for liquid immiscibility, crustal contamination and long-lived Rb/Sr enriched mantle sources. *Journal of Asian Earth Sciences*, 18(5), 585-594.
- Ray, J. S., Veizer, J., & Davis, W. J. (2003). C, O, Sr and Pb isotope systematics of carbonate sequences of the Vindhyan Supergroup, India: age, diagenesis, correlations and implications for global events. *Precambrian Research*, 121(1), 103-140.
- Ray, J. S., & Ramesh, R. (2006). Stable carbon and oxygen isotopic compositions of Indian carbonatites. *International Geology Review*, 48(1), 17-45.
- Robertson, A., & Degnan, P. (1994). The Dras arc Complex: lithofacies and reconstruction of a Late Cretaceous oceanic volcanic arc in the Indus Suture Zone, Ladakh Himalaya. *Sedimentary Geology*, 92(1), 117-145.
- Robertson, A. H. F. (2000). Formation of melanges in the Indus suture zone, Ladakh Himalaya by successive subduction-related, collisional and post-collisional processes during late Mesozoic-late Tertiary time. *Geological Society, London, Special Publications*, 170(1), 333-374.
- Rowe, K. T., & Sreaton, E. (2009, December). Permeabilities of core samples from Integrated Ocean Drilling Program Expedition 316 and implications

for shallow fluid flow due to megasplay fault movement. In *AGU Fall Meeting Abstracts* (Vol. 1, p. 1839).

Rumble III, D., Farquhar, J., Young, E. D., & Christensen, C. P. (1997). In situ oxygen isotope analysis with an excimer laser using F₂ and BrF₅ reagents and O₂ gas as analyte. *Geochimica et Cosmochimica Acta*, 61(19), 4229-4234.

Sample, J. C., Reid, M. R., Tols, H. J., & Moore, J. C. (1993). Carbonate cements indicate channeled fluid flow along a zone of vertical faults at the deformation front of the Cascadia accretionary wedge (northwest US coast). *Geology*, 21(6), 507-510.

Schärer, U., Xu, R. H., & Allègre, C. J. (1984). UPb geochronology of Gangdese (Transhimalaya) plutonism in the Lhasa-Xigaze region, Tibet. *Earth and Planetary Science Letters*, 69(2), 311-320.

Schleicher, H., Kramm, U., Pernicka, E., Schidlowski, M., Schmidt, F., Subramanian, V., Todt, W., & Viladkar, S. G. (1998). Enriched subcontinental upper mantle beneath southern India: evidence from Pb, Nd, Sr, and C–O isotopic studies on Tamil Nadu carbonatites. *Journal of Petrology*, 39(10), 1765-1785.

Searle, M. P., Pickering, K. T., & Cooper, D. J. W. (1990). Restoration and evolution of the intermontane Indus molasse basin, Ladakh Himalaya, India. *Tectonophysics*, 174(3), 301-314.

- Searle, M. P., Waters, D. J., Rex, D. C., & Wilson, R. N. (1992). Pressure, temperature and time constraints on Himalayan metamorphism from eastern Kashmir and western Zaskar. *Journal of the Geological Society*, *149*(5), 753-773.
- SEARLE, M., CORFIELD, R. I., Stephenson, B. E. N., & Mccarron, J. O. E. (1997). Structure of the North Indian continental margin in the Ladakh–Zaskar Himalayas: implications for the timing of obduction of the Spontang ophiolite, India–Asia collision and deformation events in the Himalaya. *Geological Magazine*, *134*(03), 297-316.
- Searle, M. P., Simpson, R. L., Law, R. D., Parrish, R. R., & Waters, D. J. (2003). The structural geometry, metamorphic and magmatic evolution of the Everest massif, High Himalaya of Nepal–South Tibet. *Journal of the Geological Society*, *160*(3), 345-366.
- Sen, K., & Collins, A. S. (2013). Dextral transpression and late Eocene magmatism in the trans-Himalayan Ladakh Batholith (North India): implications for tectono-magmatic evolution of the Indo-Eurasian collisional arc. *International Journal of Earth Sciences*, *102*(7), 1895-1909.
- Sen, K., Das, S., Mukherjee, B. K., & Sen, K. (2013). Bimodal stable isotope signatures of Zildat Ophiolitic Mélange, Indus Suture Zone, Himalaya:

implications for emplacement of an ophiolitic mélange in a convergent setup. *International Journal of Earth Sciences*, 102(7), 2033-2042.

Sharp Z. D., & O'Neil J. R. (1989). A laser-based carbon reduction technique for oxygen isotope analysis of silicates and oxides. *In: Annual Report of the Director, Geophysical Laboratory: 1988–1989. Carnegie Institution, Washington DC*, 89, 72–78. [6-1, App C].

Sharp, Z. D. (1990). A laser-based microanalytical method for the *in situ* determination of oxygen isotope ratios of silicates and oxides. *Geochimica et Cosmochimica Acta*, 54(5), 1353-1357.

Sharp, Z. D. (1992). *In situ* laser microprobe techniques for stable isotope analysis. *Chemical Geology: Isotope Geoscience section*, 101(1), 3-19.

Sharp, Z. D., & Kirschner, D. L. (1994). Quartz-calcite oxygen isotope thermometry: A calibration based on natural isotopic variations. *Geochimica et Cosmochimica Acta*, 58(20), 4491-4501.

Sharp, Z. (2007). *Principles of stable isotope geochemistry* (p. 344). Upper Saddle River, NJ: Pearson education.

Shiro, Y., & Sakai, H. (1972). Calculation of the reduced partition function ratios of α -, β -quartzs and calcite. *Bulletin of the Chemical Society of Japan*, 45(8), 2355-2359.

- Sibson, R. H. (1973). Interactions between temperature and pore-fluid pressure during earthquake faulting and a mechanism for partial or total stress relief. *Nature*, 243(126), 66-68.
- Sibson, R. H. (1986). Brecciation processes in fault zones: inferences from earthquake rupturing. *Pure and Applied Geophysics*, 124(1-2), 159-175.
- Sibson, R. H., Robert, F., & Poulsen, K. H. (1988). High-angle reverse faults, fluid-pressure cycling, and mesothermal gold-quartz deposits. *Geology*, 16(6), 551-555.
- Simonetti, A., Bell, K., & Viladkar, S. G. (1995). Isotopic data from the Amba Dongar carbonatite complex, west-central India: evidence for an enriched mantle source. *Chemical Geology*, 122(1), 185-198.
- Sinclair, H. D., & Jaffey, N. (2001). Sedimentology of the Indus Group, Ladakh, northern India: implications for the timing of initiation of the palaeo-Indus River. *Journal of the Geological Society*, 158(1), 151-162.
- Singh, S., & Chowdhary, P. K. (1990). An outline of the geological framework of the Arunachal Himalaya. *Journal of Himalayan Geology*, 1(2), 189-197.
- Sinha, A. K., & Upadhyay, R. (1997). Tectonics and sedimentation in the passive margin, trench, fore-arc and backarc areas of the Indus Suture Zone in Ladakh and Karakorum: a review. *Geodinamica Acta*, 10(1), 1-11.

- Smith, B. M., Reynolds, S. J., Day, H. W., & Bodnar, R. J. (1991). Deep-seated fluid involvement in ductile-brittle deformation and mineralization, South Mountains metamorphic core complex, Arizona. *Geological Society of America Bulletin*, 103(4), 559-569.
- Spicuzza, M. J., Valley, J. W., Kohn, M. J., Girard, J. P., & Fouillac, A. M. (1998). The rapid heating, defocused beam technique: a CO₂-laser-based method for highly precise and accurate determination of $\delta^{18}\text{O}$ values of quartz. *Chemical Geology*, 144(3), 195-203.
- Srivastava, R. K., & Taylor, L. A. (1996). Carbon-and oxygen-isotope variations in Indian carbonatites. *International Geology Review*, 38(5), 419-429.
- Steck, A., Spring, L., Vannay, J. C., Masson, H., Bucher, H., Stutz, E., Marchant, R., & Tieche, J. C. (1993). The tectonic evolution of the Northwestern Himalaya in eastern Ladakh and Lahul, India. *Geological Society, London, Special Publications*, 74(1), 265-276.
- Steck, A., Epard, J. L., Vannay, J. C., Hunziker, J., Girard, M., Morard, A., & Robyr, M. (1998). Geological transect across the Tso Morari and Spiti areas: The nappe structures of the Tethys Himalaya. *Eclogae Geologicae Helvetiae*, 91(1), 103-122.
- Steck, A. (2003). Geology of the NW Indian Himalaya. *Eclogae Geologicae Helvetiae*, 96(2), 147-196.

- Stipp, M., StuÈnitz, H., Heilbronner, R., & Schmid, S. M. (2002). The eastern Tonale fault zone: a 'natural laboratory' for crystal plastic deformation of quartz over a temperature range from 250 to 700 C. *Journal of Structural Geology*, 24(12), 1861-1884.
- Stipp, M., Tullis, J., Scherwath, M., & Behrmann, J. H. (2010). A new perspective on paleopiezometry: Dynamically recrystallized grain size distributions indicate mechanism changes. *Geology*, 38(8), 759-762.
- Sugimura, A., & Uyeda, S. (1973). Island arcs. *Japanese, Physics of the Earth, Physical Society of Japan*, 190-222.
- Taira, A. (2001). Tectonic evolution of the Japanese island arc system. *Annual Review of Earth and Planetary Sciences*, 29(1), 109-134.
- Taylor, H. P., & Epstein, S. (1962). Relationship Between O18/O16 Ratios in Coexisting Minerals of Igneous and Metamorphic Rocks Part 1: Principles and Experimental Results. *Geological Society of America Bulletin*, 73(4), 461-480.
- Taylor Jr, H. P. (1967). Oxygen isotope studies of hydrothermal mineral deposits. *Geochemistry of hydrothermal ore deposits*, 109-142.
- Taylor Jr, H. P., Frechen, J., & Degens, E. T. (1967). Oxygen and carbon isotope studies of carbonatites from the Laacher See District, West Germany and

the Alnö District, Sweden. *Geochimica et Cosmochimica Acta*, 31(3), 407-430.

Thakur, V. C. (1981). Regional framework and geodynamic evolution of the Indus-Tsangpo suture zone in the Ladakh Himalayas. *Transactions of the Royal Society of Edinburgh: Earth Sciences*, 72(02), 89-97.

Thakur, V. C., & Misra, D. K. (1984). Tectonic framework of the Indus and Shyok suture zones in eastern Ladakh, northwest Himalaya. *Tectonophysics*, 101(3), 207-220.

Tripathy-Lang, A., Hodges, K. V., van Soest, M. C., & Ahmad, T. (2013). Evidence of pre-Oligocene emergence of the Indian passive margin and the timing of collision initiation between India and Eurasia. *Lithosphere*, 5(5), 501-506.

Tullis, J., & Yund, R. A. (1985). Dynamic recrystallization of feldspar: a mechanism for ductile shear zone formation. *Geology*, 13(4), 238-241.

Ujiie, K., Yamaguchi, A., Kimura, G., & Toh, S. (2007). Fluidization of granular material in a subduction thrust at seismogenic depths. *Earth and Planetary Science Letters*, 259(3), 307-318.

Valdiya, K. S. (1981). Tectonics of the central sector of the Himalaya. *Zagros Hindu Kush Himalaya Geodynamic Evolution*, 87-110.

- Valdiya, K. S. (1984). Evolution of the Himalaya. *Tectonophysics*, 105(1), 229-248.
- Veena, K., Pandey, B. K., Krishnamurthy, P., & Gupta, J. N. (1998). Pb, Sr and Nd isotopic systematics of the carbonatites of Sung Valley, Meghalaya, northeast India: Implications for contemporary plume-related mantle source characteristics. *Journal of Petrology*, 39(11-12), 1875-1884.
- Vennemann, T. W., & Smith, H. S. (1990). The rate and temperature of reaction of ClF_3 with silicate minerals, and their relevance to oxygen isotope analysis. *Chemical Geology: Isotope Geoscience section*, 86(1), 83-88.
- Vernon, R. H. (1981). Optical microstructure of partly recrystallized calcite in some naturally deformed marbles. *Tectonophysics*, 78(1), 601-612.
- Virdi, N. S., Thakur, V. C., & Kumar, S. (1977). Blueschist facies metamorphism from the Indus suture zone of Ladakh and its significance. *Himal. Geol*, 7, 479-482.
- Vityk, M. O., & Bodnar, R. J. (1995). Textural evolution of synthetic fluid inclusions in quartz during reequilibration, with applications to tectonic reconstruction. *Contributions to Mineralogy and Petrology*, 121(3), 309-323.
- Vrolijk, P. (1987). Tectonically driven fluid flow in the Kodiak accretionary complex, Alaska. *Geology*, 15(5), 466-469.

- Vrolijk, P. (1990). On the mechanical role of smectite in subduction zones. *Geology*, 18(8), 703-707.
- Vrolijk, P., Fisher, A., & Gieskes, J. (1991). Geochemical and geothermal evidence for fluid migration in the Barbados accretionary prism (ODP Leg 110). *Geophysical Research Letters*, 18(5), 947-950.
- Wadia, D. N. (1953). Geology of India.
- Wadia, D. N. (1966). The Himalayan Geosyncline. In *Proc. Nat. Inst. Sci. India* (Vol. 32, p. 527).
- Weinberg, R. F., & Dunlap, W. J. (2000). Growth and deformation of the Ladakh Batholith, northwest Himalayas: implications for timing of continental collision and origin of calc-alkaline batholiths. *The Journal of Geology*, 108(3), 303-320.
- Will, T. M., Frimmel, H. E., Zeh, A., Le Roux, P., & Schmädicke, E. (2010). Geochemical and isotopic constraints on the tectonic and crustal evolution of the Shackleton Range, East Antarctica, and correlation with other Gondwana crustal segments. *Precambrian Research*, 180(1), 85-112.
- Wood, S. A. (1990). The aqueous geochemistry of the rare-earth elements and yttrium: 2. Theoretical predictions of speciation in hydrothermal solutions to 350 C at saturation water vapor pressure. *Chemical Geology*, 88(1), 99-125.

- Yamaguchi, A., Ujiie, K., Nakai, S. I., & Kimura, G. (2012). Sources and physicochemical characteristics of fluids along a subduction-zone megathrust: A geochemical approach using syn-tectonic mineral veins in the Mugi mélange, Shimanto accretionary complex. *Geochemistry, Geophysics, Geosystems*, 13(7).
- Yeh, H. W., & Savin, S. M. (1977). Mechanism of burial metamorphism of argillaceous sediments: 3. O-isotope evidence. *Geological Society of America Bulletin*, 88(9), 1321-1330.
- Yin, A., & Harrison, T. M. (2000). Geologic evolution of the Himalayan-Tibetan orogen. *Annual Review of Earth and Planetary Sciences*, 28(1), 211-280.
- Yin, A. (2006). Cenozoic tectonic evolution of the Himalayan orogen as constrained by along-strike variation of structural geometry, exhumation history, and foreland sedimentation. *Earth-Science Reviews*, 76(1), 1-131.
- Zhang, Y. G., & Frantz, J. D. (1987). Determination of the homogenization temperatures and densities of supercritical fluids in the system NaClKClCaCl₂H₂O using synthetic fluid inclusions. *Chemical Geology*, 64(3), 335-350.

APPENDIXES

APPENDIX – A:

SAMPLE LOCATIONS

Sample Locations and analytical details of all four studied sections of PAP (A-1 and A-2 for Shergol and Zildat sections, respectively) and SLAP (A-3 and A-4 for NC and LMU sections, respectively) are illustrated below.

A-1) Shergol Section of PAP:

Sample No	Latitude	Longitude	Formation	Mineralogy*	Trace & REE	Stable Isotope	Sr Isotope	Pb Isotope
ST12/6	34° 23' 57.8"	76° 17' 30.2"	SOM	QC				
ST12/7	34° 23' 57.8"	76° 17' 30.2"	SOM	Q	√			
ST12/8	34° 24' 04.6"	76° 17' 24.2"	SOM	C		√		
ST12/9	34° 24' 04.6"	76° 17' 24.2"	SOM	C	√	√		
ST12/10	34° 24' 06.0"	76° 17' 24.1"	SOM	QC	√			
ST12/11	34° 24' 06.0"	76° 17' 24.1"	SOM	QC		√		
ST12/12	34° 23' 47.0"	76° 17' 35.3"	SOM	QC	√	√		√
ST12/13	34° 23' 47.0"	76° 17' 35.3"	SOM	QC		√		
ST12/14	34° 23' 47.0"	76° 17' 35.3"	SOM	QC	√			
ST12/15	34° 23' 57.4"	76° 17' 45.0"	SOM	QC		√		
ST12/16	34° 23' 57.4"	76° 17' 45.0"	SOM	QC				
ST12/17	34° 23' 13.5"	76° 16' 55.5"	SOM	QC	√			
ST12/18	34° 23' 08.6"	76° 15' 03.0"	SOM	C		√		√
ST12/19	34° 23' 19.5"	76° 14' 51.8"	SOM	C		√		
ST12/20	34° 23' 19.5"	76° 14' 51.8"	SOM	C	√	√		
ST12/21	34° 23' 19.5"	76° 14' 51.8"	SOM	Q				
ST12/22	34° 23' 19.9"	76° 14' 53.3"	SOM	C		√		

Sample No	Latitude	Longitude	Formation	Mineralogy*	Trace & REE	Stable Isotope	Sr Isotope	Pb Isotope
ST12/23	34° 22' 58.1"	76° 13' 35.1"	SOM	C	√	√		
ST12/24	34° 22' 58.1"	76° 13' 35.1"	SOM	Q	√			
ST12/25	34° 23' 58.0"	76° 17' 45.3"	SOM	Q				
ST12/26	34° 23' 57.4"	76° 17' 45.0"	SOM	C		√		
ST12/27	34° 23' 57.4"	76° 17' 45.0"	SOM	QC	√			
ST12/28	34° 23' 57.4"	76° 17' 45.0"	SOM	C		√		
ST12/29	34° 23' 57.4"	76° 17' 45.0"	SOM	Q				
ST12/30	34° 23' 57.4"	76° 17' 45.0"	SOM	QC	√			
ST12/31	34° 23' 55.0"	76° 17' 44.7"	SOM	Q				
ST12/32	34° 23' 49.7"	76° 17' 42.1"	SOM	Q				
ST12/33	34° 23' 51.0"	76° 17' 36.9"	SOM	Q				
ST12/34	34° 23' 51.5"	76° 17' 36.9"	SOM	Q				
ST12/35	34° 24' 00.8"	76° 17' 27.9"	SOM	Q				
ST12/36	34° 24' 06.7"	76° 17' 21.9"	SOM	QC	√			
ST12/37	34° 24' 06.7"	76° 17' 21.9"	SOM	QC		√		
ST12/38	34° 24' 06.7"	76° 17' 21.9"	SOM	QC	√			
ST12/39	34° 24' 06.7"	76° 17' 21.9"	SOM	QC		√		
ST12/40	34° 24' 06.7"	76° 17' 22.8"	SOM	QC		√		
ST12/41	34° 24' 06.7"	76° 17' 22.8"	SOM	QC		√		
ST12/42	34° 24' 06.7"	76° 17' 22.8"	SOM	QC	√			√
ST12/43	34° 24' 04.2"	76° 17' 12.5"	SOM	Q				
ST12/44	34° 24' 04.2"	76° 17' 12.5"	SOM	Q	√			
ST12/45	34° 24' 04.2"	76° 17' 12.5"	SOM	Q				
ST12/46	34° 24' 20.6"	76° 17' 17.2"	SOM	C		√		
ST12/47	34° 24' 20.6"	76° 17' 17.2"	SOM	Q				
ST12/48	34° 24' 20.6"	76° 17' 17.2"	SOM	C		√		
ST12/49	34° 24' 21.0"	76° 17' 18.7"	SOM	C	√	√		
ST12/50	34° 24' 21.0"	76° 17' 18.7"	SOM	QC	√			
ST12/51	34° 24' 20.9"	76° 17' 31.0"	SOM	C		√		
ST12/52	34° 24' 20.9"	76° 17' 31.0"	SOM	C		√		
ST12/53	34° 24' 16.2"	76° 17' 38.1"	SOM	C		√		
ST12/54	34° 24' 14.6"	76° 17' 41.0"	SOM	C		√		
ST12/55	34° 24' 14.6"	76° 17' 41.0"	SOM	C		√		

*Mineralogy: Q = Quartz, C = Calcite, QC = Co paired Quartz–Calcite

Shergol ophiolitic mélangé is referred to as SOM.

A-2) Zildat Section of PAP:

Sample No	Latitude	Longitude	Formation	Mineralogy*	Trace & REE	Stable Isotope	Sr Isotope	Pb Isotope
ZV 13/1	33° 14' 06.4"	78° 03' 51.2"	ZOM	QC	√	√		
ZV 13/2	33° 14' 06.4"	78° 03' 51.2"	ZOM	C	√	√		
ZV 13/3	33° 14' 14.3"	78° 03' 36.4"	ZOM	QC	√	√		
ZV 13/4	33° 14' 14.3"	78° 03' 36.4"	ZOM	C	√	√		√
ZV 13/5	33° 14' 18.3"	78° 03' 29.2"	ZOM	C	√	√		
ZV 13/6	33° 14' 24.0"	78° 03' 18.4"	ZOM	QC	√	√		√
ZV 13/7	33° 14' 25.5"	78° 03' 15.9"	ZOM	C	√	√		
ZV 13/8	33° 14' 27.3"	78° 03' 12.6"	ZOM	QC	√	√		
ZV 13/9	33° 14' 28.0"	78° 03' 11.2"	ZOM	QC	√	√		
ZV 13/10	33° 14' 28.7"	78° 03' 09.8"	ZOM	QC	√	√		
ZV 13/11	33° 15' 06.2"	78° 02' 00.7"	ZOM	QC	√	√		√
ZV 13/12	33° 15' 09.1"	78° 01' 55.2"	ZOM	QC	√	√		

*Mineralogy: Q = Quartz, C = Calcite, QC = Co paired Quartz–Calcite

Zildat ophiolitic mélange is referred to as ZOM.

A-3) Nimu–Chilling (NC) Section of SLAP:

Sample No	Latitude	Longitude	Formation	Mineralogy*	Trace & REE	Stable Isotope	Sr Isotope	Pb Isotope
NC12/1	34° 01' 34.5"	77° 11' 48.9"	Lamayuru	C		√	√	
NC12/2	34° 01' 34.5"	77° 11' 48.9"	Lamayuru	C	√	√	√	
NC12/3	34° 01' 34.5"	77° 11' 48.9"	Lamayuru	C		√		
NC12/4	34° 01' 34.5"	77° 11' 48.9"	Lamayuru	C	√	√	√	
NC12/5	34° 01' 52.4"	77° 11' 37.8"	Lamayuru	QC		√		
NC12/6	34° 01' 52.4"	77° 11' 37.8"	Lamayuru	Q				
NC12/7	34° 02' 23.5"	77° 12' 26.2"	Nindam	QC		√		
NC12/8	34° 02' 23.5"	77° 12' 26.2"	Nindam	QC		√		

Sample No	Latitude	Longitude	Formation	Mineralogy*	Trace & REE	Stable Isotope	Sr Isotope	Pb Isotope
NC12/9	34° 02' 23.5"	77° 12' 26.2"	Nindam	C	√	√	√	
NC12/10	34° 02' 23.5"	77° 12' 26.2"	Nindam	QC		√		
NC12/11	34° 02' 23.5"	77° 12' 26.2"	Nindam	QC		√		
NC12/12	34° 02' 30.5"	77° 11' 14.1"	Nindam	C		√		
NC12/13	34° 02' 41.3"	77° 10' 51.9"	Nindam	QC		√		
NC12/14	34° 02' 54.1"	77° 10' 10.6"	Nindam	QC		√		
NC12/15	34° 02' 51.0"	77° 12' 04.0"	Nindam	Q				
NC12/16	34° 02' 48.7"	77° 12' 34.2"	Chogdo	QC	√	√		
NC12/17	34° 03' 12.1"	77° 12' 21.3"	Chogdo	C	√	√	√	
NC12/18	34° 03' 25.4"	77° 12' 32.1"	Jurutze	QC	√	√		
NC12/19	34° 03' 25.4"	77° 12' 32.1"	Jurutze	C	√	√	√	
NC12/20	34° 03' 25.4"	77° 12' 32.1"	Jurutze	QC	√	√	√	
NC12/21	34° 03' 02.9"	77° 12' 39.9"	Jurutze	QC		√		
NC12/22	34° 03' 27.0"	77° 12' 28.3"	Jurutze	Q		√		
NC12/23	34° 03' 27.0"	77° 12' 28.3"	Jurutze	QC		√		
NC12/24	34° 04' 00.5"	77° 11' 36.6"	Jurutze	QC		√		
NC12/25	34° 04' 00.5"	77° 11' 36.6"	Jurutze	QC	√	√		
NC12/26	34° 04' 21.4"	77° 12' 49.1"	Jurutze	QC		√		
NC12/27	34° 04' 23.1"	77° 12' 49.7"	Jurutze	QC		√		
NC12/28	34° 05' 21.2"	77° 12' 38.1"	Jurutze	QC	√	√	√	
NC12/29	34° 05' 43.6"	77° 12' 41.6"	Jurutze	QC	√	√	√	√
NC12/30	34° 06' 20.4"	77° 12' 51.3"	Jurutze	Q		√		
NC12/31	34° 06' 26.0"	77° 12' 53.4"	Jurutze	QC	√	√	√	
NC12/32	34° 06' 26.0"	77° 12' 53.4"	Jurutze	Q				
NC12/33	34° 06' 27.3"	77° 12' 53.5"	Jurutze	QC		√		
NC12/34	34° 06' 27.3"	77° 12' 53.5"	Jurutze	QC		√		
NC12/35	34° 06' 30.7"	77° 12' 57.7"	Contact	QC	√	√	√	
NC12/36	34° 06' 39.3"	77° 13' 04.1"	Chogdo	QC		√		
NC12/37	34° 06' 50.4"	77° 13' 06.5"	Chogdo	QC		√		
NC12/38	34° 07' 09.2"	77° 13' 44.8"	Nurla	QC		√		
NC12/39	34° 07' 09.2"	77° 13' 44.8"	Nurla	QC	√	√	√	
NC12/40	34° 07' 09.2"	77° 13' 44.8"	Nurla	QC	√	√	√	
NC12/41	34° 07' 35.4"	77° 14' 16.3"	N. Limestone	C	√	√		
NC12/42	34° 07' 35.4"	77° 14' 16.3"	N. Limestone	C		√		
NC12/43	34° 07' 32.9"	77° 15' 28.5"	N. Limestone	C		√	√	
NC12/44	34° 07' 32.9"	77° 15' 28.5"	Nurla	Q				
NC12/45	34° 07' 31.3"	77° 15' 40.3"	Nurla	QC	√	√	√	
NC12/46	34° 07' 31.3"	77° 15' 40.3"	Nurla	Q				

Sample No	Latitude	Longitude	Formation	Mineralogy*	Trace & REE	Stable Isotope	Sr Isotope	Pb Isotope
NC12/47	34° 08' 13.0"	77° 16' 45.0"	Nurla	QC	√	√	√	√
NC12/48	34° 08' 14.8"	77° 16' 48.6"	Nurla	C	√	√	√	√
NC12/49	34° 08' 20.5"	77° 16' 55.1"	Nurla	QC	√	√	√	
NC12/50	34° 08' 33.1"	77° 17' 12.2"	Nurla	Q				
NC12/51	34° 08' 33.9"	77° 17' 16.6"	Nurla	QC	√			√
NC12/52	34° 08' 31.3"	77° 18' 00.1"	Choksti	QC	√		√	
NC12/53	34° 08' 45.6"	77° 18' 27.3"	Nurla	QC	√	√		
NC12/54	34° 08' 49.1"	77° 18' 27.3"	Nurla	QC	√	√		
NC12/55	34° 09' 22.5"	77° 19' 03.2"	Nurla	Q				

*Mineralogy: Q = Quartz, C = Calcite, QC = Co paired Quartz–Calcite

A-4) Lato–Miru–Upshi (LMU) Section of SLAP:

Sample No	Latitude	Longitude	Formation	Mineralogy*	Trace & REE	Stable Isotope	Sr Isotope	Pb Isotope
LMU12/1	33° 40' 47.7"	77° 43' 36.9"	Lamayuru	C	√	√	√	
LMU12/2	33° 40' 47.7"	77° 43' 36.9"	Lamayuru	C	√	√	√	
LMU12/3	33° 40' 47.7"	77° 43' 36.9"	Lamayuru	QC	√	√	√	√
LMU12/4	33° 40' 54.5"	77° 43' 39.7"	Lato	Q		√		
LMU12/5	33° 40' 54.4"	77° 43' 40.8"	Lato	Q		√		
LMU12/6	33° 40' 54.4"	77° 43' 40.8"	Lato	Q		√		
LMU12/7	33° 40' 54.5"	77° 43' 42.5"	Lato	C	√	√	√	
LMU12/8	33° 40' 54.5"	77° 43' 42.5"	Lato	C	√	√	√	
LMU12/9	33° 41' 06.9"	77° 43' 54.8"	Rong	Q	√			
LMU12/10	33° 41' 12.4"	77° 43' 58.6"	Rong	Q				
LMU12/11	33° 41' 26.7"	77° 44' 19.5"	Rong	C	√	√		
LMU12/12	33° 41' 26.7"	77° 44' 19.5"	Rong	C		√	√	
LMU12/13	33° 41' 38.2"	77° 44' 22.3"	Rong	C	√	√	√	
LMU12/14	33° 41' 38.2"	77° 44' 22.3"	Rong	C	√	√	√	
LMU12/15	33° 41' 44.1"	77° 44' 29.6"	Rong	QC	√	√		
LMU12/16	33° 41' 44.1"	77° 44' 29.6"	Rong	C		√		
LMU12/17	33° 41' 44.1"	77° 44' 29.6"	Rong	C		√		

Sample No	Latitude	Longitude	Formation	Mineralogy*	Trace & REE	Stable Isotope	Sr Isotope	Pb Isotope
LMU12/18	33° 42' 40.6"	77° 44' 36.7"	Rong	C	√	√	√	
LMU12/19	33° 42' 40.6"	77° 44' 36.7"	Rong	C		√		
LMU12/20	33° 42' 49.0"	77° 44' 43.6"	Rong	QC		√		
LMU12/21	33° 43' 25.0"	77° 44' 26.4"	Rong	QC		√		
LMU12/22	33° 43' 54.2"	77° 44' 27.1"	Rong	QC		√		
LMU12/23	33° 43' 54.2"	77° 44' 27.1"	Rong	QC		√		
LMU12/24	33° 43' 54.2"	77° 44' 27.1"	Rong	QC	√	√	√	√
LMU12/25	33° 43' 54.2"	77° 44' 27.1"	Rong	QC	√	√	√	
LMU12/26	33° 44' 04.3"	77° 44' 31.8"	Rong	QC	√	√		
LMU12/27	33° 44' 08.5"	77° 44' 34.4"	Rong	QC	√	√	√	√
LMU12/28	33° 44' 13.9"	77° 44' 54.3"	Miru	QC			√	
LMU12/29	33° 44' 44.4"	77° 45' 19.6"	Miru	Q		√		
LMU12/30	33° 44' 44.4"	77° 45' 19.6"	Miru	Q				
LMU12/31	33° 44' 57.7"	77° 45' 32.3"	Gonmaru La	QC	√		√	
LMU12/32	33° 44' 57.7"	77° 45' 32.3"	Gonmaru La	QC	√	√	√	√
LMU12/33	33° 45' 03.8"	77° 45' 34.2"	Gonmaru La	QC		√		
LMU12/34	33° 45' 34.8"	77° 45' 37.8"	Gonmaru La	QC	√	√	√	
LMU12/35	33° 45' 56.7"	77° 45' 46.2"	Gonmaru La	QC		√		
LMU12/36	33° 45' 56.7"	77° 45' 46.2"	Gonmaru La	QC		√		
LMU12/37	33° 46' 00.1"	77° 45' 52.0"	Gonmaru La	QC	√	√		
LMU12/38	33° 46' 00.1"	77° 45' 52.0"	Gonmaru La	QC		√		
LMU12/39	33° 46' 17.0"	77° 46' 15.4"	Artsa	QC	√	√	√	
LMU12/40	33° 46' 43.8"	77° 46' 26.5"	Umlung	QC		√		
LMU12/41	33° 47' 17.3"	77° 46' 56.3"	Umlung	QC		√		
LMU12/42	33° 47' 23.5"	77° 47' 25.1"	Umlung	QC				
LMU12/43	33° 47' 23.5"	77° 47' 25.1"	Umlung	QC	√	√		
LMU12/44	33° 47' 23.5"	77° 47' 25.1"	Umlung	QC		√		
LMU12/45	33° 48' 34.4"	77° 47' 56.5"	Upshi	QC		√		
LMU12/46	33° 48' 48.0"	77° 48' 31.4"	Upshi	QC		√		
LMU12/47	33° 48' 50.8"	77° 48' 32.0"	Upshi	QC	√	√		

APPENDIX – B:

MICROTHERMOMETRIC MEASUREMENTS

The Microthermometric Measurements of various Fluid inclusions from all four studied sections of PAP (B-1 and B-2 for Shergol and Zildat sections, respectively) and SLAP (B-3 and B-4 for NC and LMU sections, respectively) are illustrated below.

Where T_{im} = initial melting temperature, T_{fm} = final melting temperature, and T_h = homogenization temperature

B-1) Shergol section of PAP:

Sample No.	Type of Inclusion	Inclusion Phase	T_{im}	T_{fm}	T_h	Fluid Composition
ST12/1	Primary	Mono Phase	-182.4	-105		CH ₄
ST12/1	Primary	Mono Phase	-182.4	-105		CH ₄
ST12/1	Primary	Mono Phase	-182.3	-104		CH ₄
ST12/1	Primary	Mono Phase	-182.3	-103		CH ₄
ST12/1	Primary	Mono Phase	-182.3	-99		CH ₄
ST12/1	Primary	Mono Phase	-182.2	-102		CH ₄
ST12/1	Primary	Mono Phase	-182.2	-101		CH ₄
ST12/1	Primary	Mono Phase	-56.7	-18.9		CO ₂
ST12/1	Primary	Mono Phase	-56.7	-18.2		CO ₂
ST12/1	Primary	Mono Phase	-56.6	-19		CO ₂
ST12/1	Primary	Mono Phase	-56.6	-18		CO ₂
ST12/1	Primary	Mono Phase	-56.6	-17.6		CO ₂

Sample No.	Type of Inclusion	Inclusion Phase	T _{im}	T _{fm}	Th	Fluid Composition
ST12/1	Primary	Mono Phase	-56.6	-17		CO ₂
ST12/1	Primary	Mono Phase	-56.6	-15		CO ₂
ST12/1	Primary	Mono Phase	-56.6	-14		CO ₂
ST12/1	Primary	Mono Phase	-56.6	-13.5		CO ₂
ST12/1	Primary	Mono Phase	-56.6	-13		CO ₂
ST12/1	Primary	Bi Phase	-21.4	-16.2	285	H ₂ O-NaCl
ST12/1	Primary	Bi Phase	-21.3	-17.2	290	H ₂ O-NaCl
ST12/1	Primary	Bi Phase	-21.3	-13.9	279	H ₂ O-NaCl
ST12/1	Primary	Bi Phase	-21.3	-13.8	278	H ₂ O-NaCl
ST12/1	Primary	Bi Phase	-21.2	-18.2	295	H ₂ O-NaCl
ST12/1	Primary	Bi Phase	-21.2	-15	283	H ₂ O-NaCl
ST12/1	Primary	Bi Phase	-21.2	-14.8	282	H ₂ O-NaCl
ST12/1	Primary	Bi Phase	-21.2	-14.5	280	H ₂ O-NaCl
ST12/1	Primary	Bi Phase	-21.2	-13.7	277	H ₂ O-NaCl
ST12/1	Primary	Bi Phase	-21.2	-13.3	275	H ₂ O-NaCl
ST12/1	Primary	Bi Phase	-21.2	-13.2	274	H ₂ O-NaCl
ST12/1	Primary	Bi Phase	-21.2	-13.1	270	H ₂ O-NaCl
ST12/1	Secondary	Bi Phase	-21.3	-4.9	150	H ₂ O-NaCl
ST12/1	Secondary	Bi Phase	-21.2	-7.9	180	H ₂ O-NaCl
ST12/1	Secondary	Bi Phase	-21.2	-7.4	179	H ₂ O-NaCl
ST12/1	Secondary	Bi Phase	-21.2	-7	175	H ₂ O-NaCl
ST12/1	Secondary	Bi Phase	-21.2	-6.2	170	H ₂ O-NaCl
ST12/1	Secondary	Bi Phase	-21.2	-5.1	164	H ₂ O-NaCl
ST12/1	Secondary	Bi Phase	-21.2	-6.1	162	H ₂ O-NaCl
ST12/1	Secondary	Bi Phase	-21.2	-5.9	160	H ₂ O-NaCl
ST12/1	Secondary	Bi Phase	-21.2	-5.3	159	H ₂ O-NaCl
ST12/1	Secondary	Bi Phase	-21.2	-5.1	155	H ₂ O-NaCl
ST12/12	Primary	Mono Phase	-58.6	-9.8		CO ₂
ST12/12	Primary	Mono Phase	-58.2	-11.9		CO ₂
ST12/12	Primary	Mono Phase	-56.8	-13.2		CO ₂
ST12/12	Primary	Mono Phase	-56.7	-10.1		CO ₂
ST12/12	Primary	Mono Phase	-56.6	-12.9		CO ₂
ST12/12	Primary	Mono Phase	-56.6	-12.9		CO ₂
ST12/12	Primary	Mono Phase	-56.6	-12.5		CO ₂
ST12/12	Primary	Mono Phase	-56.6	-11.6		CO ₂
ST12/12	Primary	Mono Phase	-56.6	-11.2		CO ₂
ST12/12	Primary	Mono Phase	-56.6	-10.2		CO ₂
ST12/12	Primary	Mono Phase	-56.6	-9.9		CO ₂
ST12/12	Primary	Mono Phase	-56.6	-9.6		CO ₂

Sample No.	Type of Inclusion	Inclusion Phase	T _{im}	T _{fm}	Th	Fluid Composition
ST12/12	Primary	Mono Phase	-56.6	-9.5		CO ₂
ST12/12	Primary	Mono Phase	-56.2	-12.2		CO ₂
ST12/12	Primary	Mono Phase	-56.2	-11.2		CO ₂
ST12/12	Primary	Bi Phase	-21.5	-15.8	279	H ₂ O-NaCl
ST12/12	Primary	Bi Phase	-21.4	-16.8	222	H ₂ O-NaCl
ST12/12	Primary	Bi Phase	-21.3	-15.8	278	H ₂ O-NaCl
ST12/12	Primary	Bi Phase	-21.3	-14.2	276	H ₂ O-NaCl
ST12/12	Primary	Bi Phase	-21.3	-12.2	260	H ₂ O-NaCl
ST12/12	Primary	Bi Phase	-21.3	-11.2	258	H ₂ O-NaCl
ST12/12	Primary	Bi Phase	-21.2	-17.8	285	H ₂ O-NaCl
ST12/12	Primary	Bi Phase	-21.2	-14.8	281	H ₂ O-NaCl
ST12/12	Primary	Bi Phase	-21.2	-16.6	280	H ₂ O-NaCl
ST12/12	Primary	Bi Phase	-21.2	-14.3	274	H ₂ O-NaCl
ST12/12	Primary	Bi Phase	-21.2	-12.4	268	H ₂ O-NaCl
ST12/12	Primary	Bi Phase	-21.2	-12.6	262	H ₂ O-NaCl
ST12/12	Primary	Bi Phase	-21.2	-12.3	261	H ₂ O-NaCl
ST12/12	Primary	Bi Phase	-21.2	-12.5	260	H ₂ O-NaCl
ST12/12	Secondary	Bi Phase	-21.6	-4.2	175	H ₂ O-NaCl
ST12/12	Secondary	Bi Phase	-21.3	-8.4	210	H ₂ O-NaCl
ST12/12	Secondary	Bi Phase	-21.3	-7.2	202	H ₂ O-NaCl
ST12/12	Secondary	Bi Phase	-21.3	-3.8	165	H ₂ O-NaCl
ST12/12	Secondary	Bi Phase	-21.2	-7.9	205	H ₂ O-NaCl
ST12/12	Secondary	Bi Phase	-21.2	-7.2	201	H ₂ O-NaCl
ST12/12	Secondary	Bi Phase	-21.2	-6.8	198	H ₂ O-NaCl
ST12/12	Secondary	Bi Phase	-21.2	-6.7	197	H ₂ O-NaCl
ST12/12	Secondary	Bi Phase	-21.2	-6.2	195	H ₂ O-NaCl
ST12/12	Secondary	Bi Phase	-21.2	-5.6	192	H ₂ O-NaCl
ST12/12	Secondary	Bi Phase	-21.2	-5.2	190	H ₂ O-NaCl
ST12/14	Primary	Mono Phase	-183.5	-102		CH ₄
ST12/14	Primary	Mono Phase	-183.2	-101		CH ₄
ST12/14	Primary	Mono Phase	-182.5	-103		CH ₄
ST12/14	Primary	Mono Phase	-182.2	-107		CH ₄
ST12/14	Primary	Mono Phase	-182.2	-105		CH ₄
ST12/14	Primary	Mono Phase	-182.2	-99		CH ₄
ST12/14	Primary	Mono Phase	-56.7	-13.8		CO ₂
ST12/14	Primary	Mono Phase	-56.6	-12.7		CO ₂
ST12/14	Primary	Mono Phase	-56.6	-12.5		CO ₂
ST12/14	Primary	Mono Phase	-56.6	-12.3		CO ₂
ST12/14	Primary	Mono Phase	-56.6	-12		CO ₂

Sample No.	Type of Inclusion	Inclusion Phase	T _{im}	T _{fm}	Th	Fluid Composition
ST12/14	Primary	Mono Phase	-56.6	-10		CO ₂
ST12/14	Primary	Mono Phase	-56.6	-8		CO ₂
ST12/14	Primary	Bi Phase	-21.5	-16.2	282	H ₂ O-NaCl
ST12/14	Primary	Bi Phase	-21.4	-18.2	298	H ₂ O-NaCl
ST12/14	Primary	Bi Phase	-21.4	-16.7	288	H ₂ O-NaCl
ST12/14	Primary	Bi Phase	-21.3	-16.8	290	H ₂ O-NaCl
ST12/14	Primary	Bi Phase	-21.3	-16.5	285	H ₂ O-NaCl
ST12/14	Primary	Bi Phase	-21.3	-16	280	H ₂ O-NaCl
ST12/14	Primary	Bi Phase	-21.3	-15	279	H ₂ O-NaCl
ST12/14	Primary	Bi Phase	-21.2	-18	295	H ₂ O-NaCl
ST12/14	Primary	Bi Phase	-21.2	-17	289	H ₂ O-NaCl
ST12/14	Primary	Bi Phase	-21.2	-14	278	H ₂ O-NaCl
ST12/14	Primary	Bi Phase	-21.2	-14	275	H ₂ O-NaCl
ST12/14	Secondary	Bi Phase	-21.3	-7.9	175	H ₂ O-NaCl
ST12/14	Secondary	Bi Phase	-21.3	-6.9	170	H ₂ O-NaCl
ST12/14	Secondary	Bi Phase	-21.3	-6.5	165	H ₂ O-NaCl
ST12/14	Secondary	Bi Phase	-21.3	-5.4	156	H ₂ O-NaCl
ST12/14	Secondary	Bi Phase	-21.2	-8.2	189	H ₂ O-NaCl
ST12/14	Secondary	Bi Phase	-21.2	-8.1	176	H ₂ O-NaCl
ST12/14	Secondary	Bi Phase	-21.2	-6.2	163	H ₂ O-NaCl
ST12/14	Secondary	Bi Phase	-21.2	-5.9	160	H ₂ O-NaCl
ST12/14	Secondary	Bi Phase	-21.2	-5.5	159	H ₂ O-NaCl
ST12/14	Secondary	Bi Phase	-21.2	-5.3	157	H ₂ O-NaCl
ST12/24	Primary	Mono Phase	-56.8	-18.5		CO ₂
ST12/24	Primary	Mono Phase	-56.7	-19.7		CO ₂
ST12/24	Primary	Mono Phase	-56.7	-17		CO ₂
ST12/24	Primary	Mono Phase	-56.6	-19		CO ₂
ST12/24	Primary	Mono Phase	-56.6	-18.6		CO ₂
ST12/24	Primary	Mono Phase	-56.5	-18		CO ₂
ST12/24	Primary	Bi Phase	-21.3	-17.5	285	H ₂ O-NaCl
ST12/24	Primary	Bi Phase	-21.3	-15	275	H ₂ O-NaCl
ST12/24	Primary	Bi Phase	-21.3	-14	274	H ₂ O-NaCl
ST12/24	Primary	Bi Phase	-21.2	-17.6	287	H ₂ O-NaCl
ST12/24	Primary	Bi Phase	-21.2	-16.6	283	H ₂ O-NaCl
ST12/24	Primary	Bi Phase	-21.2	-17	282	H ₂ O-NaCl
ST12/24	Primary	Bi Phase	-21.2	-16	282	H ₂ O-NaCl
ST12/24	Primary	Bi Phase	-21.2	-15.5	277	H ₂ O-NaCl
ST12/24	Primary	Bi Phase	-21.2	-13.5	270	H ₂ O-NaCl
ST12/24	Secondary	Bi Phase	-21.4	-3.6	187	H ₂ O-NaCl

Sample No.	Type of Inclusion	Inclusion Phase	T _{im}	T _{fm}	Th	Fluid Composition
ST12/24	Secondary	Bi Phase	-21.4	-2.9	180	H ₂ O-NaCl
ST12/24	Secondary	Bi Phase	-21.3	-4.9	217	H ₂ O-NaCl
ST12/24	Secondary	Bi Phase	-21.3	-3.9	194	H ₂ O-NaCl
ST12/24	Secondary	Bi Phase	-21.2	-6	215	H ₂ O-NaCl
ST12/24	Secondary	Bi Phase	-21.2	-4.7	212	H ₂ O-NaCl
ST12/24	Secondary	Bi Phase	-21.2	-5.8	210	H ₂ O-NaCl
ST12/24	Secondary	Bi Phase	-21.2	-5	200	H ₂ O-NaCl
ST12/28	Primary	Mono Phase	-182.6	-103		CH ₄
ST12/28	Primary	Mono Phase	-182.4	-105		CH ₄
ST12/28	Primary	Mono Phase	-182.3	-101		CH ₄
ST12/28	Primary	Mono Phase	-182.2	-110		CH ₄
ST12/28	Primary	Mono Phase	-56.6	-17.2		CO ₂
ST12/28	Primary	Mono Phase	-56.6	-16.2		CO ₂
ST12/28	Primary	Mono Phase	-56.6	-15.2		CO ₂
ST12/28	Primary	Mono Phase	-56.6	-14.2		CO ₂
ST12/28	Primary	Mono Phase	-56.6	-13.5		CO ₂
ST12/28	Primary	Mono Phase	-56.6	-12.4		CO ₂
ST12/28	Primary	Mono Phase	-56.6	-12.3		CO ₂
ST12/28	Primary	Bi Phase	-21.2	-16.8	290	H ₂ O-NaCl
ST12/28	Primary	Bi Phase	-21.2	-17.5	288	H ₂ O-NaCl
ST12/28	Primary	Bi Phase	-21.2	-17.2	285	H ₂ O-NaCl
ST12/28	Primary	Bi Phase	-21.2	-17	280	H ₂ O-NaCl
ST12/28	Primary	Bi Phase	-21.2	-16.7	278	H ₂ O-NaCl
ST12/28	Primary	Bi Phase	-21.2	-16.5	275	H ₂ O-NaCl
ST12/28	Primary	Bi Phase	-21.2	-16	270	H ₂ O-NaCl
ST12/28	Primary	Bi Phase	-21.2	-14	265	H ₂ O-NaCl
ST12/28	Secondary	Bi Phase	-21.3	-4.1	179	H ₂ O-NaCl
ST12/28	Secondary	Bi Phase	-21.2	-5.6	186	H ₂ O-NaCl
ST12/28	Secondary	Bi Phase	-21.2	-4.3	183	H ₂ O-NaCl
ST12/28	Secondary	Bi Phase	-21.2	-4.2	182	H ₂ O-NaCl
ST12/28	Secondary	Bi Phase	-21.2	-4	180	H ₂ O-NaCl
ST12/28	Secondary	Bi Phase	-21.2	-3	170	H ₂ O-NaCl
ST12/39	Primary	Mono Phase	-182.6	-112		CH ₄
ST12/39	Primary	Mono Phase	-182.5	-110		CH ₄
ST12/39	Primary	Mono Phase	-182.4	-101		CH ₄
ST12/39	Primary	Mono Phase	-182.3	-102		CH ₄
ST12/39	Primary	Mono Phase	-182.2	-113		CH ₄
ST12/39	Primary	Mono Phase	-182.2	-93		CH ₄
ST12/39	Primary	Mono Phase	-182.2	-92		CH ₄

Sample No.	Type of Inclusion	Inclusion Phase	T _{im}	T _{fm}	Th	Fluid Composition
ST12/39	Primary	Mono Phase	-56.6	-17.5		CO ₂
ST12/39	Primary	Mono Phase	-56.6	-17		CO ₂
ST12/39	Primary	Mono Phase	-56.6	-17		CO ₂
ST12/39	Primary	Mono Phase	-56.6	-16		CO ₂
ST12/39	Primary	Mono Phase	-56.6	-16		CO ₂
ST12/39	Primary	Mono Phase	-56.6	-14		CO ₂
ST12/39	Primary	Mono Phase	-56.6	-13.5		CO ₂
ST12/39	Primary	Mono Phase	-56.6	-13		CO ₂
ST12/39	Primary	Mono Phase	-56.6	-12		CO ₂
ST12/39	Primary	Bi Phase	-21.4	-16.8	281	H ₂ O-NaCl
ST12/39	Primary	Bi Phase	-21.3	-16.5	283	H ₂ O-NaCl
ST12/39	Primary	Bi Phase	-21.3	-16.9	282	H ₂ O-NaCl
ST12/39	Primary	Bi Phase	-21.3	-14	275	H ₂ O-NaCl
ST12/39	Primary	Bi Phase	-21.2	-17.4	284	H ₂ O-NaCl
ST12/39	Primary	Bi Phase	-21.2	-17	283	H ₂ O-NaCl
ST12/39	Primary	Bi Phase	-21.2	-16.2	279	H ₂ O-NaCl
ST12/39	Primary	Bi Phase	-21.2	-15.5	279	H ₂ O-NaCl
ST12/39	Primary	Bi Phase	-21.2	-16	278	H ₂ O-NaCl
ST12/39	Secondary	Bi Phase	-21.4	-9.6	194	H ₂ O-NaCl
ST12/39	Secondary	Bi Phase	-21.3	-7.8	190	H ₂ O-NaCl
ST12/39	Secondary	Bi Phase	-21.3	-5.2	175	H ₂ O-NaCl
ST12/39	Secondary	Bi Phase	-21.3	-4.8	170	H ₂ O-NaCl
ST12/39	Secondary	Bi Phase	-21.2	-10	195	H ₂ O-NaCl
ST12/39	Secondary	Bi Phase	-21.2	-9.5	193	H ₂ O-NaCl
ST12/39	Secondary	Bi Phase	-21.2	-9.2	192	H ₂ O-NaCl
ST12/39	Secondary	Bi Phase	-21.2	-6.8	184	H ₂ O-NaCl
ST12/39	Secondary	Bi Phase	-21.2	-7.5	180	H ₂ O-NaCl

B-2) Zildat section of PAP:

Sample No.	Type of Inclusion	Inclusion Phase	T_{im}	T_{fm}	T_h	Fluid Composition
ZV13/1	Primary	Mono Phase	-182.5	-90.0		CH ₄
ZV13/1	Primary	Mono Phase	-181.2	-100.0		CH ₄
ZV13/1	Primary	Mono Phase	-181.2	-95.0		CH ₄
ZV13/1	Primary	Mono Phase	-56.8	-15.0		CO ₂
ZV13/1	Primary	Mono Phase	-56.7	-15.0		CO ₂
ZV13/1	Primary	Mono Phase	-56.7	-13.6		CO ₂
ZV13/1	Primary	Mono Phase	-56.7	-13.0		CO ₂
ZV13/1	Primary	Mono Phase	-56.6	-17.0		CO ₂
ZV13/1	Primary	Mono Phase	-56.6	-14.0		CO ₂
ZV13/1	Primary	Mono Phase	-56.5	-16.0		CO ₂
ZV13/1	Primary	Mono Phase	-56.5	-12.6		CO ₂
ZV13/1	Primary	Bi Phase	-23.8	-13.8	310.0	H ₂ O-NaCl
ZV13/1	Primary	Bi Phase	-23.7	-13.4	325.0	H ₂ O-NaCl
ZV13/1	Primary	Bi Phase	-23.2	-14.1	311.0	H ₂ O-NaCl
ZV13/1	Primary	Bi Phase	-22.8	-16.2	300.0	H ₂ O-NaCl
ZV13/1	Primary	Bi Phase	-21.8	-12.2	275.0	H ₂ O-NaCl
ZV13/1	Primary	Bi Phase	-21.6	-13.2	270.0	H ₂ O-NaCl
ZV13/1	Primary	Bi Phase	-21.5	-17.2	265.0	H ₂ O-NaCl
ZV13/1	Primary	Bi Phase	-21.5	-8.6	236.0	H ₂ O-NaCl
ZV13/1	Primary	Bi Phase	-21.4	-7.1	258.0	H ₂ O-NaCl
ZV13/1	Primary	Bi Phase	-21.3	-6.1	230.0	H ₂ O-NaCl
ZV13/1	Primary	Bi Phase	-21.2	-15.2	315.0	H ₂ O-NaCl
ZV13/1	Primary	Bi Phase	-21.2	-14.6	261.0	H ₂ O-NaCl
ZV13/1	Primary	Bi Phase	-21.2	-3.1	228.0	H ₂ O-NaCl
ZV13/1	Primary	Bi Phase	-21.2	-2.1	226.0	H ₂ O-NaCl
ZV13/1	Primary	Bi Phase	-21.2	-15.6	212.0	H ₂ O-NaCl
ZV13/1	Secondary	Bi Phase	-23.1	-5.2	149	H ₂ O-NaCl
ZV13/1	Secondary	Bi Phase	-22.1	-3.2	200	H ₂ O-NaCl
ZV13/1	Secondary	Bi Phase	-22.1	-4.2	148	H ₂ O-NaCl
ZV13/1	Secondary	Bi Phase	-21.2	-3.2	185	H ₂ O-NaCl
ZV13/1	Secondary	Bi Phase	-21.2	-8.2	175	H ₂ O-NaCl
ZV13/10	Primary	Mono Phase	-182.5	-100.0		CH ₄
ZV13/10	Primary	Mono Phase	-182.3	-111.0		CH ₄
ZV13/10	Primary	Mono Phase	-182.2	-110.0		CH ₄
ZV13/10	Primary	Mono Phase	-182.2	-107.0		CH ₄
ZV13/10	Primary	Mono Phase	-182.2	-105.0		CH ₄
ZV13/10	Primary	Mono Phase	-181.9	-106.0		CH ₄

Sample No.	Type of Inclusion	Inclusion Phase	T _{im}	T _{fm}	Th	Fluid Composition
ZV13/10	Primary	Mono Phase	-181.2	-109.0		CH ₄
ZV13/10	Primary	Mono Phase	-56.8	-14.0		CO ₂
ZV13/10	Primary	Mono Phase	-56.7	-13.5		CO ₂
ZV13/10	Primary	Mono Phase	-56.7	-12.3		CO ₂
ZV13/10	Primary	Mono Phase	-56.7	-11.6		CO ₂
ZV13/10	Primary	Mono Phase	-56.6	-13.2		CO ₂
ZV13/10	Primary	Mono Phase	-56.6	-12.5		CO ₂
ZV13/10	Primary	Mono Phase	-56.6	-11.9		CO ₂
ZV13/10	Primary	Mono Phase	-56.4	-10.5		CO ₂
ZV13/10	Primary	Mono Phase	-56.3	-13.9		CO ₂
ZV13/10	Primary	Bi Phase	-21.3	-15.0	249.0	H ₂ O-NaCl
ZV13/10	Primary	Bi Phase	-21.3	-14.0	245.0	H ₂ O-NaCl
ZV13/10	Primary	Bi Phase	-21.3	-14.0	245.0	H ₂ O-NaCl
ZV13/10	Primary	Bi Phase	-21.3	-12.6	230.0	H ₂ O-NaCl
ZV13/10	Primary	Bi Phase	-21.2	-16.6	255.0	H ₂ O-NaCl
ZV13/10	Primary	Bi Phase	-21.2	-15.3	251.2	H ₂ O-NaCl
ZV13/10	Primary	Bi Phase	-21.2	-16.0	251.0	H ₂ O-NaCl
ZV13/10	Primary	Bi Phase	-21.2	-15.2	250.0	H ₂ O-NaCl
ZV13/10	Primary	Bi Phase	-21.2	-3.3	235.0	H ₂ O-NaCl
ZV13/10	Primary	Bi Phase	-21.2	-13.0	230.0	H ₂ O-NaCl
ZV13/10	Secondary	Bi Phase	-21.3	-3.9	189	H ₂ O-NaCl
ZV13/10	Secondary	Bi Phase	-21.2	-4.9	196	H ₂ O-NaCl
ZV13/10	Secondary	Bi Phase	-21.2	-4.6	195	H ₂ O-NaCl
ZV13/10	Secondary	Bi Phase	-21.2	-4.7	192	H ₂ O-NaCl
ZV13/10	Secondary	Bi Phase	-21.2	-4.5	190	H ₂ O-NaCl
ZV13/10	Secondary	Bi Phase	-21.2	-3.5	185	H ₂ O-NaCl
ZV13/10	Secondary	Bi Phase	-21.2	-3.2	183	H ₂ O-NaCl
ZV13/10	Secondary	Bi Phase	-21.2	-2.9	180	H ₂ O-NaCl
ZV13/10	Secondary	Bi Phase	-21.2	-2.6	175	H ₂ O-NaCl
ZV13/11	Primary	Mono Phase	-183.4	-110.0		CH ₄
ZV13/11	Primary	Mono Phase	-182.5	-118.0		CH ₄
ZV13/11	Primary	Mono Phase	-182.4	-119.0		CH ₄
ZV13/11	Primary	Mono Phase	-182.4	-117.0		CH ₄
ZV13/11	Primary	Mono Phase	-182.3	-120.0		CH ₄
ZV13/11	Primary	Mono Phase	-182.3	-113.0		CH ₄
ZV13/11	Primary	Mono Phase	-182.2	-115.0		CH ₄
ZV13/11	Primary	Mono Phase	-58.2	-13.5		CO ₂
ZV13/11	Primary	Mono Phase	-58.2	-13.2		CO ₂
ZV13/11	Primary	Mono Phase	-57.2	-14.7		CO ₂

Sample No.	Type of Inclusion	Inclusion Phase	T _{im}	T _{fm}	Th	Fluid Composition
ZV13/11	Primary	Mono Phase	-56.8	-15.0		CO ₂
ZV13/11	Primary	Mono Phase	-56.7	-14.8		CO ₂
ZV13/11	Primary	Mono Phase	-56.6	-14.5		CO ₂
ZV13/11	Primary	Mono Phase	-56.6	-13.2		CO ₂
ZV13/11	Primary	Mono Phase	-56.6	-12.2		CO ₂
ZV13/11	Primary	Mono Phase	-56.6	-12.0		CO ₂
ZV13/11	Primary	Bi Phase	-22.1	-19.0	260.0	H ₂ O-NaCl
ZV13/11	Primary	Bi Phase	-21.8	-18.2	258.0	H ₂ O-NaCl
ZV13/11	Primary	Bi Phase	-21.7	-16.2	252.0	H ₂ O-NaCl
ZV13/11	Primary	Bi Phase	-21.6	-14.2	250.0	H ₂ O-NaCl
ZV13/11	Primary	Bi Phase	-21.6	-15.2	250.0	H ₂ O-NaCl
ZV13/11	Primary	Bi Phase	-21.5	-13.2	245.0	H ₂ O-NaCl
ZV13/11	Primary	Bi Phase	-21.3	-17.9	256.0	H ₂ O-NaCl
ZV13/11	Primary	Bi Phase	-21.2	-17.8	255.0	H ₂ O-NaCl
ZV13/11	Primary	Bi Phase	-21.2	-16.8	251.0	H ₂ O-NaCl
ZV13/11	Primary	Bi Phase	-21.2	-15.0	249.0	H ₂ O-NaCl
ZV13/11	Secondary	Bi Phase	-21.3	-4.2	185	H ₂ O-NaCl
ZV13/11	Secondary	Bi Phase	-21.3	-3.0	175	H ₂ O-NaCl
ZV13/11	Secondary	Bi Phase	-21.3	-2.4	172	H ₂ O-NaCl
ZV13/11	Secondary	Bi Phase	-21.3	-2.5	170	H ₂ O-NaCl
ZV13/11	Secondary	Bi Phase	-21.3	-2.0	165	H ₂ O-NaCl
ZV13/11	Secondary	Bi Phase	-21.2	-5.5	200	H ₂ O-NaCl
ZV13/11	Secondary	Bi Phase	-21.2	-5.0	197	H ₂ O-NaCl
ZV13/11	Secondary	Bi Phase	-21.2	-3.5	177	H ₂ O-NaCl
ZV13/11	Secondary	Bi Phase	-21.2	-3.0	175	H ₂ O-NaCl
ZV13/11	Secondary	Bi Phase	-21.2	-4.0	172	H ₂ O-NaCl
ZV13/12	Primary	Mono Phase	-183.4	-108.0		CH ₄
ZV13/12	Primary	Mono Phase	-182.5	-109.0		CH ₄
ZV13/12	Primary	Mono Phase	-182.4	-103.0		CH ₄
ZV13/12	Primary	Mono Phase	-182.4	-103.0		CH ₄
ZV13/12	Primary	Mono Phase	-182.4	-101.0		CH ₄
ZV13/12	Primary	Mono Phase	-182.3	-101.0		CH ₄
ZV13/12	Primary	Mono Phase	-182.2	-102.0		CH ₄
ZV13/12	Primary	Mono Phase	-181.5	-110.0		CH ₄
ZV13/12	Primary	Mono Phase	-181.2	-107.0		CH ₄
ZV13/12	Primary	Mono Phase	-57.8	-7.2		CO ₂
ZV13/12	Primary	Mono Phase	-57.1	-6.2		CO ₂
ZV13/12	Primary	Mono Phase	-56.9	-8.6		CO ₂
ZV13/12	Primary	Mono Phase	-56.8	-10.0		CO ₂

Sample No.	Type of Inclusion	Inclusion Phase	T _{im}	T _{fm}	Th	Fluid Composition
ZV13/12	Primary	Mono Phase	-56.7	-11.0		CO ₂
ZV13/12	Primary	Mono Phase	-56.6	-20.1		CO ₂
ZV13/12	Primary	Mono Phase	-56.6	-18.2		CO ₂
ZV13/12	Primary	Mono Phase	-56.6	-13.2		CO ₂
ZV13/12	Primary	Mono Phase	-56.6	-11.2		CO ₂
ZV13/12	Primary	Mono Phase	-56.5	-19.2		CO ₂
ZV13/12	Primary	Bi Phase	-22.4	-14.2	235.0	H ₂ O-NaCl
ZV13/12	Primary	Bi Phase	-21.9	-12.4	230.0	H ₂ O-NaCl
ZV13/12	Primary	Bi Phase	-21.6	-13.2	234.0	H ₂ O-NaCl
ZV13/12	Primary	Bi Phase	-21.4	-14.2	233.0	H ₂ O-NaCl
ZV13/12	Primary	Bi Phase	-21.3	-18.2	241.0	H ₂ O-NaCl
ZV13/12	Primary	Bi Phase	-21.3	-14.6	232.0	H ₂ O-NaCl
ZV13/12	Primary	Bi Phase	-21.2	-16.7	240.0	H ₂ O-NaCl
ZV13/12	Primary	Bi Phase	-21.2	-13.6	233.0	H ₂ O-NaCl
ZV13/12	Primary	Bi Phase	-21.1	-14.2	233.0	H ₂ O-NaCl
ZV13/12	Secondary	Bi Phase	-22.6	-3.8	191	H ₂ O-NaCl
ZV13/12	Secondary	Bi Phase	-21.4	-4.9	196	H ₂ O-NaCl
ZV13/12	Secondary	Bi Phase	-21.3	-4.2	196	H ₂ O-NaCl
ZV13/12	Secondary	Bi Phase	-21.3	-4.4	194	H ₂ O-NaCl
ZV13/12	Secondary	Bi Phase	-21.3	-3.9	188	H ₂ O-NaCl
ZV13/12	Secondary	Bi Phase	-21.3	-4.2	180	H ₂ O-NaCl
ZV13/12	Secondary	Bi Phase	-21.2	-5.2	196	H ₂ O-NaCl
ZV13/12	Secondary	Bi Phase	-21.2	-4.6	195	H ₂ O-NaCl
ZV13/12	Secondary	Bi Phase	-21.2	-5.0	195	H ₂ O-NaCl
ZV13/12	Secondary	Bi Phase	-21.2	-2.9	182	H ₂ O-NaCl
ZV13/16	Primary	Mono Phase	-56.9	-11.2		CO ₂
ZV13/16	Primary	Mono Phase	-56.8	-12.3		CO ₂
ZV13/16	Primary	Mono Phase	-56.8	-10.0		CO ₂
ZV13/16	Primary	Mono Phase	-56.7	-12.2		CO ₂
ZV13/16	Primary	Mono Phase	-56.7	-11.9		CO ₂
ZV13/16	Primary	Mono Phase	-56.7	-7.9		CO ₂
ZV13/16	Primary	Mono Phase	-56.6	-8.0		CO ₂
ZV13/16	Primary	Mono Phase	-56.6	-6.0		CO ₂
ZV13/16	Primary	Mono Phase	-56.6	-4.0		CO ₂
ZV13/16	Primary	Bi Phase	-21.2	-18.5	295.0	H ₂ O-NaCl
ZV13/16	Primary	Bi Phase	-21.2	-18.4	294.0	H ₂ O-NaCl
ZV13/16	Primary	Bi Phase	-21.2	-18.2	293.0	H ₂ O-NaCl
ZV13/16	Primary	Bi Phase	-21.2	-17.5	290.0	H ₂ O-NaCl
ZV13/16	Primary	Bi Phase	-21.2	-17.2	289.0	H ₂ O-NaCl

Sample No.	Type of Inclusion	Inclusion Phase	T _{im}	T _{fm}	Th	Fluid Composition
ZV13/16	Primary	Bi Phase	-21.2	-17.0	288.0	H ₂ O-NaCl
ZV13/16	Primary	Bi Phase	-21.2	-16.6	286.0	H ₂ O-NaCl
ZV13/16	Primary	Bi Phase	-21.2	-16.5	285.0	H ₂ O-NaCl
ZV13/16	Primary	Bi Phase	-21.2	-16.2	280.0	H ₂ O-NaCl
ZV13/16	Primary	Bi Phase	-21.2	-15.9	279.0	H ₂ O-NaCl
ZV13/16	Primary	Bi Phase	-21.2	-14.2	274.0	H ₂ O-NaCl
ZV13/16	Primary	Bi Phase	-21.2	-13.9	272.0	H ₂ O-NaCl
ZV13/16	Secondary	Bi Phase	-21.3	-5.8	184	H ₂ O-NaCl
ZV13/16	Secondary	Bi Phase	-21.3	-4.5	179	H ₂ O-NaCl
ZV13/16	Secondary	Bi Phase	-21.3	-3.7	177	H ₂ O-NaCl
ZV13/16	Secondary	Bi Phase	-21.3	-3.6	176	H ₂ O-NaCl
ZV13/16	Secondary	Bi Phase	-21.3	-3.3	172	H ₂ O-NaCl
ZV13/16	Secondary	Bi Phase	-21.2	-7.8	191	H ₂ O-NaCl
ZV13/16	Secondary	Bi Phase	-21.2	-6.7	186	H ₂ O-NaCl
ZV13/16	Secondary	Bi Phase	-21.2	-6.6	184	H ₂ O-NaCl
ZV13/16	Secondary	Bi Phase	-21.2	-5.9	183	H ₂ O-NaCl
ZV13/16	Secondary	Bi Phase	-21.2	-4.9	180	H ₂ O-NaCl
ZV13/16	Secondary	Bi Phase	-21.2	-4.2	178	H ₂ O-NaCl
ZV13/16	Secondary	Bi Phase	-21.2	-3.9	175	H ₂ O-NaCl
ZV13/16	Secondary	Bi Phase	-21.2	-2.9	170	H ₂ O-NaCl
ZV13/3	Primary	Mono Phase	-183.2	-90.0		CH ₄
ZV13/3	Primary	Mono Phase	-183.1	-101.0		CH ₄
ZV13/3	Primary	Mono Phase	-182.3	-98.0		CH ₄
ZV13/3	Primary	Mono Phase	-182.1	-95.0		CH ₄
ZV13/3	Primary	Mono Phase	-181.2	-94.0		CH ₄
ZV13/3	Primary	Mono Phase	-57.8	-11.0		CO ₂
ZV13/3	Primary	Mono Phase	-56.7	-11.6		CO ₂
ZV13/3	Primary	Mono Phase	-56.6	-14.5		CO ₂
ZV13/3	Primary	Mono Phase	-56.6	-13.5		CO ₂
ZV13/3	Primary	Mono Phase	-56.6	-13.0		CO ₂
ZV13/3	Primary	Mono Phase	-56.6	-13.0		CO ₂
ZV13/3	Primary	Mono Phase	-56.6	-12.8		CO ₂
ZV13/3	Primary	Mono Phase	-56.6	-12.8		CO ₂
ZV13/3	Primary	Mono Phase	-56.6	-12.7		CO ₂
ZV13/3	Primary	Mono Phase	-56.6	-12.5		CO ₂
ZV13/3	Primary	Mono Phase	-56.6	-11.2		CO ₂
ZV13/3	Primary	Mono Phase	-56.4	-12.5		CO ₂
ZV13/3	Primary	Bi Phase	-22.2	-15.0	255.0	H ₂ O-NaCl
ZV13/3	Primary	Bi Phase	-21.8	-17.0	265.0	H ₂ O-NaCl

Sample No.	Type of Inclusion	Inclusion Phase	T_{im}	T_{fm}	T_h	Fluid Composition
ZV13/3	Primary	Bi Phase	-21.6	-17.0	270.0	H ₂ O-NaCl
ZV13/3	Primary	Bi Phase	-21.6	-18.0	265.0	H ₂ O-NaCl
ZV13/3	Primary	Bi Phase	-21.6	-16.0	264.0	H ₂ O-NaCl
ZV13/3	Primary	Bi Phase	-21.6	-14.5	260.0	H ₂ O-NaCl
ZV13/3	Primary	Bi Phase	-21.4	-14.6	261.0	H ₂ O-NaCl
ZV13/3	Primary	Bi Phase	-21.3	-13.2	255.0	H ₂ O-NaCl
ZV13/3	Primary	Bi Phase	-21.2	-20.0	275.0	H ₂ O-NaCl
ZV13/3	Primary	Bi Phase	-21.2	-14.2	250.0	H ₂ O-NaCl
ZV13/3	Secondary	Bi Phase	-21.5	-6.8	195	H ₂ O-NaCl
ZV13/3	Secondary	Bi Phase	-21.5	-5.2	192	H ₂ O-NaCl
ZV13/3	Secondary	Bi Phase	-21.4	-4.9	188	H ₂ O-NaCl
ZV13/3	Secondary	Bi Phase	-21.3	-8.0	200	H ₂ O-NaCl
ZV13/3	Secondary	Bi Phase	-21.3	-5.9	191	H ₂ O-NaCl
ZV13/3	Secondary	Bi Phase	-21.3	-3.0	188	H ₂ O-NaCl
ZV13/3	Secondary	Bi Phase	-21.3	-2.0	180	H ₂ O-NaCl
ZV13/3	Secondary	Bi Phase	-21.2	-4.0	190	H ₂ O-NaCl
ZV13/3	Secondary	Bi Phase	-21.2	-6.1	190	H ₂ O-NaCl

B-3) Nimu-Chilling (NC) section of SLAP:

Sample No.	Type of Inclusion	Inclusion Phase	Tim	Tfm	Th	Fluid Composition
NC11/25/ 1A/1B	Primary	Mono Phase	-184.5	-163.4		CH ₄
NC11/25/ 1A/1B	Primary	Mono Phase	-183.6	-104		CH ₄
NC11/25/ 1A/1B	Primary	Mono Phase	-183.5	-156		CH ₄
NC11/25/ 1A/1B	Primary	Mono Phase	-183.3	-157		CH ₄
NC11/25/ 1A/1B	Primary	Mono Phase	-183.2	-119		CH ₄
NC11/25/ 1A/1B	Primary	Mono Phase	-183.1	-153		CH ₄
NC11/25/ 1A/1B	Primary	Mono Phase	-181.7	-159		CH ₄
NC11/25/ 1A/1B	Primary	Mono Phase	-180.4	-149		CH ₄
NC11/25/ 1A/1B	Primary	Mono Phase	-57.8	-18		CO ₂
NC11/25/ 1A/1B	Primary	Mono Phase	-56.2	-20		CO ₂
NC11/25/ 1A/1B	Primary	Bi Phase	-23	-5.6	223	H ₂ O-NaCl
NC11/25/ 1A/1B	Primary	Bi Phase	-22.8	-5.8	256.5	H ₂ O-NaCl
NC11/25/ 1A/1B	Primary	Bi Phase	-21.2	-9.8	265	H ₂ O-NaCl
NC11/25/ 1A/1B	Secondary	Bi Phase	-23	-5.6	140	H ₂ O-NaCl
NC11/25/ 1A/1B	Secondary	Bi Phase	-21.7	-0.1	182	H ₂ O-NaCl
NC11/25/ 2A	Primary	Mono Phase	-182.3	-120		CH ₄
NC11/25/ 2A	Primary	Mono Phase	-182.3	-114		CH ₄
NC11/25/ 2A	Primary	Mono Phase	-182.3	-113.5		CH ₄
NC11/25/ 2A	Primary	Mono Phase	-182.3	-113		CH ₄

Sample No.	Type of Inclusion	Inclusion Phase	T _{im}	T _{fm}	Th	Fluid Composition
NC11/25/2A	Primary	Mono Phase	-182.3	-111		CH ₄
NC11/25/2A	Primary	Mono Phase	-182.3	-111		CH ₄
NC11/25/2A	Primary	Mono Phase	-182.3	-110		CH ₄
NC11/25/2A	Primary	Mono Phase	-182.3	-110		CH ₄
NC11/25/2A	Primary	Mono Phase	-182.3	-109		CH ₄
NC11/25/2A	Primary	Mono Phase	-182.3	-109		CH ₄
NC11/25/2A	Primary	Mono Phase	-182.3	-108		CH ₄
NC11/25/2A	Primary	Mono Phase	-182.3	-107		CH ₄
NC11/25/2A	Primary	Mono Phase	-182.3	-107		CH ₄
NC11/25/2A	Primary	Mono Phase	-182.3	-106		CH ₄
NC11/25/2A	Primary	Mono Phase	-182.3	-106		CH ₄
NC11/25/2A	Primary	Mono Phase	-182.3	-104		CH ₄
NC11/25/2A	Primary	Mono Phase	-182.3	-103		CH ₄
NC11/25/2A	Primary	Mono Phase	-182.2	-113		CH ₄
NC11/25/2A	Primary	Mono Phase	-182.2	-105		CH ₄
NC11/25/2A	Primary	Mono Phase	-182.1	-111		CH ₄
NC11/25/2A	Primary	Mono Phase	-57	-11		CO ₂
NC11/25/2A	Primary	Mono Phase	-56.5	-10.8		CO ₂
NC11/25/2A	Primary	Mono Phase	-56.4	-12.5		CO ₂
NC11/25/2A	Primary	Mono Phase	-56.1	-10.5		CO ₂

Sample No.	Type of Inclusion	Inclusion Phase	T _{im}	T _{fm}	Th	Fluid Composition
NC11/25/2A	Primary	Mono Phase	-56	-16		CO ₂
NC11/25/2A	Primary	Mono Phase	-55.8	-20		CO ₂
NC11/25/2A	Primary	Mono Phase	-55.5	-11.2		CO ₂
NC11/25/2A	Primary	Mono Phase	-55.3	-14.6		CO ₂
NC11/25/2A	Primary	Mono Phase	-55.1	-22.2		CO ₂
NC11/25/2A	Primary	Mono Phase	-55.1	-18		CO ₂
NC11/25/2A	Primary	Mono Phase	-55	-16		CO ₂
NC11/25/2A	Primary	Bi Phase	-22.2	-16.7	282	H ₂ O-NaCl
NC11/25/2A	Primary	Bi Phase	-22.1	-17.1	284	H ₂ O-NaCl
NC11/25/2A	Primary	Bi Phase	-22.1	-16.8	283	H ₂ O-NaCl
NC11/25/2A	Primary	Bi Phase	-21.5	-17.8	289	H ₂ O-NaCl
NC11/25/2A	Primary	Bi Phase	-21.4	-17.7	287	H ₂ O-NaCl
NC11/25/2A	Primary	Bi Phase	-21.3	-18.2	293	H ₂ O-NaCl
NC11/25/2A	Primary	Bi Phase	-21.3	-17.5	286	H ₂ O-NaCl
NC11/25/2A	Primary	Bi Phase	-21.3	-16.5	283	H ₂ O-NaCl
NC11/25/2A	Primary	Bi Phase	-21.3	-15	280	H ₂ O-NaCl
NC11/25/2A	Primary	Bi Phase	-21.2	-18.9	300	H ₂ O-NaCl
NC11/25/2A	Primary	Bi Phase	-21.2	-18.5	294	H ₂ O-NaCl
NC11/25/2A	Primary	Bi Phase	-21.2	-18.1	292	H ₂ O-NaCl
NC11/25/2A	Primary	Bi Phase	-21.2	-18	291	H ₂ O-NaCl

Sample No.	Type of Inclusion	Inclusion Phase	T_{im}	T_{fm}	T_h	Fluid Composition
NC11/25/2A	Primary	Bi Phase	-21.2	-17.9	290	H ₂ O-NaCl
NC11/25/2A	Primary	Bi Phase	-21.2	-17.8	290	H ₂ O-NaCl
NC11/25/2A	Primary	Bi Phase	-21.2	-16	281	H ₂ O-NaCl
NC11/25/2A	Primary	Bi Phase	-21.2	-16	281	H ₂ O-NaCl
NC11/25/2A	Primary	Bi Phase	-21.2	-14.5	275	H ₂ O-NaCl
NC11/25/2A	Primary	Bi Phase	-21.2	-14	274	H ₂ O-NaCl
NC11/25/2A	Primary	Bi Phase	-21.2	-13	273	H ₂ O-NaCl
NC11/25/2A	Secondary	Bi Phase	-23.4	-3.5	140	H ₂ O-NaCl
NC11/25/2A	Secondary	Bi Phase	-23.2	-7.6	112	H ₂ O-NaCl
NC11/25/2A	Secondary	Bi Phase	-22.5	-8.6	198	H ₂ O-NaCl
NC11/25/2A	Secondary	Bi Phase	-22.5	-6.7	187	H ₂ O-NaCl
NC11/25/2A	Secondary	Bi Phase	-22.5	-6.9	183	H ₂ O-NaCl
NC11/25/2A	Secondary	Bi Phase	-22.5	-6.2	183	H ₂ O-NaCl
NC11/25/2A	Secondary	Bi Phase	-22.5	-5.3	176	H ₂ O-NaCl
NC11/25/2A	Secondary	Bi Phase	-22.5	-5.2	175	H ₂ O-NaCl
NC11/25/2A	Secondary	Bi Phase	-22.5	-5.2	175	H ₂ O-NaCl
NC11/25/2A	Secondary	Bi Phase	-22.4	-6.3	185	H ₂ O-NaCl
NC11/25/2A	Secondary	Bi Phase	-22.3	-8.4	195	H ₂ O-NaCl
NC11/25/2A	Secondary	Bi Phase	-22.1	-5.3	115	H ₂ O-NaCl
NC11/25/2A	Secondary	Bi Phase	-22.1	-6.8	187	H ₂ O-NaCl

Sample No.	Type of Inclusion	Inclusion Phase	T_{im}	T_{fm}	Th	Fluid Composition
NC11/25/2A	Secondary	Bi Phase	-22.1	-6.7	186	H ₂ O-NaCl
NC11/25/2A	Secondary	Bi Phase	-22.1	-6.2	183	H ₂ O-NaCl
NC11/25/2A	Secondary	Bi Phase	-22.1	-5.8	179	H ₂ O-NaCl
NC11/25/2A	Secondary	Bi Phase	-21.8	-4.8	117	H ₂ O-NaCl
NC11/25/2A	Secondary	Bi Phase	-21.6	-2	171	H ₂ O-NaCl
NC11/25/2A	Secondary	Bi Phase	-21.5	-3.2	115	H ₂ O-NaCl
NC11/25/2A	Secondary	Bi Phase	-21.5	-2	115	H ₂ O-NaCl
NC11/25/2A	Secondary	Bi Phase	-21.5	-8.3	194	H ₂ O-NaCl
NC11/25/2A	Secondary	Bi Phase	-21.4	-8.2	193	H ₂ O-NaCl
NC11/25/2A	Secondary	Bi Phase	-21.3	-3.1	159.5	H ₂ O-NaCl
NC11/25/2A	Secondary	Bi Phase	-21.3	-4.4	106	H ₂ O-NaCl
NC11/25/2A	Secondary	Bi Phase	-21.3	-7.2	190	H ₂ O-NaCl
NC11/25/2A	Secondary	Bi Phase	-21.3	-6.6	186	H ₂ O-NaCl
NC11/25/2A	Secondary	Bi Phase	-21.3	-6.1	182	H ₂ O-NaCl
NC11/25/2A	Secondary	Bi Phase	-21.2	-3.6	118	H ₂ O-NaCl
NC11/25/2A	Secondary	Bi Phase	-21.2	-9	104	H ₂ O-NaCl
NC11/25/2A	Secondary	Bi Phase	-21.2	-4.2	103	H ₂ O-NaCl
NC11/25/2A	Secondary	Bi Phase	-21.2	-8.7	199	H ₂ O-NaCl
NC11/25/2A	Secondary	Bi Phase	-21.2	-7.5	192	H ₂ O-NaCl
NC11/25/2A	Secondary	Bi Phase	-21.2	-7	189	H ₂ O-NaCl

Sample No.	Type of Inclusion	Inclusion Phase	T _m	T _{fm}	T _h	Fluid Composition
NC11/25/2A	Secondary	Bi Phase	-21.2	-6.7	189	H ₂ O-NaCl
NC11/25/2A	Secondary	Bi Phase	-21.2	-6.5	184	H ₂ O-NaCl
NC11/25/2A	Secondary	Bi Phase	-21.2	-6	180	H ₂ O-NaCl
NC11/25/2A	Secondary	Bi Phase	-20.6	-3.3	90	H ₂ O-NaCl
NC11/25/2B	Primary	Mono Phase	-57.5	-20.2		CO ₂
NC11/25/2B	Primary	Mono Phase	-57.2	-16.2		CO ₂
NC11/25/2B	Primary	Mono Phase	-56.4	-16.4		CO ₂
NC11/25/2B	Primary	Mono Phase	-56.2	-21.4		CO ₂
NC11/25/2B	Primary	Mono Phase	-56.2	-18.5		CO ₂
NC11/25/2B	Primary	Mono Phase	-56.1	-21.4		CO ₂
NC11/25/2B	Primary	Mono Phase	-56	-16.8		CO ₂
NC11/25/2B	Primary	Mono Phase	-55.5	-19		CO ₂
NC11/25/2B	Primary	Mono Phase	-55.5	-18.3		CO ₂
NC11/25/2B	Primary	Mono Phase	-55.5	-12.5		CO ₂
NC11/25/2B	Primary	Mono Phase	-55.3	-13.7		CO ₂
NC11/25/2B	Primary	Bi Phase	-21.2	-3.5	311.6	H ₂ O-NaCl
NC11/25/2B	Secondary	Bi Phase	-23.6	-1.1	117	H ₂ O-NaCl
NC11/25/2B	Secondary	Bi Phase	-23.1	-1.2	109	H ₂ O-NaCl
NC11/25/2B	Secondary	Bi Phase	-22.8	-7.6	165	H ₂ O-NaCl
NC11/25/2B	Secondary	Bi Phase	-22.3	-0.9	125	H ₂ O-NaCl

Sample No.	Type of Inclusion	Inclusion Phase	T _{im}	T _{fm}	Th	Fluid Composition
NC11/25/ 2B	Secondary	Bi Phase	-21.1	-4.4	134	H ₂ O-NaCl

B-4) Lato-Miru-Upshi (LMU) section of SLAP:

Sample No.	Type of Inclusion	Inclusion Phase	T _{im}	T _{fm}	Th	Fluid Composition
LMU11/12	Primary	Mono Phase	-182.4	-105		CH ₄
LMU11/12	Primary	Mono Phase	-182.3	-110		CH ₄
LMU11/12	Primary	Mono Phase	-182.3	-109		CH ₄
LMU11/12	Primary	Mono Phase	-182.3	-108		CH ₄
LMU11/12	Primary	Mono Phase	-182.3	-107		CH ₄
LMU11/12	Primary	Mono Phase	-182.3	-106		CH ₄
LMU11/12	Primary	Mono Phase	-182.3	-106		CH ₄
LMU11/12	Primary	Mono Phase	-182.3	-103		CH ₄
LMU11/12	Primary	Mono Phase	-182.3	-103		CH ₄
LMU11/12	Primary	Mono Phase	-182.3	-98		CH ₄
LMU11/12	Primary	Mono Phase	-182.2	-110		CH ₄
LMU11/12	Primary	Mono Phase	-182.2	-110		CH ₄
LMU11/12	Primary	Mono Phase	-182.2	-107		CH ₄
LMU11/12	Primary	Mono Phase	-182.2	-106		CH ₄
LMU11/12	Primary	Mono Phase	-182.2	-105		CH ₄
LMU11/12	Primary	Mono Phase	-182.2	-101		CH ₄
LMU11/12	Primary	Mono Phase	-182.2	-100		CH ₄
LMU11/12	Primary	Mono Phase	-182.2	-99		CH ₄
LMU11/12	Primary	Mono Phase	-182.1	-107		CH ₄
LMU11/12	Primary	Mono Phase	-182.1	-104		CH ₄
LMU11/12	Primary	Mono Phase	-57.1	-19.8		CO ₂
LMU11/12	Primary	Mono Phase	-57.1	-19.8		CO ₂
LMU11/12	Primary	Mono Phase	-56.8	-18.2		CO ₂
LMU11/12	Primary	Mono Phase	-56.6	-18.1		CO ₂
LMU11/12	Primary	Mono Phase	-56.6	-14.1		CO ₂
LMU11/12	Primary	Mono Phase	-56.5	-17.1		CO ₂
LMU11/12	Primary	Mono Phase	-56.4	-17.1		CO ₂

Sample No.	Type of Inclusion	Inclusion Phase	T _{im}	T _{fm}	Th	Fluid Composition
LMU11/12	Primary	Mono Phase	-56.4	-15		CO ₂
LMU11/12	Primary	Mono Phase	-56.3	-16.3		CO ₂
LMU11/12	Primary	Mono Phase	-56.3	-16		CO ₂
LMU11/12	Primary	Mono Phase	-56.2	-16		CO ₂
LMU11/12	Primary	Mono Phase	-55.5	-16.5		CO ₂
LMU11/12	Primary	Mono Phase	-55	-15.2		CO ₂
LMU11/12	Primary	Mono Phase	-55	-12.4		CO ₂
LMU11/12	Primary	Bi Phase	-23.7	-0.5	241.2	H ₂ O-NaCl
LMU11/12	Primary	Bi Phase	-22.8	-6.5	278	H ₂ O-NaCl
LMU11/12	Primary	Bi Phase	-22.4	-6.6	276	H ₂ O-NaCl
LMU11/12	Primary	Bi Phase	-22.3	-11.2	267	H ₂ O-NaCl
LMU11/12	Primary	Bi Phase	-22.3	-10.2	265	H ₂ O-NaCl
LMU11/12	Primary	Bi Phase	-22.1	-17.1	282	H ₂ O-NaCl
LMU11/12	Primary	Bi Phase	-21.5	-4.7	282	H ₂ O-NaCl
LMU11/12	Primary	Bi Phase	-21.3	-14.2	270	H ₂ O-NaCl
LMU11/12	Primary	Bi Phase	-21.2	-4.1	253	H ₂ O-NaCl
LMU11/12	Primary	Bi Phase	-21.2	-18.9	300	H ₂ O-NaCl
LMU11/12	Primary	Bi Phase	-21.2	-18.2	300	H ₂ O-NaCl
LMU11/12	Primary	Bi Phase	-21.2	-17.6	285	H ₂ O-NaCl
LMU11/12	Primary	Bi Phase	-21.2	-17.4	284	H ₂ O-NaCl
LMU11/12	Primary	Bi Phase	-21.2	-17	281	H ₂ O-NaCl
LMU11/12	Primary	Bi Phase	-21.2	-17.2	281	H ₂ O-NaCl
LMU11/12	Primary	Bi Phase	-21.2	-16.9	280	H ₂ O-NaCl
LMU11/12	Primary	Bi Phase	-21.2	-16.5	279	H ₂ O-NaCl
LMU11/12	Primary	Bi Phase	-21.2	-16	278	H ₂ O-NaCl
LMU11/12	Primary	Bi Phase	-21.2	-16.3	275	H ₂ O-NaCl
LMU11/12	Primary	Bi Phase	-21.2	-16.2	274	H ₂ O-NaCl
LMU11/12	Primary	Bi Phase	-21.2	-15.3	274	H ₂ O-NaCl
LMU11/12	Primary	Bi Phase	-21.2	-15.2	273	H ₂ O-NaCl
LMU11/12	Primary	Bi Phase	-20.8	-1.3	302.8	H ₂ O-NaCl
LMU11/12	Secondary	Bi Phase	-23.4	-7.2	140	H ₂ O-NaCl
LMU11/12	Secondary	Bi Phase	-23.2	-0.1	160	H ₂ O-NaCl
LMU11/12	Secondary	Bi Phase	-22.6	-10.1	176	H ₂ O-NaCl
LMU11/12	Secondary	Bi Phase	-22.3	-5.2	170	H ₂ O-NaCl
LMU11/12	Secondary	Bi Phase	-22.3	-2.5	162	H ₂ O-NaCl
LMU11/12	Secondary	Bi Phase	-22.3	-3.1	161	H ₂ O-NaCl
LMU11/12	Secondary	Bi Phase	-22.3	-2.1	160	H ₂ O-NaCl
LMU11/12	Secondary	Bi Phase	-22.2	-2.1	159	H ₂ O-NaCl
LMU11/12	Secondary	Bi Phase	-21.7	-1	132	H ₂ O-NaCl
LMU11/12	Secondary	Bi Phase	-21.5	-8.5	182	H ₂ O-NaCl

Sample No.	Type of Inclusion	Inclusion Phase	T _{im}	T _{fm}	Th	Fluid Composition
LMU11/12	Secondary	Bi Phase	-21.4	-0.1	165	H ₂ O-NaCl
LMU11/12	Secondary	Bi Phase	-21.4	-5.4	105	H ₂ O-NaCl
LMU11/12	Secondary	Bi Phase	-21.4	-3.9	165	H ₂ O-NaCl
LMU11/12	Secondary	Bi Phase	-21.3	-9.5	187	H ₂ O-NaCl
LMU11/12	Secondary	Bi Phase	-21.3	-8.2	180	H ₂ O-NaCl
LMU11/12	Secondary	Bi Phase	-21.3	-8.2	179	H ₂ O-NaCl
LMU11/12	Secondary	Bi Phase	-21.3	-7.9	178	H ₂ O-NaCl
LMU11/12	Secondary	Bi Phase	-21.3	-4.1	167	H ₂ O-NaCl
LMU11/12	Secondary	Bi Phase	-21.2	-2.1	170	H ₂ O-NaCl
LMU11/12	Secondary	Bi Phase	-21.2	-10	190	H ₂ O-NaCl
LMU11/12	Secondary	Bi Phase	-21.2	-9.2	184	H ₂ O-NaCl
LMU11/12	Secondary	Bi Phase	-21.2	-6.5	176	H ₂ O-NaCl
LMU11/12	Secondary	Bi Phase	-21.2	-6.5	175	H ₂ O-NaCl
LMU11/12	Secondary	Bi Phase	-21.2	-6.1	175	H ₂ O-NaCl
LMU11/12	Secondary	Bi Phase	-21.2	-6.3	174	H ₂ O-NaCl
LMU11/12	Secondary	Bi Phase	-21.2	-6	174	H ₂ O-NaCl
LMU11/12	Secondary	Bi Phase	-21.2	-5.5	171	H ₂ O-NaCl
LMU11/12	Secondary	Bi Phase	-21.2	-4.5	169	H ₂ O-NaCl
LMU11/12	Secondary	Bi Phase	-21.2	-4.3	166	H ₂ O-NaCl
LMU11/24/ 2B	Secondary	Bi Phase	-22	-11.9	141.4	H ₂ O-NaCl
LMU11/24/ 2B	Secondary	Bi Phase	-20.8	-7.8	141	H ₂ O-NaCl
LMU11/3	Primary	Mono Phase	-57.1	-12.2		CO ₂
LMU11/3	Primary	Mono Phase	-57.1	-12.2		CO ₂
LMU11/3	Primary	Bi Phase	-22.1	-6.7	278	H ₂ O-NaCl
LMU11/3	Primary	Bi Phase	-21.8	-7.6	275	H ₂ O-NaCl
LMU11/3	Primary	Bi Phase	-21.5	-5.2	289	H ₂ O-NaCl
LMU11/3	Primary	Bi Phase	-21.4	-5.1	295	H ₂ O-NaCl
LMU11/3	Primary	Bi Phase	-21.4	-1.9	287	H ₂ O-NaCl
LMU11/3	Primary	Bi Phase	-21.4	-2.1	285	H ₂ O-NaCl
LMU11/3	Primary	Bi Phase	-21.3	-3.4	284	H ₂ O-NaCl
LMU11/3	Primary	Bi Phase	-21.2	-4.2	297	H ₂ O-NaCl
LMU11/3	Primary	Bi Phase	-21.2	-0.4	267	H ₂ O-NaCl
LMU11/3	Primary	Bi Phase	-21.1	-3.9	245	H ₂ O-NaCl
LMU11/3	Primary	Bi Phase	-21.1	-4.1	240	H ₂ O-NaCl
LMU11/3	Secondary	Bi Phase	-21.8	-0.9	159	H ₂ O-NaCl
LMU11/3	Secondary	Bi Phase	-21.4	-1.3	178.5	H ₂ O-NaCl
LMU11/3	Secondary	Bi Phase	-21.1	-0.2	120.9	H ₂ O-NaCl
LMU11/3	Secondary	Bi Phase	-21	-1.4	150	H ₂ O-NaCl

Sample No.	Type of Inclusion	Inclusion Phase	T_{im}	T_{fm}	Th	Fluid Composition
LMU11/4	Primary	Mono Phase	-181.5	-82.6		CH ₄
LMU11/4	Primary	Mono Phase	-181.5	-82.6		CH ₄
LMU11/4	Primary	Bi Phase	-21.2	-3.6	281	H ₂ O-NaCl
LMU11/4	Secondary	Bi Phase	-22.6	-5.9	137.4	H ₂ O-NaCl
LMU11/4	Secondary	Bi Phase	-22.6	-6.9	137	H ₂ O-NaCl
LMU11/4	Secondary	Bi Phase	-22.6	-7.1	127	H ₂ O-NaCl
LMU11/4	Secondary	Bi Phase	-22.3	-5.3	140	H ₂ O-NaCl
LMU11/4	Secondary	Bi Phase	-22.1	-5.5	142.1	H ₂ O-NaCl
LMU11/4	Secondary	Bi Phase	-22.1	-4.7	142	H ₂ O-NaCl
LMU11/4	Secondary	Bi Phase	-22	-6.8	131	H ₂ O-NaCl
LMU11/4	Secondary	Bi Phase	-21.9	-4	148	H ₂ O-NaCl
LMU11/4	Secondary	Bi Phase	-21.9	-4.1	145	H ₂ O-NaCl
LMU11/4	Secondary	Bi Phase	-21.8	-2.9	149.8	H ₂ O-NaCl
LMU11/4	Secondary	Bi Phase	-21.8	-8.3	137	H ₂ O-NaCl
LMU11/4	Secondary	Bi Phase	-21.5	-4.6	142	H ₂ O-NaCl
LMU11/4	Secondary	Bi Phase	-21.1	-3.8	183	H ₂ O-NaCl

APPENDIX – C:
ISOTOPIC RESULTS

Isotopic results of quartz and calcite veins from PAP (C-1 and C-2 for Shergol and Zildat sections, respectively) and SLAP (C-3 and C-4 for NC and LMU sections, respectively) are illustrated below.

C-1) Shergol section of PAP:

Sample No.	<u>Quartz</u>	Calcite					
	$\delta^{18}\text{O}$ ‰ (VSMOW) (± 0.1 ‰)	$\delta^{18}\text{O}$ ‰ (VSMOW) (± 0.1 ‰)	$\delta^{13}\text{C}$ ‰ (VPDB) (± 0.1 ‰)	$^{87}\text{Sr}/^{86}\text{Sr}$ ($\pm 2\sigma$)	$^{208}\text{Pb}/^{204}\text{Pb}$ ($\pm 2\sigma$)	$^{207}\text{Pb}/^{204}\text{Pb}$ ($\pm 2\sigma$)	$^{206}\text{Pb}/^{204}\text{Pb}$ ($\pm 2\sigma$)
ST12/1	13.4	-5.5	-	-	-	-	-
ST12/2	13.2	-5.5	-	-	-	-	-
ST12/3	13.3	-5.5	-	-	-	-	-
ST12/4	-	-	-	-	-	-	-
ST12/5	-	-	-	-	-	-	-
ST12/6	-	-	-	37.6157	15.4812	17.7279	-
ST12/7	-	-	-	-	-	-	-
ST12/8	12.5	-7.3	-	-	-	-	-
ST12/9	13.4	-7	-	-	-	-	-
ST12/10	-	-	-	-	-	-	-
ST12/11	12.7	-7.3	-	-	-	-	-
ST12/12	18.7	-1.7	-	-	-	-	-
ST12/13	18.6	-0.6	-	-	-	-	-
ST12/14	-	-	-	-	-	-	-
ST12/15	13	-6.5	-	-	-	-	-

Sample No.	Quartz	Calcite					
	$\delta^{18}\text{O}$ ‰ (VSMOW) (± 0.1 ‰)	$\delta^{18}\text{O}$ ‰ (VSMOW) (± 0.1 ‰)	$\delta^{13}\text{C}$ ‰ (VPDB) (± 0.1 ‰)	$^{87}\text{Sr}/^{86}\text{Sr}$ ($\pm 2\sigma$)	$^{208}\text{Pb}/^{204}\text{Pb}$ ($\pm 2\sigma$)	$^{207}\text{Pb}/^{204}\text{Pb}$ ($\pm 2\sigma$)	$^{206}\text{Pb}/^{204}\text{Pb}$ ($\pm 2\sigma$)
ST12/16	-	-	-	-	-	-	-
ST12/17	-	-	-	-	-	-	-
ST12/18	15.9	-6.5	-	-	-	-	-
ST12/19	17	0.8	-	-	-	-	-
ST12/20	17.1	-3.6	-	37.5164	15.4703	17.7049	-
ST12/21	-	-	-	-	-	-	-
ST12/22	17.3	0.4	-	37.6185	15.5261	17.8276	-
ST12/23	16.8	-2.6	-	-	-	-	-
ST12/24	-	-	-	-	-	-	-
ST12/25	-	-	-	-	-	-	-
ST12/26	14	-5.5	-	-	-	-	-
ST12/27	-	-	-	-	-	-	-
ST12/28	12.5	-6	-	-	-	-	-
ST12/29	-	-	-	-	-	-	-
ST12/30	-	-	-	-	-	-	-
ST12/31	-	-	-	-	-	-	-
ST12/32	-	-	-	-	-	-	-
ST12/33	-	-	-	-	-	-	-
ST12/34	-	-	-	-	-	-	-
ST12/35	-	-	-	-	-	-	-
ST12/36	-	-	-	-	-	-	-
ST12/37	12.8	-7.3	-	-	-	-	-
ST12/38	-	-	-	-	-	-	-
ST12/39	14	-6.8	-	-	-	-	-
ST12/40	13.7	-7	-	-	-	-	-
ST12/41	13.5	-7.4	-	-	-	-	-
ST12/42	-	-	-	-	-	-	-
ST12/43	-	-	-	-	-	-	-
ST12/44	-	-	-	-	-	-	-
ST12/45	-	-	-	-	-	-	-
ST12/46	16.3	-2.5	-	-	-	-	-
ST12/47	-	-	-	-	-	-	-
ST12/48	16.4	-2.5	-	-	-	-	-
ST12/49	17	-1.7	-	-	-	-	-
ST12/50	-	-	-	-	-	-	-
ST12/51	13.2	-7	-	-	-	-	-

Sample No.	<u>Quartz</u>	Calcite					
	$\delta^{18}\text{O} \text{‰ (VSMOW)}$ ($\pm 0.1 \text{‰}$)	$\delta^{18}\text{O} \text{‰ (VSMOW)}$ ($\pm 0.1 \text{‰}$)	$\delta^{13}\text{C} \text{‰ (VPDB)}$ ($\pm 0.1 \text{‰}$)	$^{87}\text{Sr}/^{86}\text{Sr} (\pm 2\sigma)$	$^{208}\text{Pb}/^{204}\text{Pb}$ ($\pm 2\sigma$)	$^{207}\text{Pb}/^{204}\text{Pb}$ ($\pm 2\sigma$)	$^{206}\text{Pb}/^{204}\text{Pb}$ ($\pm 2\sigma$)
ST12/52	17.1	1.3	-	-	-	-	-
ST12/53	18.1	0.7	-	-	-	-	-
ST12/54	18.1	-3.3	-	-	-	-	-
ST12/55	18	-2.7	-	-	-	-	-
ST13/30 (v1)	17.7	-1.4	-	-	-	-	-
ST13/30 (v1+2)	17.9	-1.7	-	-	-	-	-
ST13/30 (v2)	18	-1.4	-	-	-	-	-
ST13/30 (v3)	18	-1.8	-	-	-	-	-

C-2) Zildat section of PAP:

Sample No.	<u>Quartz</u>	Calcite					
	$\delta^{18}\text{O} \text{‰ (VSMOW)}$ ($\pm 0.1 \text{‰}$)	$\delta^{18}\text{O} \text{‰ (VSMOW)}$ ($\pm 0.1 \text{‰}$)	$\delta^{13}\text{C} \text{‰ (VPDB)}$ ($\pm 0.1 \text{‰}$)	$^{87}\text{Sr}/^{86}\text{Sr} (\pm 2\sigma)$	$^{208}\text{Pb}/^{204}\text{Pb}$ ($\pm 2\sigma$)	$^{207}\text{Pb}/^{204}\text{Pb}$ ($\pm 2\sigma$)	$^{206}\text{Pb}/^{204}\text{Pb}$ ($\pm 2\sigma$)
ZV13/1	20.2	0.9	-	-	-	-	-
ZV13/2	18.1	2	-	-	-	-	-
ZV13/3	21.8	1.3	-	-	-	-	-
ZV13/4	17.1	0.4	-	40.0833	15.7076	20.7216	-
ZV13/5	16.6	-1.4	-	-	-	-	-
ZV13/6	16.5	-0.9	-	40.18	15.6702	20.0717	-
ZV13/7	16.6	-0.8	-	-	-	-	-
ZV13/8	14.2	-1.9	-	-	-	-	-
ZV13/9	14.4	-1.8	-	-	-	-	-
ZV13/10	14.8	-0.1	-	-	-	-	-
ZV13/11	14.7	-1.3	-	40.0366	15.6652	20.102	-
ZV13/12	14.8	-0.5	-	-	-	-	-

C-3) Nimu–Chilling (NC) section of SLAP:

Sample No.	<u>Quartz</u>	Calcite					
	$\delta^{18}\text{O} \text{‰ (VSMOW)}$ ($\pm 0.1 \text{‰}$)	$\delta^{18}\text{O} \text{‰ (VSMOW)}$ ($\pm 0.1 \text{‰}$)	$\delta^{13}\text{C} \text{‰ (VPDB)}$ ($\pm 0.1 \text{‰}$)	$^{87}\text{Sr}/^{86}\text{Sr} (\pm 2\sigma)$	$^{208}\text{Pb}/^{204}\text{Pb}$ ($\pm 2\sigma$)	$^{207}\text{Pb}/^{204}\text{Pb}$ ($\pm 2\sigma$)	$^{206}\text{Pb}/^{204}\text{Pb}$ ($\pm 2\sigma$)
NC12/2	-	21.2	1.9	0.7083	-	-	-
NC12/4	-	20.7	0.9	0.7089	-	-	-
NC12/5	18.2	-	-	-	-	-	-
NC12/8	16.1	13.1	-5.8	-	-	-	-
NC12/9	-	12.1	-5.9	0.7092	-	-	-
NC12/13	16.1	12.9	-8.4	-	-	-	-
NC12/17	-	15.7	-5.5	0.7098	-	-	-
NC12/18	-	16	-9.3	-	-	-	-
NC12/19	-	12.1	-6	0.7092	-	-	-
NC12/20	20.3	11.1	-7.6	0.7092	-	-	-
NC12/21	22.3	18.8	1	-	-	-	-
NC12/22	22.1	-	-	-	-	-	-
NC12/23	23.4	19	-1	-	-	-	-
NC12/24	21.9	-	-	-	-	-	-
NC12/25	22.1	17.9	-3.9	-	-	-	-
NC12/26	23.2	19.6	-4.3	-	-	-	-
NC12/27	22.8	-	-	-	-	-	-
NC12/28	21.1	17.7	-2.5	0.7071	-	-	-
NC12/29	20.2	16.5	-3.8	0.7068	38.8309	15.6402	18.5776
NC12/30/1	19.2	-	-	-	-	-	-
NC12/30/2	18.8	-	-	-	-	-	-
NC12/31	17.1	13.7	-17.4	0.7094	-	-	-
NC12/33	17.1	13.5	-13	-	-	-	-
NC12/34	-	14.1	-13.4	-	-	-	-
NC12/35	15.9	12.6	-14.3	0.708	-	-	-
NC12/36	17.8	13.7	-17	-	-	-	-
NC12/37	-	12.5	-11.1	-	-	-	-
NC12/38	-	13.5	-12.8	-	-	-	-
NC12/39	17.3	13	-12.3	0.7056	-	-	-
NC12/40	-	14.3	-11.9	0.7056	-	-	-
NC12/41	13.9	-	-	-	-	-	-
NC12/43	-	14.9	-11.2	0.7064	-	-	-
NC12/45	17.6	13.8	-9.1	0.7056	-	-	-
NC12/47	-	8.6	-9.2	0.7061	38.9428	15.6694	18.6066

Sample No.	<u>Quartz</u>	Calcite					
	$\delta^{18}\text{O}$ ‰ (VSMOW) (± 0.1 ‰)	$\delta^{18}\text{O}$ ‰ (VSMOW) (± 0.1 ‰)	$\delta^{13}\text{C}$ ‰ (VPDB) (± 0.1 ‰)	$^{87}\text{Sr}/^{86}\text{Sr}$ ($\pm 2\sigma$)	$^{208}\text{Pb}/^{204}\text{Pb}$ ($\pm 2\sigma$)	$^{207}\text{Pb}/^{204}\text{Pb}$ ($\pm 2\sigma$)	$^{206}\text{Pb}/^{204}\text{Pb}$ ($\pm 2\sigma$)
NC12/48	-	8.8	-9.9	0.7062	39.0374	15.6816	18.6627
NC12/49	-	9.1	-11.2	0.7062	-	-	-
NC12/51	-	6	-13.1	-	39.0098	15.6742	18.657
NC12/52	-	8.4	-15.3	0.7056	-	-	-
NC12/53	13	8.2	-7.4	-	-	-	-
NC12/54	-	5.7	-8.7	-	-	-	-
NC13/1	-	11.5	-0.8	-	-	-	-
NC13/2	-	12.5	-1.1	-	-	-	-
NC13/3	-	12.3	-0.8	-	-	-	-
NC13/4	-	12.4	-1.6	-	-	-	-
NC13/1	-	11.5	-0.8	-	-	-	-
NC13/2	-	12.5	-1.1	-	-	-	-
NC13/3	-	12.3	-0.8	-	-	-	-
NC13/4	-	12.4	-1.6	-	-	-	-

C-4) Lato–Miru–Upshi (LMU) section of SLAP:

Sample No.	<u>Quartz</u>	Calcite					
	$\delta^{18}\text{O}$ ‰ (VSMOW) (± 0.1 ‰)	$\delta^{18}\text{O}$ ‰ (VSMOW) (± 0.1 ‰)	$\delta^{13}\text{C}$ ‰ (VPDB) (± 0.1 ‰)	$^{87}\text{Sr}/^{86}\text{Sr}$ ($\pm 2\sigma$)	$^{208}\text{Pb}/^{204}\text{Pb}$ ($\pm 2\sigma$)	$^{207}\text{Pb}/^{204}\text{Pb}$ ($\pm 2\sigma$)	$^{206}\text{Pb}/^{204}\text{Pb}$ ($\pm 2\sigma$)
LMU12/1	-	14.3	-6.3	0.7099	-	-	-
LMU12/2	-	14	-6.2	0.7099	-	-	-
LMU12/3	18.5	-	-	0.7102	39.2225	15.7154	18.7542
LMU12/4	19.7	-	-	-	-	-	-
LMU12/5	19.6	-	-	-	-	-	-
LMU12/6	19	-	-	-	-	-	-
LMU12/7	-	16.4	-9.1	0.7068	-	-	-
LMU12/8	-	16.4	-8.9	0.7064	-	-	-
LMU12/11	-	12.5	-10.5	-	-	-	-

Sample No.	Quartz	Calcite					
	$\delta^{18}\text{O}$ ‰ (VSMOW) (± 0.1 ‰)	$\delta^{18}\text{O}$ ‰ (VSMOW) (± 0.1 ‰)	$\delta^{13}\text{C}$ ‰ (VPDB) (± 0.1 ‰)	$^{87}\text{Sr}/^{86}\text{Sr}$ ($\pm 2\sigma$)	$^{208}\text{Pb}/^{204}\text{Pb}$ ($\pm 2\sigma$)	$^{207}\text{Pb}/^{204}\text{Pb}$ ($\pm 2\sigma$)	$^{206}\text{Pb}/^{204}\text{Pb}$ ($\pm 2\sigma$)
LMU12/12	-	14.1	-9.7	0.7077	-	-	-
LMU12/13	-	17.8	-6.8	0.708	-	-	-
LMU12/14	-	12.3	-8.4	0.7081	-	-	-
LMU12/15	15	13	-11.7	-	-	-	-
LMU12/16	-	13.3	-8.5	-	-	-	-
LMU12/17	-	12.3	-9	-	-	-	-
LMU12/18	-	14.1	-11	0.7081	-	-	-
LMU12/19	-	14.4	-10.6	-	-	-	-
LMU12/20/1	15.1	11.2	-9.6	-	-	-	-
LMU12/20/2	15.1	12.5	-8.3	-	-	-	-
LMU12/21	-	10.3	-8.9	-	-	-	-
LMU12/22	-	11.6	-7.5	-	-	-	-
LMU12/23	-	13.2	-10.7	-	-	-	-
LMU12/24	-	12.6	-8.6	0.7069	38.9725	15.6709	18.6924
LMU12/25	-	12.1	-10.3	0.7061	-	-	-
LMU12/26	-	14.7	-10.4	-	-	-	-
LMU12/27	20.8	17.4	-9.5	0.7062	38.9921	15.6656	18.6681
LMU12/28	-	-	-	0.7061	-	-	-
LMU12/29	21	-	-	-	-	-	-
LMU12/31	-	-	-	0.7077	-	-	-
LMU12/32	-	17.3	-13.3	0.7076	38.9894	15.6649	18.6444
LMU12/33	-	20.4	-9.5	-	-	-	-
LMU12/34	21.4	17.6	-9.1	0.7081	-	-	-
LMU12/35	-	19	-9.1	-	-	-	-
LMU12/36	-	18.9	-9.8	-	-	-	-
LMU12/37	21.9	24.9	-5.7	-	-	-	-
LMU12/38	-	18.8	-9.9	-	-	-	-
LMU12/39	17.6	14.8	-12.2	0.7067	-	-	-
LMU12/40	-	11.6	-7	-	-	-	-
LMU12/41	13.5	12.1	-6.9	-	-	-	-
LMU12/43	14.4	11.7	-10.5	-	-	-	-
LMU12/44	-	9.9	-8.9	-	-	-	-
LMU12/45	12.9	9.1	-7.7	-	-	-	-
LMU12/46	-	9.2	-7.8	-	-	-	-
LMU12/47	-	10.4	-7.2	-	-	-	-
LMU13/1	-	17.9	-7.7	-	-	-	-

Sample No.	Quartz	Calcite					
	$\delta^{18}\text{O}$ ‰ (VSMOW) (± 0.1 ‰)	$\delta^{18}\text{O}$ ‰ (VSMOW) (± 0.1 ‰)	$\delta^{13}\text{C}$ ‰ (VPDB) (± 0.1 ‰)	$^{87}\text{Sr}/^{86}\text{Sr}$ ($\pm 2\sigma$)	$^{208}\text{Pb}/^{204}\text{Pb}$ ($\pm 2\sigma$)	$^{207}\text{Pb}/^{204}\text{Pb}$ ($\pm 2\sigma$)	$^{206}\text{Pb}/^{204}\text{Pb}$ ($\pm 2\sigma$)
LMU13/2	-	9.9	-8	-	-	-	-
LMU13/3	-	9.8	-7.1	-	-	-	-
LMU13/4	-	9.7	-8	-	-	-	-
LMU13/5	-	8.8	-8.3	-	-	-	-

Aditya Kharya

Wadia Institute of Himalayan Geology

33, G.M.S. Road, Dehradun-248 001 UTTARAKHAND (INDIA)

Designation Senior Research Fellow (SRF)
Group/Division Petrology & Geochemistry
Phone +91-9410900908 (Mob), +91-135-2525-195/323 (Lab)
Fax +91-135-2625-212
Email aditya@wihg.res.in, adityakharya@gmail.com

Educational Qualification

High School	Science	II nd Div	2002	U. P. Board, Allahabad
Intermediate	PCM	I st Div	2004	U. P. Board, Allahabad
B.Sc. (H)	Geology	I st Div	2007	Bundelkhand University, Jhansi
M.Sc.	Geology	I st Div	2009	Bundelkhand University, Jhansi

Scholarships/Awards/Honors

- ✓ DST (JRF) tenable at Wadia Institute of Himalayan Geology, from July 2011–July 2013.
- ✓ DST (SRF) tenable at Wadia Institute of Himalayan Geology, from July 2013 to March 2014.
- ✓ SRF (Institute) at Wadia Institute of Himalayan Geology, since March 2014.

Research Interests

- ✓ Isotope Geochemistry,
- ✓ Fluid Inclusion,
- ✓ Metamorphic Petrology,
- ✓ Himalaya

Instrumentation

- ✓ Mass Spectrometer (IRMS)
- ✓ Laser Fluorination System
- ✓ Fluid Inclusion: Micro Thermometry,
- ✓ Raman spectroscopy
- ✓ Petrography Tools, Arc GIS, ERDAS and Rock Works

List of Publications:

Research Papers in Referred Journals

- 1) Bhattacharya, S., Panigrahi, M.K., Sachan, H.K., and **Kharya, A. (2014)** Oxygen isotope ratio of quartz veins from of the auriferous Ramagiri-Penakacherla schist belt and surrounding granitoids in the Eastern Dharwar Craton: A case for a possible link between gold mineralization and granite magmatism. **Ore Geology Review**, vol. 63, pp 201-208.

- 2) Sachan, H.K., Saxena, A., Verma, P., Rai, S.K. and **Kharya, A. (2013)** Fluid Inclusion Study of the Higher Himalayan Quartzitic Pelites, Garhwal Himalaya, India: Implications for Recrystallization History of Metasediments, **Journal of Geological society of India**, vol. 82, pp. 509-518.
- 3) Singh, S.P., Balram, V., Satyanarayanan, M., Sarma, D.S., Subramanyam, K.S.V., Anjaiah, K.V. and **Kharya, A. (2011)** Platinum Group Minerals from the Madawara Ultramafic-mafic Complex, Bundelkhand Massif, Central India: A Preliminary Note, **Journal of Geological society of India**, vol. 78, pp. 281-283.
- 4) Singh, S.P., Balram, V., Satyanarayanan, M., Anjaiah, K.V. and **Kharya, A. (2010)** Platinum group elements in basic and ultrabasic rocks around Madawara, Bundelkhand Massif, Central India. **Current Science**, vol. 99 (3), pp. 375-383.

Research Papers in Referred Journals (Under Review)

- 1) **Kharya, A.**, Sachan, H. K., Singh, S. K., Rai, S. K. and R. L. Lagad (2014). Tracing mantle activity during the Miocene period in the development of forearc basin of the Himalayan Orogeny. **Geology**; Under Review.
- 2) Rai, S. K., Tiwari, S. K., **Kharya, A.**, Negi, M. and Gupta, A. K. (2014) A Laser based Fluorination (BrF₅) system for the extraction of Oxygen (O₂) and its $\delta^{18}\text{O}$ measurements in the Silicate rocks from the Himalaya. **Current Science**; Under Review.

Papers/Abstracts in Conference/Symposia

- 1) **Kharya, A.**, Sachan, H. K., Singh, S. K. And Gupta, A. K. (2014) Isotopic Evidence of mantle contribution to Ladakh Accretionary Prism (India). **Goldschmidt Conference**, pp 1240.
- 2) **Kharya, A.** and Sachan, H. K. (2013) Stable isotope study of quartz-calcite veins from Ladakh Accretionary Prism, Indus-Tsangpo Suture Zone: Implications for provenance of fluids in fore-arc basin of Trans-Himalaya, **WIHG-IGU Workshop on Modern perspective in Himalayan Geoscience**, pp. 25-26.
- 3) Balram, V., Singh, S.P., Satyanarayanan, M., Anjaiah, K.V. and **Kharya, A. (2009)** Platinum Group Element (PGE) mineralization in Madawara ultramafic complex, **National Seminar on Ore Body Modeling for Genesis, Predictive Metallogeny and Resources Analysis** Bundelkhand Craton, Central India, **Goldschmidt Conference; Geochimica et Cosmica Acta** pp. A79.
- 4) Singh, S.P., Balram, V., Satyanarayanan, M., Anjaiah, K.V. and **Kharya, A. (2008)** Platinum group element (PGE) mineralization from Madawara Igneous Provenance (MIP) in Bundelkhand Massif, Central India., pp. 121-122.